Theoretical Insights into the Coupled Nuclear and Electron Dynamics in Molecules of Biological Relevance

Lena Bäuml

München 2025

Dissertation zur Erlangung des Doktorgrades
der Fakultät für Chemie und Pharmazie
der Ludwig-Maximilians-Universität München

Theoretical Insights into the Coupled Nuclear and Electron Dynamics in Molecules of Biological Relevance

Lena Bäuml
aus
München, Deutschland

2025

Erklärung

Diese Dissertation wurde im Sinne von § 7 der Promotionsordnung vom 28. November 2011 von Frau Prof. Dr. Regina de Vivie-Riedle und Herrn Prof. Dr. Christian Ochsenfeld betreut.

Eidesstattliche Versicherung

Diese Dissertation wurde eigenständig und ohne unerlaubte Hilfe erarbeitet.

München, 27.03.2025

Lena Bäuml

Dissertation eingereicht am:	28.03.2025
1. Gutachter:	Prof. Dr. Christian Ochsenfeld
2. Gutachter:	Prof. Dr. Benjamin Fingerhut
Mündliche Prüfung am:	05.06.2025

Contents

Abstract

Some of the fundamental natural processes like photosynthesis or the photostability of nucleobases depend on ultrafast phenomena. Here, especially the relaxation of a photoexcited molecule via conical intersections (CoIns) is an important phenomenon. The evolving field of attosecond spectroscopy and X-ray absorption spectra (XAS) in particular offer the crucial temporal resolution to observe nuclear and electron dynamics on their natural time scale and even follow the relaxation through CoIns. To interpret and predict the complex spectra the development of theoretical workflows that describe ever more realistic systems is necessary. In this regard this thesis represents an important contribution towards the simulation of time-resolved XAS that include the often neglected electronic coherence.

In the first part the NEMol-grid method is introduced, that allows for the calculation of the coupled nuclear and electron dynamics in molecules. With the grid-based version of NEMol the previously existing ansatz was extended to treat also very delocalized nuclear wavepackets, which often occur in higher dimensional molecular systems. In the first chapter the NEMol-grid approach was applied to the nucleobase uracil to investigate the excitation process and the ensuing relaxation through a CoIn. The second chapter treats the excited state dynamics of the natural pigment chlorophyll *a*. The coupling between the first two excited states Q_y and Q_x, as well as that of the higher lying B_x and B_y were investigated together with the $B \to Q$ relaxation. The obtained results help to better understand these processes, which are crucial for photosynthetic light-harvesting.

In the last part of this thesis a workflow is derived, that combines the coupled dynamics from NEMol with static XAS to obtain time-resolved spectra that include the electronic coherence. The calculations are performed at the XMS-CASPT2 level of theory, capturing the multireference character of the excitations. With XAS it is possible to track the population dynamics and the relaxation through a CoIn. The workflow was first derived to follow the excited states dynamics of uracil and then extended to the much larger chlorophyll molecule. For the latter time-resolved XAS offer the possibility to confirm the coupling between Q_y and Q_x.

List of Publications

This thesis is based on the following five publications listed in chronological order. They are reprinted in chapter 1 [**1**], chapter 2 [**2, 4**] and chapter 3 [**3, 5**], respectively.

[1] L. Bäuml*, T. Schnappinger*, M. F. Kling and R. de Vivie-Riedle, "Photo-Induced Coupled Nuclear and Electron Dynamics in the Nucleobase Uracil", *Front. Phys.*, **9**, 674573 (2021). DOI: 10.3389/fphy.2021.674573

[2] S. Reiter*, L. Bäuml*, J. Hauer and R. de Vivie-Riedle, "Q-Band Relaxation in Chlorophyll: New Insights from Multireference Quantum Dynamics", *Phys. Chem. Chem. Phys.*, **24**, 27212 (2022). DOI: 10.1039/D2CP02914F

[3] L. Bäuml, F. Rott, T. Schnappinger and R. de Vivie-Riedle, "Following the Nonadiabatic Ultrafast Dynamics of Uracil via Simulated X-ray Absorption Spectra", *J. Phys. Chem. A*, **127**, 9787 (2023). DOI: 10.1021/acs.jpca.3c06509

[4] E. Keil, A. Kumar, L. Bäuml, S. Reiter, E. Thyrhaug, S. Moser, C. D. P. Duffy, R. de Vivie-Riedle and J. Hauer, "Reassessing the role and lifetime of Q_x in the energy transfer dynamics of chlorophyll *a*", *Chem. Sci.*, **16**, 1684 (2025). DOI: 10.1039/d4sc06441k

[5] L. Bäuml and R. de Vivie-Riedle, "Coupled Nuclear and Electron Dynamics in Chlorophyll Unraveled by XMS-CASPT2 X-Ray Absorption Spectra", *J. Phys. Chem. B*, **129**, 2159 (2025). DOI: 10.1021/acs.jpcb.4c07787

Additional publications:

- F. Schüppel, T. Schnappinger, L. Bäuml and R. de Vivie-Riedle, "Waveform Control of Molecular Dynamics Close to a Conical Intersection", *J. Chem. Phys.*, **153**, 224307 (2020). DOI: 10.1063/5.0031398.

---

* shared first-authorship

[...] Scientific work must not be considered from the point of
view of the direct usefulness of it. It must be done for itself,
for the beauty of science, and then there is always the chance
that a scientific discovery may become [...] a benefit for humanity.
Marie Curie, The Discovery of Radium ***1921***

Introduction

Ultrafast phenomena play a role in many processes of biological relevance, such as photosynthesis [1–3] and photodamage of the genetic code [4–6]. Under light exposure one or more electrons of a molecule can be excited to energetically higher electronic states. The population subsequently decays to lower lying excited states or the ground state. The relaxation can for example take place via intersystem crossing or via conical intersections (CoIns), which are extraordinary points, seams, or even higher-dimensional crossing spaces between two or more electronic states. Here, the Born-Oppenheimer approximation, that separates nuclear from electronic motion, breaks down, as the states exhibit strong non-adiabatic coupling elements (NACs). CoIns are common, but not always energetically accessible. Through the electron motion in the excited state chemical reactions can occur and activation barriers can be overcome, like for the cis-trans isomerisation of rhodopsin during the process of vision [7–9]. As molecules in higher lying excited states are more prone to chemical reactions and modifications [6, 10, 11], their photostability is directly connected to the existence of ultrafast decay channels like CoIns. For DNA and RNA nucleobases it is especially important to have CoIns that enable an ultrafast relaxation to the ground state before photodamage can occur [4, 11, 12]. The natural pigment chlorophyll, which plays a crucial role during photosynthesis, also requires intrinsic photostability [13, 14]. Also in this case ultrafast decay channels to energetically lower lying states exist [15–17]. The process of photosynthesis is based on the excitation of central chlorophylls in the photosystem complex and a subsequent electron transfer cascade. This means that the excited electron is transferred over several chlorophyll molecules to create an electrochemical potential that ultimately fuels the conversion from photon energy, carbon dioxide, and water to glucose and oxygen [1–3, 18]. A better, fundamental understanding of the behaviour of biologically relevant molecules upon photo-excitation might form the basis for yet unforeseen future applications.

From the experimental side, the rapidly evolving field of femtosecond and attosecond spectroscopy can play an important role for observing the excited state dynamics. With the ultrashort attosecond pulses the observation of not only nuclear dynamics but also electronic motion became possible [19]. Using, for example, XAS it is possible to track the population transfer between different states and even follow the transition through a CoIn [20–22]. Theoretical XAS can aid with the interpretation of the often complex experimental spectra [20, 21, 23–41], but also initiate new experiments. The aim of the theoretical spectra is to be as accurate as possible, while still being feasible with respect to calculation time and costs.

The topics of this thesis represent important steps in the direction of ever more accurate simulated XAS. In particular, a broadly applicable method to simulate the coupled nuclear and electron dynamics in molecules (NEMol) is developed, which becomes relevant when the Born-Oppenheimer approximation breaks down, like at a CoIn, or if the states are externally coupled via a laser pulse. In most methods that are used for the simulation of XAS, the coupled nuclear and electron dynamics is neglected, while it is always present in experimental spectra. Within this thesis a procedure was derived to incorporate the coupled dynamics into the calculation of time-resolved XAS. Additionally, a workflow was developed to simulate XAS at a high level of theory (using the XMS-CASPT2 method) also for larger molecules. All of the mentioned improvements were applied to the RNA nucleobase uracil and the natural pigment chlorophyll *a*.

The first chapter gives an introduction to the NEMol approach. In its original version NEMol lacked an adequate description of very delocalised nuclear wavepackets, which occur frequently in nature. With the NEMol-grid version, developed in this work, it is now possible to treat both, very localised wavepackets with a narrow width, as well as rather delocalised wavepackets that spread across large parts of the potential energy surface (PES). Additionally, for processes that can be described by the transition of one electron between two orbitals, a simplification, the one-electron-two-orbital (1e-2o) picture was derived. The NEMol-grid ansatz was then applied to the nucleobase uracil, where the nuclear wavepacket quickly delocalises after excitation into S_2. The excitation process via an explicitly simulated laser pulse and the subsequent relaxation through a CoIn seam between S_2 and S_1 were both studied in this work. It was shown that the newly developed NEMol-grid ansatz can describe the excited states dynamics of uracil well, both in its density notation, but also with the simplified 1e-2o picture.

In the second part, the coupled dynamics of the natural pigment chlorophyll *a* was simulated. This molecule exhibits a very localised nuclear wavepacket, as the excited state PESs are nearly harmonic. It therefore represents a good test case for the universal applicability of the NEMol-grid method also to more localised wavepackets. The first study of this chapter investigates the Q-band dynamics and the coupling situation between the first two excited states Q_y and Q_x. Whether these two states should be seen as separate states or rather as a single system of highly coupled states is still not definitely decided in the community [42]. The second study focuses on the dynamics after excitation into the energetically higher lying B-band and the subsequent $B \rightarrow Q$ relaxation. Here, a combined theoretical and experimental study was conducted. The Q_y and Q_x, as well as the B_x and B_y were found to be coupled and exhibited an ultrafast population transfer. In addition to the two studies, an outlook is given on different possibilities for the inclusion of solvent effects.

In the third chapter the coupled nuclear and electron dynamics of uracil and chlorophyll *a*, that were presented in the first chapters of this thesis, are studied using simulated time-resolved XAS. Here, the NEMol dynamics are coupled with static XAS to obtain time-resolved XAS that do not only include the nuclear wavepacket dynamics, but also the electronic coherence. With the presented method it is also possible to determine the influence of the electronic coherence on the spectra and therefore to determine in which cases it is necessary to include it. After a description of the workflow to obtain the time-resolved XAS, the application to uracil is discussed. To be able to simulate XAS also for the significantly larger chlorophyll model some adaptations to the workflow were necessary. These are, together with the resulting time-resolved XAS of chlorophyll *a*, discussed in the second part of chapter 3. For both molecules the excited state dynamics could be followed via characteristic spectral features in the time-resolved XAS.

1

Coupled Nuclear and Electron Dynamics

One of the cornerstones of quantum mechanics simulations is the Born-Oppenheimer approximation. In this approximation the coupling between nuclear dynamics and electronic motion is assumed to be negligible. As the mass of the nuclei is several magnitudes larger than that of the electrons, it is assumed that the electrons readjust instantaneously to nuclear motion. However, the Born-Oppenheimer approximation breaks down when the time scales of nuclear and electronic motion approach each other. This is the case if adiabatic PES of different electronic states come close to each other or even intersect, like at CoIns or avoided crossings. CoIns are, depending on the number of degrees of freedom, extraordinary points, seams or even higher dimensional crossing spaces. Also the coupling of different electronic states via a laser pulse has as consequence that even small changes in the nuclear geometry have a large impact on the electronic wavefunction. In both of these situations the nuclear dynamics and electronic motion cannot be separated any more and their coupling has to be considered. Most methods, that are able to treat the electron dynamics are often explicitly time-dependent versions of their well-known quantum-chemical counter parts, such as time-dependent Hartree-Fock [43], TD-DFT [44], time-dependent CI [45, 46] and time-dependent CC [47, 48], and neglect the nuclear motion. Techniques for the simulation of electron dynamics that include the nuclear dynamics often treat the nuclear motion classically and the electron dynamics quantum mechanically and are based on the semiclassical Ehrenfest ansatz [49–57]. However, in cases where the Born-Oppenheimer approximation breaks down, the quantum nature of the nuclei, as well as their interplay with the electrons becomes relevant [58]. A (nearly) exact solution for the full electron-nuclear dynamics can only be achieved for small cases such as H_2^+ [59] and even for these the resulting three-body non-Born-Oppenheimer time-dependent Schrödinger equation (TDSE) is often beyond current capabilities [60]. To treat larger systems, a pool of methods has been developed, often tailored to specific problems. The nuclear-electron orbital (NEO) methods are, for example, well suited to describe proton-coupled electron transfer [61, 62]. In NEO only some of the nuclei (typically protons) are treated quantum mechanically. Recently, a combination of

NEO with quantum computing was tested, which might in the long run enable to conduct also long-time simulations of complex systems [63, 64]. The computationally demanding multi-configuration ansatz [65, 66] is especially suited to describe the first excitation step via a laser pulse. Here, the computation of PES and NACs is not needed. However, it is limited to small molecules and less adapted for longer propagations. Alternatives include multi-configurational Ehrenfest [67], the coupled description of nuclear and electronic flux [68, 69] as well as the more widely used exact factorisation approach [70–74]. Here, the complete wavefunction is factorised into an electronic and a nuclear wavefunction, which move on the same time-dependent PES. Its applicability to CoIns has already been tested [73].

1.1 The NEMol Approach

A less computationally expensive alternative is the NEMol [75] ansatz. Here, the feedback of the electron motion to the nuclear dynamics is less directly included than in the exact factorisation formalism. NEMol offers the possibility to simulate the coupled nuclear and electron dynamics for both, laser pulse induced dynamics, as well as CoIn driven motion. The nuclei are thereby described quantum mechanically and coupled to the electronic wavefunctions propagated in the eigenstate basis. In this thesis and the papers included therein a modified version of the original NEMol ansatz [76–78], the NEMol-grid version [79, 80], was applied. This adapted method allows for the correct simulation of more complex situations like very delocalized wavepackets. In the following section first the general idea of NEMol is introduced, which is the same for both versions. Then the adaptions carried out with the NEMol-grid are illustrated.

To describe the coupled nuclear and electron dynamics one has to determine the temporal evolution of the total molecular wavefunction $\Psi_{tot}(r, R, t)$, which can be written as the sum of the time-dependent electronic wavefunctions $\varphi_i(r, t; R)$ and nuclear wavefunctions $\chi_i(R, t)$ with the coordinates of the nuclei R, the electronic coordinates r and the time t [76–78]:

$$\Psi_{tot}(r, R, t) = \sum_i \chi_i(R, t) \cdot \varphi_i(r, t; R). \tag{1.1}$$

The electronic wavefunctions $\varphi_i(r, t; R)$ are thereby parametrically dependent on the nuclear coordinates R. They define a multi-dimensional vector that includes the involved electronic states. The nuclear wavefunctions $\chi_i(R, t)$ residing in the ith PES form a multi-dimensional vector χ_{tot}. The temporal evolution of χ_{tot} is simulated on coupled PES, which can be done with any quantum dynamics method. In all papers included in this thesis the `QDng` [81] program, developed in house, was applied to describe the nuclear quantum dynamics. To derive an expression for the coupled total electronic wavefunction the total molecular wavefunction $\Psi_{tot}(r, R, t)$ is multiplied from the left with χ_{tot} and integrated over the nuclear coordinates [76–78].

$$\Phi_{tot}(r,t;\langle R\rangle(t)) = \int \chi^{*}_{tot}(R,t)\cdot\Psi_{tot}(r,R,t)dR \tag{1.2}$$

The individual components Φ_j of this vector are defined by the following equation:

$$\Phi_j(r,t;\langle R\rangle(t)) = A_{jj}(t)\cdot\varphi_j(r,t;\langle R\rangle(t)) + \sum_{k\neq j} A_{jk}(t)\cdot\varphi_k(r,t;\langle R\rangle(t)), \tag{1.3}$$

$$\text{with } A_{jk}(t) = \langle\chi_j(R,t)|\chi_k(R,t)\rangle_R. \tag{1.4}$$

The time-dependent population $A_{jj}(t)$ and the time-dependent nuclear overlap terms $A_{jk}(t)$ can be obtained from the nuclear quantum dynamics simulation. The overlap term A_{jk} is directly related to the degree of coherence induced between the involved states. Therefore, it approaches zero for weakly coupled electronic states. In these situations the coupled electronic wavefunctions $\Phi_j(r,t;\langle R\rangle(t))$ equal the uncoupled ones $\varphi_j(r,t;\langle R\rangle(t))$. Both of them depend parametrically on the temporal evolution of the nuclear coordinates $\langle R\rangle(t)$, which means that the electronic structure is modified by the nuclear dynamics. The time-evolution of the real-valued electronic wavefunctions $\varphi_j(r,t;\langle R\rangle(t))$ is achieved by propagation in the electronic phase space [76–78].

$$\varphi_j(r,t;\langle R\rangle(t)) = \varphi_j(r;\langle R\rangle(t))\cdot e^{-i\xi_j(t)} \tag{1.5}$$

The electronic phase factor $\xi_j(t)$ is obtained via numerical integration of the electronic eigenenergies $E_j(\langle R\rangle(t))$ over time.

$$\xi_j(t) = \int_0^t E_j(\langle R\rangle(t))dt. \tag{1.6}$$

As $E_j(\langle R\rangle(t))$ changes with the propagation time, the electronic phase factor $\xi_j(t)$ has to be calculated recursively to retain the memory of the progressing electronic phase.

$$\xi_j(t) = E_j(\langle R\rangle(t))\Delta t + \xi_j(t-\Delta t) \tag{1.7}$$

In the original NEMol approach the time step Δt has to be much smaller than the one chosen for the nuclear dynamics, to ensure a smooth propagation in the complex plane. As the coupled total electronic wavefunction is a high-dimensional, complex quantity, the coupled one-electron density $\rho(r,t;\langle R\rangle(t))$ is used in NEMol instead [76–78].

$$\rho(r,t;\langle R\rangle(t)) = \sum_j A_{jj}(t)\rho_{jj}(r;\langle R\rangle(t)) + \sum_{k>j} 2Re\{A_{jk}(t)\rho_{jk}(r;\langle R\rangle(t))e^{-i\xi_{jk}(t)}\}, \tag{1.8}$$

$$\text{with } \xi_{jk}(t) = \Delta E_{jk}(\langle R\rangle(t))\Delta t + \xi_{jk}(t-\Delta t). \tag{1.9}$$

It is comprised of two terms, the first one consists of the state specific electronic density $\rho_{jj}(r;\langle R\rangle(t))$ multiplied with the corresponding time-dependent population $A_{jj}(t)$. The second one describes the coherent electronic density and consists of the one-electron transition density $\rho_{jk}(r;\langle R\rangle(t))$ weighted by the time-dependent overlap $A_{jk}(t)$ and an exponential that includes the pure electronic phase $\xi_{jk}(t)$, that is proportional to the energy difference ΔE_{jk} between the states j and k. With the original NEMol approach only one geometry per time step, the expectation value of the position, is used to determine $\rho(r,t;\langle R\rangle(t))$. This works well when the nuclear wavepacket is localised. The more delocalised the wavepacket gets the more the description via $\langle R\rangle(t)$ fails. This is due to only parts of the delocalised wavepacket giving rise to large nuclear overlap terms. However, the position of these parts of the wavepacket do not have to coincide with $\langle R\rangle(t)$. For two- and higher-dimensional systems the occurrence of delocalised wavepackets becomes more and more likely. To generalise NEMol beyond the single geometry approximation the NEMol-grid [79, 80] was introduced.

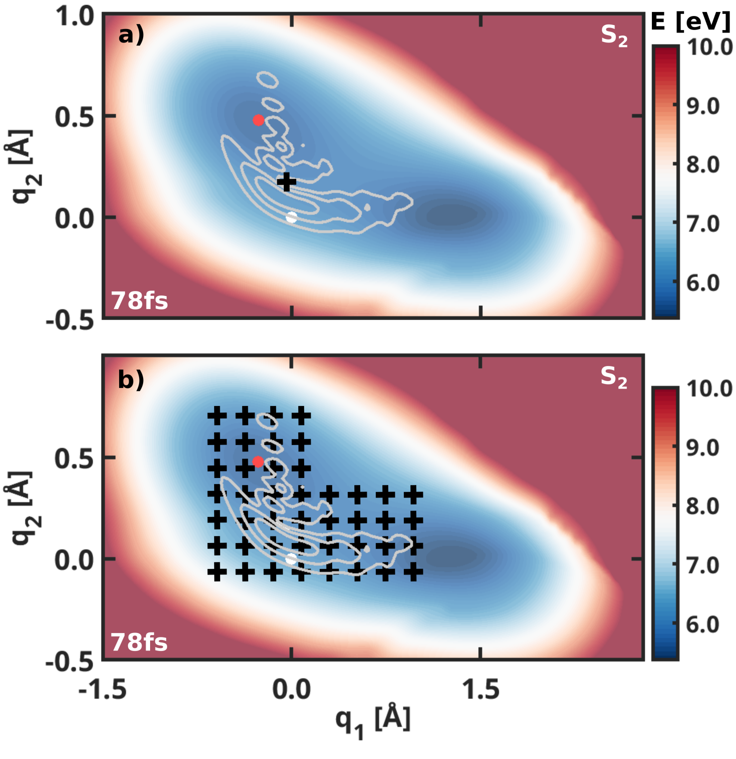

Figure 1.1: The nuclear wavepacket of uracil after laser excitation to the S_2. Illustration of a) the original NEMol approach, that determines the one-electron density for the expectation value of the position and b) the NEMol-grid approach where the density is coupled to multiple grid points. The FC point is marked by a white dot, the S_2 minimum by a red one.

In the NEMol-grid ansatz the nuclear coordinate space is split up into $M \times L$ segments for each of which a partial density ρ_{ml} is calculated. In the limit the NEMol-grid equals the grid of the nuclear wavepacket propagation, but it is possible to choose a coarser one or even a non-regular one if some areas of the PES, e.g. a CoIn should be treated with greater accuracy. The partial densities are calculated by [79, 80]:

$$\rho_{ml}(r,t;R_{ml}) = \sum_{j} \alpha_{jj}^{ml}(t)\rho_{jj}(r;R_{ml}) + \sum_{k>j} 2Re\big\{\alpha_{jk}^{ml}(t)\rho_{jk}(r;R_{ml})e^{-i\xi_{jk}^{ml}(t)}\big\}, \tag{1.10}$$

$$\text{with } \xi_{jk}^{ml}(t) = \Delta E_{jk}(R_{ml})\Delta t + \xi_{jk}^{ml}(t-\Delta t). \tag{1.11}$$

The form of equation 1.10 is very similar to equation 1.8 of the original NEMol. However, with the NEMol-grid the position of R_{ml} does not vary with time. Therefore, a larger time step for the calculation of the phase term can be chosen. The population and overlap terms α_{jj}^{ml} and α_{jk}^{ml} are determined for each segment ml by integration over the wavepackets within the boundaries of the segment. If the NEMol-grid is smaller than the PES, then the population and overlap terms that are arising outside the NEMol-grid are added to the nearest segment, to conserve the total amount of population. In most cases these contributions will be small, as usually a NEMol-grid is chosen that mostly covers the areas where the nuclear wavepacket traverses. For the centre of each segment the state specific electronic densities $\rho_{jj}(r;R_{ml})$, the one-electron transition densities $\rho_{jk}(r;R_{ml})$ and the pure electronic phase $\xi_{jk}^{ml}(t)$ are determined. The total coupled one-electron density $\rho(r,t;R)$ that describes the electron dynamics coupled to multiple grid points is then obtained by summation over the partial densities $\rho_{ml}(r,t;R_{ml})$ [79, 80].

$$\rho(r,t;R) = \sum_{m=1}^{M}\sum_{l=1}^{L} \rho_{ml}(r,t;R_{ml}) \tag{1.12}$$

For cases where the entire dynamics or the relevant part of it are described by the transition of one electron between two coupled states, it is possible to further simplify the NEMol approach by changing the description of the electron density to the 1e-2o picture [79, 80]. This simplification can be applied to both, the original NEMol and the NEMol-grid version. Here, the combination of the 1e-2o picture with the NEMol-grid method is shown for the partial density $\rho_{1e2o}^{ml}(r,t;\langle R_{ml}\rangle(t))$.

$$\begin{aligned}\rho_{1e2o}^{ml}(r,t;\langle R_{ml}\rangle(t)) &= A_{11}^{ml}(t)|\theta_1(r;\langle R_{ml}\rangle(t))|^2 + A_{22}^{ml}(t)|\theta_2(r;\langle R_{ml}\rangle(t))|^2 \\ &+ 2Re\big\{A_{12}^{ml}(t)\theta_1(r;\langle R_{ml}\rangle(t))\theta_2(r;\langle R_{ml}\rangle(t))e^{-i\xi_{12}^{ml}(t)}\big\}\end{aligned} \tag{1.13}$$

In this picture the wavefunctions of the two coupled states are described by two Slater determinants, which only differ in the occupation of one spin orbital θ. The state specific electronic density and the one-electron transition density can then be expressed via the spin orbitals. Neglecting all doubly occupied orbitals $\rho_{1e2o}^{ml}(r,t;\langle R_{ml}\rangle(t))$ is comprised of three terms. The first two correspond to the state specific electronic density weighted by the time-dependent population $A_{11}^{ml}(t)$ and $A_{22}^{ml}(t)$ of the corresponding states. The third one resembles the one-electron transition density weighted by the time-dependent overlap $A_{12}^{ml}(t)$ and the exponential term, that includes the electronic phase $\xi_{12}^{ml}(t)$. Studies [79, 80] showed, that the simplified 1e-2o picture is sufficient to describe the coupled nuclear and electron dynamics in molecules. The NEMol-grid approach has been applied to situations exhibiting very delocalized nuclear wavepackets [80], as well as to localised ones [82]. With the obtained coupled dynamics it is possible to, e.g., observe the carrier-envelop-phase control of a photochemical reaction [79], or to combine it with XAS [83, 84] to simulate more accurate spectra, that include the electronic coherence. The latter possibility will be discussed in detail in chapter 3. In the current chapter the general NEMol-grid approach, as well as the simplified 1e-2o picture were applied to the nucleobase uracil.

1.2 Uracil: A Case of a Delocalised Nuclear Wavepacket

Uracil is one of the five canonical nucleobases that are the building blocks of RNA and DNA. The nucleobases and their specific ordering in the RNA and DNA strands store the genetic information [85–88]. It is assumed that the nucleobases evolved in the prebiotic stage, before the formation of the protective ozone layer in the atmosphere. They must therefore have been exposed to a substantial amount of UV radiation [89, 90]. This might explain their intrinsic photostability which could have evolved due to evolutionary pressure. The ability to absorb and efficiently dissipate the harmful UV radiation posed an evolutionary advantage in early earth history [89, 90]. The intrinsic photostability of the nucleobases is attributed to CoIns between the excited states and the ground state that enable ultrafast relaxation after photoexcitation [12, 91]. While in the excited state, the nucleobases are more susceptible to chemical modifications, methylation, or base alteration. The modified nucleobases can then cause mutations and genomic instabilities that can ultimately result in cancer [6, 10, 92–95]. Nucleobases have been extensively studied both experimentally, as well as theoretically to better understand their excited state dynamics. In the present chapter we focus on the nucleobase uracil, which is present in RNA. Various experiments have been conducted [5, 11, 12, 96–98], that found in average two decay constants, one lying below 200 fs and the other one between 2.0 ps to 3.3 ps. The exact value depends on factors such as the specific excitation wavelength and the resolution of the experiment. Usually the faster time constant is attributed to ultrafast relaxation from the bright S_2 to the dark S_1 state. The S_2 is characterized by an excitation from a π to a π^* orbital, whereas the S_1 is described by the transfer of an electron from a non-bonding to a π orbital. The picosecond decay time is assigned to the subsequent relaxation back to the ground state. The excited state lifetimes change depending on whether a nucleobase monomer is studied in the gas phase or in solution, or if single or double stranded DNA or RNA is investigated [97, 99–102]. In theoretical simulations also the level of theory of the underlying electronic structure theory has shown to be a decisive factor [103]. The paper presented in this chapter investigates the excited state dynamics of uracil after photoexcitation into the bright S_2 state and its relaxation through the S_1/S_2 CoIn. Initially the nuclear wavepacket of uracil is quite localized, but as the simulation time progresses it becomes more and more delocalised, spreading over larger parts of the excited state PES (see Figure 1.2). The quite delocalized nature of the nuclear wavepacket leads to a seemingly long-lived electronic coherence [104]. It is therefore an ideal test case for the NEMol-grid approach.

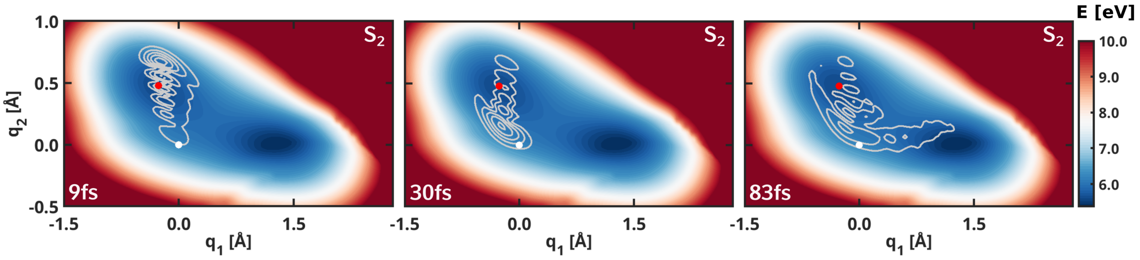

Figure 1.2: The nuclear wavepacket (grey) after laser excitation to the S_2 for different points in time. The FC point is marked by a white dot, the S_2 minimum by a red one.

The article "Photo-Induced Coupled Nuclear and Electron Dynamics in the Nucleobase Uracil" was published in *Frontiers in Physics*. In the following the key points of the article are summarised.

- A grid based ansatz for the NEMol approach was derived. NEMol treats both the nuclear and the electron dynamics purely quantum-mechanically. It enables the simulation of coupled dynamics along a photo-induced relaxation process, including both the interaction with a laser pulse, as well as non-adiabatic events such as the relaxation through a CoIn.

- A simplified version of the NEMol approach, the 1e-2o picture was developed, that is able to describe situations where the dynamics take place between two coupled states. Apart from minor deviations, this approach leads to the same results at lower computational cost as using the total coupled electron density for both the excitation induced dynamics as well as the coupled dynamics near the CoIn.

- After exciting the vast majority of the wavepacket to the S_2 with an excitation pulse, the nuclear wavepacket describes an oscillatory path between the Franck-Condon (FC) point and the S_2 minimum. After an initial oscillation period of 80 fs the wavepacket splits into parts that continue to oscillate, while others propagate to the CoIn seam and relax to the S_1. In this way a constant relaxation of parts of the wavepacket is present. The very delocalised nature of the wavepacket causes apparently long-lived electronic coherence.

- The excitation pulse induced dynamics is described by the excitation of an electron from a bonding π orbital into an anti-bonding π^* orbital. With the NEMol approach this change could be observed in the changing electron density. The induced dipole moment is a potential experimental observable. This exhibits a slow oscillation caused by the initial path of the nuclear wavepacket on the PES and a fast oscillation. A Fourier transform of the fast features revealed them to be at nearly the same frequency as that of the excitation pulse. Comparing the oscillations in the induced dipole moment with the field of the excitation pulse, good agreement with a maximum phase shift of about $0.5\,\pi$ could be observed, as expected. In a time-windowed Fourier transform of the induced dipole moment not only features at the point in time of maximal laser power, but also a second occurrence at the end of the pump pulse is observed. This is caused by parts of the wavepacket having travelled back to the FC point and which are now interacting again with the pulse.

- The relaxation through the CoIn could be observed in the electron density, that changed from a pure non-binding character to a mixed non-bonding and π character. In the time-windowed Fourier transform of the induced dipole moment two main features were present. The frequencies at earlier times were lying at higher energies and are attributed to parts of the nuclear wavepacket reaching the coupling region, but not directly the CoIn seam. At later times features of lower energy appear, as the wavepacket now reaches the CoIn.
- The NEMol-grid approach was successfully applied to treat the delocalized wavepacket dynamics in uracil. With the NEMol-grid version of the ansatz for the coupled nuclear and electron dynamics it is now possible to tackle a whole new range of scientific questions not accessible with the original NEMol approach.

In the following the article "Photo-Induced Coupled Nuclear and Electron Dynamics in the Nucleobase Uracil" published in *Frontiers in Physics* under a Creative Commons Attribution 4.0 International License (CC BY 4.0, URL: https://creativecommons.org/licenses/by/4.0) is reproduced from *Frontiers in Physics*, **9**, 674573 (2021). The supporting information of this article is available under https://www.frontiersin.org/articles/10.3389/fphy.2021.674573.

frontiers in Physics

ORIGINAL RESEARCH
published: 20 May 2021
doi: 10.3389/fphy.2021.674573

Photo-Induced Coupled Nuclear and Electron Dynamics in the Nucleobase Uracil

Lena Bäuml[1†], *Thomas Schnappinger*[1†], *Matthias F. Kling*[2,3] *and Regina de Vivie-Riedle*[1*]

[1] *Department of Chemistry, Ludwig-Maximilians-University Munich, Munich, Germany,* [2] *Max Planck Institute of Quantum Optics, Garching, Germany,* [3] *Department of Physics, Ludwig-Maximilians-University Munich, Garching, Germany*

Photo-initiated processes in molecules often involve complex situations where the induced dynamics is characterized by the interplay of nuclear and electronic degrees of freedom. The interaction of the molecule with an ultrashort laser pulse or the coupling at a conical intersection (CoIn) induces coherent electron dynamics which is subsequently modified by the nuclear motion. The nuclear dynamics typically leads to a fast electronic decoherence but also, depending on the system, enables the reappearance of the coherent electron dynamics. We study this situation for the photo-induced nuclear and electron dynamics in the nucleobase uracil. The simulations are performed with our ansatz for the coupled description of the nuclear and electron dynamics in molecular systems (NEMol). After photo-excitation uracil exhibits an ultrafast relaxation mechanism mediated by CoIn's. Both processes, the excitation by a laser pulse and the non-adiabatic relaxation, are explicitly simulated and the coherent electron dynamics is monitored using our quantum mechanical NEMol approach. The electronic coherence induced by the CoIn is observable for a long time scale due to the delocalized nature of the nuclear wavepacket.

Keywords: quantum dynamics, coupled nuclear and electron dynamics, electronic coherence, conical intersection, photo-excitation, uracil

OPEN ACCESS

Edited by:
Tamar Seideman,
Northwestern University, United States

Reviewed by:
Burkhard Schmidt,
Freie Universität Berlin, Germany
Jiri Pittner,
J. Heyrovsky Institute of Physical Chemistry (ASCR), Czechia

Correspondence:
Regina de Vivie-Riedle
Regina.de_Vivie@cup.uni-muenchen.de

[†] *These authors have contributed equally to this work and share first authorship*

Specialty section:
This article was submitted to Physical Chemistry and Chemical Physics,
a section of the journal Frontiers in Physics

Received: *01 March 2021*
Accepted: *19 April 2021*
Published: *20 May 2021*

Citation:
Bäuml L, Schnappinger T, Kling MF and de Vivie-Riedle R (2021) Photo-Induced Coupled Nuclear and Electron Dynamics in the Nucleobase Uracil. Front. Phys. 9:674573. doi: 10.3389/fphy.2021.674573

1. INTRODUCTION

The interaction of molecular systems with light induces numerous chemical processes which can be natural, such as vision [1–3] and photosynthesis [4–7], or artificial like organic photovoltaics [8–12] and photocatalysis [13, 14]. In these processes a molecule often absorbs light with a wavelength in the visible or ultraviolet range where electrons are promoted from the molecular ground state to higher electronic states. The excited molecule can undergo radiative or non-radiative decay processes. Only the non-radiative processes can lead to photo-chemical reactions which are often mediated by non-adiabatic transitions [15]. The necessary non-adiabatic couplings (NACs) between the states involved are only present in the vicinity of a conical intersection (CoIn) [16–18] or an avoided crossing. Depending on the number of degrees of freedom these CoIn's are extraordinary points, seams or even higher dimensional crossing spaces. Besides the possibility of non-radiative relaxation they lead to the breakdown of the adiabatic separation between nuclear and electronic motion and equalize the time scales of their dynamics. Overall the excitation process and the non-adiabatic transitions are complex situation where both nuclear and electronic motion and their interaction play a key role. In order to simulate these situations a theoretical approach is needed that can describe the coupled nuclear and electron dynamics in a molecular system.

Most methods which can describe the electron dynamics are often modified versions of their well-known quantum-chemical counter parts and neglect the influence of the nuclear motion [19–23] or treat it classically [24–27]. One of the possibilities to treat both the nuclear and the electron dynamics in a molecular systems is the quantum-mechanical NEMol ansatz [28–32]. Within this ansatz the electronic wavefunctions are propagated in the eigenstate basis and coupled to the nuclear wavepacket propagated on coupled potential surfaces. Compared to similar but more expensive approaches based on the coupled propagation of the nuclear and electronic wavefunction on a single time-dependent potential energy surface [33–36], in NEMol the feedback of the electron motion to the nuclear dynamics is less directly included. In the beginning we give a brief introduction to the NEMol ansatz and how we determine the time-dependent electron density. This density is used to distinguish the Born-Oppenheimer part of the dynamics from the coherent electron dynamics. With the help of the NEMol ansatz the electron and nuclear dynamics along a photo-induced relaxation process in molecular systems can be simulated, including both interaction with a laser pulse and non-adiabatic events.

In the main part of this paper we apply NEMol to derive photo-induced dynamics in uracil which is one of the four nucleobases in RNA. Like all other nucleobases uracil absorbs mainly in the UV range due to an accessible $\pi \rightarrow \pi^*$ transition [37, 38]. After the excitation uracil can undergo harmful chemical modifications, such as methylation or base alteration [39–41]. The altered structures and the subsequent changed base pairings can lead to mutations, genomic instability and cancer [37, 40, 42]. To prevent potential mutations in advance, the inherent photostability of the nucleobases is a key factor, assuring that the vast majority of photoexcitations do not lead to harmful modifications [37]. The photostability of all nucleobases is due to the presence of fast relaxation mechanisms back to the ground state. Uracil exhibits an ultrafast relaxation mechanism with experimentally observed relaxation times between 50 fs and 2.4 ps [37, 43–46]. The relaxation is mediated via CoIn's between the first two excited states and has been well-studied using quantum-dynamics on two-dimensional surfaces [47, 48], as well as semi-classical approaches allowing for all degrees of freedom [38, 49–51]. As already demonstrated [52] the coherence induced by these CoIn's is long-lived since the non-adiabatic transition is rather a continuous process due to the delocalized nature of the nuclear wavepacket. We are following the photoinduced dynamics in uracil starting with the explicit simulation of the excitation processes via a laser pulse up to the relaxation via CoIn's. During the whole process NEMol is used to monitor the temporal evolution of the electron dynamics. The simulations demonstrate that the electron dynamics even in large molecular systems reflect coherence, decoherence, and reappearance due to nuclear motion. In previous work the effect of decoherence has been discussed from the nuclear dynamics side [53–55], and the reappearance has been reported for small molecular systems [56–58].

2. COUPLED NUCLEAR AND ELECTRON DYNAMICS IN MOLECULES (NEMol)

To describe the coupled nuclear and electron dynamics it is necessary to determine the temporal evolution of the total molecular wavefunction. This is realized with our NEMol ansatz [28–30]. In a system with multiple electronic states the total wavefunction $\Psi_{tot}(r, R, t)$ can be expressed as a sum over the products consisting of the electronic wavefunctions $\varphi(r, t; R)$ and the wavefunctions of the nuclei $\chi(R, t)$ (see Equation 1), with the nuclear and electronic coordinates R and r and the time t. In this ansatz both the electronic and the nuclear wavefunctions are explicitly time-dependent.

$$\Psi_{tot}(r, R, t) = \sum_i \chi_i(R, t) \cdot \varphi_i(r, t; R). \tag{1}$$

The electronic wavefunctions φ_i are parametrically depending on the nuclear coordinates R and define a multi-dimensional vector comprising the electronic states involved. Analogously, the total nuclear wavefunction χ_{tot} is given by a multi-dimensional vector composed of the nuclear wavefunctions χ_i residing in the i potential surfaces. Its temporal evolution is simulated on coupled potential energy surfaces (PES), for details see **Supplementary Section I**. Multiplying $\Psi_{tot}(r, R, t)$ from the left with χ_{tot} and the subsequent integration over the nuclear coordinates results in an expression of the coupled total electronic wavefunction [28–30].

$$\Phi_{tot}(r, t; \langle R\rangle(t)) = \int \chi^*_{tot}(R, t) \cdot \Psi_{tot}(r, R, t) dR \tag{2}$$

The individual components Φ_j of this vector are defined by the following equation:

$$\begin{aligned}\Phi_j(r, t; \langle R\rangle(t)) &= A_{jj}(t) \cdot \varphi_j(r, t; \langle R\rangle(t)) \\ &\quad + \sum_{k \neq j} A_{jk}(t) \cdot \varphi_k(r, t; \langle R\rangle(t)), \end{aligned} \tag{3}$$

$$\text{with } A_{jk}(t) = \left\langle \chi_j(R, t) \middle| \chi_k(R, t) \right\rangle_R . \tag{4}$$

The time-dependent populations $A_{jj}(t)$ and the time-dependent nuclear overlap terms $A_{jk}(t)$ are determined by the nuclear quantum-dynamics simulation. The overlap terms specify the degree of coherence induced between two states j and k. If the coupling between the electronic states is weak, the nuclear wavefunctions propagate independently and the overlap term becomes zero. In this case, the coupled electronic wavefunctions Φ_j in Equation (3) become equivalent to the uncoupled electronic wavefunction φ_j. All electronic wavefunctions coupled and uncoupled are parametrically depending on the time-dependent expected value of the position $\langle R\rangle(t)$. This means that the coupled electronic wavefunctions are evaluated at one single nuclear geometry which changes with time. The time evolution of the $\varphi_j(r, t; \langle R\rangle(t))$ is determined by the deformation of the electronic structure induced by the nuclear motion and the propagation in the electronic phase space [28–30].

$$\varphi_j(r, t; \langle R\rangle(t)) = \varphi_j(r; \langle R\rangle(t)) \cdot e^{-i\xi_j(t)} \tag{5}$$

Here the $\varphi_j(r;\langle R\rangle(t))$ are the real-valued electronic wavefunctions of the relevant electronic states and $\xi_j(t)$ is the electronic phase factor computed by numerical integration of the electronic eigenenergies $E_j(\langle R\rangle(t))$ over time.

$$\xi_j(t) = \int_0^t E_j(\langle R\rangle(t))dt. \tag{6}$$

In practice the calculation of $\xi_j(t)$ has to be done recursively to retain the memory of the progressing electronic phase since $E_j(\langle R\rangle(t))$ changes with propagation time

$$\xi_j(t) = E_j(\langle R\rangle(t))\Delta t + \xi_j(t-\Delta t). \tag{7}$$

Thereby the propagation velocity of the phase in the complex plane changes smoothly in time while the nuclear wavepacket propagates. Within the original NEMol a much smaller time step must be used for the calculation of the phase term $\xi_j(t)$. The coupled total electronic wavefunction is used to determine the coupled one-electron density $\rho(r,t;\langle R\rangle(t))$ [28–30].

$$\begin{aligned}\rho(r,t;\langle R\rangle(t)) &= \sum_j A_{jj}(t)\rho_{jj}(r;\langle R\rangle(t))\\ &\quad + \sum_{k>j} 2Re\left\{A_{jk}(t)\rho_{jk}(r;\langle R\rangle(t))e^{-i\xi_{jk}(t)}\right\}, \qquad (8)\\ \text{with } \xi_{jk}(t) &= \Delta E_{jk}(\langle R\rangle(t))\Delta t + \xi_{jk}(t-\Delta t). \qquad (9)\end{aligned}$$

The first summation consists of the state specific electronic density $\rho_{jj}(r;\langle R\rangle(t))$ weighted with the corresponding time-dependent population $A_{jj}(t)$. The second summation defines the coherent contribution to the coupled electron density and consists of the time-dependent overlap $A_{jk}(t)$, the one-electron transition density $\rho_{jk}(r;\langle R\rangle(t))$ and its pure electronic phase $\xi_{jk}(t)$ defined by the energy difference ΔE_{jk} between the electronic states involved. This coherent part of the density can be induced by an interaction with a laser pulse or by non-adiabatic coupling events. For non-dissociative molecular dynamics like in uracil the time-dependent overlap determines the disappearance and especially the potential reappearance of the coherent electron dynamics.

To go beyond this single geometry approximation we introduced the NEMol-grid [32] where the full nuclear coordinate space is split up into segments for which partial densities are calculated. In the limit the NEMol-grid is equal to the grid for the nuclear wavepacket propagation, but in practice we choose a coarser one. The partial densities $\rho_{ml}(r,t;R_{ml})$ are defined by:

$$\begin{aligned}\rho_{ml}(r,t;R_{ml}) &= \sum_j \alpha_{jj}^{ml}(t)\rho_{jj}(r;R_{ml})\\ &\quad + \sum_{k>j} 2Re\left\{\alpha_{jk}^{ml}(t)\rho_{jk}(r;R_{ml})e^{-i\xi_{jk}^{ml}(t)}\right\}, \qquad (10)\\ \text{with } \xi_{jk}^{ml}(t) &= \Delta E_{jk}(R_{ml})\Delta t + \xi_{jk}^{ml}(t-\Delta t). \qquad (11)\end{aligned}$$

The population terms $\alpha_{jj}^{ml}(t)$ and the overlap terms $\alpha_{jk}^{ml}(t)$ are calculated by integration over the wavepackets within the boundaries of the segments. At the center R_{ml} of each segment the state specific electronic densities $\rho_{jj}(r;R_{ml})$, the one-electron transition densities $\rho_{jk}(r;R_{ml})$, and the pure electronic phase $\xi_{jk}^{ml}(t)$ are determined. Since the positions R_{ml} do not vary with time the time step for the calculation of the phase term can be chosen larger than for the original NEMol. In this work a time step of 1 a.u. is used. To obtain the total coupled electron density the individual contributions for each segment are summed up.

$$\rho(r,t;R) = \sum_{m=1}^{M}\sum_{l=1}^{L}\rho_{ml}(r,t;R_{ml}). \tag{12}$$

This total coupled one-electron density $\rho(r,t;R)$ (also called full electron density in the following) contains the information of all partial densities determined at multiple grid points weighted with the corresponding population and overlap terms. This is a significant difference from the original NEMol where the electronic structure was only considered at one geometry. To visualize the coupled one-electron density the weighted average R of all R_{ml} is formed. The NEMol-grid extension is used to sample the nuclear wavefunction to improve the resolution of the spatial dependence of the electronic phase term. This is crucial for situations where the nuclear wavepacket is delocalized and only parts of the wavepacket induce coherence in the system. As this is increasingly the case for two and more dimensional systems, the expected value of the position $\langle R\rangle(t)$ is no longer appropriate to capture the electron the electron dynamics. Since uracil is such case we apply the NEMol-grid for all calculations in this work. To study the electron dynamics the induced dipole moment vector $\vec{\mu}$ is calculated using the coupled one-electron density:

$$\vec{\mu}(t) = \int d\vec{r}\rho(r,t;R)\cdot\vec{r}. \tag{13}$$

If the entire dynamics or at least parts of it can be described by two coupled states, it is possible to obtain a simplified description of the electron density in the one-electron-two-orbital (1e-2o)

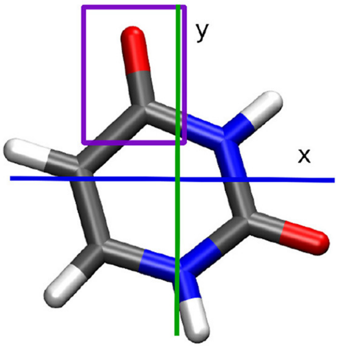

FIGURE 1 | Uracil molecule at the Franck-Condon point. The studied carbonyl group is indicated in purple. Carbon atoms are shown in gray, hydrogen in white, oxygen in red, and nitrogen in blue.

picture, which was derived and successfully applied in reference [32]. Based on the assumption that the two states are described by two Slater determinants, which only differ in the occupation of one spin orbital θ, it is possible to condense the coupled dynamics in a simple 1e-2o-density. The following Equation (14) is based on the original NEMol ansatz (see Equation 8), but the 1e-2o-density can also be determined in combination with the NEMol-grid.

$$\begin{aligned}\rho_{1e2o}(r,t;\langle R\rangle(t)) &= A_{11}(t)|\theta_1(r;\langle R\rangle(t))|^2 + A_{22}(t)|\theta_2(r;\langle R\rangle(t))|^2 \\ &\quad + 2Re\left\{A_{12}(t)\theta_1(r;\langle R\rangle(t))\theta_2(r;\langle R\rangle(t))e^{-i\xi_{12}(t)}\right\}.\end{aligned} \tag{14}$$

Neglecting the contributions of the equally occupied orbitals, the first two terms represent the remaining two orbitals weighted with their respective population $A_{jj}(t)$. The third term denotes the coherence between the states characterized by the product of the two orbitals.

3. PHOTO-INDUCED DYNAMICS OF URACIL

In this work we investigate the photo-induced nuclear and electron dynamics of the nucleobase uracil with NEMol. The geometry of uracil at the Franck-Condon (FC) point is depicted in **Figure 1**. Uracil is characterized by an ultrafast photo-relaxation channel starting in the second excited state (S_2) which is mediated by CoIn's. As shown in previous studies [47, 48], the photo-excitation and the initial steps of the subsequent relaxation can be well-described on two-dimensional PES. We adopt these adiabatic PES, which were first reported by Keefer et al. [47] and later modified [52, 59]. The underlying two-dimensional coordinate space spanned by the vectors q_1 and q_2 includes all relevant structures, the FC point, the S_2 minimum, the optimized S_2/S_1 CoIn and also parts of the associated CoIn seam. Both vectors are depicted on the right side of **Figure 2**. The resulting PES for the bright S_2 state is shown on the left of **Figure 2**. The potential surface exhibits a double-well structure with a small barrier separating the S_2 minimum on the top left from the CoIn seam on the bottom right (black). Further information about the simulations can be found in the **Supplementary Section I**. The molecular orientation within the laboratory frame is chosen in such a way that the molecular plane is equal to the *xy*-plane at the FC point and the center of mass defines the origin of the laboratory frame (see **Figure 1**). To initiate the dynamics and promote the system from the electronic ground state to the S_2 state we use a Gaussian shaped pulse. Its parameters were adapted from a previous work [47]. The pulse has a central frequency ω_0 of 6.12 eV, a full width at half maximum (FWHM) of 30 fs and a maximum field strength of 0.036 GV cm^{-1}. This maximum is reached after 40 fs simulation time. The light-matter interaction is treated within the dipole approximation. We assume that the electric component of the pulse is optimally aligned with the transition dipole moment whose absolute value is used. The complete temporal evolution of the population of all three states is shown in **Figure 3**. The excitation pulse is active in the time period between 10 and 75 fs and leads to an S_2 population yield close to 90%. The motion of the wavepacket in the S_2 state is indicated in white in **Figure 2**. The wavepacket evolves from the FC point toward the S_2 minimum and oscillates back near the FC region. After this first oscillation period (about 80 fs) a part of the wavepacket splits and travels toward the CoIn seam. At around 100 fs the population of the S_2 state starts to decay. During the following oscillations this behavior continues leading to a rather continuous flow of population into the S_1 state.

The NEMol simulations are used to monitor the coupled nuclear and electron dynamics of uracil during the first 200 fs. We assume that the coherent part of the electron dynamics

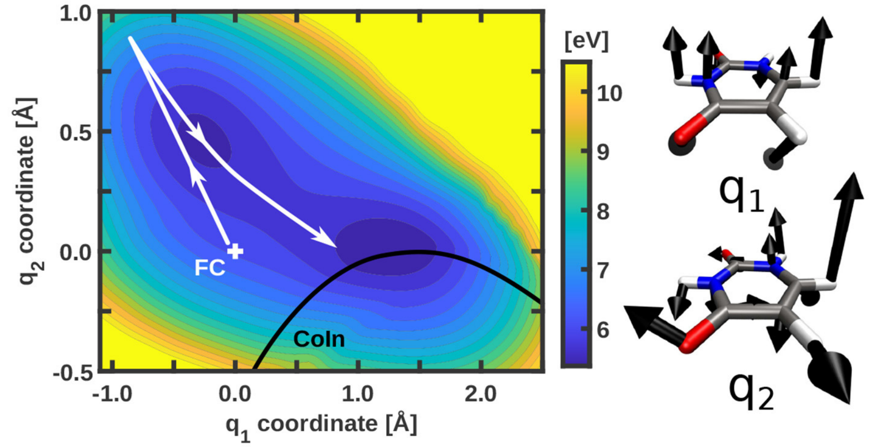

FIGURE 2 | Potential energy surface of the bright S_2 state of uracil with indicated CoIn seam (black) and a schematic representation of the path of the wavepacket (white). The energy scale is given with respect to the global minimum of the S_0 potential energy surface. The two coordinate vectors defining the two-dimensional coordinate space are shown on the right. Only contributions larger than 0.3 Å are depicted.

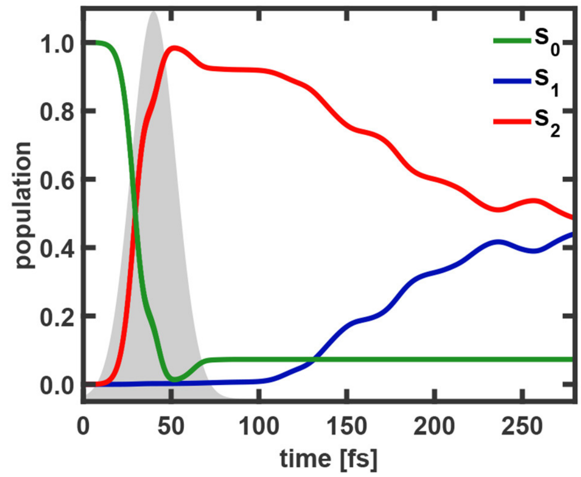

FIGURE 3 | Populations of the S_0, S_1, and S_2 state as a function of the simulation time. The envelope of the excitation pulse is indicated in gray.

is only active during the laser pulse excitation and when the wavepacket is interacting with the CoIn seam. Since these two events are spatially and temporally separated from each other we split our simulation into two parts. Within the interval of the excitation process (0–75 fs) we calculate the coupled electron density including only the properties (densities, population and overlap) of the S_0 and S_2 states. In the second part (75–200 fs), characterized by the relaxation via the CoIn seam, we include only the properties of the S_1 and S_2 states. For both cases we use a NEMol-grid of 14 × 10 segments equally distributed between −0.37 and 1.57 Å in the q_1 coordinate and from −0.57 to 0.86 Å in the q_2 coordinate, shown in **Supplementary Figure 1**. For each of these segments the population terms and the overlap terms of the involved states were determined. The population outside the NEMol-grid was added to the nearest segment on the edge of the grid. For the detailed analysis of the electron dynamics we focus on two quantities, the induced dipole moment and the temporal evolution of the local density at the upper carbonyl group (marked in purple in **Figure 1**). Both are observables, e.g., the fluctuations in the local density could be probed by transient X-ray absorption spectroscopy [60, 61]. Both observables show qualitatively very similar features. The results for the induced dipole moment are presented and discussed in the manuscript, while the ones for the local density are shown in the **Supplementary Material**. We should note that for the excitation dynamics it is important to ensure that the phase information of the laser pulse is solely imprinted on the electronic wavefunction and not also on the nuclear wavefunctions. In our previous work [62, 63], this was realized by calculating the dynamics in the rotating-wave-approximation to describe the laser-induced coupling between the molecular states. In this work we have chosen to remove the phase information of the laser pulse from the nuclear overlap terms.

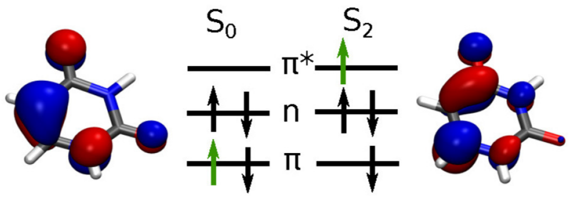

FIGURE 4 | Molecular orbital schemes for the $S_0 \rightarrow S_2$ excitation with the active electron indicated in green and corresponding orbitals at the Franck-Condon point. Orbitals are shown with an isovalue of 0.05.

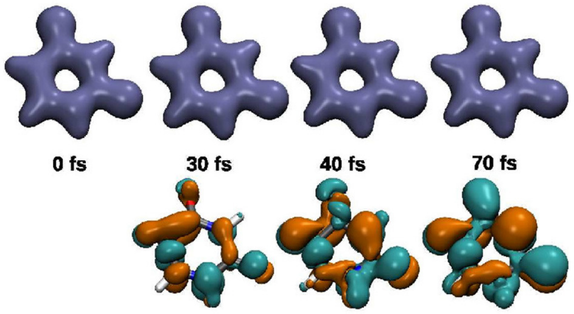

FIGURE 5 | Snapshots of the electron density and the difference in density relative to the density at $t = 0$ fs (green electron-loss, orange electron-gain) for the excitation-pulse induced dynamics between 0 and 75 fs. The isovalues used are 0.08, respectively ±0.003.

3.1. Excitation-Pulse Induced Dynamics

The dynamics induced by the laser pulse excitation is basically characterized by the excitation of one electron from a bonding π orbital into an anti-bonding π^* orbital. This process is illustrated in **Figure 4**. For the following analysis we calculate the full coupled electron density according to Equation (12).

Snapshots of the full coupled electron density are depicted in **Figure 5**. The excitation process follows with slight delay the profile of the resonant light pulse (**Figure 3**). Close to its maximum we observe a slight backtransfer from S_2 to S_0. Thereafter the S_2 population smoothly further increases up to nearly 100% reached at 52 fs. Toward the end of the pulse (at 60–70 fs) about 5% of the population is transferred back to the ground state. In total, 92% of the population was promoted into the S_2 state. With the naked eye nearly no variation is visible in the temporal evolution of the full electron density (top row **Figure 5**). However, studying the difference in density (bottom row) recorded with respect to the one at $t = 0$ fs the change in the bonding/anti-bonding pattern of the π-system becomes observable. In addition the deplanarization of the molecule leads to changes in the σ-system. The corresponding snapshots of the 1e-2o-density can be found in **Supplementary Figure 4**.

The temporal evolution of the induced dipole moment (DM) is determined with and without the coherent part of the coupled electron density included. The difference ΔDM is used to monitor the part of the dipole moment which is induced by the

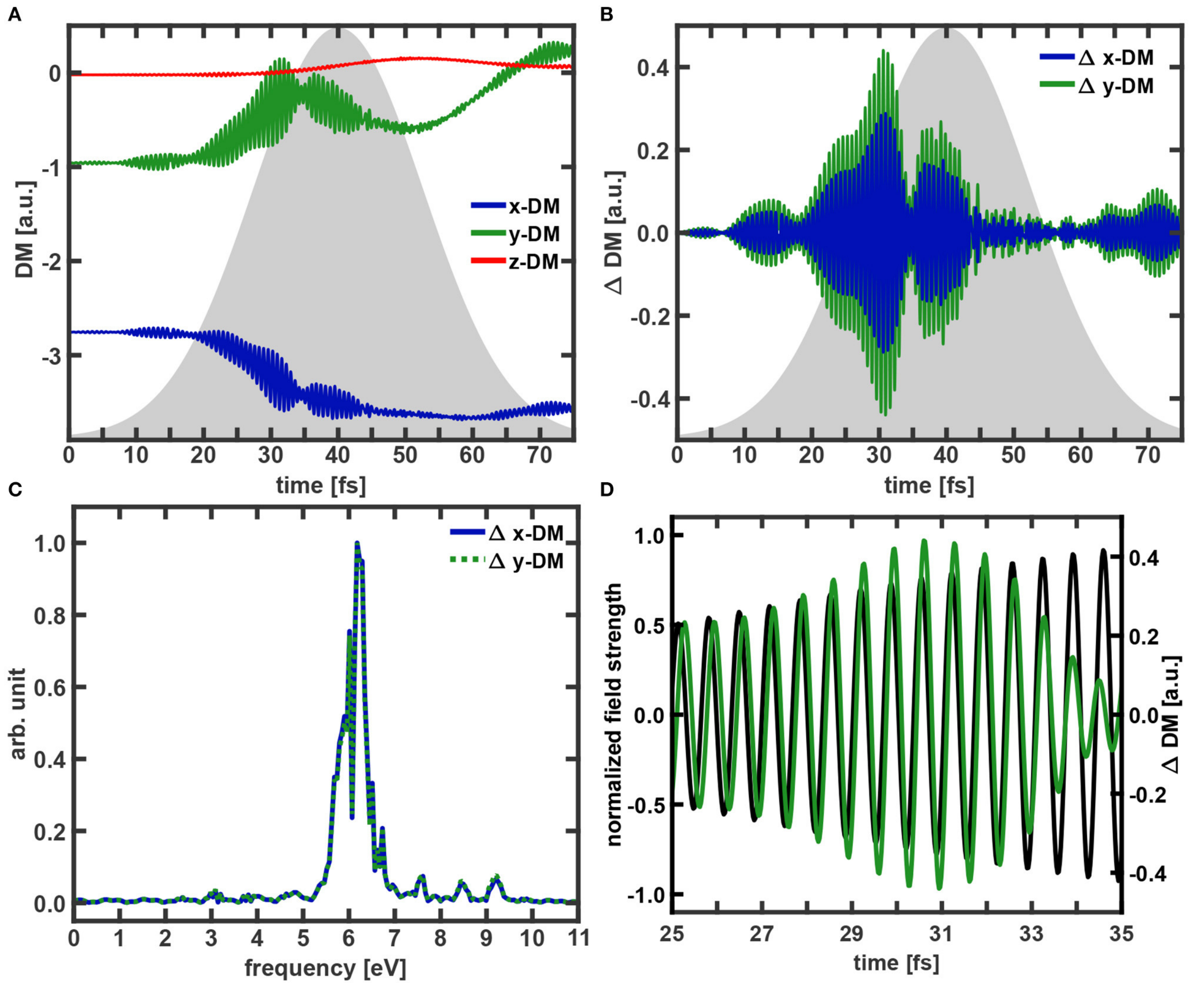

FIGURE 6 | Temporal evolution of the dipole moment components for **(A)** the calculation with the full density and **(B)** for the difference (Δ*DM*) between the dipole moment calculated with and without the coherence term included. The Δ*DM* are only shown for the for *x*- and *y*-components. The envelope of the excitation pulse is indicated in gray. **(C)** Fourier spectra of *x*-Δ*DM* and *y*–Δ*DM*. All spectra are normalized to one. **(D)** Comparison of *y*–Δ*DM* (green) and the electric field of the excitation pulse (black).

coherent electron dynamics. The *DM* components, the Δ*DM* along the *x*- and *y*-coordinate and their Fourier transforms are shown in **Figure 6**. In addition also the comparison of the *y*–Δ*DM* signal and the laser field is depicted. In the beginning of the excitation process the wavepacket mostly remains near the FC point and the molecular geometry stays planar in the *xy*-plane. Therefore, up to 30 fs the *z*-component of the induced dipole moment stays zero. After this period the wavepacket movement toward the S_2 minimum breaks up the planar structure and small modulations of the *z*-component are observed. Compared to the other two components it does not change significantly and is neglected for the further analysis. Regarding the *x*- and *y*-components of the *DM*, two main features are apparent. There is an overall increase (*y*-component), respectively decrease (*x*-component) in the *DM* which is modulated by a slow oscillation with a period of about 40 fs caused by the initial nuclear wavepacket motion around the S_2 minimum. The second feature is an extremely fast oscillation which is especially dominant in the range of 10–45 fs. With the help of the Δ*DM* components (**Figure 6B**) these fast oscillations can be attributed to the coherent electron dynamics. Close to the pulse maximum a pronounced destructive interference appears around 35 fs which coincides with the slight backtransfer of the population (**Figure 3**). The Fourier transforms (**Figure 6C**) of the two Δ*DM* signals clearly reveal that both components share the same main frequencies at 6.18 eV. These frequencies agree very well with the excitation frequency of 6.12 eV. A table of all observed frequencies with an intensity larger than 0.1 can be found in

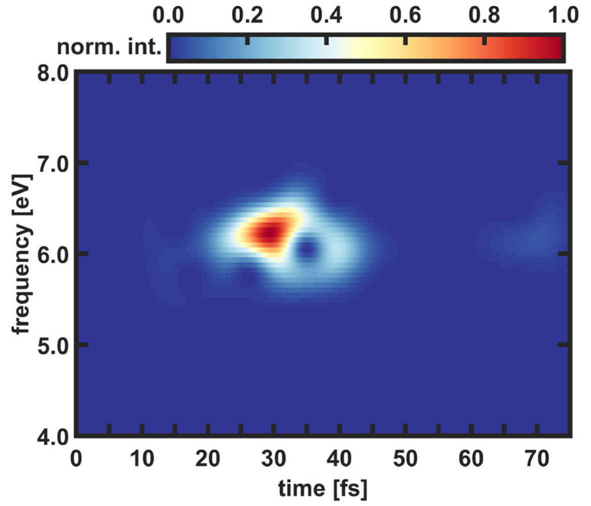

FIGURE 7 | Time-windowed Fourier transform of the y-component of Δ*DM*. The Fourier spectrogram is normalized and a Gaussian window function with a width of 120 data points corresponding to a time of 2.9 fs is used.

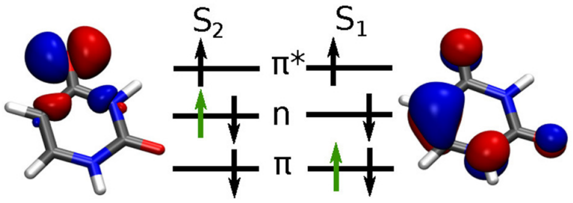

FIGURE 8 | Molecular orbital schemes for the $S_2 \rightarrow S_1$ relaxation with the active electron indicated in green and corresponding orbitals at the Franck-Condon point. Orbitals are shown with an isovalue of 0.05.

Supplementary Table 1. If we now compare the time evolution of the electric field of the pulse with the evolution of y–ΔDM (**Figure 6D**) this good agreement is confirmed and furthermore a maximum phase shift of about 0.5π between the field and the coherent part of the induced dipole moment can be recognized as expected [62, 63]. That means there is a briefly delayed response of the electron dynamics to the laser pulse. Also the beginning of the destructive interference of the electron wavefunctions at 33 fs is visible. In a final step of the analysis we have used a time-windowed Fourier transform of the y–ΔDM signal to determine the time at which the observed frequencies occur. In **Figure 7** the result of the time-windowed Fourier transform is shown applying a Gaussian window function with a width of 120 data points corresponding to a time of 2.9 fs.

In the spectrogram only frequencies in an energy window between 5.5 and 7 eV are visible. During the simulation these frequencies are occurring twice, once between 10 and 45 fs with the maximum being located between 25 and 35 fs, and a second time much weaker from 60 fs onward. The first one is directly induced by the laser pulse and the starting point of this signal matches with the beginning of the population transfer into S_2 state. The second occurrence takes place at the end of the excitation pulse. Until then parts of the wavepacket traveled back to the FC area and are again resonant with the excitation pulse. This enables backtransfer from the S_2 state to the ground state creating again non-zero nuclear overlap terms in Equation (10) and thus coherent electron dynamics. As described in the theory section instead of using the total coupled electron density it is also possible to perform the calculations in the 1e-2o picture (see Equation 14). Besides small deviations, the results in the 1e-2o picture are quite similar and can be found in the **Supplementary Material**. A complete summary of all performed analyses of the coupled electron density can be found in **Supplementary Section IIIA**. In summary, the laser pulse builds up electronic coherence in the molecule. The subsequent nuclear movement leads to decoherence within 10 fs, but about 40 fs later a weak reappearance of the signal due to laser coupling is observed.

3.2. Conical Intersection Induced Dynamics

Since the coupled dynamics of the excitation process is well-described in the 1e-2o picture, we also performed the simulation for the conical intersection induced dynamics in this picture. The two active orbitals which are required to describe the NEMol-dynamics according to Equation (14) are shown in **Figure 8** at the FC point. In this simplified picture the CoIn dynamics is characterized by the transfer of one electron from a non-bonding orbital into a bonding π orbital.

The population dynamics in the time window from 75 to 200 fs and snapshots of the coupled electron density in the 1e-2o picture are depicted in **Figure 9**. The corresponding snapshots obtained with the full electron density are show in **Supplementary Figure 11**. A slow but steady decay of the S_2 population indicating two shallow steps (from 110 to 160 fs and from 170 to 200 fs) is visible. This rather continuous relaxation process is due to the delocalized nature of the nuclear wavepacket. In the 1e-2o picture the variation in the temporal evolution of the electron density is clearly visible (top row **Figure 9B**). For illustration also the difference in density with respect to the one at $t = 75$ fs is depicted. The snapshots reveal a transition from an exclusive non-bonding character at 75 fs to a mixed non-bonding and π character at 195 fs. Over the observed time the majority of the density is located at the upper oxygen atom, but the two left carbon atoms gain more and more density and a π-bond is formed.

For further analysis the temporal evolution of the induced dipole moment calculated with and without the coherent part of the electron density included was determined. The resulting *DM* components, the ΔDM of the x- and y-components and their Fourier transforms are shown in **Figure 10**. In addition the time-windowed Fourier transform of the y–ΔDM signal is depicted there, applying a Gaussian window function with a width of 2.9 fs. As for the excitation dynamics, the z-component of the induced dipole moment does not play a major role and is neglected also in the discussion of the CoIn induced dynamics.

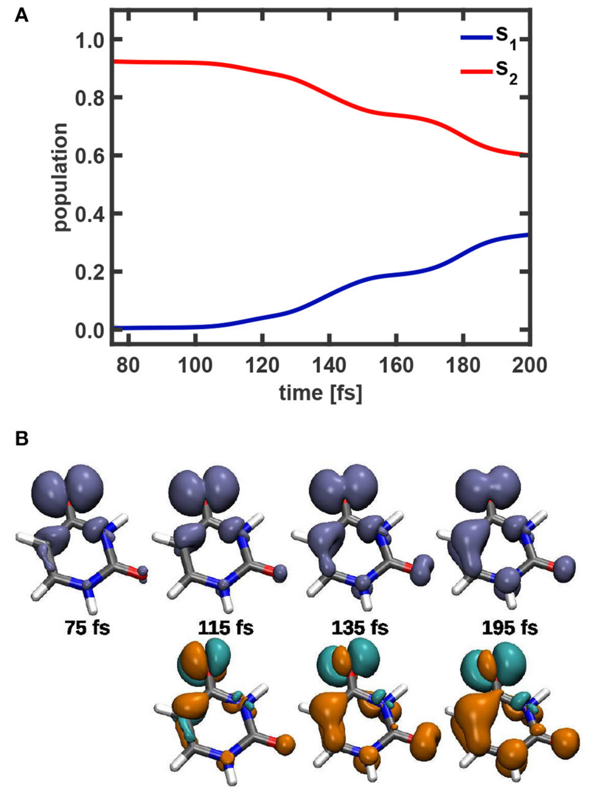

FIGURE 9 | (A) Temporal evolution of the population of the S_1 and S_2 state during the time period between 75 and 200 fs. **(B)** Snapshots of the 1e-2o electron density and the difference in density relative to the density at $t = 75$ fs (green electron-loss, orange electron-gain) in the 1e-2o picture.The isovalues used are 0.002, respectively ±0.0008.

In the overall picture the x-component exhibits a slow and rather small increase, only the y-component shows significant changes and decreases step-wise analogously to the population in S_2. Since the electron density moves mainly along the y-coordinate (see **Figure 9B**), it is logical that this component changes most. Superimposed weak and fast oscillations can be recognized for the y-DM signal and to some extent also for the x-DM signal. As in the previous analysis of the laser induced dynamics these oscillations can be assigned to the coherent electron dynamics. Using the ΔDM components (see **Figure 10B**), intervals with fast oscillations and with slow oscillations can be identified. For the y-component the fast ones appear in the range from 75 to 100 fs, around 120 and 180 fs while the slow ones have larger amplitudes and appear from 100 to 120 fs, 130 to 170 fs, and after 180 fs. Correspondingly two prominent frequency bands occur in the Fourier transforms (**Figure 10C**) of these two ΔDM signals. For the y-component, e.g., the stronger band is centered in a range from 0.25 to 0.75 eV and a weaker band is located between 0.9 and 1.25 eV. A table of all observed frequencies with an intensity larger than 0.1 can be found in **Supplementary Table 3**. Again, as final step of the analysis we performed a time-windowed Fourier transform of the y–ΔDM signal using a Gaussian window function with a width of 2.9 fs. Compared to the case of the laser induced ΔDM (see **Figure 7**) the spectrogram (**Figure 10D**) shows significantly more structured signals. We observe two main peaks in an energy range from 0 to 0.75 eV at 170 and 195 fs and additionally many weaker signals in the same energy region, as well as for higher frequencies (1.0–1.25 eV). The frequencies appearing at early times (75–100 fs) origin from the first parts of the nuclear wavepacket reaching the coupling region but not actually the CoIn seam. This explains the higher energy reflecting the actual energy gap ΔE. Later at 100 fs also lower frequencies appear as the wavepacket now hits the CoIn seam and the energy gap between the states closes. From now on parts of the moving nuclear wavepacket can be found close to the CoIn or in its environment. The intense signals at 170 and 195 fs correlate with the efficient transitions through the CoIn (see **Figure 9A**). The same simulations were also performed to obtain the total coupled electron density according to Equation (12). Comparing the results of the full and the 1e-2o density, the same frequencies and pattern are observed in the electron dynamics. However, the intensities for the higher frequencies are dominant for full density. The results for the full density can be found in the **Supplementary Material**. A complete summary of all performed analyses of the total coupled electron density can be found in **Supplementary Section IIIB**.

In summary, two observations can be made from our NEMol simulation of the conical intersection induced dynamics. The first one is, that the CoIn induces coherent electron dynamics which slows down the closer the system approaches the CoIn. This is expected since CoIn's equalize the time scales of the electron and nuclear dynamics [16, 17]. The second aspect is the longevity of the observed coherence. Due to the delocalized character of the nuclear wavepacket parts of it induce almost continuously coherence in the vicinity of the CoIn leading to a long lived observable signal. This is in good agreement with recently published simulations [52] of TRUECARS signals (transient redistribution of ultrafast electronic coherences in attosecond Raman signals) of the uracil S_2/S_1 CoIn. There, the long lived signal of coherence is also observed and the time-resolved vibronic frequency maps are in the same energy region.

4. CONCLUSION

In this paper, we applied our ansatz for the calculation of the coupled electron and nuclear dynamics in molecular systems (NEMol) [28–32] to the nucleobase uracil. We use the recently formulated extended version [32] operating on the NEMol-grid. As the interplay between nuclear and electron dynamics plays a crucial role in excitation processes as well as during non-adiabatic transitions both situations were studied. The NEMol ansatz treats the nuclear and the electron dynamics both quantum-mechanically. The electronic wavefunctions are propagated in the eigenstate bases and coupled to the nuclear dynamics simulated on coupled potential energy surfaces.

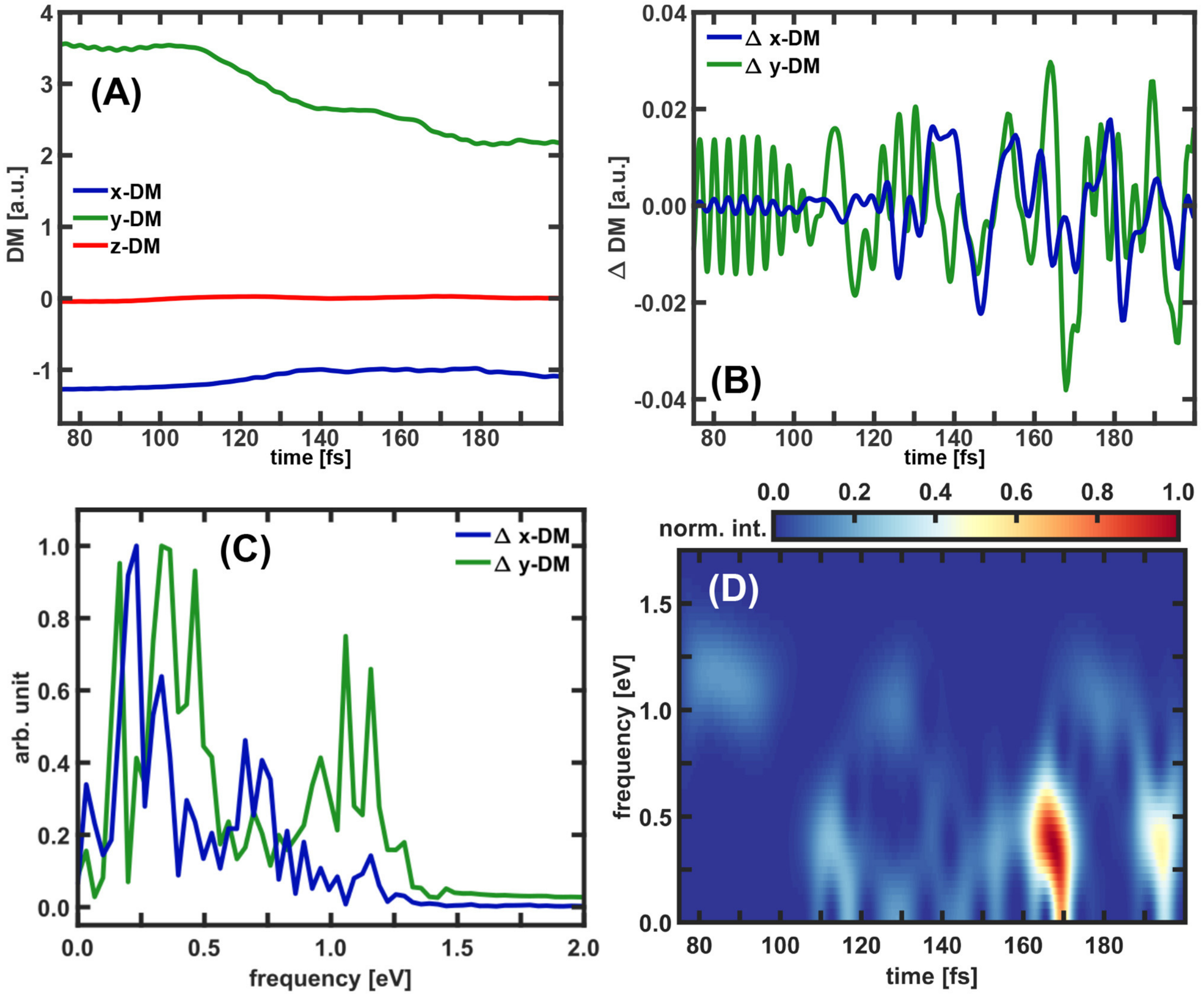

FIGURE 10 | Temporal evolution of the dipole moment for **(A)** the calculation with the 1e-2o picture density and **(B)** for the difference between the dipole moment calculated with and without the coherence term included. The Δ*DM* are only shown for the for *x*- and *y*-components. **(C)** Fourier spectra of *x*-Δ*DM* and *y*–Δ*DM*. All spectra are normalized to one. **(D)** Time-windowed Fourier transform of the y-component of Δ*DM*. The Fourier spectrogram is normalized and a Gaussian window function with a width of 120 data points corresponding to a time of 2.9 fs is used.

With a simple approximation it was possible to simplify the description of the excitation and relaxation processes by expressing the total electron density in the one-electron-two-orbital (1e-2o) picture [32]. In this work, both, the total coupled electron density and the simplified 1e-2o picture, were applied.

The NEMol simulations were used to study the photo-excitation and the CoIn mediated relaxation in uracil. By the choice of ultrashort light pulses these two processes are temporally and spatially separated and can be treated separately. During the excitation one electron is promoted from a bonding π orbital into an anti-bonding π^* orbital. This general change is clearly visible in the NEMol dynamics but it also enables us to analyze the excitation process in greater depth. As a possible observable in an experiment we choose to focus on the induced dipole moment. Studying its temporal evolution, fast oscillations are observed which could be directly attributed to the coherent electron dynamics. Their frequencies are close to the central frequency of the excitation pulse. The coherent dynamics is induced by the laser pulse and subsequent nuclear movement leads to decoherence. A partial reappearance is induced at the end of the laser pulse when the S_2 wavepacket has reentered the FC area. The good agreement between the results obtained with the total electron density and that of the 1e-2o picture supports that the simplified 1e-2o picture can be sufficient to describe the coupled electron dynamics. This 1e-2o picture was used to monitor the coupled electron dynamics induced by the S_2/S_1 conical intersection. The electronic coherence is induced by parts of the rather delocalized nuclear wavepacket and its recurrences at the CoIn and thus can be observed for long times. The frequencies in the induced dipole moment are now rather small, as expected since at the CoIn's the electron dynamics slows down [16–18]. A distinct modulation of these frequencies is observed in the time-windowed Fourier transform reflecting the movement of the nuclear wavepacket around the CoIn seam. Both the longevity and the modulation of the coherence by the nuclear motion is in good agreement with the recent simulation of the TRUECARS signal of the uracil S_2/S_1 CoIn [52]. Here, we demonstrated the capability of the NEMol ansatz to describe the coupled nuclear and electron dynamics in a complex molecular system like uracil. We were able to investigate the electronic coherence that is built up by the laser excitation and modulated by the subsequent nuclear motion. The following relaxation via a conical intersection induces again electronic coherence in the system, which is also treated within the NEMol approach. The verified 1e-2o picture will allow to simulate even larger system.

DATA AVAILABILITY STATEMENT

The raw data supporting the conclusions of this article are available from the corresponding author upon reasonable request.

AUTHOR CONTRIBUTIONS

TS, MK, and RV-R initiated the project. LB performed the calculations. LB, TS, and RV-R analyzed and interpreted the results. All authors contributed to the final version of the manuscript.

ACKNOWLEDGMENTS

The authors gratefully acknowledge the support by the German Research Foundation via VI 144/9-1 and KL-1439/11-1 and the center of excellence Munich Centre of Advanced Photonics (MAP).

SUPPLEMENTARY MATERIAL

The Supplementary Material for this article can be found online at: https://www.frontiersin.org/articles/10.3389/fphy.2021.674573/full#supplementary-material
See the **Supplementary Material** for the details of the wavepacket simulation setup and additional figures and tables for the analyses of the NEMol-dynamics. Animations of the coupled electron density in the 1e-2o picture and the ones using the full density for dynamics induced by the excitation pulse and the CoIn are also shown in the **Supplementary Material**.

Supplementary Data Sheet 1 | Movie_electron dynamics at CoIn.

Supplementary Data Sheet 2 | Movie of electron dynamics during excitation.

REFERENCES

1. Khorana HG. Rhodopsin, photoreceptor of the rod cell–an emerging pattern for structure and function. *J Biol Chem*. (1992) 267:1–4. doi: 10.1016/S0021-9258(18)48444-X
2. Send R, Sundholm D. Stairway to the conical intersection: a computational study of the retinal isomerization. *J Phys Chem A*. (2007) 111:8766–73. doi: 10.1021/jp073908l
3. Polli D, Altoè P, Weingart O, Spillane KM, Manzoni C, Brida D, et al. Conical intersection dynamics of the primary photoisomerization event in vision. *Nature*. (2010) 467:440–3. doi: 10.1038/nature09346
4. Webber AN, Lubitz W. P700: the primary electron donor of photosystem I. *Biochim Biophys Acta*. (2001) 1507:61–79. doi: 10.1016/S0005-2728(01)00198-0
5. Mirkovic T, Ostroumov EE, Anna JM, van Grondelle R, Govindjee, Scholes GD. Light absorption and energy transfer in the antenna complexes of photosynthetic organisms. *Chem Rev*. (2017) 117:249–93. doi: 10.1021/acs.chemrev.6b00002
6. Loll B, Kern J, Saenger W, Zouni A, Biesiadka J. Towards complete cofactor arrangement in the 3.0 angstrom resolution structure of photosystem II. *Nature*. (2005) 438:1040–4. doi: 10.1038/nature04224
7. Scholes GD, Fleming GR, Olaya-Castro A, van Grondelle R. Lessons from nature about solar light harvesting. *Nat Chem*. (2011) 3:763–74. doi: 10.1038/nchem.1145
8. Collings AF, Critchley C. *Artificial Photosynthesis: From Basic Biology to Industrial Application*. London: Wiley (2005). doi: 10.1002/3527606742
9. Andrea Rozzi C, Maria Falke S, Spallanzani N, Rubio A, Molinari E, Brida D, et al. Quantum coherence controls the charge separation in a prototypical artificial light-harvesting system. *Nat Commun*. (2013) 4:1602. doi: 10.1038/ncomms2603
10. Roncali J, Leriche P, Blanchard P. Molecular materials for organic photovoltaics: small is beautiful. *Adv Mater*. (2014) 26:3821–38. doi: 10.1002/adma.201305999
11. Mazzio KA, Luscombe CK. The future of organic photovoltaics. *Chem Soc Rev*. (2015) 44:78–90. doi: 10.1039/C4CS00227J
12. Pelzer KM, Darling SB. Charge generation in organic photovoltaics: a review of theory and computation. *Mol Syst Des Eng*. (2016) 1:10–24. doi: 10.1039/C6ME00005C
13. Ismail AA, Bahnemann DW. Photochemical splitting of water for hydrogen production by photocatalysis: a review. *Solar Energy Mater Solar Cells*. (2014) 128:85–101. doi: 10.1016/j.solmat.2014.04.037
14. Wenderich K, Mul G. Methods, mechanism, and applications of photodeposition in photocatalysis: a review. *Chem Rev*. (2016) 116:14587–619. doi: 10.1021/acs.chemrev.6b00327
15. Nelson TR, White AJ, Bjorgaard JA, Sifain AE, Zhang Y, Nebgen B, et al. Non-adiabatic excited-state molecular dynamics: theory and applications for modeling photophysics in extended molecular materials. *Chem Rev*. (2020) 120:2215–87. doi: 10.1021/acs.chemrev.9b00447
16. Yarkony DR. Diabolical conical intersections. *Rev Mod Phys*. (1996) 68:985–1013. doi: 10.1103/RevModPhys.68.985
17. Baer M. Introduction to the theory of electronic non-adiabatic coupling terms in molecular systems. *Phys Rep*. (2002) 358:75–142. doi: 10.1016/S0370-1573(01)00052-7
18. Domcke W, Yarkony D, Köppel H. *Conical Intersections: Electronic Structure, Dynamics and Spectroscopy*. Vol. 15. Singapore: World Scientific (2004). doi: 10.1142/5406
19. Runge E, Gross EKU. Density-functional theory for time-dependent systems. *Phys Rev Lett*. (1984) 52:997–1000. doi: 10.1103/PhysRevLett.52.997
20. Klamroth T. Laser-driven electron transfer through metal-insulator-metal contacts: time-dependent configuration interaction singles calculations for a Jellium model. *Phys Rev B*. (2003) 68:245421. doi: 10.1103/PhysRevB.68.245421

21. Rohringer N, Gordon A, Santra R. Configuration-interaction-based time-dependent orbital approach for ab initio treatment of electronic dynamics in a strong optical laser field. *Phys Rev A*. (2006) 74:043420. doi: 10.1103/PhysRevA.74.043420
22. Skeidsvoll AS, Balbi A, Koch H. Time-dependent coupled-cluster theory for ultrafast transient-absorption spectroscopy. *Phys Rev A*. (2020) 102:023115. doi: 10.1103/PhysRevA.102.023115
23. Vila FD, Rehr JJ, Kas JJ, Kowalski K, Peng B. Real-time coupled-cluster approach for the cumulant Green's function. *J Chem Theory Comput*. (2020) 16:6983–92. doi: 10.1021/acs.jctc.0c00639
24. Ojanperä A, Havu V, Lehtovaara L, Puska M. Nonadiabatic Ehrenfest molecular dynamics within the projector augmented-wave method. *J Chem Phys*. (2012) 136:144103. doi: 10.1063/1.3700800
25. Alonso JL, Castro A, Echenique P, Rubio A. In: Marques MAL, Maitra NT, Nogueira FMS, Gross EKU, Rubio A, editors. On the combination of TDDFT with molecular dynamics: new developments. In: *Fundamentals of Time-Dependent Density Functional Theory*. Berlin; Heidelberg: Springer Berlin Heidelberg (2012). p. 301–15. doi: 10.1007/978-3-642-23518-4_15
26. Takatsuka K. Theory of molecular nonadiabatic electron dynamics in condensed phases. *J Chem Phys*. (2017) 147:174102. doi: 10.1063/1.4993240
27. Takatsuka K. Nuclear wavepackets along quantum paths in nonadiabatic electron wavepacket dynamics. *Chem Phys*. (2018) 515:52–9. doi: 10.1016/j.chemphys.2018.07.006
28. Geppert D, von den Hoff P, de Vivie-Riedle R. Electron dynamics in molecules: a new combination of nuclear quantum dynamics and electronic structure theory. *J Phys B Atomic Mol Opt Phys*. (2008) 41:074006. doi: 10.1088/0953-4075/41/7/074006
29. von den Hoff P, Znakovskaya I, Kling MF, de Vivie-Riedle R. Attosecond control of the dissociative ionization via electron localization: a comparison between D2 and CO. *Chem Phys*. (2009) 366:139–47. doi: 10.1016/j.chemphys.2009.09.021
30. Znakovskaya I, von den Hoff P, Zherebtsov S, Wirth A, Herrwerth O, Vrakking MJJ, et al. Attosecond control of electron dynamics in carbon monoxide. *Phys Rev Lett*. (2009) 103:103002. doi: 10.1103/PhysRevLett.103.103002
31. Kling MF, von den Hoff P, Znakovskaya I, de Vivie-Riedle R. (Sub-)femtosecond control of molecular reactions via tailoring the electric field of light. *Phys Chem Chem Phys*. (2013) 15:9448–67. doi: 10.1039/c3cp50591j
32. Schnappinger T, de Vivie-Riedle R. Coupled nuclear and electron dynamics in the vicinity of a conical intersection. *J Chem Phys*. (2021) 154:134306. doi: 10.1063/5.0041365
33. Cederbaum LS. Born–Oppenheimer approximation and beyond for time-dependent electronic processes. *J Chem Phys*. (2008) 128:124101. doi: 10.1063/1.2895043
34. Abedi A, Maitra NT, Gross EKU. Exact factorization of the time-dependent electron-nuclear wave function. *Phys Rev Lett*. (2010) 105:123002. doi: 10.1103/PhysRevLett.105.123002
35. Abedi A, Maitra NT, Gross EKU. Correlated electron-nuclear dynamics: exact factorization of the molecular wavefunction. *J Chem Phys*. (2012) 137:22A530. doi: 10.1063/1.4745836
36. Chiang YC, Klaiman S, Otto F, Cederbaum LS. The exact wavefunction factorization of a vibronic coupling system. *J Chem Phys*. (2014) 140:054104. doi: 10.1063/1.4863315
37. Middleton CT, de La Harpe K, Su C, Law YK, Crespo-Hernández CE, Kohler B. DNA excited-state dynamics: from single bases to the double helix. *Annu Rev Phys Chem*. (2009) 60:217–39. doi: 10.1146/annurev.physchem.59.032607.093719
38. Barbatti M, Aquino AJA, Lischka H. The UV absorption of nucleobases: semi-classical ab initio spectra simulations. *Phys Chem Chem Phys*. (2010) 12:4959–67. doi: 10.1039/b924956g
39. Esposito L, Banyasz A, Douki T, Perron M, Markovitsi D, Improta R. Effect of C5-methylation of cytosine on the photoreactivity of DNA: a joint experimental and computational study of TCG trinucleotides. *J Am Chem Soc*. (2014) 136:10838–41. doi: 10.1021/ja5040478
40. Tommasi S, Denissenko MF, Pfeifer GP. Sunlight induces pyrimidine dimers preferentially at 5-methylcytosine bases. *Cancer Res*. (1997) 57:4727–30.
41. Pfeifer GP, You YH, Besaratinia A. Mutations induced by ultraviolet light. *Mutat Res Fundam Mol Mech Mutagen*. (2005) 571:19–31. doi: 10.1016/j.mrfmmm.2004.06.057
42. de Gruijl FR. Skin cancer and solar UV radiation. *Eur J Cancer*. (1999) 35:2003–9. doi: 10.1016/S0959-8049(99)00283-X
43. He YG, Wu CY, Kong W. Decay pathways of thymine and methyl-substituted uracil and thymine in the gas phase. *J Phys Chem A*. (2003) 107:5145–8. doi: 10.1021/jp034733s
44. Kang H, Lee KT, Jung B, Ko YJ, Kim SK. Intrinsic lifetimes of the excited state of DNA and RNA bases. *J Am Chem Soc*. (2002) 124:12958–9. doi: 10.1021/ja027627x
45. Crespo-Hernandez CE, Cohen B, Hare PM, Kohler B. Ultrafast excited-state dynamics in nucleic acids. *Chem Rev*. (2004) 104:1977–2019. doi: 10.1021/cr0206770
46. Ullrich S, Schultz T, Zgierski MZ, Stolow A. Electronic relaxation dynamics in DNA and RNA bases studied by time-resolved photoelectron spectroscopy. *Phys Chem Chem Phys*. (2004) 6:2796–801. doi: 10.1039/b316324e
47. Keefer D, Thallmair S, Matsika S, de Vivie-Riedle R. Controlling photorelaxation in uracil with shaped laser pulses: a theoretical assessment. *J Am Chem Soc*. (2017) 139:5061–6. doi: 10.1021/jacs.6b12033
48. Reiter S, Keefer D, de Vivie-Riedle R. RNA environment is responsible for decreased photostability of uracil. *J Am Chem Soc*. (2018) 140:8714–20. doi: 10.1021/jacs.8b02962
49. Hudock HR, Levine BG, Thompson AL, Satzger H, Townsend D, Gador N, et al. Ab initio molecular dynamics and time-resolved photoelectron spectroscopy of electronically excited uracil and thymine. *J Phys Chem A*. (2007) 111:8500–8. doi: 10.1021/jp0723665
50. Richter M, Mai S, Marquetand P, Leticia Gonzalez L. Ultrafast intersystem crossing dynamics in uracil unravelled by *ab initio* molecular dynamics. *Phys Chem Chem Phys*. (2014) 16:24423–36. doi: 10.1039/C4CP04158E
51. Fingerhut BP, Dorfman KE, Mukamel SJ. Probing the conical intersection dynamics of the RNA base uracil by UV-pump stimulated-Raman-probe signals; *ab initio* simulations. *J Chem Theory Comput*. (2014) 10:1172–88. doi: 10.1021/ct401012u
52. Keefer D, Schnappinger T, de Vivie-Riedle R, Mukamel S. Visualizing conical intersection passages via vibronic coherence maps generated by stimulated ultrafast X-ray Raman signals. *Proc Natl Acad Sci USA*. (2020) 117:24069–75. doi: 10.1073/pnas.2015988117
53. Vacher M, Mendive-Tapia D, Bearpark MJ, Robb MA. Electron dynamics upon ionization: control of the timescale through chemical substitution and effect of nuclear motion. *J Chem Phys*. (2015) 142:094105. doi: 10.1063/1.4913515
54. Jenkins AJ, Vacher M, Twidale RM, Bearpark MJ, Robb MA. Charge migration in polycyclic norbornadiene cations: winning the race against decoherence. *J Chem Phys*. (2016) 145:164103. doi: 10.1063/1.4965436
55. Arnold C, Vendrell O, Santra R. Electronic decoherence following photoionization: full quantum-dynamical treatment of the influence of nuclear motion. *Phys Rev A*. (2017) 95:033425. doi: 10.1103/PhysRevA.95.033425
56. von den Hoff P, Siemering R, Kowalewski M, de Vivie-Riedle R. Electron dynamics and its control in molecules: from diatomics to larger molecular systems. *IEEE J Select Top Quantum Electron*. (2012) 18:119–29. doi: 10.1109/JSTQE.2011.2107893
57. Nikodem A, Levine RD, Remacle F. Quantum nuclear dynamics pumped and probed by ultrafast polarization controlled steering of a coherent electronic state in LiH. *J Phys Chem A*. (2016) 120:3343–52. doi: 10.1021/acs.jpca.6b00140
58. Jia D, Manz J, Yang Y. Timing the recoherences of attosecond electronic charge migration by quantum control of femtosecond nuclear dynamics: a case study for HCCI+. *J Chem Phys*. (2019) 151:244306. doi: 10.1063/1.5134665
59. Schüppel F, Schnappinger T, Bäuml L, de Vivie-Riedle R. Waveform control of molecular dynamics close to a conical intersection. *J Chem Phys*. (2020) 153:224307. doi: 10.1063/5.0031398
60. Bhattacherjee A, Leone SR. Ultrafast X-ray transient absorption spectroscopy of gas-phase photochemical reactions: a new universal probe of photoinduced molecular dynamics. *Acc Chem Res*. (2018) 51:3203–11. doi: 10.1021/acs.accounts.8b00462

61. Zinchenko KS, Ardana-Lamas F, Seidu I, Neville SP, van der Veen J, Lanfaloni VU, et al. Sub-7-femtosecond conical-intersection dynamics probed at the carbon K-edge. *Science*. (2021) 371:489–94. doi: 10.1126/science.abf1656
62. Bayer T, Braun H, Sarpe C, Siemering R, von den Hoff P, de Vivie-Riedle R, et al. Charge oscillation controlled molecular excitation. *Phys Rev Lett*. (2013) 110:123003. doi: 10.1103/PhysRevLett.110.123003
63. Braun H, Bayer T, Sarpe C, Siemering R, de Vivie-Riedle R, Baumert T, et al. Coupled electron-nuclear wavepacket dynamics in potassium dimers. *J Phys B Atomic Mol Opt Phys*. (2014) 47:124015. doi: 10.1088/0953-4075/47/12/124015

Conflict of Interest: The authors declare that the research was conducted in the absence of any commercial or financial relationships that could be construed as a potential conflict of interest.

2

Ultrafast Relaxation Dynamics of Chlorophyll *a*

The ubiquitous natural pigment chlorophyll plays a crucial role in photosynthetic light harvesting. It is found in plants, as well as in other species such as algae or cyanobacteria. It is not only photo- and thermally stable, but also a strong absorbent, especially in the red part of the spectrum. According to geological investigations chlorophylls have evolved between 3.5 billion years and 2.2 billion years ago [1]. They form a class of differently substituted molecules based on the structurally similar molecules porphyrin, chlorin, and bacteriochlorin (see Figure 2.1) [105]. The most prominent chlorophyll is the chlorin based chlorophyll *a*. While organisms with oxygenic photosynthetic functions exist, that are only based on chlorophyll *a*, there are none that exclusively make use of any other chlorophyll type [106]. Among others, it is present in photosystem I and II (PSI and PSII), which are crucial for the light-harvesting in chloroplasts. In both plants and algae, chloroplasts are the organelles that conduct photosynthesis. Depending on its immediate protein environment chlorophyll *a* can take on versatile functions ranging from the creation of a radical anion at $1\,\mathrm{V}$ or higher in PSI over being redox silent to the creation of a radical cation at $-1\,\mathrm{V}$ or lower in PSII [106]. Depending on its position in the photosynthetic compound chlorophyll *a* can act for example as part of the antenna complex that funnels photon-energy to the reaction centre, or also as the reaction centre and the special pair, which is the primary electron donor. The chlorophylls of the antenna complex and the special pair are chemically identical. However, due to their different protein environment they take over very different functions during photosynthetic light-harvesting [1, 107]. Due to their natural abundance and versatile functions chlorophylls and especially chlorophyll *a* have been extensively investigated, both experimentally, as well as theoretically. There have even been three Nobel Prizes in Chemistry awarded for studies ranging from the determination of the structure of chlorophylls (R. Willstätter in 1915 and H. Fischer in 1930) to their total synthesis (R. B. Woodward in 1965). In recent years, studies on the construction of bio-nanohybrids that incorporate photosystems into nanomaterials have been conducted to evaluate possibilities for semi-artificial photosynthesis (for an overview see Ref. [108]). Even though chlorophylls and chlorophyll *a* in particular are well studied there still remain open questions concerning the relaxation process after photo-excitation. In the 1960s Gouterman developed a four orbital model (see Figure 2.2a) to explain UV and visible absorption spectra of porphyrin and its derivatives [109, 110], such as chlorophyll *a*. He thereby used disubstituted porphyrin as a reference and considered other porphyrin based structures and analogues as perturbations. This model enabled qualitative, but not quantitative predictions of electronic spectra [110]. The first two excited states are thereby named Q_y and Q_x, whereas the high-energy excited states are called B_x and B_y. In the absorption spectrum (see Figure 2.2b) the assignment of Q_x poses some difficulties, as further discussed in section 2.1. In recent years especially the Q_y and Q_x are thought to form a system of highly coupled states [42]. Therefore, the NEMol approach [75] discussed in chapter 1 seems well suited to simulate the relaxation process of chlorophyll *a*, in order to shed light on the complex relaxation dynamics. In subsection 2.1 quantum dynamics simulations are applied to investigate the vibronic coupling between the first two excited states, Q_y and Q_x. A corresponding study on the coupling between the higher lying excited states B_x and B_y is conducted in subsection 2.2. Without thorough knowledge of these fundamental processes a complete understanding of photosynthesis and its potential exploitation as a green energy source are not possible. The chapter is closed by an outlook on different ways to include the solvent environment into the simulation of the relaxation dynamics.

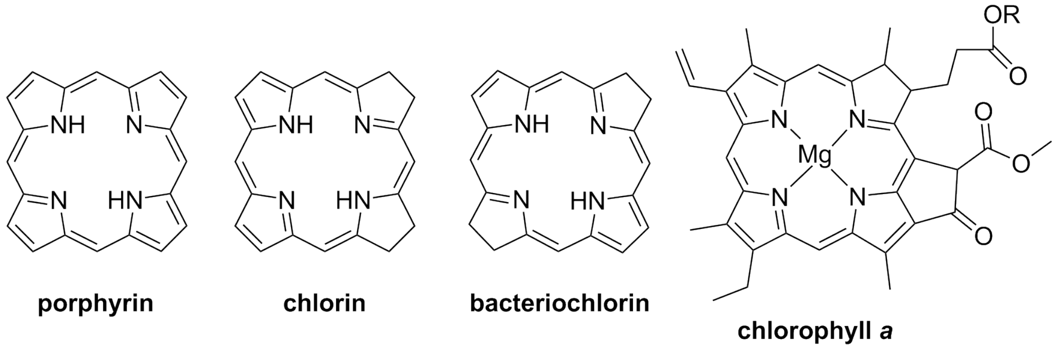

Figure 2.1: Molecular structures of porphyrin, chlorin, bacteriochlorin, and chlorophyll *a*.

2.1 Q-Band Dynamics

The first two excited states of chlorophyll *a* form the Q-band. The first excited state is called Q_y, whereas the second excited state is named Q_x after the orientation of their respective transition dipole moment vectors. In the absorption spectrum the Q-band is located in the red part, at around 700 nm. It exhibits an extensive pattern of vibrational sidebands. Within the Gouterman model both Q-states are described by two excitations, Q_y by $\pi_1 \rightarrow \pi_1^*$ and $\pi_2 \rightarrow \pi_2^*$, Q_x by excitation from $\pi_1 \rightarrow \pi_2^*$ and $\pi_2 \rightarrow \pi_1^*$, as depicted in

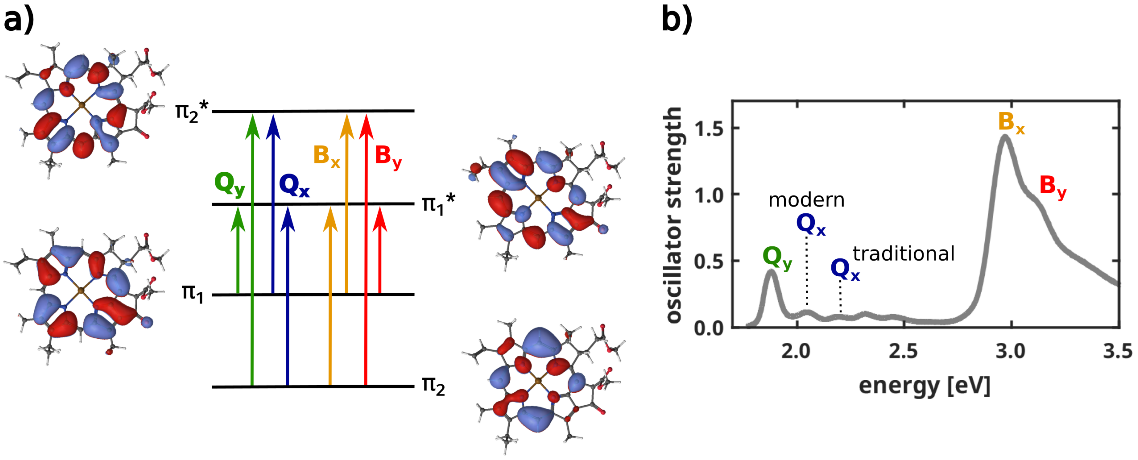

Figure 2.2: a) The Gouterman four orbital model with the relevant excitations for the chlorophyll *a* Q- and B-band. b) Absorption spectrum of chlorophyll *a* with different possible assignments of the Q_x signal.

Figure 2.2a). This simplistic model can, however, not fully explain the ultrafast internal conversion dynamics observed in chlorophyll *a* [42, 111, 112]. The assignment of the two Q-states in spectra of chlorophyll *a* has posed difficulties for decades. The Q_y 0-0 band maximum is easily assigned, whereas the comparatively weak Q_x signal is overshadowed by the vibrational sideband of Q_y and its assignment is an ongoing controversy. Especially magnetic circular dichroism and polarized fluorescence spectra exhibit two x-polarized bands instead of the expected one band [42, 113–115]. In the "traditional" assignment of the 1960s and 70s the higher-energy component was assumed as the Q_x origin [115, 116], whereas the "modern" assignment, used from the 1980s onward, instead favoured the lower-energy band [113, 117] (see Figure 2.2b). For the last decade Q_y and Q_x are more and more seen as a single system of inseparably coupled states. This interpretation resulted from a re-evaluation of experimental spectra with the help of vibronic coupling models [42]. The two Q-states are thought to be vibrationally coupled, which spreads the x-polarization across the whole Q-band and facilitates ultrafast population transfer between the states [42]. The ultrafast internal conversion process has experimentally been observed and exhibits a strong solvent and coordination dependence [15–17, 112, 118].

In the current chapter, the ultrafast relaxation dynamics of chlorophyll *a* was studied in the gas phase. Possibilities for the inclusion of solvent effects are discussed in section 2.3. Theoretical studies often use semi-classical approaches, most prominently non-adiabatic excited-state molecular dynamics, which propagates the nuclei classically [16, 111, 119]. As Q_y and Q_x are assumed to exhibit vibrational coupling, a quantum dynamical treatment of both electrons and nuclei, as well as their interplay becomes relevant, as extensively discussed in chapter 1. Therefore, the NEMol approach [75] was applied to simulate the coupled nuclear and electron dynamics of the Q-band of chlorophyll *a* to shed light on the ultrafast relaxation dynamics and the vibrational coupling between Q_y and Q_x. The focus of this chapter lies on the fundamental understanding of the relaxation dynamics and the coupling situation. The results were published in the article "Q-Band relaxation in chlorophyll: new insights from multireference quantum dynamics" in *Physical Chemistry Chemical Physics*. The key findings presented in the article are:

- A wide range of density functionals was tested to calculate the chlorophyll excitation energies, focusing on the Q_y/Q_x energy gap. Even tough some functionals showed promising results, DFT/MRCI reproduced the experimental data most accurately and showed a significant multireference character in the Q-band. For the calculation of the PES however, XMS-CASPT2 was used, as for DFT/MRCI the necessary gradients to construct NACs between Q_y and Q_x are not available. The Q_y/Q_x energy gap at the DFT/MRCI level of theory was used as a reference to fine tune the parameters of the XMS-CASPT2 calculations.

- Tests of different density functionals for TD-DFT showed a significant blue-shift, as double excitations are neglected. Neither range-separation nor the inclusion of London dispersion forces lead to improvements. For all tested functionals the Q_y/Q_x energy gap was considerably overestimated.

- A comparison of a DFT/MRCI steady-state absorption spectrum with an experimental one showed excellent agreement with only a systematic blue-shift of the entire spectrum by 0.11 eV. These results showed the need for a multireference method to account for the effect of higher-order excitations.

- After an extensive benchmark of the active space, state-averaging, IPEA and imaginary shifts, the XMS-CASPT2 method with SA4-CASSCF/SA6-CASCI/XMS-CASPT2(6,6) and an IPEA and imaginary shift of 0.1 was applied for the construction of the PES. The initial CASSCF step with state-averaging over four roots is followed by a re-optimisation of the CI coefficients (CASCI) with state-averaging over six roots. The ensuing XMS-CASPT2 calculation includes all six roots. This procedure is a compromise to ensure stability of the active space and the correct state ordering over the whole PES while ensuring an Q_y/Q_x energy gap close to the DFT/MRCI one.

- As coordinates for the PES, the normal modes with the highest overlap with the NAC vector at the Q_y geometry were chosen. For verification three additional sets of PESs were constructed with less strongly coupled modes. As expected, the population transfer slows down with decreasing coupling strength. The general dynamics, however, remain the same for all PESs. In none of the coordinate spaces a CoIn was observed in an energetically accessible region.

- When an explicitly simulated excitation pulse is applied, the Q_y is initially more populated due to its significantly larger transition dipole moment. If the pump pulse is only allowed to interact with Q_y, the dynamics stay very similar to the excitation into both states, whereas excitation only into Q_x significantly lowers the amount of excited population. In both cases, however, an immediate population transfer from the excited state into the remaining Q-state is observed.

- The oscillations in the temporal evolution of the population were slower than under the consideration of a delta excitation into Q_x. This can be attributed to the laser still pumping population into Q_y while Q_x is already populated and in this way smoothing the observed population transfer. The major factor, however, is that with the delta excitation all vibrational levels of the target state are populated whereas an explicit pulse only populates some of them. As several vibrational energy levels of Q_y and Q_x were found to be quasi degenerate, the population transfer speeds up when more of them are populated.
- The NEMol approach [75] was applied to determine the coupled nuclear and electron dynamics for the coupling between Q_y and Q_x. With the electronic difference densities between the initial electronic density (Q_x density) and the one at a certain point in time the oscillating population between the two Q-states could also be detected. The long-lived electronic coherence reaffirmed the vibrational coupling between Q_y/Q_x.
- According to the combined results, the Q-band of chlorophyll a should rather be seen as a single system of vibronically coupled states, with a strong mixing of the electronic states.

On the following pages the article "Q-Band relaxation in chlorophyll: new insights from multireference quantum dynamics" is reproduced from *Physical Chemistry Chemical Physics*, **24**, 27212 (2022) with permission from the PCCP Owner Societies. The supporting information of this article is available under https://doi.org/10.1039/D2CP02914F.

PCCP

ROYAL SOCIETY OF CHEMISTRY

PAPER

View Article Online
View Journal | View Issue

Check for updates

Cite this: *Phys. Chem. Chem. Phys.*, 2022, **24**, 27212

Q-Band relaxation in chlorophyll: new insights from multireference quantum dynamics†

Sebastian Reiter, ‡[a] Lena Bäuml,‡[a] Jürgen Hauer [b] and Regina de Vivie-Riedle *[a]

Received 27th June 2022,
Accepted 20th September 2022

DOI: 10.1039/d2cp02914f

rsc.li/pccp

The ultrafast relaxation within the Q-bands of chlorophyll plays a crucial role in photosynthetic light-harvesting. Yet, despite being the focus of many experimental and theoretical studies, it is still not fully understood. In this paper we look at the relaxation process from the perspective of non-adiabatic wave packet dynamics. For this purpose, we identify vibrational degrees of freedom which contribute most to the non-adiabatic coupling. Using a selection of normal modes, we construct four reduced-dimensional coordinate spaces and investigate the wave packet dynamics on XMS-CASPT2 potential energy surfaces. In this context, we discuss the associated computational challenges, as many quantum chemical methods overestimate the Q_x–Q_y energy gap. Our results show that the Q_x and Q_y potential energy surfaces do not cross in an energetically accessible region of the vibrational space. Instead, non-adiabatic coupling facilitates ultrafast population transfer across the potential energy surface. Moreover, we can identify the excited vibrational eigenstates that take part in the relaxation process. We conclude that the Q-band system of chlorophyll *a* should be viewed as a strongly coupled system, where population is easily transferred between the *x* and *y*-polarized electronic states. This suggests that both orientations may contribute to the electron transfer in the reaction center of photosynthetic light-harvesting systems.

1 Introduction

Chlorophylls are a group of natural pigments that play a vital role in photosynthetic light-harvesting.[1–3] There is a variety of differently substituted chlorophylls[4] but in general, the absorption spectrum is dominated by two main bands in the visible range, labeled B- and Q-bands. While the B or Soret band appears as a strong absorption around 400 nm, the weaker Q band resides in the red part of the spectrum around 700 nm and exhibits an extensive pattern of vibrational side bands.

Underlying both absorption bands are four excited states, labeled Q_x/Q_y and B_x/B_y, according to the polarization of the transition dipole moment vector (Fig. 1). These states have historically been characterized with the Gouterman model[6,7] in terms of independent electronic transitions between the four frontier orbitals. In this context, Q_y and B_y are both characterized mainly by the HOMO → LUMO and HOMO−1 → LUMO+1 excitations, albeit with different weights. Similarly, Q_x and B_x are comprised mainly of the HOMO−1 → LUMO and HOMO → LUMO+1 excitations. However, this simplistic model does not explain the ultrafast internal conversion within the Q-bands,[8–11]

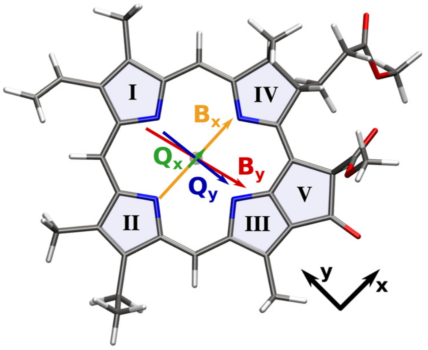

Fig. 1 Transition dipole moments of the Q and B bands overlaid on the molecular structure of our chlorophyll model system. Arrows are scaled with the length of the respective transition dipole vector. Roman numerals signify the ring numbering convention used in this work.[5]

---

[a] *Department of Chemistry, Ludwig-Maximilians-Universität München, Butenandtstr. 11, 81377 Munich, Germany. E-mail: regina.de_vivie@cup.uni-muenchen.de*

[b] *Department of Chemistry, Technical University of Munich, Lichtenbergstr. 4, 85747 Garching, Germany*

† Electronic supplementary information (ESI) available: Details on the chosen methods with sample OpenMolcas input, optimized geometries and coordinate vectors, potential energy surfaces, non-adiabatic coupling matrix elements, transition dipole moments and additional quantum dynamics simulations. See DOI: **https://doi.org/10.1039/d2cp02914f**

‡ These authors contributed equally to this work.

which plays an important role in energy and exciton transfer during photosynthetic light-harvesting.[12] In particular, magnetic circular dichroism (MCD) and polarized fluorescence spectra of chlorophyll *a* exhibit not just one but two *x*-polarized bands, whose energetic positions are also strongly dependent on the solvent.[8,13–16] Relative to the Q_y 0–0 band maximum, the lower-energy component appears at 700 cm^{-1} (1100 cm^{-1}) in diethylether (pyridine), while the higher-energy band occurs at 1700 cm^{-1} (2100 cm^{-1}). Their assignment to an electronic state has been the subject of debate for several decades. The "traditional" assignment[15,17] identifies the higher energy band as the Q_x origin, while the "modern" assignment[16,18] favors the lower energy component. Adding to the confusion, the historical assignment of the Q_x state to the lower- or higher-energy band also changes with the solvent coordination pattern of the central magnesium ion.[19] A recent re-evaluation of existing experiments in combination with vibronic coupling models[8] indicated that the two transitions are better thought of as a single system of inseparably mixed vibronic states. The strong vibronic coupling between Q_x and Q_y spreads *x*-polarization across the whole Q band system and allows ultrafast population transfer on a timescale of 100 fs to 226 fs, depending on the solvent.[8,20,21]

Here, high-level quantum mechanical calculations can complement experimental findings.[8,22–24] In particular, non-adiabatic dynamics simulations can shed light on the mechanism behind the strong vibronic coupling. Most studies employ a semiclassical ansatz, where the internal molecular dynamics are modeled as point masses moving in a quantum mechanical electrostatic potential.[9–11,25] While this approach is able to capture the molecular dynamics in full dimensionality, it is inherently limited by the need to calculate energy gradients in every time step for many trajectories with simulation times up to several picoseconds. These requirements limit the level of theory, as most multireference methods quickly become prohibitively expensive if gradients are involved. Moreover, a classical treatment of nuclear motion neglects the coherence of the wave packets in strongly coupled potentials as well as the interaction with the laser field.

In this paper, we therefore investigate the ultrafast relaxation within the Q-bands of a chlorophyll *a* analogue through the lens of wave packet quantum dynamics in reduced dimensionality. We first evaluate a variety of quantum chemical methods for their ability to adequately describe both states in question. Next, we present multiple two-dimensional coordinate spaces to construct XMS-CASPT2 potential energy surfaces (PESs), on which we model the ultrafast population transfer. We discuss the topography of the excited state potentials and its implications on the wave packet dynamics. In particular, we show how population can be transferred not only from the energetically higher Q_x state to the lower Q_y state, but also the other way round after laser excitation into vibrational side bands of Q_y. Finally, the results are complemented by a simulation of the coupled nuclear and electron dynamics within the Q-band, using the NEMol ansatz.[26–30] Our results shed light on the intimate coupling of the two Q states in chlorophyll and provide a reference for future theoretical and experimental studies.

2 Methods

All calculations in this work use a reduced model of chlorophyll *a*, where the phytyl chain is replaced by a methyl group. This reduces the number of atoms from 137 to 82 and speeds up the calculations at negligible errors in the absorption energies, which has been shown before[5,31] and was validated again by us (Fig. S1, ESI†).

Molecular visualizations within this work were created with VMD 1.9.3.[32,33] Orbitals for CASSCF/-PT2 calculations were visualized with Luscus 0.8.6.[34]

2.1 Geometry optimizations

The ground state geometry of our chlorophyll model was optimized with the CAM-B3LYP density functional[35] and the 6-311G(d) basis set[36–38] using Gaussian 16.[39] The Q_y and Q_x states were optimized with the same functional and basis set at the TDDFT level. Optimized geometries were verified as energy minima by the absence of imaginary vibrational frequencies.

2.2 Excited state calculations

We tested a range of density functionals, namely CAM-B3LYP,[35] ωB97X-D,[40] ωB97X-D4,[41] BHLYP,[42,43] LC-ωHPBE[44] and M062X[45] to calculate chlorophyll excitation energies with a special focus on the Q_x–Q_y energy gap. These test calculations were conducted with Gaussian 16 and the 6-311G(d) basis set,[36–38] with the exception of ωB97X-D4,[41] which is implemented in Orca 5.0[46–48] and where the def2-TZVP basis[49] was employed.

While some of the density functionals gave promising results for the position of the Q-bands at the Franck–Condon (FC) geometry, investigating the ultrafast non-adiabatic population transfer requires the use of a multireference method. Therefore, we used the DFT/MRCI method[50–52] with the redesigned R2018 Hamiltonian[53] as a benchmark reference for all other methods. The Kohn–Sham reference orbitals were calculated at the BHLYP[42,43]/def2-SV(P)[49] level of theory using the resolution of the identity approximation for Coulomb and exchange integrals[54,55] (RI-JK) with the def2-SVP/C[56] and def2/JK[57] auxiliary basis sets, as implemented in Orca 4.2.[46,47] An MRCI reference space was constructed iteratively for 50 roots, starting from a CISD expansion of four electrons in the four frontier orbitals, until the leading configurations of all roots were contained in the reference space. In the DFT/MRCI formalism, a parametrized damping function is applied to the MRCI matrix elements. This is done to avoid double counting of dynamic electron correlation, which has already been accounted for by the DFT part, and brings along an energy-based selection of configurations.[52,53] In this work, we have used the short selection threshold of 0.8 E_h with the corresponding parameter set. The short MRCI expansion speeds up the calculations considerably, while providing an excellent absorption spectrum for our chlorophyll analogue.

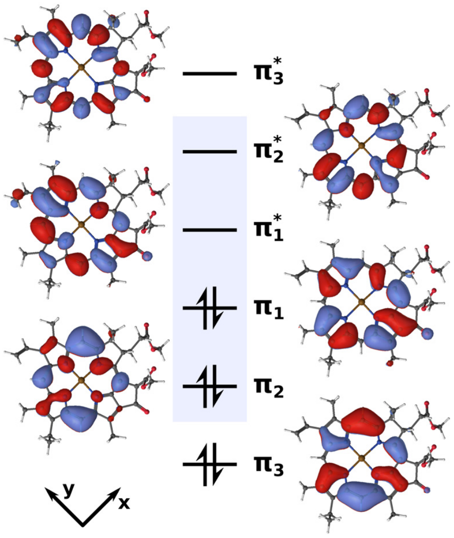

Fig. 2 Active space of six electrons in six orbitals (isovalue 0.02) used for the XMS-CASPT2 calculations. The blue box highlights the four Gouterman orbitals.

CASSCF[58] and (X)MS-CASPT2[59–64] calculations were conducted with OpenMolcas 19.11[65,66] using the ANO-RCC-VDZP[67–69] basis set. Great care must be taken in the selection of active spaces for multi-configurational approaches. Previous theoretical investigations have achieved reasonable results with small,[70] medium-sized[71,72] and very large[22,23] active spaces. After initial testing, we settled on an active space of six electrons in six orbitals (Fig. 2) to construct a PES, as we will detail later.

A balanced description of both Q_y and Q_x was achieved by state-averaging over six roots (SA6) in the CASSCF wave function and allowing all of them to mix in the subsequent XMS-CASPT2 calculation. Using both an IPEA and imaginary shift of 0.1, we obtained a Q_x–Q_y energy gap of 0.21 eV at the FC point, which matched the one calculated with DFT/MRCI (0.23 eV) almost exactly. However, this strategy turned out to be problematic for computing a PES. The higher excited states would cause rotations between active and inactive orbitals at geometries away from the FC region, thus introducing discontinuities in the PES. To mitigate this issue, we reduced the number of roots to four, resulting in an SA4-CASSCF(6,6) reference wave function. Here, the active space remained stable across the PES at the cost of strongly overestimating the Q_x–Q_y energy gap at the FC point with 0.54 eV. To get the best of both worlds, we calculated the CASSCF wave function in two steps. In the first step, the molecular orbitals were optimized in a SA4-CASSCF(6,6) scheme to arrive at a stable active space. In the second step, these orbitals were used in a SA6-CASCI(6,6) calculation where only the CI coefficients were re-optimized. Finally, all six roots were mixed in the subsequent XMS-CASPT2 calculation, using an IPEA[73] and imaginary level shift[74] of 0.1. In this way, we were able to stabilize the active space composition across the PES and still achieve a Q_x–Q_y gap of 0.39 eV, closer to the DFT/MRCI reference than in a pure SA4-XMS-CASPT2(4,4) scheme. Energies for both of the state-averaging schemes with various level shifts, along with an exemplary OpenMolcas input are provided in the ESI.† To account for the remaining deviation of the Q_x–Q_y gap from the DFT/MRCI reference, the calculated Q_x PESs were finally shifted down by −0.16 eV.

2.3 Quantum dynamics

For the wave packet quantum dynamics, the time-dependent Schrödinger equation was solved on a spatial grid of 256 × 256 points, using the Chebyshev[75] propagation scheme in a program of our own design. Energies, transition dipole moments and non-adiabatic coupling matrix elements (NACs) were calculated at 45 grid points (Fig. S5–S11, ESI†) and interpolated to the target grid with thin-plate splines.[76] Since the use of XMS-CASPT2 gradients would have been too expensive, NACs were calculated in the SA4-CASSCF(6,6)/SA6-CASCI(6,6) scheme introduced above. To still account for the correct energy difference between the Q_x and Q_y state, we scaled the NACs with the ratio of the energy gap at the XMS-CASPT2 and the CASSCF level. Furthermore, the full-dimensional NAC vector was projected onto the respective 2D coordinate space. The kinetic energy in the reduced-dimensional coordinate space was expressed in the Wilson G-matrix formalism[77–80] and matrix elements are provided in Table S9, ESI.† Vibrational eigenfunctions of the 2D potentials were calculated by propagation in imaginary time.[81]

2.4 Coupled nuclear and electron dynamics in molecules (NEMol)

The coupled nuclear and electron dynamics was determined using the NEMol ansatz[26–30] developed in our group. Within this purely quantum-mechanical ansatz the electronic wave functions are propagated in the eigenstate basis and coupled to the nuclear wave packet propagated on coupled PESs. In this work a NEMol-grid[29,30] of 45 grid points with the same dimensions and spacing as for the calculations of the energies, transition dipole moments and NACs was used. Using the NEMol ansatz, the coupled one-electron density is determined. Applying the NEMol-grid the integration over the full nuclear coordinate space is split up into segments. Summing up over the partial densities of all of these segments, the total electron density coupled to multiple nuclear grid points is obtained.

3 Results and discussion

3.1 Assessment of quantum-chemical methods

The Q-band relaxation of chlorophyll strongly depends on the energy gap between the Q_x and Q_y state. Any theoretical investigation of the process therefore first requires a method which can adequately model both excited states and ideally also the rest of the observed spectrum. To assess different methods in this regard, we computed steady-state absorption spectra and compared them against an experimental spectrum[82,83] for chlorophyll *a* measured in diethyl ether (Fig. 3a)).

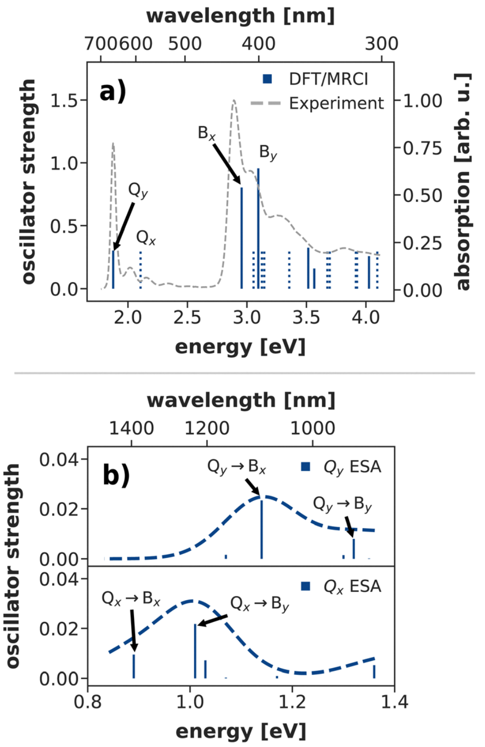

Fig. 3 (a) Calculated steady state absorption spectrum of a chlorophyll model system at the DFT/MRCI level of theory, compared to an experimental spectrum of chlorophyll *a* in diethyl ether.[82,83] The depicted absorption lines are red-shifted by 0.11 eV to the position of the experimental Q_y band. (b) Excited state absorption spectra from the Q-bands at the DFT/MRCI level of theory (unshifted).

We shall start our comparison with the DFT/MRCI method. Here, we only observe a small systematic blue-shift of the entire spectrum by 0.11 eV. The calculated absorption lines coincide well with the experimental band shape, even though the blue-shift is slightly stronger in the B bands. Both Q_y and Q_x exhibit a significant double excitation character of 9% and 12%, respectively. The contribution from double excitations only increases in the B band with 14% for B_x and 18% for B_y, highlighting the need for a multireference method. In contrast to earlier DFT/MRCI calculations,[84] which report an additional doubly excited state in the visible region, we observe B_x as the third excited state. However, a dark state with 19% double-excitation character occurs at 392 nm, between B_x and B_y in our calculations. The difference may be due to our use of the revised R2018 DFT/MRCI Hamiltonian[52] as well as a different optimized geometry.

To further assess the quality of DFT/MRCI for chlorophyll excitations, we computed transient spectra from both the Q_x and Q_y bands (Fig. 3b)). An experimental spectrum is available for a peridinin–chlorophyll-protein complex.[85] After 0.5 ps, when all initial population in Q_x should have decayed, it features an excited state absorption around 1290 nm which is consequently assigned to a series of transitions from Q_y to energetically higher states.[85] In comparison, the Q_y absorption predicted by DFT/MRCI occurs at lower wavelengths around 1100 nm. The difference is in part due to the overestimation of the B–Q energy gap by DFT/MRCI, and partly due to protein–chlorophyll interactions that may shift the excited state absorption in the experiment.

Overall, the DFT/MRCI method is in excellent agreement with the experimental absorption spectrum and, most importantly, it provides a balanced description of the major absorption bands. From this we conclude that the position of the Q_x band and thereby the Q_x–Q_y energy gap is correctly reproduced by DFT/MRCI. Therefore, we have used this method as a theoretical benchmark for all other methods in this work.

Apart from DFT/MRCI we also tested different density functionals and active space methods. The resulting vertical excitation energies are reported in Table 1. For the comparison of the different methods we mainly focused on the Q_x–Q_y energy gap, as this is the main parameter that determines the coupling between the two electronic states. In general, TDDFT considerably blue-shifts all vertical excitation energies, which has been observed before[24] and is a result of neglecting double excitations. Consequently, the error increases with higher excited states, where the doubles' contributions become more important. All tested functionals apart from M062X are range-separated but the range-separation does not seem to be crucial for chlorophyll, as M062X stands out as one of the best functionals to describe the Q_x–Q_y gap at the TDDFT level. The consideration of London dispersion forces as in ωB97X-D and its more recent analogue ωB97X-D4 also does not lead to an improvement in accuracy and even further increases the Q_x–Q_y gap. Out of the tested functionals, M062X and CAM-B3LYP (Fig. 3) agree best with the DFT/MRCI results and experimental band assignments. However, all functionals significantly overestimate the Q_x–Q_y gap, which may be a problem for simulating the Q-band dynamics of chlorophyll at the TDDFT level.

Even though DFT/MRCI provides excellent results in this regard, we did not use it to compute PESs modeling the Q-band dynamics, as it does not provide the gradients needed to construct the NAC between the two states. As an alternative, we investigated the CASSCF and (X)MS-CASPT2 methods. We compared the size and composition of the active space as well as the type and magnitude of applied level shifts with the goal to reproduce the Q_x–Q_y gap at a small enough computational cost to calculate PESs. In particular, we investigated four active spaces of different sizes. The smallest AS(6,6) contained the four Gouterman orbitals and a further pair of π/π^*-orbitals, amounting to six electrons in six molecular orbitals (Fig. 2). The larger spaces AS(8,8) and AS(10,10) respectively contained one or two additional pairs of π/π^*-orbitals (Fig. S2 and S3, ESI†) The largest space we tested featured 22 electrons in 22 orbitals in a restricted active space (RAS) scheme, with the four Gouterman orbitals in the RAS2 subspace, and nine π/π^* orbitals each in the RAS1 and RAS3 subspaces (Fig. S4, ESI†). Excitations from RAS1 and into RAS3 were restricted to singles or doubles respectively, while all excitations were allowed within RAS2. All active space based approaches overestimate the experimentally

Table 1 Vertical excitation energies (in eV) of chlorophyll a model system calculated at various levels of theory. The prefix SA*n* refers to state-averaging over *n* states in the CASSCF calculations

	Q_y	Q_x	$\lvert Q_x–Q_y \rvert$	B_x	B_y
CAM-B3LYP	2.17	2.56	0.39	3.48	3.74
wB97X-D	2.09	2.71	0.62	3.58	3.92
wB97X-D4	2.03	2.67	0.64	3.51	3.87
BHandHLYP	2.21	2.61	0.40	3.55	3.83
LC-wHPBE	2.06	2.79	0.73	3.61	3.97
M062X	2.21	2.59	0.38	3.48	3.72
DFT/MRCI	1.99	2.22	0.23	3.07	3.21
SA4-XMS-CASPT2(6,6)[a]	2.28	2.82	0.54	—	—
SA6-XMS-CASPT2(6,6)[b]	2.19	2.40	0.21	3.51	4.15
SA6-XMS-CASPT2(6,6)[a]	2.67	2.98	0.31	4.14	4.82
SA6-XMS-CASPT2(8,8)[a]	2.64	3.17	0.53	4.28	4.40
SA6-XMS-CASPT2(10,10)[a]	2.64	3.04	0.40	4.06	4.36
SA6-MS-RASPT2(22,1,1;9,4,9)[a]	2.34	2.74	0.40	3.39	4.00
SA6-MS-RASPT2(22,2,2;9,4,9)[a]	2.34	2.75	0.41	3.51	3.99
SA4-/SA6-XMS-CASPT2(6,6)[bc]	2.28	2.67	0.39	3.67	4.35
Exp. ("modern")	1.85[d]/1.88[e]	1.94[d]/2.00[e]	0.09[d]/0.12[e]	—	—
Exp. ("traditional")	1.88[f]	2.16[f]	0.28[f]	2.90	2.90

[a] IPEA shift: 0.25, imaginary shift: 0.1. [b] IPEA shift: 0.1, imaginary shift: 0.1. [c] SA4-CASSCF/SA6-CASCI/XMS-CASPT2(6,6). [d] "modern" assignment in pyridine.[16,19] [e] "modern" assignment in diethyl ether.[16] [f] "traditional" assignment in diethyl ether.[15,17,19]

determined excitation energies. While the Q_y state is systematically stabilized when increasing the size of the active space, the Q_x state and consequently the Q_y–Q_x energy gap do not follow this trend. Instead, adding orbitals to the active space favors one state over the other, depending on whether the additional orbitals are oriented more along the *x* or *y* molecular axis. The same behavior is observed for the B_x and B_y states. It is reminiscent of the L_a/L_b states in pyrene, which are also characterized by orthogonally polarized transitions and where a minimal active space proved beneficial for a balanced description of both states.[86] This again highlights the fact that choosing an active space should not rely solely on size criteria.[87,88] In light of these findings, we chose the small AS(6,6) for all further calculations to achieve a Q_y–Q_x energy gap that is close to the DFT/MRCI results at a reasonable computational cost. To keep this active space stable, also for geometries away from the FC region, we finally opted for a consecutive SA4-CASSCF/SA6-CASCI/XMS-CASPT2(6,6) scheme as outlined in the methods section.

Apart from the size and composition of the active space, the use of level shifts can strongly affect the results of CASPT2 calculations. Level shifts, particularly the IPEA[73] and imaginary shift[74] techniques, are a common way to remove intruder states. Indeed, using no level shift at all in the XMS-CASPT2(6,6) calculations introduces a spurious excitation from π_3 to $\pi_1{}^*$ as the first excited state. Therefore, we tested various combinations of IPEA and imaginary shifts to alleviate this issue (Tables S3–S6, ESI†). Applying any shift removes the intruder state, but the Q_x–Q_y gap is very sensitive to the exact combination of the two shift values. As the use of the IPEA shift is controversial,[89–92] in particular for porphyrin-based systems,[90,93] we tested applying only an imaginary shift. However, depending on the initial guess for the CASSCF reference, this leads to root-flipping at the FC point, such that Q_y becomes the higher and Q_x the lower energy excited state (Table S3, ESI†). Adding an IPEA shift helped resolve this issue and we therefore regard its use as justified in this case to preserve the correct state-ordering. In the end, combining an IPEA and imaginary shift of 0.1 emerged as a good choice to remove intruder states, ensure the correct state ordering across the PES and maintain a reasonable Q_x–Q_y gap.

3.2 Potential energy surfaces

Studying the quantum dynamics of the Q-band relaxation in chlorophyll requires not only an adequate method, but also a reduced-dimensional coordinate space, which can capture the essence of the relaxation process. To identify suitable coordinates, we calculated the overlap s_i of the normal modes $\mathbf{q}_i$ (with $i = 1,2,\ldots,3N - 6$) in mass-weighted Cartesian coordinates, and the normalized NAC vector $\mathbf{f}$ at the minimum geometry of the lower-energy state Q_y:

$$s_i = \sum_{j}^{3N} f_j \cdot q_{ij} \tag{1}$$

A similar technique has been used before in the context of semiclassical dynamics.[10] As the normal modes span an orthogonal coordinate space, the squared overlap s_i^2 corresponds to the percentage of non-adiabatic coupling contained in each mode $\left(\sum_i s_i^2 = 1\right)$. A complete list of all normal modes, their respective squared overlap with the NAC vector and their harmonic vibrational frequency can be found in Table S10 in the ESI.† Fig. 4 illustrates the magnitude of s_i^2 in each normal mode. We find that many modes are involved in the coupling but three modes stand out, together accounting for 38% of non-adiabatic coupling. The normal mode with the strongest overlap, mode 195 (s^2 = 15.62%), describes an in-plane vibration of the entire porphyrin scaffold and appears at 1596 cm^{-1}. A 1D potential along this mode (Fig. 5) reveals that the Q_x and Q_y

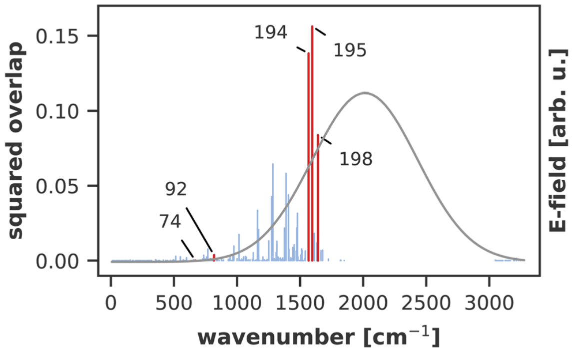

Fig. 4 Squared overlap of each normal mode with the NAC vector at the ground state minimum geometry. Normal modes highlighted in red were used to construct 2D coordinate spaces for the non-adiabatic quantum dynamics. The grey line illustrates the spectral width of the simulated laser pulse. Wavenumbers are given relative to the zero-point energy of Q_y, obtained at the TD-DFT/CAM-B3LYP/6-311G(d) level.

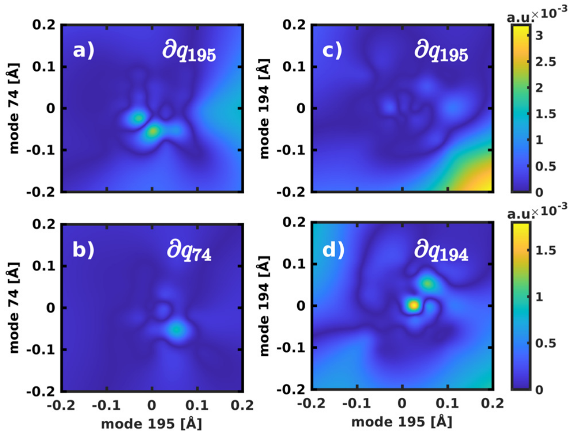

Fig. 6 Visualization of the NACs, projected into the 2D spaces spanned by normal modes 195/74 and 195/194, respectively. The notation ∂q_i refers to the projection of the NACs onto the respective normal mode to yield $\left\langle \Psi_1 \middle| \frac{\partial}{\partial q_i} \middle| \Psi_2 \right\rangle$.

state do not cross in an energetically accessible region of space. Instead, the two potentials run almost parallel to each other, facilitating non-adiabatic coupling across the coordinate space. This is further supported by the fact that the energetic order of the two states, computed at the DFT/MRCI level, is the same at the FC point as at their respective minimum geometries (Table S8, ESI†). So far, a true Q_x/Q_y conical intersection in chlorophyll-like systems has only been identified for free-base porphyrin.[71] Its structure involves displacement of the pyrrolic protons – a coordinate which is not accessible in chlorophylls and other metal–porphyrins.

The normal mode with the second-highest overlap, mode 194 (s^2 = 13.82%) appears at 1568 cm^{-1} and describes a similar collective in-plane vibration as mode 195. Given the strong coupling along these two modes, we used them to construct a 2D coordinate space for non-adiabatic quantum dynamics. To justify this choice of coordinates and to check whether our results also hold up in different coordinate spaces, we also tested three other 2D coordinate spaces between mode 195 and less strongly coupled modes from different spectral regions, namely modes 198 (s^2 = 8.37%), 92 (s^2 = 0.36%) and 74 (s^2 = 0.005%).

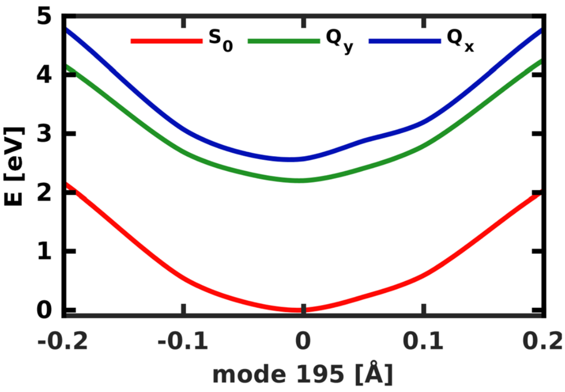

Fig. 5 1D electronic potentials along normal mode 195. Q_x and Q_y do not cross but run almost parallel to each other.

For the 2D spaces spanned by modes 195/194 and 195/74 the NACs are visualized in Fig. 6 respectively to illustrate the extreme cases of strong and weak coupling. The weaker coupling in mode 74 is especially visible when comparing the projection of the NACs onto the respective second normal mode in Fig. 6b and d. However, in all tested coordinate spaces the non-adiabatic coupling is larger than zero across the PES, not localized at singular geometries as would be typical for a conical intersection.

3.3 Non-adiabatic quantum dynamics

To model the non-adiabatic dynamics within the Q-bands, we simulated the evolution of a nuclear wave packet in all four 2D coordinate spaces. For the following analysis, the excited state wave packet was prepared by placing the ground state vibrational eigenfunction of the S_0 potential on the Q_x surface. As we do not simulate coupling to environmental modes or decoherence effects, which take over at long time scales, we will restrict our analysis to the first 150 fs of the dynamics. The temporal evolution of the population in the two spaces 195/194 and 195/74 is illustrated in Fig. 7.

The difference in the coupling strength is clearly reflected in the time it takes until half the population is transferred from Q_x to Q_y. In the strongly coupled 2D space 195/194, the transfer time is less than 10 fs, while in the weakly coupled space 195/74, it is 60 fs. The other weakly coupled 2D space we tested (195/92) fits into this trend with a transfer time of 25 fs. Only mode 198 appears to be more strongly coupled than the other modes, as indicated by higher NACs across the coordinate space (Fig. S9, ESI†), and yields a transfer time of <10 fs, only interrupted by strong back-coupling from Q_x to Q_y. The overall

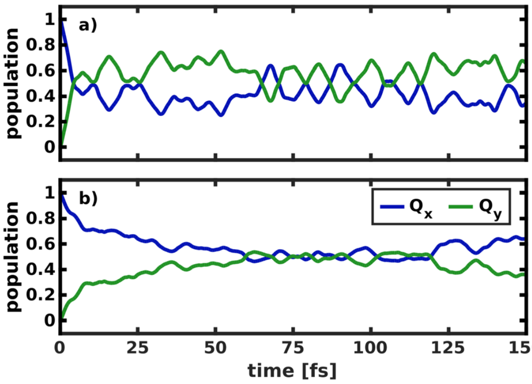

Fig. 7 Population transfer between Q_x and Q_y in the 2D coordinate spaces spanned (a) by normal modes 195/194 and (b) by normal modes 195/74.

trends we observe in the population dynamics are consistent in all tested coordinate spaces and we therefore expect the results to be reliable. After half the population is transferred, back-coupling into Q_x can be observed, as the wave packet cannot dissipate into other nuclear degrees of freedom in the quasi-harmonic 2D space on the Q_y surface. For the same reason, the oscillations caused by this back-coupling do not decay in time. Given that the two potentials run mostly parallel to each other (Fig. 5), it is reasonable to assume a 50/50 population of both states at long time scales, under the assumption that energy is conserved within the Q-band system. If dissipation due to environmental coupling was included, the population would eventually decay to the vibrational ground state of Q_y. These population dynamics are fully in line with the conclusions by Reimers *et al.*, who argued that the Q-bands of chlorophyll should be regarded as an inseparably mixed system of two strongly vibronically coupled states.[8]

To simulate the wave packet dynamics after laser excitation, a pump pulse with a central frequency ω_0 of 2.43 eV, a full width at half maximum (FWHM) of 30 fs and a maximum field strength of 4.9×10^{-3} GV cm^{-1} was used to excite the vibronic ground state eigenfunction in the space 195/194. As the zero-point vibrational energy in the 2D ground state potential is 0.19 eV, the energy of the laser pulse is tuned for excitation into the vibrational ground state of Q_x at 2.62 eV. Its spectrum is broad enough to populate all the modes spanning the reduced-dimensional coordinate space (*cf.* grey line in Fig. 4). The temporal evolution of the population and the simulated laser pulse are depicted in Fig. 8.

Initially, the laser was allowed to interact with both electronic states (Fig. 8a), as would be the case in an experiment. The laser pulse starts to transfer population at 20 fs. Most of the population (52%) is initially transferred to Q_y, as its transition dipole moment is significantly larger than that of Q_x. In the first 40 fs of the excitation, fast oscillations at twice the frequency of the laser pulse can be observed in the Q_y population curve, indicating that the intense laser field moves population back and forth between the ground and excited state. Immediately after the start of the laser pulse, population is also transferred into Q_x. The population curves in Fig. 8b and c, where only one of the two states can interact with the laser, confirm that most of this population transfer into Q_x does not stem from direct photo-excitation but from the vibronic coupling to Q_y. Conversely, even if the transition dipole moment of Q_y is explicitly turned off (Fig. 8c), such that the laser can only directly excite Q_x, most of the population is instantly transferred into Q_y. This is especially relevant to the assignment of the two experimentally observed absorption bands with *x*-polarization, because it means that even excitation into vibronic side bands of Q_y immediately transfers population to Q_x and *vice versa*. This again corroborates the position that Q_x and Q_y should not be regarded as independent electronic states but rather as a single, strongly coupled system of absorption bands, where *x*- and *y*-polarization is spread across the entire band.

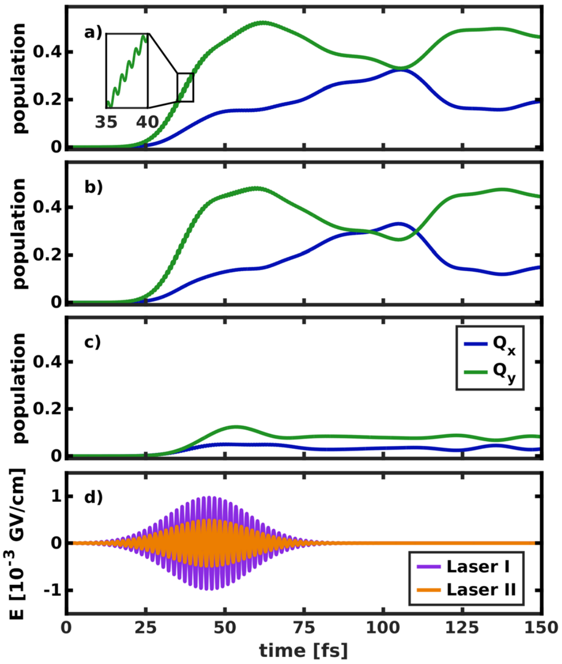

Fig. 8 Temporal evolution of the population in both electronic states after laser excitation into (a) both the Q_y and Q_x state, (b) only the Q_y state and (c) only the Q_x state. (d) Visualization of the simulated laser pulses, where E denotes the electric field strength. The more intense laser I was used only for excitation into the nearly dark Q_x state. The inset in (a) illustrates fast oscillations in the Q_y population, induced by the interaction with the laser field.

The crossing point where half the population is transferred between the two states occurs at 105 fs, 25 fs after the laser field has decayed. This is around five times as long as in the delta pulse propagation in Fig. 7a and there are also fewer oscillations between the two states. There are two effects that can explain this behavior. First, the laser keeps transferring population into Q_y while the vibronic coupling already populates Q_x, thereby effectively smoothing the fast oscillations visible in Fig. 7a. Second, the laser energy and spectral width are tuned to match the vibrational ground state of Q_x. In contrast, assuming a delta-pulse by placing an eigenfunction to the S_0 potential on the Q_x surface adds higher-energy components to the excited-state wave packet, which may induce faster oscillations in the population transfer.

To gain deeper insight into the processes after laser excitation, the nuclear wave packet in the Q_y and Q_x electronic potentials is visualized at different points in time in Fig. 9. In the Q_y state (upper panel in Fig. 9), the wave packet exhibits one nodal plane during the laser excitation at 40 fs, barring interferences in regions of stronger vibronic coupling for the moment. It then proceeds to oscillate between two different orientations over time, corresponding to a superposition of the $\nu = 1$ and $\nu = 2$ eigenfunctions of the Q_y potential. At 40 fs and 92 fs, the orientation of the wave packet resembles the $\nu = 2$ vibrational eigenfunction of the Q_y PES, as the energy of this eigenstate matches the central frequency of the laser pulse and is nearly degenerate with the vibronic ground state of Q_x ($\nu = 0$, Fig. 10). At 72 fs and 105 fs, the wave packet rotates to resemble the $\nu = 1$ eigenstate of Q_y. The rotations decay over time and stop around 130 fs with a linear combination of the $\nu = 1$ and $\nu = 2$ eigenstates of Q_y. On the Q_x surface (bottom panel in Fig. 9), a wave packet corresponding to $\nu = 0$ appears immediately after laser excitation and increases in amplitude over time due to vibronic coupling to Q_y. The region of stronger coupling around $q_{195} = 0.025$ Å/$q_{194} = 0.025$ Å (*cf.* Fig. 6d)) is clearly reflected in interferences in this part of the PES. Maintaining the coherence between the two electronic states, the Q_x wave packet also rotates along with its counterpart on Q_y. As back-coupling sets in around 50 fs, a second node appears on the Q_y wave packet, corresponding to the current population in Q_x.

3.4 Coupling of nuclear and electronic dynamics

Applying the NEMol ansatz we are able to visualize not only the nuclear but also the coupled nuclear and electron dynamics. We performed this analysis for the propagation in the 2D space spanned by modes 195/194 by placing the ground state vibrational eigenfunction of the S_0 potential onto the Q_x surface. The corresponding population curve of the nuclear dynamics is shown in Fig. 7. Using the NEMol ansatz it would also be possible to study the excitation pulse induced dynamics, but as we are mainly interested in characterizing the coupling between Q_x and Q_y we have considered only the process after delta pulse excitation. The dipole moment induced by the

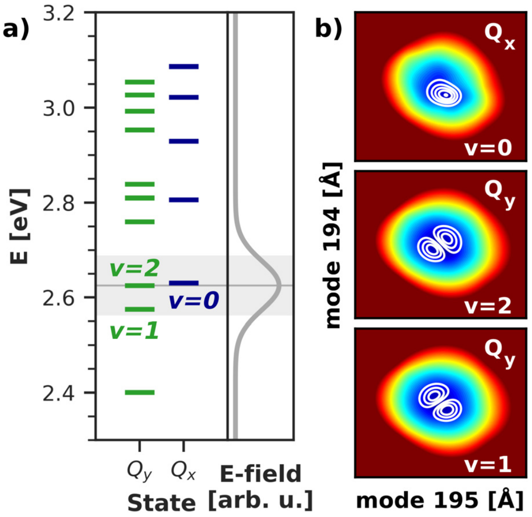

Fig. 10 (a) Vibrational energy levels of the electronic Q_y and Q_x states in a 2D space spanned by normal modes 195/194. The highlighted area illustrates the spectral width (FWHM) of the simulated laser pulse. Energies are given relative to the energy of the electronic ground state. (b) Visualization of the relevant vibrational eigenfunctions in the Q_x and Q_y potentials. Axis ranges and color scheme are identical to those in Fig. 9.

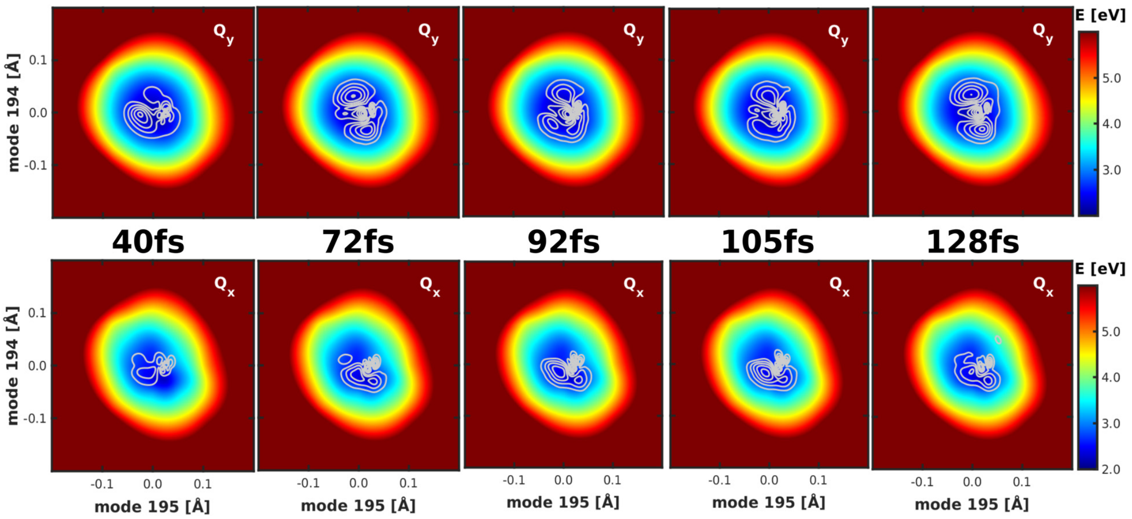

Fig. 9 Visualization of the wave packet after laser excitation into the Q_x state at four different points in time on the Q_y (upper panel) and the Q_x (lower panel) PES spanned by modes 195/194.

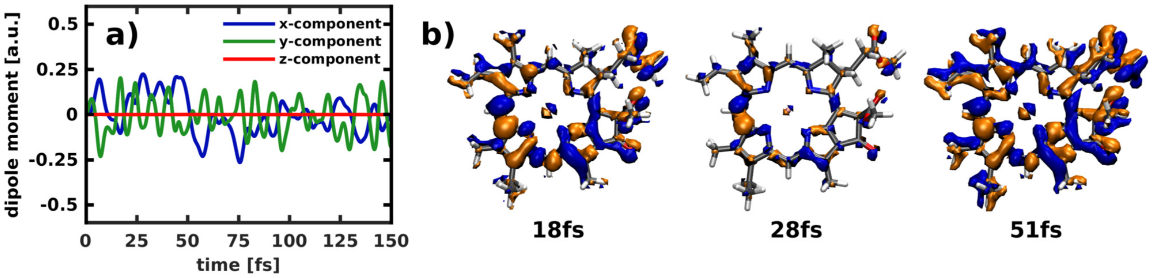

Fig. 11 Temporal evolution of (a) the induced dipole moment obtained by building the difference between a calculation with and without electronic coherence and (b) the difference in density relative to the first frame of the simulation (isovalue: ±0.001). As the propagation starts in the Q_x state, all non-vanishing difference density is indicative for population of the Q_y state. Electron-gain is visualized in blue, electron-loss in orange. These results refer to the propagation after delta pulse excitation depicted in (Fig. 7a).

electronic coherence is depicted in (Fig. 11a). It is calculated by taking the difference between the dipole moment obtained with and without electronic coherence and applying a Fourier transform of the obtained values. There is no dipole moment induced in the *z*-direction, whereas there are fast oscillations visible for both *x*- and *y*-component. They have a similar oscillation period with the ones of the *y*-component being slightly faster. As Q_y is the lower electronic state, the wave packet can couple to more vibrational overtones, which also leads to faster oscillations in the coherence-induced dipole moment.

Another way to visualize the oscillating dynamics between the two states is *via* the electronic difference densities shown in (Fig. 11b). They illustrate the difference between the electronic density at a point in time relative to the first frame of the simulation ($t = 0$). As the propagation starts in the Q_x state, all non-vanishing difference density is indicative for population of the Q_y state. The difference density at 51 fs shows the largest difference as the Q_y states exhibits a maximum in population at this point in time. At 18 fs the Q_y population in (Fig. 7a) exhibits a local maximum, which is also reflected in the difference density. In contrast, the frame at 28 fs shows smaller but still non-negligible differences to the Q_x density, which corresponds well to the nearly equally population of both states at this point in time. The strongest feature in the difference density is the change at the bridging carbon between rings I and II, which is still present when Q_x and Q_y are equally populated. The more population is present in Q_y the more changes also occur throughout the rest of the molecule, as is clearly visible in the snapshot at 51 fs. Using the difference density obtained with the NEMol ansatz therefore allows to visualize the electronic wave packet created due to the non-adiabatic coupling between the first two excited states, taking into account the quantum nature of both nuclear and electronic motion. Its long-lived coherence reaffirms the existence of a strongly coupled Q_x/Q_y system, rather than two independent electronic states.

4 Conclusions

We have simulated the internal conversion dynamics in the Q-bands of chlorophyll, fully taking into account the quantum nature of electronic and nuclear motion. This requires a computational method that reproduces the energy gap between the two excited states. Here, we are faced with the challenge of balancing computational cost with accuracy. Many affordable methods like TD-DFT overestimate the Q_y–Q_x gap, which may adversely affect the simulated coupling between the two states. Our tests once again[24] highlight the need for high-level, ideally multireference methods like DFT/MRCI to capture the effect of higher-order excitations on the spectral features of chlorophylls.

A conical intersection between Q_x and Q_y could not be found as the PESs studied along the selected normal mode coordinates run parallel to each other and the energetic state-ordering is retained upon relaxation in the excited states. Our results instead show the presence of strong vibronic coupling between Q_y and Q_x across the PES in multiple 2D coordinate spaces, due to strongly delocalized non-adiabatic coupling. A simple description of the Q-band system in terms of the Born-Oppenheimer approximation can therefore not be sufficient. In agreement with previous conclusions,[8] but at a higher level of theory and from a different perspective, we conclude that the Q-band of chlorophyll is better thought of as a single system of strongly vibronically coupled states, where *x*-polarization can be spread across the vibronic side bands of Q_y and *vice versa*. Using the NEMol ansatz, we could visualize how the electronic density, coupled to the nuclear motion, oscillates back and forth between *x*- and *y*-polarization. This strong mixing of the electronic states in chlorophyll *a* may have important implications for the charge transport in the reaction center of photosynthetic light-harvesting complexes. After excitation into the higher-energy absorption bands, the population will eventually decay into the Q-bands and from there facilitate electron transfer to neighboring pigments. This process may become more efficient if both *x*- and *y*-polarizations can contribute to it.

Author contributions

Sebastian Reiter: conceptualization, data curation, formal analysis, investigation, methodology, software, validation, visualization, writing – original draft, writing – review & editing; Lena Bäuml: conceptualization, data curation, formal analysis, investigation, methodology, software, validation, visualization, writing – original draft, writing – review & editing; Jürgen Hauer – funding acquisition, supervision, writing – review & editing; Regina de Vivie-Riedle – conceptualization, funding acquisition, project administration, resources, supervision, writing – review & editing.

Conflicts of interest

There are no conflicts to declare.

Acknowledgements

We thank Eva Sextl for support in the preliminary test calculations. We gratefully acknowledge funding by the Deutsche Forschungsgemeinschaft (DFG, German Research Foundation) through the cluster of excellence e-conversion under Germany's Excellence Strategy – EXC 2089/1 – 390776260.

Notes and references

1 R. E. Blankenship, *Molecular Mechanisms of Photosynthesis*, Wiley, 3rd edn, 2021.

2 A. N. Melkozernov, J. Barber and R. E. Blankenship, *Biochemistry*, 2006, **45**, 331–345.

3 J. R. Reimers, M. Biczysko, D. Bruce, D. F. Coker, T. J. Frankcombe, H. Hashimoto, J. Hauer, R. Jankowiak, T. Kramer, J. Linnanto, F. Mamedov, F. Müh, M. Rätsep, T. Renger, S. Styring, J. Wan, Z. Wang, Z.-Y. Wang-Otomo, Y.-X. Weng, C. Yang, J.-P. Zhang, A. Freiberg and E. Krausz, *Biochim. Biophys. Acta Bioenerg.*, 2016, **1857**, 1627–1640.

4 M. Taniguchi and J. S. Lindsey, *Photochem. Photobiol.*, 2021, **97**, 136–165.

5 D. Sundholm, *Chem. Phys. Lett.*, 2000, **317**, 545–552.

6 M. Gouterman, *J. Mol. Spectrosc.*, 1961, **6**, 138–163.

7 M. Gouterman, G. H. Wagnière and L. C. Snyder, *J. Mol. Spectrosc.*, 1963, **11**, 108–127.

8 J. R. Reimers, Z.-L. Cai, R. Kobayashi, M. Rätsep, A. Freiberg and E. Krausz, *Sci. Rep.*, 2013, **3**, 1–8.

9 W. P. Bricker, P. M. Shenai, A. Ghosh, Z. Liu, M. G. M. Enriquez, P. H. Lambrev, H.-S. Tan, C. S. Lo, S. Tretiak, S. Fernandez-Alberti and Y. Zhao, *Sci. Rep.*, 2015, **5**, 13625.

10 P. M. Shenai, S. Fernandez-Alberti, W. P. Bricker, S. Tretiak and Y. Zhao, *J. Phys. Chem. B*, 2016, **120**, 49–58.

11 M. Fortino, E. Collini, J. Bloino and A. Pedone, *J. Chem. Phys.*, 2021, **154**, 094110.

12 M. Rätsep, J. M. Linnanto and A. Freiberg, *J. Phys. Chem. B*, 2019, **123**, 7149–7156.

13 F. Bär, H. Lang, E. Schnabel and H. Kuhn, *Z. Elektrochem., Ber. Bunsenges. phys. Chem.*, 1961, **65**, 346–354.

14 M. Gouterman and L. Stryer, *J. Chem. Phys.*, 1962, **37**, 2260–2266.

15 C. Weiss, *J. Mol. Spectrosc.*, 1972, **44**, 37–80.

16 M. Umetsu, Z.-Y. Wang, M. Kobayashi and T. Nozawa, *Biochim. Biophys. Acta, Bioenerg.*, 1999, **1410**, 19–31.

17 C. Houssier and K. Sauer, *J. Am. Chem. Soc.*, 1970, **92**, 779–791.

18 R. A. Avarmaa and K. K. Rebane, *Spectrochim. Acta, Part A*, 1985, **41**, 1365–1380.

19 L. L. Shipman, T. M. Cotton, J. R. Norris and J. J. Katz, *J. Am. Chem. Soc.*, 1976, **98**, 8222–8230.

20 Y. Shi, J.-Y. Liu and K.-L. Han, *Chem. Phys. Lett.*, 2005, **410**, 260–263.

21 E. Meneghin, C. Leonardo, A. Volpato, L. Bolzonello and E. Collini, *Sci. Rep.*, 2017, **7**, 11389.

22 A. Anda, T. Hansen and L. De Vico, *J. Chem. Theory Comput.*, 2016, **12**, 1305–1313.

23 A. Anda, T. Hansen and L. De Vico, *J. Phys. Chem. A*, 2019, **123**, 5283–5292.

24 A. Sirohiwal, R. Berraud-Pache, F. Neese, R. Izsák and D. A. Pantazis, *J. Phys. Chem. B*, 2020, **124**, 8761–8771.

25 F. Zheng, S. Fernandez-Alberti, S. Tretiak and Y. Zhao, *J. Phys. Chem. B*, 2017, **121**, 5331–5339.

26 D. Geppert, P. von den Hoff and R. de Vivie-Riedle, *J. Phys. B: At., Mol. Opt. Phys.*, 2008, **41**, 074006.

27 P. von den Hoff, I. Znakovskaya, M. F. Kling and R. de Vivie-Riedle, *Chem. Phys.*, 2009, **366**, 139–147.

28 I. Znakovskaya, P. von den Hoff, S. Zherebtsov, A. Wirth, O. Herrwerth, M. J. J. Vrakking, R. de Vivie-Riedle and M. F. Kling, *Phys. Rev. Lett.*, 2009, **103**, 103002.

29 T. Schnappinger and R. de Vivie-Riedle, *J. Chem. Phys.*, 2021, **154**, 134306.

30 L. Bäuml, T. Schnappinger, M. F. Kling and R. de Vivie-Riedle, *Front. Phys.*, 2021, **9**, 1–12.

31 D. Sundholm, *Chem. Phys. Lett.*, 1999, **302**, 480–484.

32 W. Humphrey, A. Dalke and K. Schulten, *J. Mol. Graphics*, 1996, **14**, 33–38.

33 J. Stone, *An Efficient Library for Parallel Ray Tracing and Animation*, Master's thesis (M.S.), University of Missouri-Rolla, 1998, **https://scholarsmine.mst.edu/masters_theses/1747**.

34 G. Kovačević and V. Veryazov, *J. Cheminf.*, 2015, **7**, 16.

35 T. Yanai, D. P. Tew and N. C. Handy, *Chem. Phys. Lett.*, 2004, **393**, 51–57.

36 A. D. McLean and G. S. Chandler, *J. Chem. Phys.*, 1980, **72**, 5639–5648.

37 R. Krishnan, J. S. Binkley, R. Seeger and J. A. Pople, *J. Chem. Phys.*, 1980, **72**, 650–654.

38 M. M. Francl, W. J. Pietro, W. J. Hehre, J. S. Binkley, M. S. Gordon, D. J. DeFrees and J. A. Pople, *J. Chem. Phys.*, 1982, **77**, 3654–3665.

39 M. J. Frisch, G. W. Trucks, H. B. Schlegel, G. E. Scuseria, M. A. Robb, J. R. Cheeseman, G. Scalmani, V. Barone, G. A. Petersson, H. Nakatsuji, X. Li, M. Caricato, A. V. Marenich, J. Bloino, B. G. Janesko, R. Gomperts, B. Mennucci, H. P. Hratchian, J. V. Ortiz, A. F. Izmaylov, J. L. Sonnenberg, D. Williams-Young, F. Ding, F. Lipparini, F. Egidi, J. Goings, B. Peng, A. Petrone, T. Henderson, D. Ranasinghe, V. G. Zakrzewski, J. Gao, N. Rega, G. Zheng, W. Liang, M. Hada, M. Ehara, K. Toyota, R. Fukuda, J. Hasegawa, M. Ishida, T. Nakajima, Y. Honda,

O. Kitao, H. Nakai, T. Vreven, K. Throssell, J. A. Montgomery Jr., J. E. Peralta, F. Ogliaro, M. J. Bearpark, J. J. Heyd, E. N. Brothers, K. N. Kudin, V. N. Staroverov, T. A. Keith, R. Kobayashi, J. Normand, K. Raghavachari, A. P. Rendell, J. C. Burant, S. S. Iyengar, J. Tomasi, M. Cossi, J. M. Millam, M. Klene, C. Adamo, R. Cammi, J. W. Ochterski, R. L. Martin, K. Morokuma, O. Farkas, J. B. Foresman and D. J. Fox, *Gaussian16, Revision A.03*, Gaussian Inc., Wallingford CT, 2009, **https://www.gaussian.com**.

40 J.-D. Chai and M. Head-Gordon, *Phys. Chem. Chem. Phys.*, 2008, **10**, 6615–6620.

41 A. Najibi and L. Goerigk, *J. Comput. Chem.*, 2020, **41**, 2562–2572.

42 A. D. Becke, *J. Chem. Phys.*, 1993, **98**, 1372–1377.

43 C. Lee, W. Yang and R. G. Parr, *Phys. Rev. B: Condens. Matter Mater. Phys.*, 1988, **37**, 785–789.

44 T. M. Henderson, A. F. Izmaylov, G. Scalmani and G. E. Scuseria, *J. Chem. Phys.*, 2009, **131**, 044108.

45 Y. Zhao and D. G. Truhlar, *Theor. Chem. Acc.*, 2008, **120**, 215–241.

46 F. Neese, *WIREs Comput. Mol. Sci.*, 2012, **2**, 73–78.

47 F. Neese, *WIREs Comput. Mol. Sci.*, 2018, **8**, e1327.

48 F. Neese, *WIREs Comput. Mol. Sci.*, 2022, e1606.

49 F. Weigend and R. Ahlrichs, *Phys. Chem. Chem. Phys.*, 2005, **7**, 3297–3305.

50 S. Grimme and M. Waletzke, *J. Chem. Phys.*, 1999, **111**, 5645–5655.

51 M. Kleinschmidt, C. M. Marian, M. Waletzke and S. Grimme, *J. Chem. Phys.*, 2009, **130**, 044708.

52 C. M. Marian, A. Heil and M. Kleinschmidt, *WIREs Comput. Mol. Sci.*, 2018, **9**, e1394.

53 A. Heil, M. Kleinschmidt and C. M. Marian, *J. Chem. Phys.*, 2018, **149**, 164106.

54 F. Weigend, M. Kattannek and R. Ahlrichs, *J. Chem. Phys.*, 2009, **130**, 164106.

55 S. Kossmann and F. Neese, *Chem. Phys. Lett.*, 2009, **481**, 240–243.

56 A. Hellweg, C. Hättig, S. Höfener and W. Klopper, *Theor. Chem. Acc.*, 2007, **117**, 587–597.

57 F. Weigend, *J. Comput. Chem.*, 2008, **29**, 167–175.

58 B. O. Roos, in *Advances in Chemical Physics*, ed. K. P. Lawley, John Wiley & Sons, Ltd, 1987, pp. 399–445.

59 B. O. Roos, P. Linse, P. E. M. Siegbahn and M. R. A. Blomberg, *Chem. Phys.*, 1982, **66**, 197–207.

60 K. Andersson, P. A. Malmqvist, B. O. Roos, A. J. Sadlej and K. Wolinski, *J. Phys. Chem.*, 1990, **94**, 5483–5488.

61 K. Andersson, P.-A. k Malmqvist and B. O. Roos, *J. Chem. Phys.*, 1992, **96**, 1218–1226.

62 J. Finley, P.-A. k Malmqvist, B. O. Roos and L. Serrano-Andrés, *Chem. Phys. Lett.*, 1998, **288**, 299–306.

63 A. A. Granovsky, *J. Chem. Phys.*, 2011, **134**, 214113.

64 T. Shiozaki, W. Győrffy, P. Celani and H.-J. Werner, *J. Chem. Phys.*, 2011, **135**, 081106.

65 I. Fdez. Galván, M. Vacher, A. Alavi, C. Angeli, F. Aquilante, J. Autschbach, J. J. Bao, S. I. Bokarev, N. A. Bogdanov, R. K. Carlson, L. F. Chibotaru, J. Creutzberg, N. Dattani, M. G. Delcey, S. S. Dong, A. Dreuw, L. Freitag, L. M. Frutos, L. Gagliardi, F. Gendron, A. Giussani, L. González, G. Grell, M. Guo, C. E. Hoyer, M. Johansson, S. Keller, S. Knecht, G. Kovačević, E. Källman, G. Li Manni, M. Lundberg, Y. Ma, S. Mai, J. A. P. Malhado, P. A. K. Malmqvist, P. Marquetand, S. A. Mewes, J. Norell, M. Olivucci, M. Oppel, Q. M. Phung, K. Pierloot, F. Plasser, M. Reiher, A. M. Sand, I. Schapiro, P. Sharma, C. J. Stein, L. K. Sørensen, D. G. Truhlar, M. Ugandi, L. Ungur, A. Valentini, S. Vancoillie, V. Veryazov, O. Weser, T. A. Wesołowski, P.-O. Widmark, S. Wouters, A. Zech, J. P. Zobel and R. Lindh, *J. Chem. Theory Comput.*, 2019, **15**, 5925–5964.

66 F. Aquilante, J. Autschbach, A. Baiardi, S. Battaglia, V. A. Borin, L. F. Chibotaru, I. Conti, L. De Vico, M. Delcey, I. F. Galván, N. Ferré, L. Freitag, M. Garavelli, X. Gong, S. Knecht, E. D. Larsson, R. Lindh, M. Lundberg, P. A. K. Malmqvist, A. Nenov, J. Norell, M. Odelius, M. Olivucci, T. B. Pedersen, L. Pedraza-González, Q. M. Phung, K. Pierloot, M. Reiher, I. Schapiro, J. Segarra-Martí, F. Segatta, L. Seijo, S. Sen, D.-C. Sergentu, C. J. Stein, L. Ungur, M. Vacher, A. Valentini and V. Veryazov, *J. Chem. Phys.*, 2020, **152**, 214117.

67 P.-O. Widmark, P.-A. k Malmqvist and B. O. Roos, *Theoret. Chim. Acta*, 1990, **77**, 291–306.

68 B. O. Roos, R. Lindh, P.-A. K. Malmqvist, V. Veryazov and P.-O. Widmark, *J. Phys. Chem. A*, 2004, **108**, 2851–2858.

69 B. O. Roos, V. Veryazov and P.-O. Widmark, *Theor. Chem. Acc.*, 2004, **111**, 345–351.

70 J. Chmeliov, W. P. Bricker, C. Lo, E. Jouin, L. Valkunas, A. V. Ruban and C. D. P. Duffy, *Phys. Chem. Chem. Phys.*, 2015, **17**, 15857–15867.

71 K. Falahati, C. Hamerla, M. Huix-Rotllant and I. Burghardt, *Phys. Chem. Chem. Phys.*, 2018, **20**, 12483–12492.

72 V. V. Poddubnyy, M. I. Kozlov and I. O. Glebov, *Chem. Phys. Lett.*, 2021, **778**, 138792.

73 G. Ghigo, B. O. Roos and P.-A. K. Malmqvist, *Chem. Phys. Lett.*, 2004, **396**, 142–149.

74 N. Forsberg and P.-A. K. Malmqvist, *Chem. Phys. Lett.*, 1997, **274**, 196–204.

75 H. Tal-Ezer and R. Kosloff, *J. Chem. Phys.*, 1984, **81**, 3967–3971.

76 R. Franke, *Comput. Math. with Appl.*, 1982, **8**, 273–281.

77 E. B. Wilson, J. C. Decius and P. C. Cross, *Molecular Vibrations: The Theory of Infrared and Raman Vibrational Spectra*, Dover Publications, 1980.

78 L. J. Schaad and J. Hu, *J. Mol. Struct. THEOCHEM*, 1989, **185**, 203–215.

79 J. Stare and G. G. Balint-Kurti, *J. Phys. Chem. A*, 2003, **107**, 7204–7214.

80 M. Kowalewski, J. Mikosch, R. Wester and R. de Vivie-Riedle, *J. Phys. Chem. A*, 2014, **118**, 4661–4669.

81 R. Kosloff and H. Tal-Ezer, *Chem. Phys. Lett.*, 1986, **127**, 223–230.

82 M. Taniguchi, H. Du and J. S. Lindsey, *Photochem. Photobiol.*, 2018, **94**, 277–289.

83 M. Taniguchi and J. S. Lindsey, *Photochem. Photobiol.*, 2018, **94**, 290–327.

84 A. B. J. Parusel and S. Grimme, *J. Phys. Chem. B*, 2000, **104**, 5395–5398.

85 D. Zigmantas, R. G. Hiller, V. Sundström and T. Polívka, *Proc. Natl. Acad. Sci. U. S. A.*, 2002, **99**, 16760–16765.

86 M. K. Roos, S. Reiter and R. de Vivie-Riedle, *Chem. Phys.*, 2018, **515**, 586–595.

87 J. D. Coe and T. J. Martínez, *J. Phys. Chem. A*, 2006, **110**, 618–630.

88 P. Chakraborty, Y. Liu, T. Weinacht and S. Matsika, *J. Chem. Phys.*, 2020, **152**, 174302.

89 C. Camacho, R. Cimiraglia and H. A. Witek, *Phys. Chem. Chem. Phys.*, 2010, **12**, 5058–5060.

90 N. Ben Amor, A. Soupart and M.-C. Heitz, *J. Mol. Model.*, 2017, **23**, 53.

91 J. P. Zobel, J. J. Nogueira and L. González, *Chem. Sci.*, 2017, **8**, 1482–1499.

92 G. Giuliani, F. Melaccio, S. Gozem, A. Cappelli and M. Olivucci, *J. Chem. Theory Comput.*, 2021, **17**, 605–613.

93 A. Kerridge, *Phys. Chem. Chem. Phys.*, 2013, **15**, 2197–2209.

2.2 B-Band Dynamics

Energetically above the Q-band lies the B- or Soret-band. It is comprised of the two states B_y and B_x, named after their respective transition dipole moment orientations. Within the Gouterman model they are described by excitations from $\pi_2 \to \pi_1^*$ and $\pi_1 \to \pi_2^*$ (B_x) and by excitations from $\pi_2 \to \pi_2^*$ and $\pi_1 \to \pi_1^*$ (B_y) [109, 110], as shown in Figure 2.2a (page 27). The B-band exhibits a strong absorption around 400 nm, making chlorophylls prone to excitations into these high-energy states. Recent theoretical studies [120, 121] suggested, that especially in PSII blue light exhibits a damaging potential to the reaction centre. Rate models suggest that chlorophyll a is able to undergo $B \to B$ excitation energy transfer once excited to a B-state, competing with ultrafast internal conversion to the Q-band [120, 121]. Both carotenoids and chlorophyll b may act as a trap for the potentially harmful B-state population, as they both exhibit a high spectral overlap with chlorophyll a in this energy region. The $B \to B$ excitation energy transfer from chlorophyll a to either carotenoids or chlorophyll b was reported to be favoured, whereas the back transfer was discovered to be less likely [120, 121]. If a chlorophyll a monomer is excited to the B-band it is mainly assumed, that the relaxation pathway goes from $B \to Q_x \to Q_y$ [15, 16, 119, 122, 123]. As in the case of the Q-band dynamics, also the relaxation from the B-band is highly solvent dependent [15, 118, 122, 124]. So far theoretical and experimental studies focused on the relaxation from the B-band to the Q-band, leaving aside the dynamics and coupling situation between the two B-states. Furthermore, most theoretical simulations are based on semi-classical approaches and are not treating the nuclear motion quantum dynamically [16, 119]. However, a quantum dynamical description of the nuclear dynamics becomes necessary, as the excited states are lying close together in energy.

The article “Reassessing the role and lifetime of Q_x in the energy transfer dynamics of Chlorophyll a” was published in *Chemical Science*. From the experimental side the $B \to Q$ transfer and especially the role of Q_x is investigated. The accompanying quantum dynamics simulations cover the full ultrafast relaxation dynamics from B_y all the way to Q_y, shedding light also on the coupling situation between B_y and B_x. The following points briefly summarise the article, focusing on the results from quantum dynamics.

- A combined experimental and theoretical investigation of the ultrafast relaxation process in chlorophyll a was conducted using polarization-controlled static and ultrafast optical spectroscopy, quantum dynamics simulations and effective heat dissipation models.

- The quantum dynamics simulations were performed on 2D PES at the high XMS-CASPT2 level of theory with a CAS(6/6) active space. As coordinates the normal modes with the highest overlap with the NAC vector at the Q_y minimum were chosen, in analogy to the calculations for the Q-band. In a first step, a CASSCF calculation with state-averaging over four roots was conducted, followed by one with state-averaging over eight states. The ensuing XMS-CASPT2 calculation was performed for the states of interest, namely S_0, Q_y, Q_x, B_x, and B_y. Thereby an IPEA and imaginary shift of 0.1 was used, which lead to a Q_y/Q_x energy difference of 0.225 eV at the FC, which is in close agreement with the reference value of 0.23 eV [82].

- To determine the role of Q_x for the relaxation process, the wavepacket dynamics, under the assumption of a delta excitation was performed three times. The first time the couplings between all states were taken into account. The second time only the Q_x state was coupled to the B-band and the third time only the Q_y state. Compared to the simulation where all couplings were considered the one including only coupling to Q_x was very similar, while for treating only coupling to Q_y the $B \rightarrow Q$ population transfer was slowed down significantly. This indicates, that Q_x plays a major role in the relaxation process after B-band excitation. However, experimentally no Q_x features in stimulated emission or excited-state absorption spectra could be detected. This leads to the conclusion, that the relaxation from Q_x to a vibrationally hot Q_y state is faster than the experimental time resolution of ≈30 fs.
- The wavepacket dynamics was also simulated applying an explicit excitation pulse, that pumps about as much population into the B-states as the experimental one. In this dynamics a nearly instantaneous inter-band transfer from $B_y \rightarrow B_x$ or later on from $Q_x \rightarrow Q_y$ was observed. The relaxation from the B-band to the Q-band is slower. Depending on the choice of coordinates it varies between 50 fs to 150 fs, with faster relaxation times for modes with higher overlap with the NAC vector and slower ones for the coordinates with smaller overlap. The experimentally observed $B \rightarrow Q$ relaxation time was determined as 110 fs, which is in good agreement with the theoretical values.
- Additionally, MD simulations of chlorophyll *a* in three different solvents (acetone, benzonitrile, ethanol) were performed. From these the shape of the first solvation shell was determined for each of the different solvents. To do so chlorophyll *a* was divided into different fragments for which the radial distribution function of solvent atoms surrounding each fragment was determined and averaged over the whole trajectory. From this analysis also the number of solvent molecules in the first solvation shell and its volume were estimated. These parameters were then fed into a rate constant model.
- The simplified numerical model predicted a molecule-to-solvation shell transfer time of ≈1 ps, a thermal broadening effect of the Q_y over ≈1 ps and a spectral narrowing over ≈10 ps, as the first solvation shell re-equilibrates with the rest of the solvent. These values could be identified experimentally after B-band excitation, although the line shape changes were very small.
- After B-band excitation the experiments exhibit four kinetic components attributed to the $B \rightarrow Q$ relaxation (110 fs), the intra-molecular vibrational redistribution to a hot pseudo-thermal Q_y state (solvent dependent lifetime of 400 fs to 2 ps), the relaxation

from this hot thermal state (7 ps to 11 ps) and the excited state lifetime of chlorophyll a (5 ns). The $B \rightarrow Q$ transfer time matches well with the quantum chemical results, while the 400 fs to 2 ps and the 7 ps to 11 ps components can be explained with the rate constant model.

- With these complementary findings of experiments and high-level quantum dynamics simulations we could shed light on the relaxation process of chlorophyll a and especially the previously debated role of Q_x during the relaxation.

Hereafter, the article "Reassessing the role and lifetime of Q_x in the energy transfer dynamics of Chlorophyll a" published in *Chemical Science* under a Creative Commons Attribution 4.0 International License (CC BY 3.0, URL: https://creativecommons.org/licenses/by/3.0) is reproduced from *Chemical Science*, **16**, 1684 (2025). The supporting information of this article is available under https://doi.org/10.1039/d4sc06441k.

Chemical Science

EDGE ARTICLE

View Article Online
View Journal | View Issue

Check for updates

Cite this: *Chem. Sci.*, 2025, **16**, 1684

All publication charges for this article have been paid for by the Royal Society of Chemistry

Reassessing the role and lifetime of Q_x in the energy transfer dynamics of chlorophyll *a*†

Erika Keil, [a] Ajeet Kumar, [a] Lena Bäuml, [b] Sebastian Reiter, [b] Erling Thyrhaug, [a] Simone Moser, [c] Christopher D. P. Duffy, [d] Regina de Vivie-Riedle [b] and Jürgen Hauer *[a]

Chlorophylls are photoactive molecular building blocks essential to most photosynthetic systems. They have comparatively simple optical spectra defined by states with near-orthogonal transition dipole moments, referred to as B_x and B_y in the blue/green spectral region, and Q_x and Q_y in the red. Underlying these spectra is a surprisingly complex electronic structure, where strong electronic-vibrational interactions are crucial to the description of state characters. Following photoexcitation, energy-relaxation between these states is extremely fast and connected to only modest changes in spectral shapes. This has pushed conventional theoretical and experimental methods to their limits and left the energy transfer pathway under debate. In this work, we address the electronic structure and photodynamics of chlorophyll *a* using polarization-controlled static – and ultrafast – optical spectroscopies. We support the experimental data analysis with quantum dynamical simulations and effective heat dissipation models. We find clear evidence for B → Q transfer on a timescale of ∼100 fs and identify Q_x signatures within fluorescence excitation and transient spectra. However, Q_x is populated only fleetingly, with a lifetime well below our ∼30 fs experimental time resolution. Outside of these timescales, the kinetics are determined by vibrational relaxation and cooling. Despite its ultrashort lifetime, our theoretical analysis suggests that Q_x plays a crucial role as a bridging state in B → Q energy transfer. In summary, our findings present a unified and consistent picture of chlorophyll relaxation dynamics based on ultrafast and polarization-resolved spectroscopic techniques supported by extensive theoretical models; they clarify the role of Q_x in the energy deactivation network of chlorophyll *a*.

Received 23rd September 2024
Accepted 25th November 2024

DOI: 10.1039/d4sc06441k

rsc.li/chemical-science

Introduction

Photosynthetic systems efficiently harness sunlight by absorbing it and transferring the excitation energy to a reaction center where charge separation occurs.[1,2] Globally, the vast majority of light-harvesting and charge-separation functionality relies on chlorophylls (Chls) or bacteriochlorophylls (BChls). They play essential roles in energy transfer and charge separation and serve as the principal cofactors in the early steps of photosynthesis. For this reason, much effort has been devoted to understanding their electronic structure and ultrafast relaxation dynamics using various experimental and theoretical methods.[3–8]

Despite their structural diversity, all Chls share two prominent spectral bands: the lowest energy Q-band (550–720 nm) and the Soret- or B-band (350–480 nm). Historically, these bands have been characterized using the Gouterman four-orbital model of the π–π^* transitions in porphyrins.[9,10] In this model, the Q-band consists of two distinct electronic states, which we name $Q_{x,\mathrm{el}}$ and $Q_{y,\mathrm{el}}$. Their indices relate to the direction of the respective transition dipole moment within the plane of the macrocycle (Fig. 1a). Later, increasingly sophisticated quantum chemical calculations and experiments aimed to refine the assignment of the observed absorption bands to the two electronic states. However, the energetic position of the $Q_{x,\mathrm{el}}$ state remained ambiguous. In 2013, Reimers *et al.*[3] proposed a new band assignment based on vibronic coupling, mixing the states within the Q-band. We refer to the states after incorporating such coupling effects as Q_x and Q_y. This coupling strongly influences the spectral properties of Chl *a*. For example, the angle between the Q_x and Q_y transition dipole moments would naively be expected to be close to 90°, but the experimentally measured value for Chl *a* is ∼70–78°.[11,12] In

---

[a] *Technical University of Munich, TUM School of Natural Sciences, Department of Chemistry, Lichtenbergstrasse 4, 85748 Garching, Germany. E-mail: juergen.hauer@tum.de*

[b] *Department of Chemistry, Ludwig-Maximilians-Universität München, Butenandtstr. 11, 81377 Munich, Germany*

[c] *Institute of Pharmacy, Department of Pharmacognosy, University of Innsbruck, Austria*

[d] *Digital Environment Research Institute, Queen Mary University of London, London E1 4NS, UK*

† Electronic supplementary information (ESI) available. See DOI: https://doi.org/10.1039/d4sc06441k

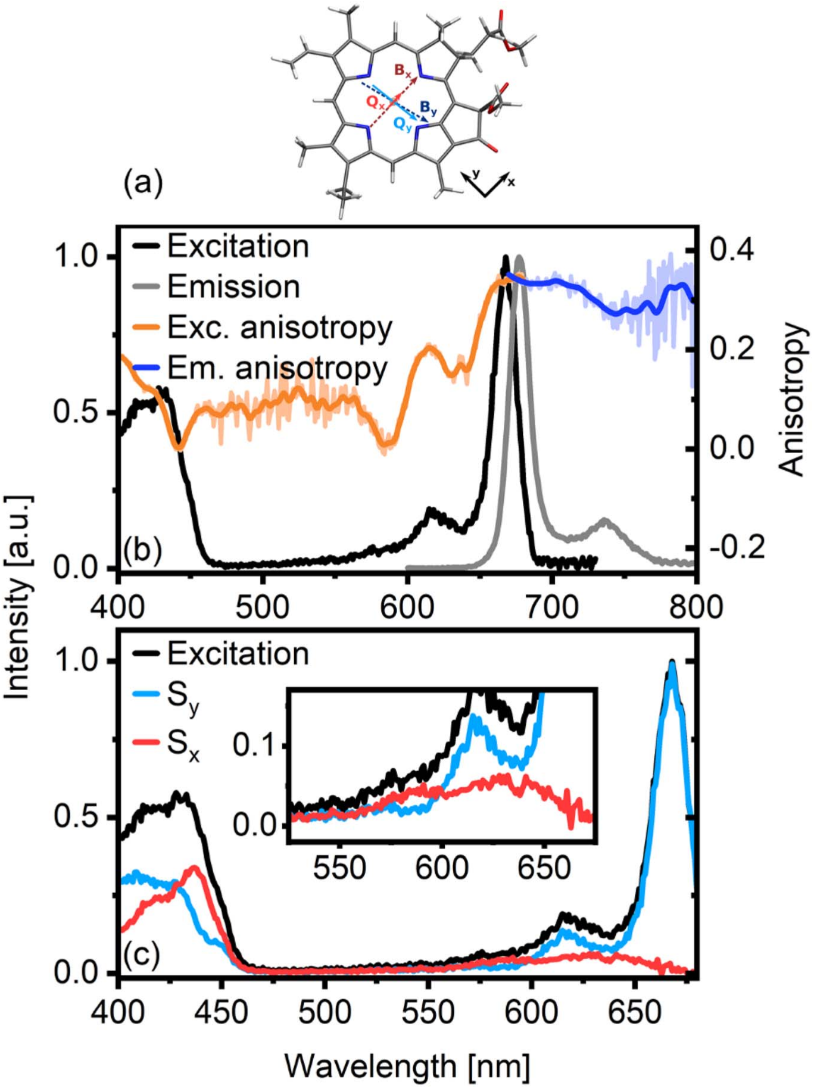

Fig. 1 Molecular structure of Chl *a* including the relative orientations of the main transition dipole moments along the porphyrin rings (a). There are two sets of optical transitions (B and Q), each comprising two almost perpendicular TDMs (subscripts *x* and *y*). Panel (b) shows the excitation and emission anisotropy of Chl *a* in an isopropanol glass. The emission anisotropy (r_{em}, blue line) was measured for $\lambda_{\text{exc}} = 660$ nm, while the excitation anisotropy (r_{exc}, orange line) was measured for $\lambda_{\text{em}} = 690$ nm. The excitation anisotropy clearly shows the presence of differently oriented transitions. We therefore decompose it into *x*-polarized (S_x) and *y*-polarized (S_y) excitation spectra (c) for $\beta = 17°$.

several subsequent two-dimensional electronic spectroscopy (2DES) studies, vibronic coupling was discussed as the basis of fast signal oscillations,[13,14] the vibronic origin of which was proven by polarization-controlled studies.[7] A similar conclusion was reached from theoretical studies, where it was shown that the Q_x and Q_y potential energy surfaces do not cross in an energetically accessible region, and non-adiabatic coupling facilitates ultrafast population transfer across the potential energy surfaces.[5] Previous to 2DES studies, results from transient absorption (TA) spectroscopy were interpreted so that $Q_x \rightarrow Q_y$ transfer shows a strong and unusual solvent dependence, with Q_x-lifetimes ranging from 100–250 fs in different solvents.[8,15]

In this work, we reinterpret the internal conversion dynamics of Chl *a*, as determined by TA spectroscopy with ~20 fs excitation and ultra-broadband probing. To offer a comprehensive picture of the relevant deactivation pathways in Chl *a*, we perform TA experiments exciting the B and the Q-band selectively and compare our results with theoretical models. We can unambiguously determine a B → Q transfer time of ~100 fs from our experimental data and corroborate our findings using theoretical models. We also show that coupling effects within the Q bands lead to almost instantaneous intraband relaxation.

To test our hypothesis of near-instantaneous $Q_x \rightarrow Q_y$ transfer, we go beyond global analysis of TA data and search for

Q_x-signals using polarization-selective spectroscopy, followed by isolation of polarization-associated spectra.[16] Given reported Q_x lifetimes of up to several hundreds of femtoseconds,[15] we should observe x-polarized stimulated emission (SE) from Q_x, along with Q_x ground-state bleach (GSB) and excited-state absorption (ESA). While we successfully isolate the GSB signature of Q_x, we find no sign of x-polarized SE or ESA features to indicate a transiently populated Q_x state. We attribute this to vibronic mixing and rule out the conventional interpretation of Q_x as a state with up to 300 fs lifetime.[15] Instead, we offer an interpretation of the kinetic components found in TA based on intra-molecular vibrational redistribution and subsequent vibrational cooling, as described by an effective model.

The paper is structured as follows: to identify GSB signatures of Q_x, we first analyze polarization-associated spectra derived from cryogenic fluorescence excitation spectra ("Assignment of Q_x and Q_y transitions"). Direct excitation of Q_x is a non-ideal starting ground for studying dynamics, as the absorption features of Q_x and Q_y overlap strongly. Instead, we excite the B-band and try to isolate transient Q_x features. We compare these results with TA data after direct Q_x/Q_y excitation ("Ultrafast relaxation dynamics of Chl a").

Similarly to the dissection of linear spectra, we attempt to isolate Q_x- and Q_y-related excited state absorption features in transient absorption anisotropy (TAA) ("Isolating Q_x-features by polarization control") and compare our measured results to theoretical predictions ("System and system-bath relaxation dynamics at different timescales"). We show that neither TA experiments with sub 20 fs pump pulses nor polarization-controlled experiments can establish a timescale for $Q_x \rightarrow Q_y$ transfer. Instead, our work offers a new perspective on the energy transfer dynamics in Chl *a*. We relate the experimentally observed ultrafast dynamics to solvent relaxation processes and obtain a robust and consistent picture supporting strong mixing between Q-states.

Results

Assignment of Q_x and Q_y transitions

Fig. 1b shows the normalized excitation (black line) and emission (grey line) spectra of Chl *a* in an isopropanol glass. The small Stokes shift of the fluorescence spectrum indicates a minor displacement of the excited state potential surface, as also discussed in earlier work.[14,17] Accordingly, the emission and absorption spectra are similar in shape, although not exactly symmetric. The differences are mainly in the sidebands, where the breakdown in mirror-image symmetry has been connected to vibronic coupling interactions.[17,18] The excitation spectrum in the Q band region has one dominant peak at *ca.* 670 nm and two shoulders at *ca.* 620 nm and 570 nm. Based on previous work, the main peak can be assigned to the Q_y transition.[19] However, assigning the shoulders – particularly determining the position of the Q_x transition – is not straightforward.[6,17] The locations of the Q_x and Q_y transitions in Chl *a* vary with the solvent and the coordination of the molecule. In isopropanol, where the system is penta-coordinated,[20] the Q_x band overlaps with Q_y vibrational bands,[17] making a definite assignment of the shoulder bands challenging. Several groups have investigated the transition energy of Q_x and its vibronic sidebands, either by calculation[4,5] or experiment.[3,17] In this work, we employ polarized excitation and emission spectroscopy of Chl *a* in an isopropanol glass.

Alongside the excitation and emission spectra, Fig. 1b also shows fluorescence anisotropy traces. The emission anisotropy (r_{em}, blue line) was measured for $\lambda_{\mathrm{exc}} = 660$ nm, while the fluorescence excitation anisotropy (r_{exc}, orange line) was measured for $\lambda_{\mathrm{Em}} = 690$ nm. In the Q band region, $\mathrm{r}_{\mathrm{exc}}$ of the main transition centered at 670 nm is almost flat. It reaches a value of 0.35, indicating near-parallel emission and absorption dipoles. As emission occurs from Q_y, this band must be y-polarized. The same high value is obtained from r_{em} upon excitation at 660 nm, proving the measurements to be consistent. While the main transition at 670 nm belongs to Q_y, $\mathrm{r}_{\mathrm{exc}}$ shows clearly that the high-energy side of the Q band region contains contributions from electronic states with different polarizations, as anisotropy values here are as low as zero.

Several approaches have been developed to decompose optical spectra by leveraging the information on transition dipole moment (TDM) directions available from anisotropies.[21–23] Most commonly, in the absence of a macroscopically oriented sample, these methods "project" the isotropic spectrum into contributions either parallel or orthogonal to a reference TDM. For excitation anisotropy measurements, this reference is the TDM of the emissive transition, while for emission anisotropy, the reference TDM is that of the pumped transition. In many cases, however, the TDMs of a given molecule are not exactly orthogonal, and the decomposition of the spectra in orthogonal components is not ideal. As earlier work has shown that the Chl *a* Q_x and Q_y TDMs are not orthogonal,[11] this type of spectral decomposition will not result in optimal separation of the contributions. In a recent study, we developed a slightly modified decomposition approach, which is suitable for systems where TDMs are not orthogonal.[16] In this approach, we can cleanly separate spectral contributions not only when the underlying TDMs are at an angle $\theta = 90°$, but at any angle $\theta = 90° - \beta$. The parameter angle β introduced here can be thought of as the rotation angle of an orthogonal molecular coordinate system defined by the reference TDM. For details, we refer to the corresponding publications.[16,24]

In Fig. 1c we show the decomposition of the Chl *a* excitation spectrum into components polarized parallel (here: S_y, blue in Fig. 1c) and orthogonal (here: S_x, red) to the emissive transition (Q_y fluorescence) according to the procedure outlined above. We note that besides Q_x features, S_x also contains signals with a TDM parallel to B_x, while S_y contains both Q_y and B_y contributions. If we assume orthogonal Q_x and Q_y transitions (corresponding to $\beta = 0$), we clearly achieve sub-optimal separation of the spectrum with noticeable contamination of the S_x spectrum by features associated with the y-polarized transitions (see Fig. S1†). Increasing the value of β to 17°, however, maximizes the 670 nm peak in the S_y spectrum and simultaneously achieves optimal separation of the spectrum into "pure" but overlapping Q_x and Q_y contributions, each with their respective vibronic progressions. Note that both the S_x spectral maximum at approximately 640 nm and the relative angle between Q_x and Q_y of $\theta = 90 - \beta = 73°$ are in good agreement with previously reported results.[4] In essence, polarization-associated analysis of Chl *a* excitation spectra is a straightforward and effective way of isolating overlapping Q_x and Q_y ground state transitions.

Ultrafast relaxation dynamics of Chl *a*

Although Chl *a* has been studied extensively, open questions remain concerning the exact mechanism of energy transfer dynamics within this molecule. The most common scheme employed to explain Chl *a* energy relaxation is a sequential one, *i.e.*, $B_x \rightarrow Q_x \rightarrow Q_y$. B → Q transfer seems to occur within 100–150 fs, as inferred by time-resolved fluorescence depletion spectroscopy[15] or UV pump, NIR probe TA.[25] A time-constant in the 100–250 fs range with notable strong and unusual solvent dependence has been attributed to the subsequent $Q_x \rightarrow Q_y$ transfer.[15]

To better elucidate the mechanism of energy transfer dynamics in Chl *a*, we perform TA experiments under different excitation conditions (B- and Q-band excitation) and in various solvents (acetone, ethanol (EtOH), and benzonitrile (BN)). In particular, we expect to observe direct evidence of B → Q transfer and to understand the origin of the reported solvent dependence of the $Q_x \rightarrow Q_y$ energy transfer step. In the following, we show a representative set of data for Chl *a* in acetone. The corresponding plots for the other two solvents are shown in ESI Fig S2 and S3.† Absorption and pump pulse spectra are shown in Fig. 2a (Fig. S2†). Chirp-corrected TA data

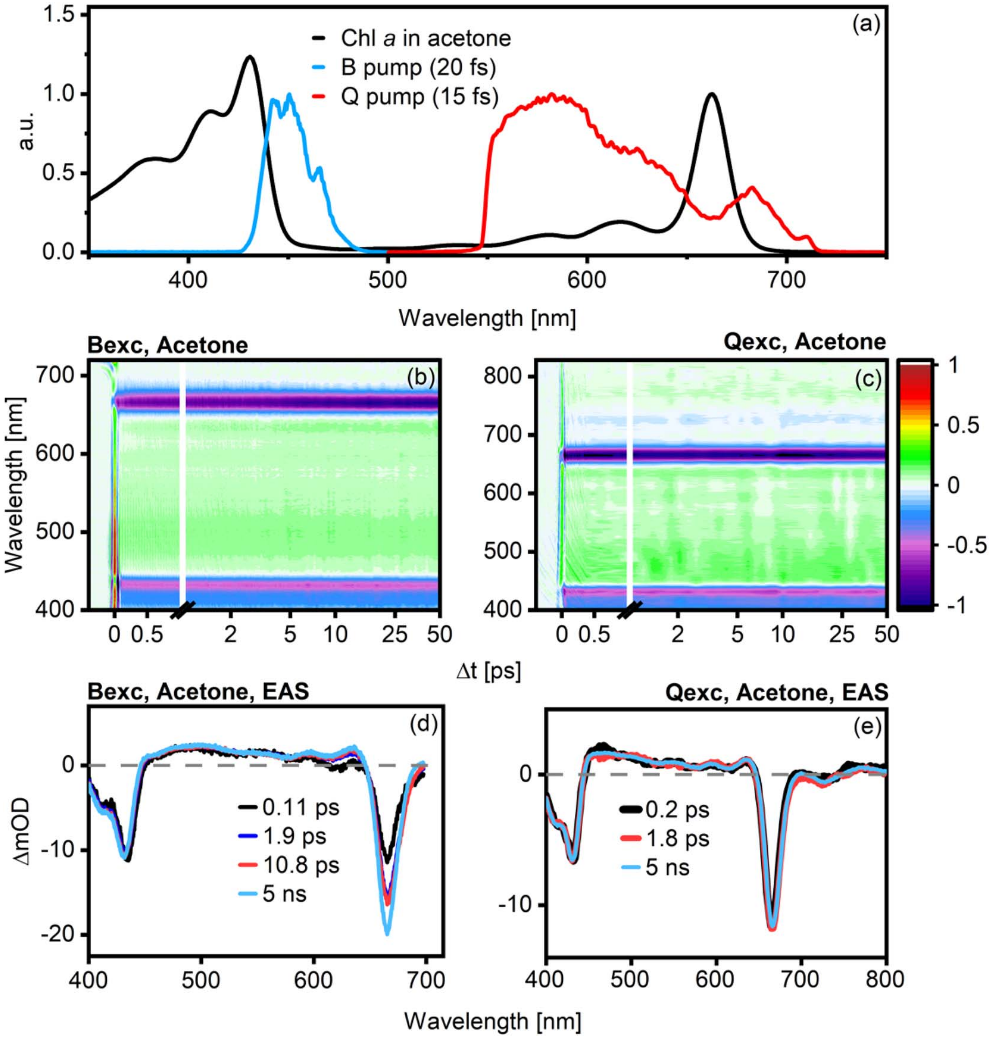

Fig. 2 Absorption spectrum of Chl *a* in acetone plotted against the pump spectra for B-band (blue line) and Q-band (red line) excitation (a). Chirp-corrected TA data for both excitation conditions are shown in (b) and (c). Visible changes in the dynamics are present after B excitation, with a clear increase of the Q-band GSB signal over time, but this is not true after Q excitation. The EAS and lifetimes extracted from global analysis of Chl *a* in acetone are shown in (d) after excitation in the B-band and in (e) after excitation in the Q band. The corresponding plots for Chl *a* in EtOH and benzonitrile are shown in Fig. S2.†

in magic angle (MA) configuration after B- and Q-band are shown in Fig. 2b and c, and the global analysis results are shown in Fig. 2d and e (Fig. S3†). The lifetimes corresponding to the individual spectral components are reported in each panel. Only the evolution-associated spectra (EAS) are shown for simplicity, while the decay-associated spectra for all solvents are shown in ESI Fig. S4.†

In the case of B-band excitation (Fig. 2b and d), the best fit is achieved with four kinetic components. The shortest component has a lifetime of ∼110 fs (black line), with negligible solvent dependence. It is characterized by a decrease and blue shift of the signal in the B-band region (430 nm) and a concomitant increase of the main Q-band signal (660 nm). This behavior is consistent with B → Q transfer, and the B → Q transfer time agrees with previously reported values.[8] The second component (dark blue line) shows minimal spectral evolution; the only noticeable feature is a slight broadening of the Q_y band. From the global fits, it appears to be strongly solvent-dependent, varying from *ca.* 400 fs (BN, *cf.* Fig. S3†) to 2 ps (acetone). Notably, the amplitude of this component is near-negligible, and it is not associated with any spectral evolution typical of state-to-state energy transfer. As changes to small-amplitude components do not substantially affect the goodness-of-fit, the lifetime associated with this component is inevitably highly uncertain. As such, although this component appears to exhibit some solvent dependence, we do not make strong quantitative claims about this behavior. We emphasize, however, that this component does not contain significant changes to stimulated emission or excited state absorption, implying that it is not related to population transfer. The third kinetic component (red line), with a lifetime of about 7–11 ps, correlates with a narrowing of the Q_y band and an increase in its amplitude. Finally, the last kinetic component (light blue line, fixed to 5 ns) is readily assigned to the excited state lifetime of Chl *a* as known from fluorescence lifetime measurements.[26]

In the case of Q-band excitation (Fig. 2c and e), only three components are necessary to obtain a satisfactory data fit. We again observe an ultrafast component of 100–300 fs (black line) that was previously assigned to $Q_x \rightarrow Q_y$ transfer.[8,15] If this component was associated with population transfer, we would expect a signal decrease in the 520–630 nm Q_x-region concomitant with an increase in the Q_y ground-state bleach (GSB)/stimulated emission (SE) amplitude around 660 nm. As in the B-band excitation case, however, we do not observe any such features, leaving this component inconsistent with a population transfer process. An intermediate 1.5–15 ps component (red line) with extremely small amplitude similarly does not relate to significant spectral changes, suggesting a small structural reorganization process. The longest component is again the excited state lifetime of Chl *a*, fixed at 5 ns (light blue line).

Isolating Q_x features by polarization control

General problems with the analysis of the Q_x features of Chl *a* are the weakness of the transition and its strong spectral overlap with the Q_y-related signals (*cf.* Fig. 1). It could then be conceivable that the lack of $Q_x \rightarrow Q_y$ population transfer features in MA-TA stems from their smaller amplitudes being covered by the larger Q_y signals.

To isolate Q_x-signatures and to determine their transient behavior, we have measured transient absorption anisotropy (TAA) data for Chl *a* in acetone after B-band excitation. With these data, we can decompose the TA signals into polarized components in an analogous procedure to that described for excitation anisotropy.[16,24] In this case, a value of $\beta = 32°$ is necessary to fully suppress the Q_y peak. In the employed representation, S_x contains signals with a TDM parallel to that of B_x, including all Q_x features, while S_y contains the Q_y and B_y contributions. Representative spectra are shown for a time delay $\Delta t = 120$ fs in Fig. 3a. At this delay time, effects due to pump-and-probe pulse overlap are negligible, and there is already population in the Q-band resulting from B → Q transfer (*cf.* Fig. 2b and d).

In search for Q_x-features, we identify two weak negative peaks at 580 nm (*ca.* 17 200 cm^{-1}) and 625 nm (*ca.* 16 000 cm^{-1}), matching the Q_x features observed in the excitation anisotropy measurements (Fig. 3a, red line and inset). They show an energy spacing of about 1100 cm^{-1} as calculated by fitting a bi-gaussian function to the peaks (Fig. 3a, inset, black lines), in excellent agreement with magnetic circular dichroism spectra for pentacoordinated Chl *a*.[3]

The lineshape of the S_x spectrum remains identical for time delays between 100 fs and several ps (Fig. S5†). This means that while we observe the Q_x GSB, no Q_x SE (or excited-state absorption (ESA)) features are discernible. We support this statement further by performing a global analysis of the polarization-decomposed TA maps shown in the ESI (Fig. S6†). Similar time constants are needed to fit S_x and S_y, and there is no evidence for a transient population of an excited Q_x state.

We further examine the possibility of Q_x ESA features by comparing the experimental excited state spectrum to calculations for both B-excitation (Fig. 3b) and Q-excitation (Fig. 3c). The experimental excited state spectrum is determined from the measured TA spectrum by subtracting the GSB.[27,28] The latter is approximated by a scaled absorption spectrum. The resulting spectra only contain ESA and SE contributions. We then compare the lineshapes of these spectra at early and late times with calculations for the Q_x- and Q_y-associated ESA, considering one acetone molecule coordinating to the central Mg of a Chl *a* molecule. Notably, the excited-state spectrum at early times after B-band excitation has a positive feature at 655 nm which is absent at later times and in the case of Q-band excitation. We attribute this to ESA from the B-band, which is cancelled by the Q-band GSB, explaining why we do not observe this feature in the magic angle TA data in Fig. 2d. While the calculated Q_y ESA-peaks correspond to measured features at both early and late times, the features related to Q_x ESA are missing. In particular, two intense Q_x-features are expected in the 16 000–21 000 cm^{-1} region at early times. However, the measured spectra in this region at early and late times are effectively identical. While ESA from Q_y is clearly visible, the lack of excited-state signatures associated with Q_x means that Q_x is either not significantly involved in the energy relaxation network or its lifetime is shorter than the experimental time resolution.

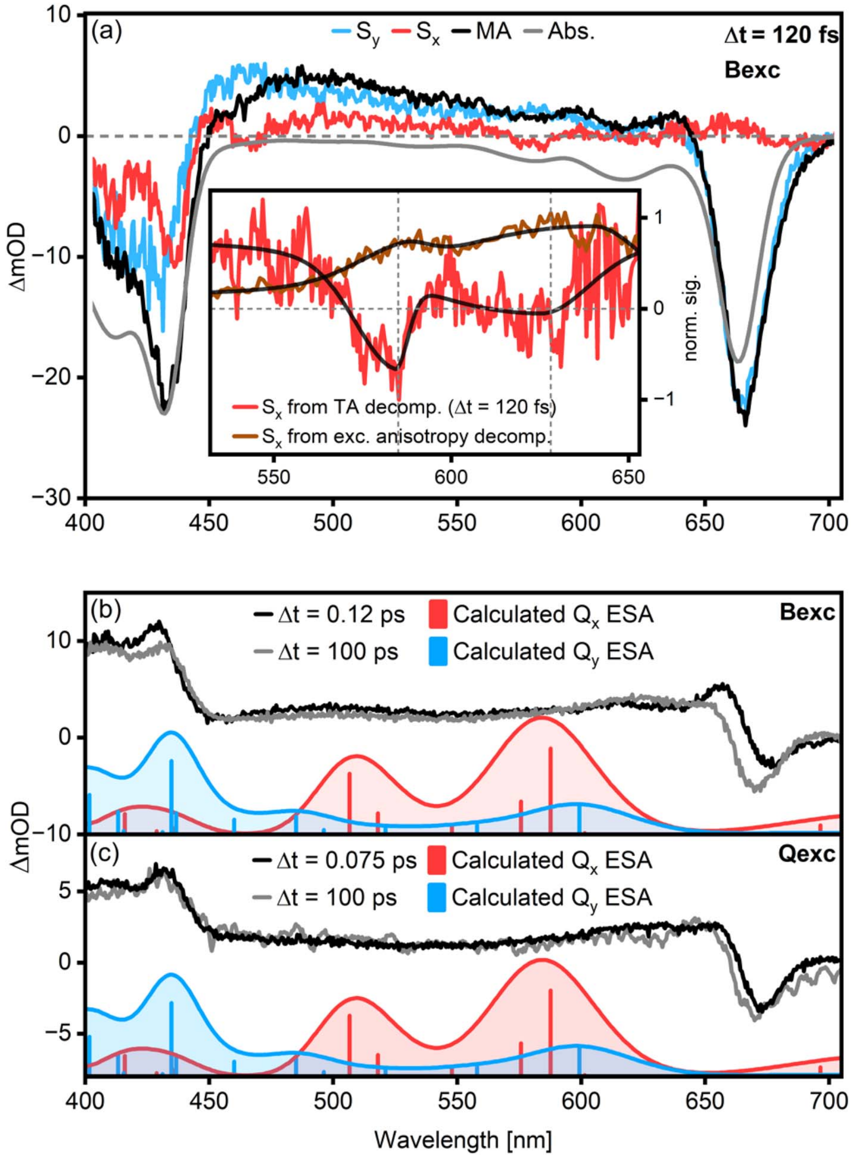

Fig. 3 Results of the Chl *a* TA data decomposition into polarized components at $\Delta t = 120$ fs (a) for $\beta = 32°$. Here, S_x is chosen to indicate the direction parallel to the pumped TDM and contains all contributions with this polarization. Accordingly, the Q_y transitions are suppressed and appear only in S_y. The Q_x GSB transitions extracted from polarized TA and steady-state anisotropy match well (a, inset). They show an energy spacing of about 1100 cm^{-1} as calculated by fitting a bi-gaussian function to the peaks. Excited-state associated spectra of Chl *a* after excitation in the B-band (b) and the Q-band (c) were calculated for different time delays (grey and black lines) and are compared to theoretical Q_x and Q_y ESA band positions (blue and red histograms and curves, oscillator strength unscaled). The theoretical ESA band positions were calculated considering one acetone molecule coordinating to the central Mg of a Chl *a* molecule. Calculated ESA transitions from Q_y match the experimental spectrum well, while Q_x-ESA features are absent.

System and system-bath relaxation dynamics at different timescales

We compare our experimental results with quantum dynamics calculations (details in Fig. S7, S8 and Table T1†). Our XMS-CASPT2 results predict that the excited-state potentials of Chl *a* are nested on top of each other with minimal curve displacement. This is illustrated in Fig. 4a with a cut through the potential energy surface (PES) along the mode with the highest projection onto the non-adiabatic coupling (NAC) vector, with a vibrational frequency of 1489 cm^{-1} (mode 171 in the frequency analysis). Cuts along modes with weaker coupling and different frequencies show the same trend (Fig. S8†). We did not observe any crossings in the central region of the PES where most of the population resides. The temporal evolution of the population of the adiabatic states is depicted in Fig. 4b. We note that while the dynamics simulations include the non-

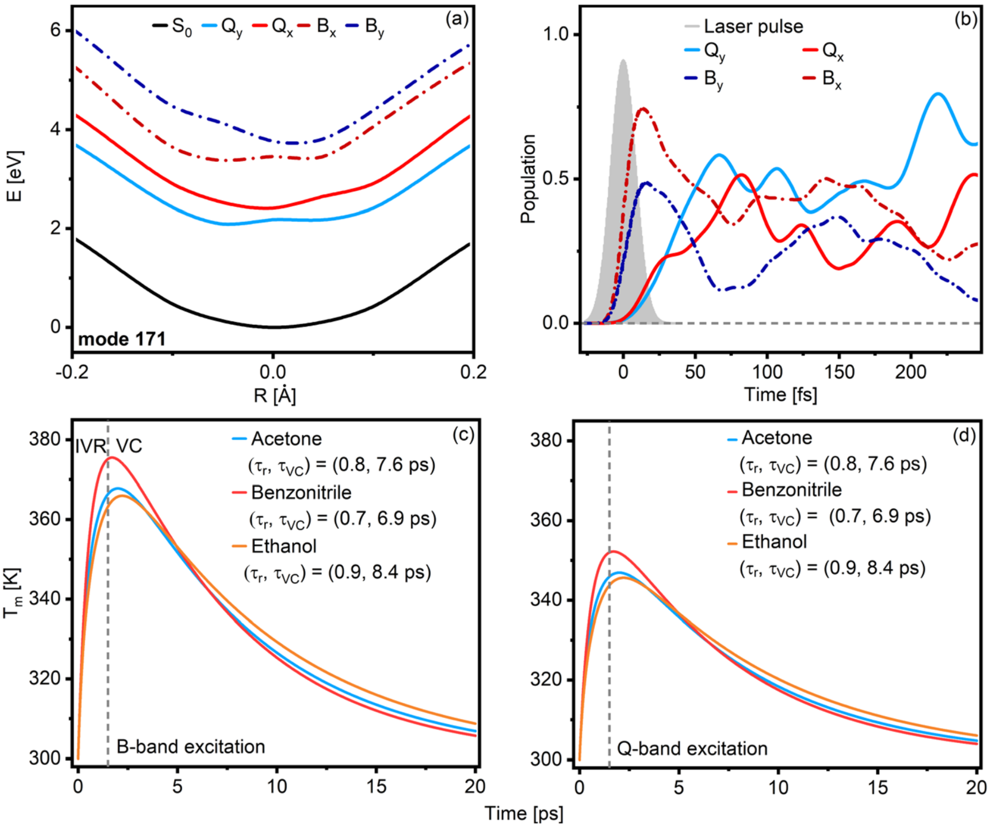

Fig. 4 Cuts through the potential energy surfaces of Chl *a* along the mode with the strongest projection on the non-adiabatic coupling vector (a). The curve displacement between the excited states is negligible, resulting in nested potentials with no evident curve crossings. B_x and B_y, as well as Q_x and Q_y, show a small energy gap and therefore large coupling, which explains the almost instantaneous population transfer between them. The comparatively large energy gap between B_x and Q_x, on the other hand, leads to predicted transfer times of ~100 fs (b). At longer timescales, energy relaxation occurs *via* intra-molecular vibrational redistribution (IVR), followed by slower equilibration with the surrounding solvent (vibrational cooling VC). We capture the effects of biphasic energy relaxation in a simplified model for B-band (c) and Q-band (d) excitation scenarios and for different solvents. Since less energy is deposited into the Q_y vibrational manifold, the peak local temperature is less than for B-band excitation.

adiabatic coupling terms, the depicted populations correspond to those of the electronic states within the Born–Oppenheimer approximation and not the vibronic states observed in experiment. After excitation to the B-band with an explicitly simulated pump pulse, a population transfer from B to Q occurs on a moderately longer timescale than the intra-band transfer. This is explained by the significant energy difference between the B and Q bands (Fig. 4a). The exact timescale of the B → Q transfer depends on the amount of initially excited vibrational levels contained in the wavepacket. On PES constructed with normal modes of lower overlap with the NAC vector and in different spectral ranges, the dynamics are generally slower than normal modes of high overlap (Fig. S8†). Nonetheless, all simulations have in common that the intra-band transfer in both the B and the Q band is almost instantaneous. In contrast, the B to Q transfer takes about 50–150 fs. This is in excellent agreement with our experimental data presented in the discussion of Fig. 2. Further, we find that the B → Q transfer heavily depends on coupling the B band with Q_x. If this coupling is turned off, the B → Q transfer slows down significantly. On the contrary, if B/Q_y coupling is turned off, the population dynamics do not change much (Fig. S8†).

While we can readily explain ultrafast time constants with our quantum dynamics simulations, the dynamics at longer times are not practically accessible with this type of calculation. At these longer timescales, we expect energy redistribution and dissipation to the solvent to be the dominating contributions to the dynamics.[28] As such, the bath must be considered when trying to reproduce the longer kinetic components observed in TA.

We construct a simplified numerical model to test our hypothesis of cooling dynamics on multiple timescales. Excitation of Chl *a* with a visible laser pulse always means that a large amount of energy is deposited into the vibrational modes of the molecule. Energy deposited – directly or indirectly – into a high-lying state of Q_y will relax in a non-linear sequence of intra-molecular vibrational redistribution (IVR) events, solute-to-solvent energy transfer, and solvent equilibration. Using an effective molecular temperature T_m (details and modeling parameters in the ESI text, Table T2, Fig. S9 and S10†) that increases with the energy deposited into the system, we predict a molecule-to-solvation shell transfer time of ~1 ps. This is consistent with observations from our previous work on carotenoids.[29–31] The dynamics of T_m are determined by two timescales: $\tau_{IVR} \sim 1$ ps, which accounts for the rise in T_m due to thermalization of the Q_y state, and $\tau_{VC} \sim 7–9$ ps, which is the relaxation of the solute due to vibrational cooling (VC) into the solvation shell. The exact values of the time constants vary with the solvent (Fig. 4c and d). The results indicate that the relaxation kinetics are almost independent of whether one excites Q_y directly or indirectly *via* the B-band. However, the maximum T_m reached should be affected by excitation wavelength, as this defines the amount of energy that thermalizes (Fig. 4c and d). As τ_{IVR} is associated with heating and τ_{VC} with cooling, we expect to observe thermal broadening effects of the Q_y-band over ~1 ps as the maximum T_m is achieved, followed by spectral narrowing over ~10 ps as the population of low-frequency vibrational modes drops while the solute and first solvation shell re-equilibrate with the bulk solvent. Careful inspection of the decay-associated and evolution-associated spectra (DAS and EAS, respectively) in the Q-band region (Fig. S11†) confirms these predictions for excitation in the B-band, although the observed lineshape changes are minimal. After Q-band excitation, IVR and cooling are much less pronounced. In particular, we do not observe a narrowing in ~10 ps as expected. Instead, we observe a minimal but continuous redshift typical of Stokes shift dynamics (Fig. S11†).[28]

Discussion

The results presented in this work clarify some essential aspects of the mechanism of energy relaxation in Chl *a*. When excited in the B-band, population transfer to the Q band occurs within 120 fs, as demonstrated by TA experiments (Fig. 2d) and quantum dynamical calculations (Fig. 4b). The Q band contains Q_x and Q_y, two distinct but strongly coupled states with overlapping but discernible absorption spectra (Fig. 1). However, polarized TA measurements show no evidence of *x*-polarized excited state features (Fig. 3). As such, we can conclude that either Q_x is not involved in B → Q energy relaxation in Chl *a*, or that the $Q_x \rightarrow Q_y$ transfer is faster than our time resolution (*ca.* 30 fs). Our quantum chemical calculations strongly support the latter interpretation, as the B → Q transfer was shown to slow significantly if the B/Q_x coupling is turned off (Fig. S8†).

An implication of these observations is that none of the time constants found in MA-TA (*cf.* Fig. 2) can be assigned to $Q_x \rightarrow Q_y$ transfer. The small amplitudes and only subtle influence on the spectra of the kinetic components other than the one related to B → Q transfer suggest instead an association with IVR and subsequent heat dissipation to the solvent.

In Fig. 5, we propose a comprehensive scheme for the internal conversion dynamics of Chl *a*. After the initial B → Q transfer, the state we detect is y-polarized. Therefore, if Q_x is participating in the energy transfer as suggested by the quantum dynamics calculations, its relaxation towards a vibrationally hot, *y*-polarized state must be faster than our time resolution. The relaxation from there to the vibrationally relaxed Q_y occurs through IVR, leading to heat exchange with the first solvation shell. Further relaxation to bulk solvent (VC) then occurs on slower timescales. Overall, IVR and VC are sufficient to explain the timescales in the evolution of the Chl *a* TA spectra beyond the first few hundred fs after B-band excitation: ~1 ps for IVR to a hot pseudo-thermal state, ~10 ps for relaxation of the hot thermal state (Fig. 4c and *cf.* Fig. 2d). The effect of IVR and VC on the lineshape is much less pronounced after Q-band excitation. In this case, the changes in the lineshape can be explained by Stokes shift dynamics.[28]

In summary, our findings shed new light on the internal conversion dynamics in Chl *a*. Although the heating–cooling cycle on the Q_y surface of Chl *a* is highly complicated and requires further investigation from both experimental and theoretical sides, we reach a good agreement between model and experiment. We present experimental and theoretical evidence for B → Q transfer on a ~120 fs timescale. The relaxation dynamics in the Q band are dominated by the strong coupling of the Q_x and Q_y states and occur on a <30 fs timescale. This leads to the absence of *x*-polarized excited-state signatures in TAA experiments. We attribute this ultrafast Q_x lifetime to the

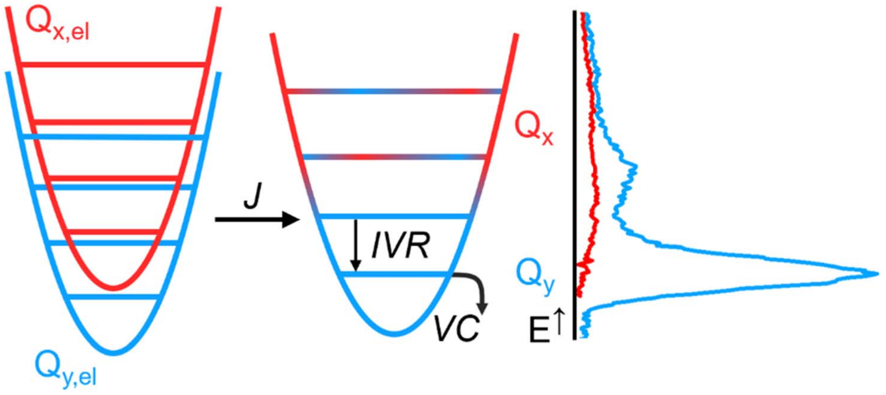

Fig. 5 Vibronic mixing (*J*) in the Q band leads to strongly coupled states Q_x (red) and Q_y (blue). Ultrafast transfer *via* Q_x populates a vibrationally excited Q_y, which in turn relaxes *via* intra-molecular vibrational redistribution (IVR), followed by slower equilibration with the surrounding solvent (vibrational cooling VC). The right panel shows a sketch of the spectral profiles of Q_x and Q_y, as discussed in Fig. 1.

small and internal-coordinate-independent energy gap between Q_x and Q_y. Regardless of its short lifetime, Q_x seems important for efficient B → Q relaxation, as the B → Q transfer rate slows down if B/Q_x coupling is deactivated. Based on these results, we reinterpret the solvent-dependent, longer time constants found in TA measurements as a combination of IVR, VC, and possibly Stokes shift dynamics on Q_y. Overall, our unique combination of extensive theoretical modeling, numerical methods, and highly sensitive TA experiments allows us to paint a clear and consistent picture of the energy transfer in Chl *a* under the excitation conditions relevant to photosynthetic systems and to shed light on the previously controversial role of the Q_x state in the Chl *a* dynamics.

Materials and methods

Materials

HPLC and spectroscopy grade solvents acetonitrile (ACN), ethyl acetate (EtOAc), acetone, ethanol (EtOH), BN and methanol (MeOH) were obtained from VWR (Ismaning, Germany) and ultra-pure water (18 MΩ cm^{-1}) from a Millipore S.A.S. Milli-Q Academic system (18.2 MΩ cm^{-1}, Molsheim, France).

Chromatography

Analytical HPLC. An Agilent 1260 Infinity II LC system was used with a 1260 Infinity Degasser, a 1260 Series quaternary pump and 1260 Series diode array detector; Merck LiChrospher® 100 RP-18 (5 µm) LiChroCART® 125-4, with or without a Phenomenex ODS 4 × 2 mm i.d. pre-column; injection volume: 100 µL. Isocratic mobile phase: ACN/MeOH/EtOAc 6/2/2,[32] flow rate 0.5 mL min^{-1}. Data were processed with OpenLab CDS Data Analysis 2.3.

Semi-preparative HPLC. Büchi Pure C-830 with prep HPLC pump 300 bar, fraction collector, and prep sample injection valve. Gynkotek LC-System with manual sampler, M480 pump, Phenomenex DG-301 online degasser, Gynkotek UVD 640 diode array detector and a Rheodyne injection valve with 5 mL loop. Column: Phenomenex Luna C8(2), 100 Å, 250 × 100 mm with a Phenomenex pre-column C18 15 × 21.2 mm; mobile phase ACN/MeOH/EtOAc 6/2/2, isocratic conditions, flow rate 4 mL min^{-1}. Data were processed with Gynkosoft 5.50 or Büchi Pure software 1.5.

Spectroscopy

HR-MS were measured at the MS facility of the Department of Chemistry, University of Munich. Data were processed using Xcalibur.

UV-vis spectra were measured on a PerkinElmer Lambda 365 spectrometer. Emission spectra were measured on a Spectrofluorometer FS5 (Edinburgh Instruments). All spectra are background-corrected.

Extraction procedure for Chl *a*

Frozen spinach was purchased at a local supermarket (Edeka junger Spinat). 8 portions of frozen spinach (approximately 15 g each) were thawed by soaking the spinach in water; water was removed from the soaked spinach by squeezing the spinach with a table cloth. The spinach was then mixed with a blender in 100 mL of cold acetone/MeOH (9/1 v/v). The resulting slurry was centrifuged at 4 °C for 5 min at 1000 rpm. The supernatant was filtered; the filtrate was collected on ice and directly applied to semi-preparative HPLC. The Chl *a* fraction was collected on ice, and the solvents were evaporated *in vacuo*, yielding 9.7 mg of Chl *a*.

HR ESI-MS (positive ion mode): m/z (found) = 893.5426; m/z (calculated) = 893.5426, Δ = 0.56 ppm.

TA spectroscopy

Chl *a* samples were prepared by dissolving the pigment in acetone, EtOH or BN to an OD of 0.2–0.3 and then degassing the solution with nitrogen for about one minute.

TA experiments were performed for Chl *a* in acetone, ethanol (EtOH), and benzonitrile (BN). Chl *a* was excited in the B and Q bands in separate experiments for all solvents. The pulse duration of the two pump pulses was comparable, with the B-pump at 20 fs and the Q-pump at 15 fs as measured by SD-FROG and SHG-FROG, respectively. The measured and retrieved FROG traces, as well as the retrieved spectral and temporal phase profiles, are shown in the ESI (Fig. S12†). The TA setups used for B- and Q-band excitation have been described in detail before.[33,34] Briefly, a 5 kHz, 2.5 mJ, 25 fs amplified laser system (Coherent Legend Elite Duo HE+ Ti : Sapphire MOPA) is used to seed a 1 m long, commercial hollow-core fiber (HCF) with a core diameter of 250 µm filled with 1 bar of Argon gas. The resulting supercontinuum is either frequency-doubled in an achromatic second-harmonic scheme to yield the B-band pump pulse[33] or spectrally filtered to obtain the Q-band pump pulse.[34] In the first case, the pump is compressed by a three-prism configuration, while in the second case, the compression is achieved by chirped mirrors. In both experiments, the probe pulse is given by a supercontinuum obtained by seeding a CaF_2 crystal with the NIR part of the HCF output. For B-band excitation, a double-chopping scheme was employed to reduce scatter, and the pump energy was 60 nJ per pulse with a focal spot diameter of 200 µm; for Q-band excitation, the pump pulse was not chopped and its energy was 16 nJ per pulse with a focal spot of 140 µm. The data was recorded at MA (54.7°) configuration between pump and probe for B- and Q-pumping. Additionally, datasets with parallel and perpendicular polarization of pump and probe were recorded for B-band excitation of Chl *a* in acetone in order to calculate the TAA.

Global analysis was performed with the open-source software Glotaran.[35,36]

Quantum dynamics simulations

The quantum dynamics simulations were performed on 2D PES at the XMS-CASPT2 (ref. 37–39) level of theory, using the basis set ANO-RCC-VDZP[40–42] and a CAS(6/6) active space in the gas phase. As coordinates, we chose the normal modes exhibiting the highest overlap with the non-adiabatic coupling vector at the Q_y minimum geometry,[5] optimized at the CAM-B3LYP/6-311G* level.[43] These modes are 171 and 198, lying at 1489 cm^{-1} and 1639 cm^{-1}, respectively. Other normal modes (239 and 103) with smaller overlap with the NAC vector and in a different spectral range were also tested for PES construction. Geometries are available in the ESI.† The resulting quantum dynamics is similar for all modes, but the timescales slow down with decreasing overlap with the NAC vector (Fig. S9†). At each point of the PES, a RASSCF calculation was performed with state averaging over four states, followed by one with state averaging over eight states (Fig. S8†). The ensuing XMS-CASPT2 calculation was performed for the states of interest, namely the S_0, Q_y, Q_x, B_x, and B_y. An IPEA[44] and an imaginary shift[45] of 0.1 were applied, as in our previous study.[5] With this approach, an energy difference between Q_x and Q_y at the FC point of 0.225 eV is obtained, which corresponds well with our reference value of 0.23 eV.[5] The non-adiabatic coupling elements were computed at the XMS-CASPT2 level of theory. All PES, NAC, and TDM calculations were performed with the OpenMolcas 23.06 program package.[46–48] The QDng software package[49] was used for the subsequent quantum dynamic simulations. The propagation was initially performed by assuming a delta excitation into B_y, therefore populating this state's manifold of vibrational levels. Later, an explicitly simulated pump pulse with a maximum field strength of 0.0026 GV cm^{-1}, an FWHM of 20 fs, and a central frequency of $\omega_0 = 3.60$ eV was also applied to excite the population from the ground state into the B Band. The laser parameters were chosen to excite a similar population (about 5%) into the B-band as in our experimental studies.

Calculated ESA spectra

Geometries of the Q_y and Q_x states of Chl *a* with one axially coordinated acetone molecule were optimized using Gaussian 16C.02 (ref. 50) with the CAM-B3LYP density functional[51] and the 6-311G* basis set.[43,52,53] Bulk solvent effects were described with the polarizable continuum model (PCM).[54,55] Five roots were included in the optimization. Optimized geometries were verified as energy minima by the absence of imaginary vibrational frequencies.

Excited state absorption spectra for the optimized geometries were simulated at the double-hybrid TDDFT level using the ORCA 5.0.3 software package.[56–58] The SCS-ωPBEPP86 density functional[59] was used in the Tamm–Dancoff approximation[60] along with the def2-TZVPD[61,62] basis. The calculation was accelerated by employing the RIJCOSX approximation[63,64] with the def2/J[65] and def2-TZVPD/C[66] auxiliary basis sets. A tighter-than-usual integration grid (ORCA keyword DefGrid3) and convergence criteria (ORCA keywords VeryTightSCF TightPNO) were employed. The bulk solvent was described implicitly *via* the linear-response conductor-like polarizable continuum model (LR-CPCM),[67,68] assuming equilibrium solvation in the excited state.

Data availability

Data for this article, including absorption spectra, pump pulse spectra, transient absorption and transient absorption anisotropy maps are available at **https://zenodo.org/records/14033283**.

Author contributions

EK and AK performed the experiments; SM provided the sample; SR, LB, CD, and RdVR performed calculations; EK, AK, ET, SR, LB, RdVR, CDPD, and JH analyzed and interpreted the data; EK and JH prepared the plots; EK, AK, ET and JH wrote the main text. All authors reviewed the manuscript before submission.

Conflicts of interest

The authors declare no competing interests.

Acknowledgements

J. H., A. K., S. R., L. B. and R. d. V.-R. gratefully acknowledge funding by the Deutsche Forschungsgemeinschaft (DFG, German Research Foundation) through the cluster of excellence e-conversion under Germany's Excellence Strategy – EXC 2089/1 – 390776260 and *via* project 514636421. S. M. would like to thank Rita Socher for technical support.

References

1 R. E. Blankenship, *Molecular Mechanisms of Photosynthesis*, Wiley/Blackwel, Chichester, West Sussex, 2nd edn, 2014.
2 R. Croce and H. van Amerongen, Natural strategies for photosynthetic light harvesting, *Nat. Chem. Biol.*, 2014, **10**, 492–501.
3 J. R. Reimers, Z.-L. Cai, R. Kobayashi, M. Rätsep and E. Krausz, Assignment of the Q-Bands of the Chlorophylls: Coherence Loss via Q_x-Q_y Mixing, *Sci. Rep.*, 2013, **3**, 2761.
4 C. Zahn, T. Stensitzki and K. Heyne, Femtosecond anisotropy excitation spectroscopy to disentangle the Q_x and Q_y absorption in chlorophyll *a*, *Chem. Sci.*, 2022, **13**, 12426–12432.
5 S. Reiter, L. Bäuml, J. Hauer and R. de Vivie-Riedle, Q-Band relaxation in chlorophyll: new insights from multireference quantum dynamics, *Phys. Chem. Chem. Phys.*, 2022, **24**, 27212–27223.
6 Y. Song, A. Schubert, E. Maret, R. Burdick, B. Dunietz, E. Geva and J. Ogilvie, Vibronic structure of photosynthetic pigments probed by polarized two-dimensional electronic spectroscopy and ab initio calculations, *Chem. Sci.*, 2019, **10**, 8143–8153.
7 E. Bukarté, A. Haufe, D. Paleček, C. Büchel and D. Zigmantas, Revealing vibronic coupling in chlorophyll c1 by polarization-controlled 2D electronic spectroscopy, *Chem. Phys.*, 2020, **530**, 110643.
8 W. P. Bricker, P. Shenai, A. Ghosh, Z. Liu, M. Enriquez, P. Lambrev, H.-S. Tan, C. Lo, S. Tretiak, S. Fernandez-Alberti and Y. Zhao, Non-radiative relaxation of photoexcited chlorophylls: Theoretical and experimental study, *Sci. Rep.*, 2015, **5**, 13625.
9 M. Gouterman, Spectra of porphyrins, *J. Mol. Spectrosc.*, 1961, **6**, 138–163.

10 M. Gouterman, G. H. Wagnière and L. C. Snyder, Spectra of Porphyrins Part II. Four Orbital Model, *J. Mol. Spectrosc.*, 1963, **11**, 108–127.

11 M. Linke, A. Lauer, T. Von Haimberger, A. Zacarias and K. Heyne, Three-dimensional orientation of the Q_y electronic transition dipole moment within the chlorophyll *a* molecule determined by femtosecond polarization resolved VIS pump-IR probe spectroscopy, *J. Am. Chem. Soc.*, 2008, **130**, 14904–14905.

12 R. Simonetto, M. Crimi, D. Sandonà, R. Croce, G. Cinque, J. Breton and R. Bassi, Orientation of chlorophyll transition moments in the higher-plant light- harvesting complex CP29, *Biochemistry*, 1999, **38**, 12974–12983.

13 E. Meneghin, C. Leonardo, A. Volpato, L. Bolzonello and E. Collini, Mechanistic insight into internal conversion process within Q-bands of chlorophyll *a*, *Sci. Rep.*, 2017, **7**, 1–7.

14 V. Tiwari, W. K. Peters and D. M. Jonas, Electronic resonance with anticorrelated pigment vibrations drives photosynthetic energy transfer outside the adiabatic framework, *Proc. Natl. Acad. Sci. U. S. A.*, 2013, **110**, 1203–1208.

15 Y. Shi, J. Y. Liu and K. L. Han, Investigation of the internal conversion time of the chlorophyll *a* from S3, S2 to S1, *Chem. Phys. Lett.*, 2005, **410**, 260–263.

16 Y. Xu, L. Mewes, E. Thyrhaug, V. Sláma, F. Šanda, H. Langhals and J. Hauer, Isolating Pure Donor and Acceptor Signals by Polarization-Controlled Transient Absorption Spectroscopy, *J. Phys. Chem. Lett.*, 2023, **14**, 5390–5396.

17 M. Rätsep, J. Linnanto and A. Freiberg, Mirror symmetry and vibrational structure in optical spectra of chlorophyll *a*, *J. Chem. Phys.*, 2009, **130**, 194501.

18 J. R. Reimers, M. Rätsep, J. M. Linnanto and A. Freiberg, Chlorophyll Spectroscopy: Conceptual Basis, Modern High-Resolution Approaches, and Current Challenges, *Proc. Est. Acad. Sci.*, 2022, **71**, 127.

19 C. Houssier and K. Sauer, Circular dichroism and magnetic circular dichroism of the chlorophyll and protochlorophyll pigments, *J. Am. Chem. Soc.*, 1970, **92**, 779–791.

20 S. Krawczyk, The effects of hydrogen bonding and coordination interaction in visible absorption and vibrational spectra of chlorophyll *a*, *Biochim. Biophys. Acta, Bioenerg.*, 1989, **976**(2–3), 140–149.

21 E. W. Thulstrup, J. Michl and J. H. Eggers, Polarization spectra in stretched polymer sheets, II.1 Separation of π–π* absorption of symmetrical molecules into components, *J. Phys. Chem.*, 1970, **74**, 3868–3878.

22 A. C. Albrecht, Polarizations and assignments of transitions: The method of photoselection, *J. Mol. Spectrosc.*, 1961, **6**, 84–108.

23 E. Thyrhaug, T. J. Sørensen, I. Gryczynski, Z. Gryczynski and B. W. Laursen, Polarization and symmetry of electronic transitions in long fluorescence lifetime triangulenium dyes, *J. Phys. Chem. A*, 2013, **117**, 2160–2168.

24 Y. Xu, M. Peschel, M. Jänchen, R. Foja, G. Storch, E. Thyrhaug, R. de Vivie-Riedle and J. Hauer, Determining Excited-State Absorption Properties of a Quinoid Flavin by Polarization-Resolved Transient Spectroscopy, *J. Phys. Chem. A*, 2024, **128**, 3830–3839.

25 P. M. Shenai, S. Fernandez-Alberti, W. P. Bricker, S. Tretiak and Y. Zhao, Internal Conversion and Vibrational Energy Redistribution in Chlorophyll *a*, *J. Phys. Chem. B*, 2016, **120**, 49–58.

26 J. S. Connolly, F. A. Janzen and E. B. Samuel, Fluorescence lifetimes of chlorophyll *a* : solvent, concentration and oxygen dependence, *Photochem. Photobiol.*, 1982, **36**(5), 559–563.

27 D. A. Cherepanov, F. Gostev, I. Shelaev, A. Aibush, A. Semenov, M. Mamedov, V. Shuvalov and V. Nadtochenko, Visible and Near Infrared Absorption Spectrum of the Excited Singlet State of Chlorophyll *a*, *High Energy Chem.*, 2020, **54**, 145–147.

28 P. Martinsson, J. Oksanen, M. Hilgendorff, P. Hynninen, V. Sundström and E. Akesson, Dynamics of ground and excited state chlorophyll *a* molecules in pyridine solution probed by femtosecond transient absorption spectroscopy, *Chem. Phys. Lett.*, 1999, **309**(5–6), 386–394.

29 V. Šebelík, C. D. P. Duffy, E. Keil, T. Polívka and J. Hauer, Understanding Carotenoid Dynamics via the Vibronic Energy Relaxation Approach, *J. Phys. Chem. B*, 2022, **126**(22), 3985–3994.

30 V. Balevičius, A. Pour, J. Savolainen, C. Lincoln, V. Lukeš, E. Riedle, L. Valkunas, D. Abramavicius and J. Hauer, Vibronic energy relaxation approach highlighting deactivation pathways in carotenoids, *Phys. Chem. Chem. Phys.*, 2015, **17**, 19491–19499.

31 V. Balevičius, C. Lincoln, D. Viola, G. Cerullo, J. Hauer and D. Abramavicius, Effects of tunable excitation in carotenoids explained by the vibrational energy relaxation approach, *Photosynth. Res.*, 2018, **135**(1–3), 55–64.

32 S. M. Petrovic, J. B. Zvezdanović and D. Z. Marković, The identification of chlorophyll and its derivatives in the pigment mixtures: HPLC-chromatography, visible and mass spectroscopy studies, *Adv. Technol.*, 2012, **1**, 16–24.

33 E. Keil, P. Malevich and J. Hauer, Achromatic frequency doubling of supercontinuum pulses for transient absorption spectroscopy, *Opt. Express*, 2021, **29**, 39042.

34 A. Kumar, P. Malevich, L. Mewes, S. Wu, J. Barham and J. Hauer, Transient absorption spectroscopy based on uncompressed hollow core fiber white light proves pre-association between a radical ion photocatalyst and substrate, *J. Chem. Phys.*, 2023, **158**, 144201.

35 J. J. Snellenburg, S. P. Laptenok, R. Seger, K. M. Mullen and I. H. M. Van Stokkum, Glotaran: A Java-Based Graphical User Interface for the R Package TIMP, *J. Stat. Software*, 2012, **49**(3), 1–22.

36 I. H. M. Van Stokkum, D. S. Larsen and R. Van Grondelle, Global and target analysis of time-resolved spectra, *Biochim. Biophys. Acta, Bioenerg.*, 2004, **1657**(2–3), 82–104.

37 T. Shiozaki, W. Győrffy, P. Celani and H.-J. Werner, Communication: Extended multi-state complete active space second-order perturbation theory: Energy and nuclear gradients, *J. Chem. Phys.*, 2011, **135**, 081106.

38 A. A. Granovsky, Extended multi-configuration quasi-degenerate perturbation theory: The new approach to multi-state multi-reference perturbation theory, *J. Chem. Phys.*, 2011, **134**, 214113.

39 J. Finley, P.-Å. Malmqvist, B. O. Roos and L. Serrano-Andrés, The multi-state CASPT2 method, *Chem. Phys. Lett.*, 1998, **288**(2–4), 299–306.

40 B. O. Roos, V. Veryazov and P.-O. Widmark, Relativistic atomic natural orbital type basis sets for the alkaline and alkaline-earth atoms applied to the ground-state potentials for the corresponding dimers, *Theor. Chem. Acc.*, 2004, **111**, 345–351.

41 B. O. Roos, R. Lindh, P.-Å. Malmqvist, V. Veryazov and P.-O. Widmark, Main Group Atoms and Dimers Studied with a New Relativistic ANO Basis Set, *J. Phys. Chem. A*, 2004, **108**(15), 2851–2858.

42 P.-O. Widmark, P.-Å. Malmqvist and B. O. Roos, Density matrix averaged atomic natural orbital (ANO) basis sets for correlated molecular wave functions, *Theor. Chim. Acta*, 1990, 77, 291–306.

43 T. Yanai, D. P. Tew and N. C. Handy, A new hybrid exchange–correlation functional using the Coulomb-attenuating method (CAM-B3LYP), *Chem. Phys. Lett.*, 2004, **393**, 51–57.

44 G. Ghigo, B. O. Roos and P.-Å. Malmqvist, A modified definition of the zeroth-order Hamiltonian in multiconfigurational perturbation theory (CASPT2), *Chem. Phys. Lett.*, 2004, **396**, 142–149.

45 N. Forsberg and P.-Å. Malmqvist, Multiconfiguration perturbation theory with imaginary level shift, *Chem. Phys. Lett.*, 1997, **274**, 196–204.

46 G. Li Manni, *et al.*, The OpenMolcas Web: A Community-Driven Approach to Advancing Computational Chemistry, *J. Chem. Theory Comput.*, 2023, **19**, 6933–6991.

47 F. Aquilante, *et al.*, Modern quantum chemistry with [Open] Molcas, *J. Chem. Phys.*, 2020, **152**, 214117.

48 I. Fernandez-Galván, *et al.*, OpenMolcas: From Source Code to Insight, *J. Chem. Theory Comput.*, 2019, **15**(11), 5925–5964.

49 M. Kowalewski and R. de Vivie-Riedle, *QDng: A Grid Based Molecular Quantum Dynamics Package (1.0.0)*, Deposited 8 April 2024, Zenodo, DOI: **10.5281/zenodo.10944497**.

50 M. J. Frisch, G. W. Trucks, H. B. Schlegel *et al.*, *Gaussian 16 Rev. C.02*, Wallingford, CT, 2016.

51 R. Krishnan, J. S. Binkley, R. Seeger and J. A. Pople, Self-consistent molecular orbital methods. XX. A basis set for correlated wave functions, *J. Chem. Phys.*, 1980, **72**, 650–654.

52 A. D. McLean and G. S. Chandler, Contracted Gaussian basis sets for molecular calculations. I. Second row atoms, Z = 11–18, *J. Chem. Phys.*, 1980, **72**, 5639–5648.

53 M. M. Francl, W. J. Pietro, W. J. Hehre, S. Binkley, M. S. Gordon, D. J. DeFrees and J. A. Pople, Self-consistent molecular orbital methods. XXIII. A polarization-type basis set for second-row elements, *J. Chem. Phys.*, 1982, **77**, 3654–3665.

54 J. Tomasi, B. Mennucci and R. Cammi, Quantum Mechanical Continuum Solvation Models, *Chem. Rev.*, 2005, **105**, 2999–3094.

55 G. Scalmani and M. J. Frisch, Continuous surface charge polarizable continuum models of solvation. I. General formalism, *J. Chem. Phys.*, 2010, **132**, 114110.

56 F. Neese, The ORCA program system, *Wiley Interdiscip. Rev.: Comput. Mol. Sci.*, 2012, **2**, 73–78.

57 F. Neese, F. Wennmohs, U. Becker and C. Riplinger, The ORCA quantum chemistry program package, *J. Chem. Phys.*, 2020, **152**, 224108.

58 F. Neese, Software update: The ORCA program system—Version 5.0, *Wiley Interdiscip. Rev.: Comput. Mol. Sci.*, 2022, **12**, e1606.

59 M. Casanova-Páez, M. B. Dardis and L. Goerigk, ωB2PLYP and ωB2GPPLYP: The First Two Double-Hybrid Density Functionals with Long-Range Correction Optimized for Excitation Energies, *J. Chem. Theory Comput.*, 2021, **17**, 5165–5186.

60 S. Hirata and M. Head-Gordon, Time-dependent density functional theory within the Tamm-Dancoff approximation, *Chem. Phys. Lett.*, 1999, **314**, 291–299.

61 F. Weigend and R. Ahlrichs, Balanced basis sets of split valence, triple zeta valence and quadruple zeta valence quality for H to Rn: Design and assessment of accuracy, *Phys. Chem. Chem. Phys.*, 2005, **7**, 3297–3305.

62 D. Rappoport and F. Furche, Property-optimized Gaussian basis sets for molecular response calculations, *J. Chem. Phys.*, 2010, **133**, 134105.

63 F. Neese, F. Wennmohs, A. Hansen and U. Becker, Efficient, approximate and parallel Hartree-Fock and hybrid DFT calculations. A 'chain-of-spheres' algorithm for the Hartree-Fock exchange, *Chem. Phys.*, 2009, **356**, 98–109.

64 R. Izsák and F. Neese, An overlap fitted chain of spheres exchange method, *J. Chem. Phys.*, 2011, **135**, 144105.

65 F. Weigend, Accurate Coulomb-fitting basis sets for H to Rn, *Phys. Chem. Chem. Phys.*, 2006, **8**, 1057–1065.

66 A. Hellweg, C. Hättig, S. Höfener and W. Klopper, Optimized accurate auxiliary basis sets for RI-MP2 and RI-CC2 calculations for the atoms Rb to Rn, *Theor. Chem. Acc.*, 2007, **117**, 587–597.

67 R. Cammi, B. Mennucci and J. Tomasi, Fast Evaluation of Geometries and Properties of Excited Molecules in Solution: A Tamm-Dancoff Model with Application to 4-Dimethylaminobenzonitrile, *J. Phys. Chem. A*, 2000, **104**, 5631–5637.

68 M. Cossi, N. Rega, G. Scalmani and V. Barone, Energies, structures, and electronic properties of molecules in solution with the C-PCM solvation model, *J. Comput. Chem.*, 2003, **24**, 669–681.

2.3 Outlook on Solvent Dependence

The next step on the way to a better understanding of the photosynthetic processes is the realisation of quantum dynamics simulations in solvent environment. These studies on one hand pave the way to the ultimate aim of understanding chlorophyll dynamics in its natural protein environment. On the other hand they also offer crucial insights for the interpretation of spectroscopic experiments, which are often conducted on pure chlorophyll in different solvents, and the construction of semi-artificial photosynthesis devices. As mentioned in section 2.1, the spectra of chlorophyll exhibit a strong solvent dependence [15–17, 112, 118]. This was, among others, observed in absorption, fluorescence or Raman spectra [113, 125–131]. The time scale of the relaxation process varies noticeably, e.g., between solvents of different polarity [15, 118]: A study using four solvents of different polarity found, that an increase in solvent polarity lead to a decrease of the internal conversion rate [15]. The effect on the $B \rightarrow Q_y$ transfer was thereby slightly weaker than that for the $Q_x \rightarrow Q_y$ relaxation [15]. However, the solvent polarity seems to have a smaller impact than other properties like H-bonding [127, 128, 131] and especially the coordination number at the central magnesium atom [113, 125, 126, 129]. Upon hydrogen bonding, a noticeable redshift of Q_y was reported, which was about a factor of ten larger than the effect of polarity [128]. Due to its small oscillator strength the impact of the solvent on Q_x cannot be measured directly. The influence of the coordination number of the solvent to the central magnesium atom was the topic of several studies. They found that mostly a redshift is observed when going from penta- to hexacoordination [113, 125, 126, 129]. In non-polar solvents usually pentacoordination prevails, while stronger nucleophilic solvents, lower temperatures and higher pressure favour the hexacoordination [125, 129]. In some solvents, like diethyl ether, the coordination number increases when the temperature is decreased [125]. Additionally, also a multitude of other factors such as solvent aromaticity and refraction index contribute to the observed changes in spectra and relaxation times. Theoretical simulations could confirm the change in relaxation time upon solvation in different media [111, 122, 124]. A study on the Q-band relaxation in methanol that applied non-adiabatic excited-state molecular dynamics found the Q_x and Q_y to be lying closer together in energy and being more strongly coupled than in the gas phase. The observed relaxation time decreased from the gas phase calculation over one treating the solvent only implicitly to a mixed implicit-explicit solvation model [111]. There are several different possibilities to include solvent effects into theoretical simulations. The choice depends on the system, the properties of interest, as well as the respective time scales of solvent and solute motion. In cases where their dynamics takes place on similar time scales the two have to be propagated in parallel, which can, for example, be achieved using the Ehrenfest approach [132]. If one of the two is much faster than the other, it is possible to separate their time scales. One can neglect the solvent motion if the solute dynamics is very fast. In cases where the solvent exhibits the faster motion it is possible to average over the solvent dynamics. Here, the applicable methods range from the description of the solvent as harmonic degrees of freedom, over (polarized) continuum models, to their explicit treatment via mixed quantum and molecular mechanic (QM/MM) approaches. An overview over several of these methods are given in the reviews [133–137].

In the appendix A two possibilities for the inclusion of solvent effects are exemplarily presented with respect to their application to the Q-band dynamics of chlorophyll *a*. In section A.1, the inclusion of explicit solvent molecules into a quantum dynamics calculation at a high level of theory (XMS-CASPT2) is discussed together with the results of such calculations for chlorophyll in combination with two ethanol molecules. A more evolved possibility is the inclusion of not only a few explicit solvent molecules, but the additional consideration of a multitude of solvent molecules that surround the molecule of interest. This can be achieved via a mixed quantum and molecular dynamics (QD/MD) approach, which is visualised in Figure 2.3.

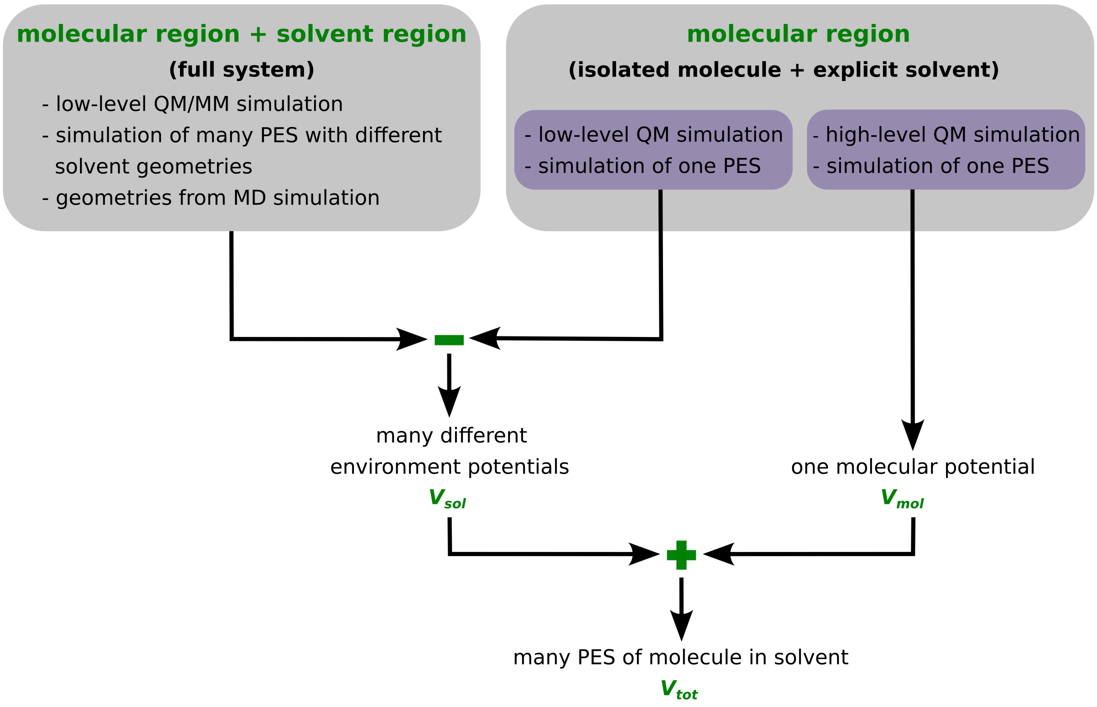

Figure 2.3: Schematic overview of the applied QD/MD workflow.

With the QD/MD approach many PESs of the molecule with different solvent geometries are obtained. Each of these potentials V_{tot} is constructed by adding the potential of the solvent box V_{sol} to the potential V_{mol} of the molecule with explicit solvent. V_{mol} can thereby be calculated at a high level of theory (e.g., XMS-CASPT2), while the solvent potential V_{sol} is simulated at a lower theory level like TD-DFT. A detailed explanation of the QD/MD approach, which is a modified version of the one that was already successfully employed for a study on the nucleobase uracil [100], is given in section A.2.

3

Following the Coupled Dynamics using X-ray Absorption Spectra

In the previous chapters the coupled nuclear and electron dynamics have been discussed for the nucleobase uracil and the natural pigment chlorophyll *a*. The first exhibits a local CoIn seam, whereas the latter is an example of globally coupled PESs without an accessible CoIn. To be able to experimentally observe the proposed nuclear, as well as electronic wavepacket dynamics, extremely short laser pulses are necessary. The first laser pulses reaching the few femtosecond scale were reported in the 1980s [138, 139]. By 1991 pulses as short as 60 fs [140] were achieved and in 1999 the Nobel Prize in Chemistry was awarded to A. Zewail for his studies of the transition states of chemical reactions using femtosecond spectroscopy. Only two years later, in 2001, the group of F. Krausz achieved the first isolated attosecond pulse [19]. In 2023 the Nobel Prize in Physics was awarded to F. Krausz, P. Agostini, and A. L'Huillier for developing the experimental methods to generate attosecond pulses and their application for the study of electron dynamics. With these developments the rapidly evolving field of X-ray spectroscopy offers the resolution power to observe electron dynamics on an attosecond time scale [20–22, 35, 141–145] and resolve even the passage through a CoIn [21, 22]. Available X-ray sources range from synchrotron facilities down to tabletop devices based on high-harmonic generation. Detailed information on the various experimental methods for attosecond pulse generation can be found in Refs. [36, 146]. X-ray spectroscopy not only offers the necessary temporal resolution to study both nuclear and electronic motion, but is also sensitive toward chemical elements, charge and the population of different electronic states and its changes [19, 21, 22, 35, 142, 145, 147].

In parallel, but often also preceding to the experimental evolutions, theoretical methods have been developed to simulate spectra such as XAS [24, 148–150], resonant inelastic X-ray scattering (RIXS) [151, 152], or time-resolved photoelectron spectra (TRPES) [98, 153, 154]. The focus of this work lies on the simulation of static as well as time-resolved XAS. As the interpretation of experimental XAS can get quite complex, the measurement and simulation of the spectra often go hand in hand. In the field of X-ray spectroscopy one can find numerous examples of successful interpretation of experimental results with the help of theoretical simulations [20, 21, 23–41]. However, also the prediction of yet unmeasured spectra is valuable to steer and initiate experiments. By now various methods are available to simulate XAS, covering among others density based methods [148, 155] and wavefunction based ones [24], as well as techniques combining the two [150]. A significant step on the way to the calculation of XAS of larger molecules was the core-valence-separation (CVS) developed in the early 1980s [156, 157]. As the valence- and core-excited states are well-separated in energy, the CVS approximates the couplings between them to be negligibly small and sets them to zero. Therefore, it is possible to separate the calculation of the valence- and core-excited states from each other, greatly reducing the computational effort. The CVS has been incorporated into the most prominent methods for the simulation of XAS, which are, depending on the system of interest, TD-DFT [148], CC [149, 158] and RASSCF or RASPT2 [24]. If processes like the transition through a CoIn are studied, multireference methods like RASSCF or RASPT2 are necessary. However, they are significantly more demanding in calculation time and therefore limited in system size. Alternative approaches are among others DMRG [159, 160], DCD-CAS [161], MC-PDFT [150] or stochastic-GAS [162]. In the subsequent section the workflow to simulate (time-resolved) XAS using RASPT2 in combination with the coupled nuclear and electron dynamics is outlined. This method has been applied to study the excited state dynamics of uracil (see section 3.2) and chlorophyll *a* (see section 3.3). Despite the computational cost of RASPT2, the presented workflow, especially with the adaptions outlined in section 3.3, offers a way to simulate time-resolved XAS on a high level of theory for molecules as large as chlorophyll (82 atoms) and potentially even larger systems. This is crucial to study situations with high non-adiabatic couplings and especially the transition through CoIns in biologically relevant systems.

3.1 Simulation of X-ray Absorption Spectra

Time-resolved XAS are obtained via a pump-probe experiment. The pump pulse thereby initiates a valence excitation, whereas the time-delayed probe pulse excites an inner valence or core electron. The edges are denominated K, L, M, ... corresponding to their principal quantum number (1, 2, 3, ...) with subscripts for the s, p, d, ... electrons. The K-edge therefore probes the $1s$ orbital, the L_1-edge the $2s$ orbital and the $\mathrm{L}_{2/3}$-edge the $2p_{(1/2)}/2p_{(3/2)}$ orbital. In this work the K-edge of oxygen and magnesium were probed. The RASSCF approach with a subsequent XMS-CASPT2 calculation was used to simulate the XAS. The active space is thereby divided into three parts (see Figure 3.1).

The main active space, the RAS2, includes the relevant valence orbitals and takes into account all possible excitations. The optional RAS3 consists of additional unoccupied orbitals and RAS1 includes the core orbitals that are probed. While all excitations are allowed in RAS2, the order of excitation into RAS3 and out of RAS1 is limited. The XAS in this chapter are based on the coupled nuclear and electron dynamics presented

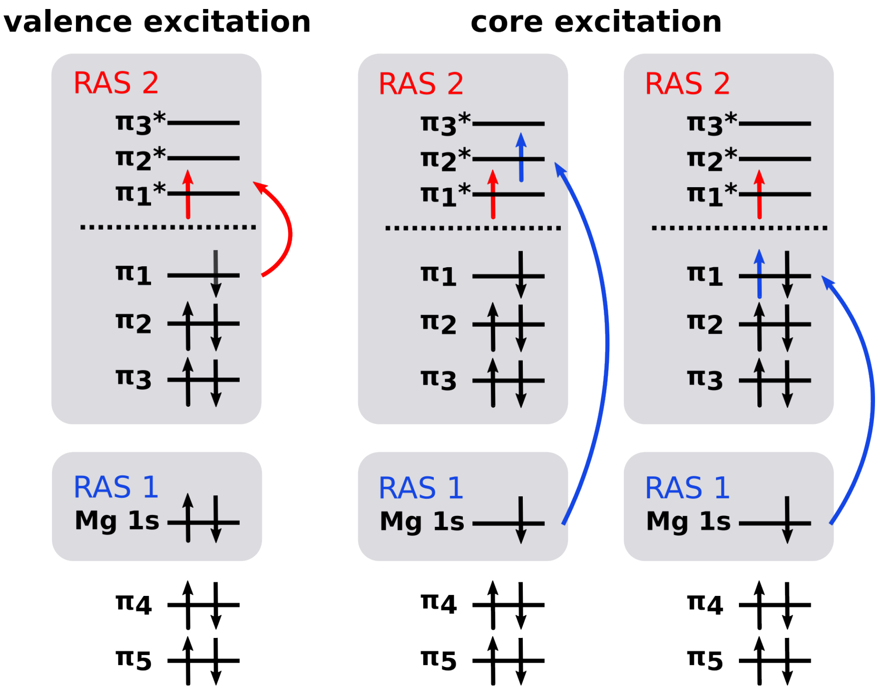

Figure 3.1: Illustration of the RASSCF method and possible valence and core excitations for a magnesium K-edge XAS of chlorophyll with a CAS(6/6) active space in RAS2. The magnesium 1*s* of RAS1 is rotated to lie directly beneath the RAS2 and above the occupied orbitals outside of the active space.

in chapter 1 and 2. These dynamics have been calculated on 2D PES with the nuclear coordinate space being split up into grid points, the NEMol-grid. To obtain time-resolved XAS, as a first step for each of these grid points a static XAS is calculated. A detailed description of the computational steps necessary to obtain the static XAS can be found in both publications of this chapter [83, 84] and the dissertation of Florian Rott [163]. The focus of this work lies on the combination of static XAS with the coupled nuclear and electron dynamics to obtain time-resolved XAS that include the electronic coherence. The description of the necessary steps to extract the static XAS are therefore only presented shortly. Under consideration of the CVS, the calculation of the valence excitations and core excitations can be treated separately. Therefore, two calculations were conducted on the XMS-CASPT2 level [164–166]: one for the valence and one for the core excitations. This procedure is illustrated in Figure 3.1, where apart from an exemplary valence excitation into Q_y also two of the numerous possibilities for core excitations are shown. To include the interaction between all of the states the RASSI method [167–169] with the valence and core wavefunctions as basis is used. In this way one obtains electronic dipole moments and excitation energies of the desired core excited states for all relevant valence states, thus a static XAS. This procedure is repeated for all of the grid points of the NEMol-grid. The resulting stick spectra can be convoluted with either a Lorentzian or Gaussian broadening or a combination of the two. In the literature there is no uniform procedure to determine the value of the broadening. Often it is chosen empirically so that the theoretical spectra fit the experimental XAS [26, 40, 170–174]. In some cases the experimental resolution, limited by the chosen laser source and other equipment, such as detectors, is considered [24, 39]. An illustration of the derived workflow is depicted in Figure 3.2, which is a reproduction of Figure 1 from Ref. [83], reprinted in section 3.2.

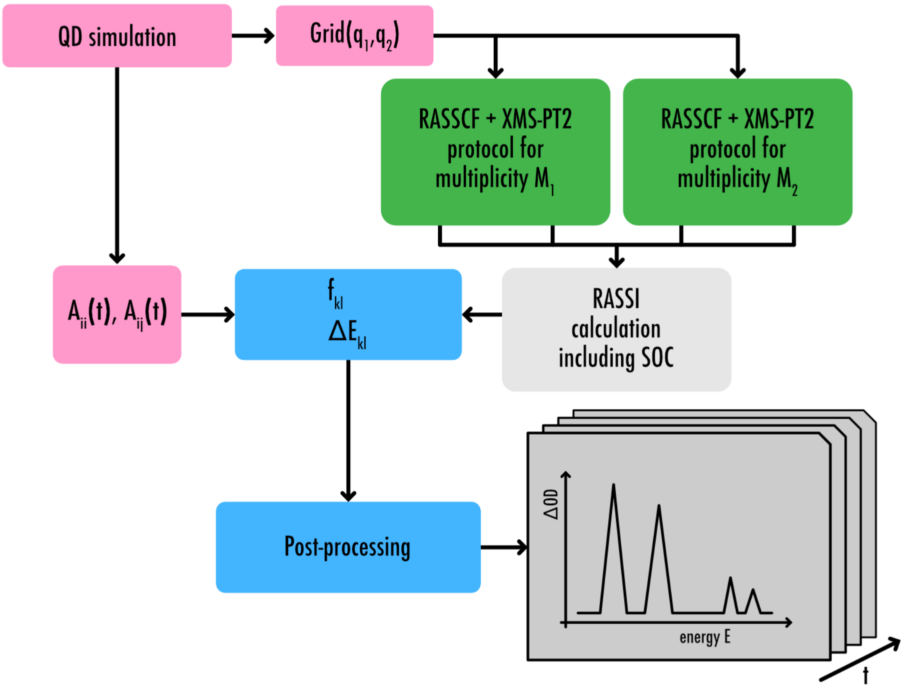

Figure 3.2: Flowchart of the simulation of time-resolved XAS by combination of the RASPT2 results with time-dependent population (A_{ii}) and overlap (A_{ij}) terms. Reprinted with permission from *The Journal of Physical Chemistry A*, **127**, 9787 (2023). Copyright 2023 American Chemical Society.

To derive the time-resolved XAS the static spectra are combined with the coupled nuclear and electron dynamics obtained with NEMol [75]. In the following, the important steps and equations are described, following closely the description in the two publications of this chapter [83, 84]. For both of the presented examples, uracil and chlorophyll *a*, a delta pulse is used as probe pulse. For this no specific alignment of the molecules is assumed. However, for the pump pulse it is assumed that the electric component of the pulse is optimally aligned with the transition dipole moment of the molecule. The probe pulse simultaneously excites the superposition of the considered valence states into the multitude of core-hole states. In this way the probe pulse creates a nuclear wavepacket $\chi_c(R,t)$ for each core-hole state c, that includes the information of all considered valence states. Depending on the system and process of interest, different valence states are of importance and therefore selected for the calculation of the transient XAS. As a first approximation, we construct $\chi_c(R,t)$ as a superposition of the nuclear wavepackets in the considered valence states. We thereby take into account the interference that can occur, since the core-hole state c can be populated by the various valence states simultaneously. With this approximation the total wavefunction $\Psi_c(r,R,t)$ of the core-hole state can be defined as a linear combination of the nuclear wavefunctions of the valence states and the electronic wavefunction of the core-hole state:

$$\Psi_c(r,R,t) = \chi_c(R,t)\varphi_c(r;R) = \sum_j^{N_{val}} \chi_j(R,t)\varphi_c(r;R). \tag{3.1}$$

The transition dipole moment $\mu_{ic}(t)$ between a specific core-hole state c and valence state i can then be written as:

$$\mu_{ic}(t) = \langle \chi_i(R,t)\varphi_i(r;R)|\hat{\mu}| \sum_j^{N_{val}} \chi_j(R,t)\varphi_c(r;R)\rangle. \tag{3.2}$$

The operator $\hat{\mu}$ is assumed to be only depending on the electronic wavefunctions, as the probe pulse is short under experimental conditions. This enables the separation of the electronic transition dipole moment integral from the nuclear wavefunctions, leading to the following approximation for μ_{ic}:

$$\begin{aligned}\mu_{ic}(t) &= \langle \varphi_i(r;R)|\hat{\mu}|\varphi_c(r;R)\rangle \sum_j^{N_{val}} \langle \chi_i(R,t)|\chi_j(R,t)\rangle \\ &= \mu_{ic}^P(t) + \mu_{ic}^C(t).\end{aligned} \tag{3.3}$$

The sum over all valence states $\sum_j^{N_{val}}$ can be split into two parts. The first one, μ_{ic}^P is based on the nuclear wavepacket dynamics in a specific valence state i. It is defined by i and j being equal and can thus be formulated as the electronic transition dipole moment multiplied by the time-dependent population $A_{ii}(t) = \langle \chi_i(R,t)|\chi_i(R,t)\rangle$:

$$\mu_{ic}^P(t) = \langle \varphi_i(r;R)|\hat{\mu}|\varphi_c(r;R)\rangle A_{ii}(t). \tag{3.4}$$

The second part, μ_{ic}^C contains the electronic coherence, as it takes into account the time-dependent overlap of the nuclear wavepacket in different valence states i and j:

$$\mu_{ic}^C(t) = \langle \varphi_i(r;R)|\hat{\mu}|\varphi_c(r;R)\rangle \sum_{(j\neq i)}^{N_{val}} A_{ij}(t), \tag{3.5}$$

with the time-dependent overlap $A_{ij}(t) = \langle \chi_i(R,t)|\chi_j(R,t)\rangle$.

The oscillator strength f_{ic}, that describes the probability of a transition between valence state i and core-hole state c, is based on the population-induced component μ_{ic}^P, as well as the coherence-induced part μ_{ic}^C of the transition dipole moment:

$$f_{ic} = \frac{2}{3}\Delta E_{ic}|\mu_{ic}^P(t) + \mu_{ic}^C(t)|^2. \tag{3.6}$$

Following the described steps, a time-resolved XAS for each grid point is obtained, combining the time-dependent population and overlap terms resulting from the NEMol simulation with the electronic dipole moments and excitation energies calculated with the XMS-CASPT2 and RASSI methods. To derive the complete transient XAS the spectra of all grid points are summed up, forming a single time-resolved XAS. As the time-resolved XAS are based on the coupled nuclear and electron dynamics it is possible to determine the influence the electronic coherence has on the XAS. One can obtain a spectrum that just includes the signals of the electronic coherence by subtracting a XAS that is only based on the contribution μ_{ic}^{P} of the nuclear wavepacket dynamics from the complete XAS, which includes both μ_{ic}^{P} and μ_{ic}^{C}. Other methods for the simulation of time-resolved XAS usually neglect the electronic coherence. The presented combination with the NEMol approach can be used to obtain more accurate spectra and to evaluate the influence of the electronic coherence, which varies strongly from system to system. The two molecules presented in this chapter illustrate two very different situations in which the electronic coherence becomes relevant.

3.2 Uracil: A Case of Strong Localised Coupling

The nucleobase uracil exhibits a CoIn seam between the S_2 and S_1. This seam presents a quite localized area, where the NACs between the two involved states are large. The electronic coherence is directly connected to the amount of coupling between the states, becoming stronger when the wavepacket is located in an area with strong NACs. In addition, significant coupling between states occurs when an excitation pulse is applied, as the pulse artificially couples states involved in the excitation process. Thus, uracil offers the possibility to determine and compare the influence of the electronic coherence induced by the excitation pulse as well as the one induced by the CoIn-mediated dynamics. The excited state dynamics of uracil described in chapter 1 also revealed, that upon excitation to S_2, the nuclear wavepacket first oscillates between the FC region and the S_2 minimum, before it splits and parts of the wavepacket travel successively to the CoIn seam where they relax to S_1. This characteristic movement of the nuclear wavepacket can be tracked using time-resolved XAS.

The article "Following the Nonadiabatic Ultrafast Dynamics of Uracil via Simulated X-ray Absorption Spectra" was published in *The Journal of Physical Chemistry A*. In the following, the key points of the article are summarised.

- A workflow that combines XAS at the XMS-CASPT2 level of theory with the coupled nuclear and electron dynamics obtained with the NEMol approach [75] was derived. The resulting time-resolved XAS include the nuclear wavepacket dynamics as well as the electronic coherence.

- The quantum dynamics simulations of the nucleobase uracil, described in chapter 1, revealed the excited state dynamics. In the present work the observed oscillation of the nuclear wavepacket on the S_2 PES with a step wise relaxation to the S_1, as well as the excitation pulse induced dynamics was followed with theoretical time-resolved XAS.

- A comparison of a static XAS at the FC point for the oxygen K-edge with experimental data [23] showed a difference in the spacing of the peaks. This is caused by the spacing of the valence excitations which strongly depends on the calculation method [103], as well as the neglect of orbital relaxation during the simulation of XAS. To match experimental data the calculated spectrum have to be shifted by 3.90 eV towards higher energies.

- The oxygen K-edge was determined to be best suited for potential experimental observation. The excitation process $\mathrm{FC}(S_0) \rightarrow \mathrm{FC}(S_2)$ can be observed using the signals at 528 eV, characteristic for the ground state, and at 523 eV, only present in the excited state. The ensuing oscillation on the S_2 PES can be tracked via the alternating spectral features at 527 eV ($\mathrm{FC}(S_2)$) and 522 eV ($S_2\mathrm{min}(S_2)$). The relaxation through the CoIn is harder to distinguish as the relevant features at 525 eV and 527 eV are only present for the CoIn in the S_2, but disappear upon relaxation to S_1.

- Going from the static to the time-resolved picture, the relevant signals to track the geometric changes significantly change as more geometries than the FC point, the S_2 minimum, and CoIn contribute to the XAS. In the time-resolved XAS the oscillation of the nuclear wavepacket on the S_2 PES could be followed via the alternating signals at 529 eV ($\mathrm{FC}(S_2)$) and 533 eV ($S_2\mathrm{min}(S_2)$). Tracking the intensity of the signals at 524 eV, which are present for all geometries in the S_2 state, makes it possible to observe the relaxation through the CoIn seam.

- The influence of the electronic coherence, that is created by the overlapping wavepackets of different electronic states, was determined to be much stronger for the excitation pulse induced dynamics (until a delay time of 35 fs), than for the CoIn induced dynamics. In both cases the effect of the electronic coherence is relevant. As it mainly depends on the wavepacket overlap, the electronic coherence is more prominent in cases of very localised nuclear wavepackets as during the excitation pulse induced dynamics.

- During the excitation process fast oscillations that are of the same frequency as the pump pulse could be observed when neglecting the ground state bleach. In contrast, much slower oscillations were observed during the CoIn induced dynamics, in accordance with the small energy gap between the involved states.

In the following the article "Following the Nonadiabatic Ultrafast Dynamics of Uracil via Simulated X-ray Absorption Spectra" published in *The Journal of Physical Chemistry A* is reprinted with permission from *The Journal of Physical Chemistry A*, **127**, 9787 (2023).

Supplementary information of this article is available under https://doi.org/10.1021/acs.jpca.3c06509.

THE JOURNAL OF PHYSICAL CHEMISTRY A
A JOURNAL OF THE AMERICAN CHEMICAL SOCIETY
pubs.acs.org/JPCA
Article

Following the Nonadiabatic Ultrafast Dynamics of Uracil via Simulated X-ray Absorption Spectra

Lena Bäuml, Florian Rott, Thomas Schnappinger,* and Regina de Vivie-Riedle

Cite This: *J. Phys. Chem. A* 2023, 127, 9787−9796
Read Online

ACCESS | Metrics & More | Article Recommendations | Supporting Information

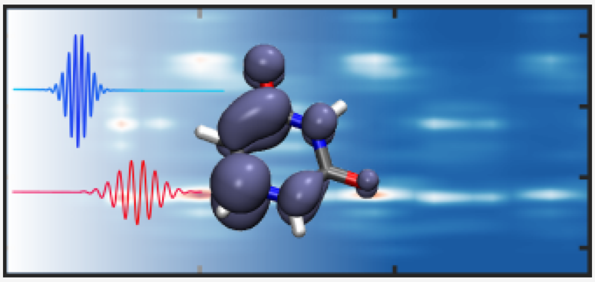

ABSTRACT: The nucleobase uracil exhibits high photostability due to ultrafast relaxation processes mediated by conical intersections (CoIns), where the interplay between nuclear and electron dynamics becomes crucial. In our previous study, we observed seemingly long-lived traces of electronic coherence for the relaxation process through the S_2/S_1 CoIn by applying our ansatz for coupled nuclear and electron dynamics in molecules (NEMol). In this work, we theoretically investigate how time-dependent transient X-ray absorption spectroscopy can be used to observe this ultrafast dynamics. Therefore, we calculated X-ray absorption spectra (XAS) for the oxygen K-edge, using a multireference protocol in combination with NEMol dynamics. Thus, we have access to both the transient XAS based on the nuclear wavepacket dynamics and the modulation of the signals caused by the electronic coherence induced by the excitation process and the presence of a CoIn seam. In both cases, we were able to qualitatively predict its influence on the resulting XAS.

INTRODUCTION

Nucleobases such as uracil are the essential building blocks of DNA and RNA strands that store genetic information.[1−4] Exposure to electromagnetic radiation, especially in the ultraviolet region, can excite electrons in nucleobases following $\pi \rightarrow \pi^*$ transitions.[5,6] After photoexcitation the nucleobases can undergo harmful chemical modifications, such as methylation or base alteration.[7,8] To prevent potential mutations in advance, the inherent photostability of nucleobases is a key factor.[5] It is determined by the excited state dynamics of the molecule,[9,10] for which the fast relaxation mechanisms to the ground state are crucial. In uracil, the ultrafast relaxation occurs via conical intersections (CoIns), which, depending on the number of degrees of freedom, are extraordinary points, seams, or even higher-dimensional crossing spaces between two or more adiabatic electronic states. In the vicinity of CoIns, the quantum nature of the nuclei becomes important. Their dynamics can be described by nuclear wave functions that propagate on coupled potential energy surfaces (PESs). Furthermore, the time scales of nuclear and electron dynamics approach each other and the Born−Oppenheimer approximation breaks down.[11−13] The coupling mediated by CoIns induces not only population transfer but also electronic coherence, whose lifetime is modified by the motion of the nuclear wavepacket.[14] One possibility of simulating the coupled nuclear and electron dynamics in molecules is the NEMol ansatz developed in our group.[14−19] In this purely quantum-mechanical approach, the electronic wave functions are propagated in an eigenstate basis and are coupled to the nuclear wavepacket, which is propagated on coupled PESs, as described in more detail in our previous work.[14−19] Using the NEMol ansatz to study the coupled dynamics of uracil[14] we could show the presence of electronic coherence on the attosecond to femtosecond time scale. This coherence is present for a few hundred femtoseconds, which could be explained by the delocalized nature of the nuclear wavepacket, making the nonadiabatic transition a rather continuous process. This result agrees well with simulations of TRUECARS signals of the S_2/S_1 CoIn of uracil.[20] Extremely short laser pulses are necessary to observe nuclear wavepackets or even electronic coherence in photophysical or photochemical processes mediated by CoIns. Over the last decades, a variety of X-ray sources have been developed, ranging from synchrotron radiation to tabletop high-harmonic generation setups.[21−24] These enable scientists to experimentally resolve not only nuclear dynamics,[25,26] but also electronic motion[27−31] following photoinitiated processes. There are several different possibilities to study the dynamics and electronic coherence induced by CoIns using simulated spectra.[20,32−36] In experiments, attosecond transient absorption spectroscopy (ATAS) has been successfully applied to resolve coupled nuclear and electron dynamics with great

Received: September 29, 2023
Revised: October 26, 2023
Accepted: October 27, 2023
Published: November 13, 2023

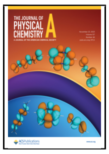

ACS Publications

https://doi.org/10.1021/acs.jpca.3c06509
J. Phys. Chem. A 2023, 127, 9787−9796

spectral and temporal resolution.[37−39] Theoretical simulations could show that these spectra can be used among other to determine the population of different states,[40] investigate the nuclear dynamics,[41] or follow the wavepacket dynamics at a CoIn.[42] To describe the dynamics at CoIn a multiconfigurational treatment is necessary, whereas most key features have been demonstrated to be also qualitatively reproduced using computationally cheaper approaches like MOM/TDDFT (maximum overlap method time-dependent density functional theory), enabling the treatment of larger molecular systems.[43] Attosecond pulses in the X-ray regime are capable of not only creating well-localized electronic wavepackets but also exhibiting sensitivity toward chemical elements, charge, and the population of electronic states. This is due to the probe of the inner valence and core states of the excited molecules.[29,37,39,44−50]

In this paper, we build on our findings by applying the NEMol ansatz in the NEMol-grid extension to the nucleobase uracil.[14] There we studied the electronic coherence caused by the superposition of nuclear wavepackets on different electronic states created by the excitation pulse and at the S_2/S_1 CoIn, which is the first CoIn reached during the relaxation process. On the basis of our simulations, we proposed two experimental observables, the induced dipole moment and changes in electron density at the oxygen atoms. Now, we are investigating another experimental possibility, namely X-ray absorption spectra (XAS), to study ultrafast relaxation dynamics. By simulating the time-resolved XAS of the oxygen K-edge, we can follow the complex coupled dynamics of uracil induced by photoexcitation. Our methodology allows us not only to observe the spectral features of the population dynamics but also to shed light on the qualitative contribution of electronic coherence in transient XAS.

■ THEORY

Ab Initio Level of Theory. The XAS are simulated with a protocol using the restricted active space perturbation theory (RASPT2) ansatz. The protocol is based on our previous study on ultrafast strong field dissociation of vinyl bromide.[37] In the restricted active space self-consistent field (RASSCF) method, the active space can be divided into a maximum of three subspaces. In RAS2 all possible configurations are allowed, resembling the AS in the complete active space self-consistent field (CASSCF) formalism. For RAS1 the maximal number of electrons that can be excited out of this space is restricted, and for RAS3 the maximal number of electrons that are allowed to occupy the subspace can be defined. With i, j, and k as the number of orbitals in RAS1, RAS2, and RAS3 and the total number of electrons n, the maximum number of holes in RAS1 l, and the maximum number of electrons in RAS3 m one can systematically label the applied RAS(n,l,m;i,j,k). This partitioning of the orbital space makes RASSCF a very intuitive formalism for describing the core-excitation process. For the simulation of the XAS, a CAS calculation was performed first, followed by a restricted active space configuration interaction (RASCI) calculation for the valence-excited states and one for the core-excited states. Unlike RASSCF, RASCI does not reoptimize the molecular orbits along with the CI coefficients, which is a reasonable assumption for core-excited states.[51−53] In addition, the core−valence separation[54−57] was utilized for them. For both RASSCF wave functions, dynamic electron correlation was included by an extended multistate complete active space perturbation theory (XMS-CASPT2)[58−60] calculation. As these calculations, especially for the core-excited states, are prone to intruder states, we benchmarked adequate values for the ionization-potential electron-affinity (IPEA)[61] and imaginary shift.[62] To include spin−orbit coupling, RASPT2 calculations of the valence and core-excited states have been performed for both singlet and triplet multiplicity. Thus, a total of four wave functions per each valence and core pairing are used as a basis in the restricted active space state interaction (RASSI) method,[63−65] where the interactions between all states are calculated. As these wave functions are not necessarily orthogonal, a correction is introduced to the overall Hamiltonian.[65] Identifying the desired valence-excited spin−orbit state, the oscillator strengths and excitation energies are extracted from the RASSI calculation and plotted against each other to obtain the static XAS.

NEMol for X-ray Absorption Spectroscopy. In the following, we outline the key details of how we combine the RASPT2 protocol with the NEMol ansatz to obtain time-resolved spectra that include electronic coherence. We take into account the first three valence states (S_0, S_1, and S_2) relevant to describe the dynamics in all our simulations. Each of them is characterized by its nuclear wave function $\chi_i(R, t)$ and electronic wave function $\varphi_i(r; R)$. Here, R denotes the nuclear coordinates, r the electronic coordinates, and t is the time. These three states are pairwise coupled, first S_0 and S_2 by an excitation pulse, and then S_2 and S_1 by a CoIn seam. The coupled quantum dynamics simulation is performed on a two-dimensional spatial grid constructed from molecular structures that are known to play an important role in the S_2 photorelaxation of uracil.[9,20,66] A detailed description of the simulation protocol can be found in the Supporting Information section I. In our method the probe step is assumed to be a delta pulse that simultaneously excites the superposition of all three valence states, or in other words, the coupled wavepacket, into the manifold of core-hole states. From the perspective of a single core-hole state c the probe pulse creates a wavepacket, described by $\chi_c(R, t)$, containing components from all three valence states. As a first approximation, we construct this wavepacket as a superposition of the nuclear wavepackets in the three valence states. By doing so, we take into account the interference that can occur, since the core-hole state c can be populated by all three valence states simultaneously. In addition, this approximation allows us to formulate the corresponding total wave function $\Psi_c(r, R, t)$ of the core-hole state as a linear combination of the nuclear wave functions of the valence states and the electronic wave function of the core-hole state:

$$\Psi_c(r, R, t) = \chi_c(R, t)\varphi_c(r; R) = \sum_{j}^{N_{\mathrm{val}}} \chi_j(R, t)\varphi_c(r; R) \tag{1}$$

With this formulation of $\Psi_c(r, R, t)$ the transition dipole moment $\mu_{i,c}(t)$ between an individual core-hole state c and a specific valence state i becomes

$$\mu_{ic}(t) = \langle \chi_i(R, t)\varphi_i(r; R)|\hat{\mu}|\sum_{j}^{N_{\mathrm{val}}} \chi_j(R, t)\varphi_c(r; R)\rangle \tag{2}$$

Following the argumentation of the Franck−Condon principle,[67,68] we assume that the operator $\hat{\mu}$ is only dependent on the electronic wave functions, which can be justified by the fact that the probe pulse is short even under experimental conditions. Therefore, the nuclear wave functions can be separated from the electronic transition dipole moment

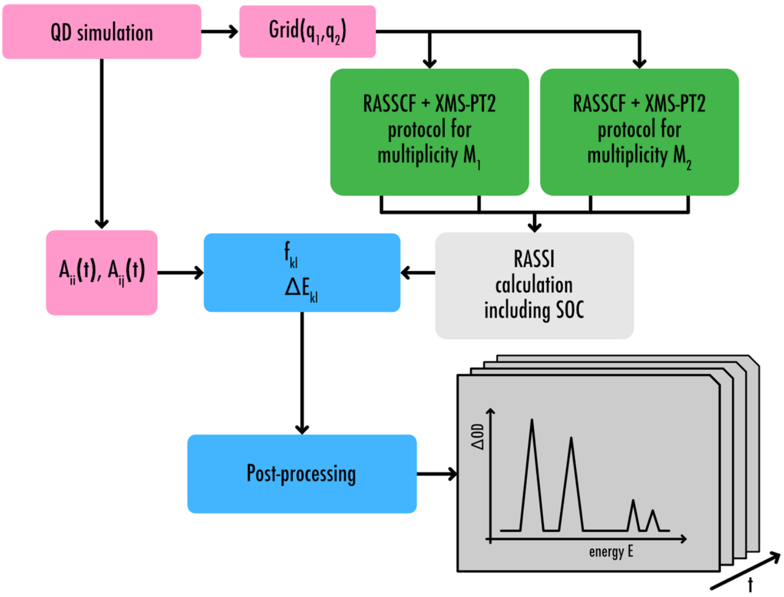

Figure 1. Flowchart of the simulation of time-resolved XAS by combination of the RASPT2 results with time-dependent population (A_{ii}) and overlap (A_{ij}) terms.

integral, which defines the probability of the transition occurring. This allows us to derive the following approximation for μ_{ic}:

$$\mu_{ic}(t) = \langle \varphi_i(r;R)|\hat{\mu}|\varphi_c(r;R)\rangle \sum_{j}^{N_{\text{val}}} \langle \chi_i(R,t)|\chi_j(R,t)\rangle = \mu_{ic}^{P}(t) + \mu_{ic}^{C}(t) \tag{3}$$

The summation over all valence states can be decomposed into two parts. The first part μ_{ic}^P is defined by i being equal to j and can be expressed as the electronic transition dipole moment multiplied by the time-dependent population $A_{ii}(t) = \langle \chi_i(R,t)|\chi_i(R,t)\rangle$:

$$\mu_{ic}^{P}(t) = \langle \varphi_i(r;R)|\hat{\mu}|\varphi_c(r;R)\rangle A_{ii}(t) \tag{4}$$

Due to $A_{ii}(t)$ the temporal evolution of μ_{ic}^P is determined by the nuclear wavepacket dynamics in the individual state i. The second part μ_{ic}^C contains the remaining contributions from all other valence states:

$$\mu_{ic}^{C}(t) = \langle \varphi_i(r;R)|\hat{\mu}|\varphi_c(r;R)\rangle \sum_{j\neq i}^{N_{\text{val}}} A_{ij}(t) \tag{5}$$

Here, $A_{ij}(t) = \langle \chi_i(R,t)|\chi_j(R,t)\rangle$ is the time-dependent overlap of the nuclear wavepackets in the valence states i and j, which also includes the electronic coherence determined by the energy difference of the involved states. The subsequently calculated oscillator strength f_{ic}, which describes the transition probability between the valence state i and the core-hole state c, includes both a population-induced component $\mu_{ic}^P(t)$ and coherence-induced components $\mu_{ic}^C(t)$ of the transition dipole moment:

$$f_{ic} = \frac{2}{3}\Delta E_{ic}|\mu_{ic}^{P}(t) + \mu_{ic}^{C}(t)|^2 \tag{6}$$

By including $\mu_{ic}^C(t)$ the valence state i is not treated separately, but as part of the coupled dynamics of the valence states. The needed energy difference ΔE_{ic} and the electronic transition dipole moment are extracted from the RASPT2 calculations. The terms $A_{ii}(t)$ and $A_{ij}(t)$ are determined according to the NEMol ansatz in combination with the NEMol-grid extension.[14,19] In this extension, the nuclear coordinate space is divided into segments, for each of which, we obtained the partial population and nuclear wavepacket overlap by integrating the wavepackets within the boundaries of the segments. The ΔE_{ic} and the electronic transition dipole moment are calculated for each segment and weighted with the corresponding time-dependent population and nuclear overlap, as described in eq 6. Next, all segments for given transitions i to c are added and all relevant core-hole excitations are subsequently combined, to obtain the complete time-resolved XAS. A flowchart of this whole procedure is shown in Figure 1. To test our ansatz we compared the static XAS for the FC point in the ground state and S_2 state with the ones obtained using our nonstationary approach. The results can be found in the SI.

Computational Details. For the simulation of the XAS we applied a pump−probe scheme with the pump pulse lying in the strong-field regime and the probe pulse in the weak-field regime. In our calculations, the pump pulse is explicitly simulated. We used an excitation pulse[14] with a central frequency of ω_0 of 6.12 eV, a full width at half-maximum (fwhm) of 30 fs and a maximum field strength of 0.036 GVcm^{-1}, that was optimized to excite the maximal amount of population from the ground state to the second excited state. The subsequent dynamical response of the molecule has been simulated using the NEMol ansatz with a NEMol-grid defined as follows: The nuclear coordinate space is divided into 14 × 10 segments equally distributed between −0.37 Å to 1.57 Å in the q_1 coordinate and from 0.57 to 0.86 Å in the q_2 coordinate, whereby q_1 and q_2 are reaction coordinates adequate for the fast relaxation process in uracil.[9,10,14] To obtain the XAS, we utilized the RASPT2 protocol outlined above, under the assumption of an instantaneous delta pulse for the probe step. The applied RAS(18,1,0;2,10,0) active space is shown in

Figure 2. It consists of 10 orbitals in RAS2 (seven occupied orbitals and three virtual ones), which include both lone pairs of the oxygen atoms, as well as the RAS1 space comprised of both oxygen *1s* orbitals.

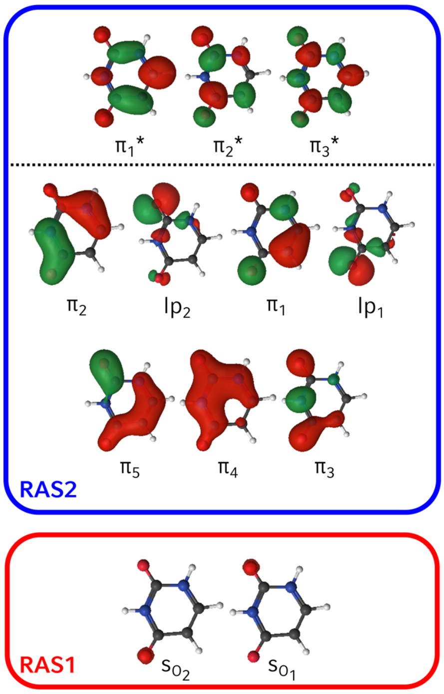

Figure 2. Active space for the RAS2 and the oxygen *1s* orbitals in the RAS1. All orbitals are rendered with an isovalue of 0.04.

For the simulation of the XAS, first a CAS(14,10) (RAS2 in Figure 2) calculation with state averaging over six states was performed, followed by a restricted active space configuration interaction (RASCI) calculation for the valence-excited states using RASCI with six states and one for the core-excited states using RASCI with 40 states. To broaden the calculated line spectrum an overall Gaussian convolution with $\sigma = 0.3$ eV was applied. For the probe pulse we do not consider a specific alignment of the molecules, whereas for the pump pulse it is assumed that the electric component of the pulse is optimally aligned with the transition dipole moment of the molecule. This leads to an excitation ratio slightly higher than 90%. For randomly aligned molecules, the amount of population pumped into the S_2 will be lower. In Figures S12 and S13 of the SI we illustrate the effect a much smaller excitation ratio of 10% would have on the time-resolved XAS.

For all simulations of XAS at the oxygen K-edge we used the relativistic atomic natural orbital basis (ANO-RCC),[69−73] contracted to VTZP quality (ANO-RCC-VTZP), with the XMS-CASPT2 method[59,60] as implemented in OpenMolcas,[74,75] using an imaginary shift of 0.6 and an IPEA shift of 0.25. The basis set, the shift parameters used in the RASPT2, and the size and composition of the active space have been derived from extensive benchmark calculations and comparisons with experimental data, which are outlined in the SI.

In order to simplify the analysis of the XAS, the excitation process (−40 to 35 fs) and the dynamics on the S_2 PES (from 35 fs onward) have been treated separately, meaning that the corresponding transient XAS and the depiction of the wavepacket overlap have been normalized, respectively.

■ RESULTS AND DISCUSSION

Let us begin by briefly describing the initial relaxation dynamics for uracil. The applied two-dimensional PESs, defined by the optimized geometries of the Franck−Condon (FC) point, the S_2 minimum and the S_2/S_1 CoIn, have previously been reported[9] and used in several studies.[20,76,77] The adequacy of the two-dimensional PESs to describe the initial relaxation dynamics of uracil has been demonstrated by extensive benchmark calculations.[9,10] Starting from the vibrational ground state of the S_0 potential, laser excitation into the S_2 state generates a wavepacket that begins to oscillate between the FC region and the S_2 minimum. After the first oscillation period of about 80 fs the wavepacket splits and a part of it travels toward the CoIn seam, while other parts continue to oscillate. Over time, more and more parts of the wavepacket reach the CoIn and relax to the S_1 state. The propagation of the wavepacket on the S_2 PES is sketched in white in the top part of Figure 3, while the temporal evolution of the population is depicted in the bottom part.

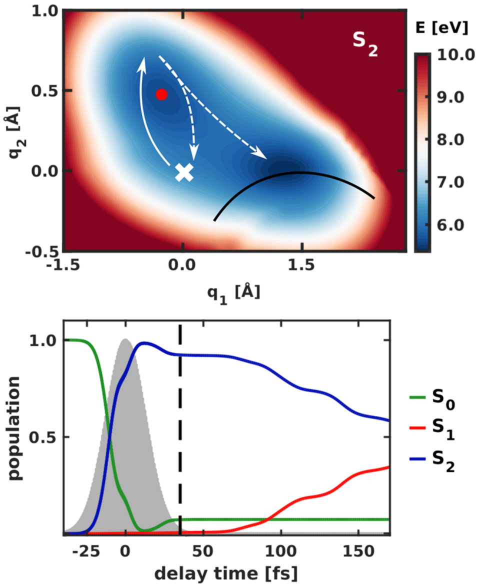

Figure 3. Top: Potential energy surface of the S_2 state with indicated CoIn seam (black line), S_2 minimum (red dot), Franck−Condon point (white cross) and a schematic representation of the path of the wavepacket (white lines). The energy scale is given with respect to the global minimum of the S_0 potential energy surface. Bottom: Temporal evolution of the population of the S_0, S_1, and S_2 states shown in green, red, and blue, respectively. The normalized pump pulse is shown in gray.

Static X-ray Absorption Spectra. In this section, we show the static XAS of the oxygen K-edge for three critical points on the PES, namely the FC, the optimized S_2 minimum, and the optimized S_2/S_1 CoIn. From an analysis of the three possible K-edges, probing the local environment of the oxygen atoms is the most intuitive choice, since during the S_2-S_1 relaxation an electron moves from the oxygen lone pair lp_1 to a vacancy in the π_1 orbital. In addition, it was found that the characteristic signals for the three critical points on the PES overlap the least when the oxygen edge is used, making it the best candidate for experimental observation. A detailed comparison of the different K-edges together with their respective static XAS and a list of all peaks with oscillator strengths greater than or equal to 0.001 together with their character can be found in Figures S8−S10 and Tables S5−S13 in the SI section IV.

A comparison of the oxygen K-edge spectrum, obtained with the optimal parameters, with the corresponding experimental data is given in Figure 4. To match the experimental data, one would have to shift the simulated spectrum to higher energies by 3.90 eV. The differences between the experimental and calculated splitting of the signals in Figure 4 are probably due to the RASCI treatment that neglects orbital relaxation and directly influenced by the splitting present for the valence excitations, which strongly depends on the calculation method.[78] The peak at 528 eV can be assigned to two excitations, one from s_{O_1} to the π_1^* orbital and the other one from s_{O_2} to the π_2^* orbital.

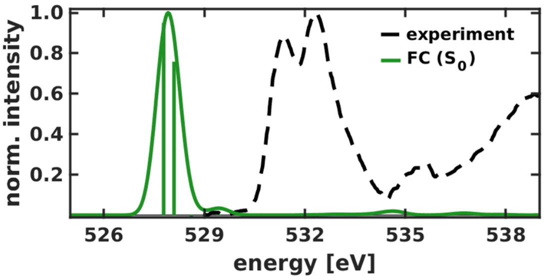

Figure 4. XAS for the oxygen K-edge using XMS-CASPT2, the basis set ANO-RCC-VTZP, an imaginary shift of 0.6, an IPEA shift of 0.25 and a RAS(18,1,0;2,10,0) with the two oxygen *1s* orbitals in the RAS1. Calculated spectrum broadened using an overall Gaussian convolution with σ = 0.3 eV. Experimental oxygen K-edge spectrum in black.[79]

For experimental observability, especially the peaks that appear or disappear in the area of lower energies are of importance, since peaks at higher energies might be overshadowed by the more intense ionization bands and Rydberg series, as also seen in the experimental spectrum in Figure 4. The calculated XAS for all critical points along the excitation process, the dynamics in the S_2 state and the relaxation through the S_2/S_1 CoIn are shown in Figure 4.[79]

For the excitation process, we can identify a suitable peak characteristic for the S_2 state at the FC geometry at 523 eV (see Figure 5a). It is well separated from the intense peak of the ground state at 528 eV. The characteristic peak of the S_2 state at 523 eV corresponds to an excitation from the s_{O_2} orbital to the vacancy in the π_1 orbital present in this state. To follow the dynamics in the S_2 state, between the FC geometry, the optimized S_2 minimum, and the S_2/S_1 CoIn, the signals of these three points should ideally be distinguishable. From Figure 5b) we conclude that it should be possible to observe the oscillation between the FC geometry and the S_2 minimum through the alternating appearance of the peaks at 527 eV (FC geometry) and the signal of the S_2 minimum at 522 eV. Consequently, the change in the signals around 523 eV can be used to study the excitation process, while the features around 527 eV are relevant for the dynamics in the S_2 state.

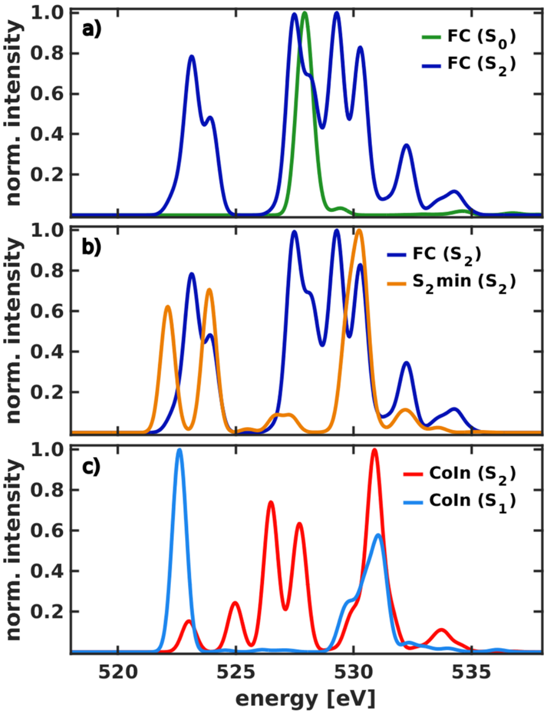

Figure 5. Oxygen K-edge XAS for the excitation process (a), the dynamics on the S_2 PES (b) and the relaxation through the S_2/S_1 CoIn (c). Calculated spectra broadened using an overall Gaussian convolution with σ = 0.3 eV.

For the XAS of the S_2 state calculated with the CoIn geometry, the two peaks at 525 and 527 eV are the most characteristic (see Figure 5c). These signals disappear, however, at the CoIn in the S_1 state, leaving only spectral features that are very close in energy to signals found at the FC geometry or the S_2 minimum in the S_2 state. This indicates that the characteristic features of the CoIn will be harder to distinguish in the transient XAS. From the static spectra, we expect that the peaks at 527 eV (FC geometry), 522 eV (S_2 minimum), and 525 eV (CoIn) are good candidates to follow the dynamics on the S_2 PES. All dominant spectral signatures are described by excitations from one of the oxygen *1s* orbitals to the π_1 vacancy, whose energy is shifted by the change in nuclear configuration. An overview of all excitations for peaks with oscillator strength greater than or equal to 0.001 is given in Tables S5−S7 in the SI.

Time-Resolved X-ray Absorption Spectra. Time-resolved XAS are obtained by extracting the static XAS of the three states involved (S_0, S_1, and S_2) at each point of the nuclear grid weighted with the corresponding time-dependent population and overlap terms according to eqs 4, 5, and 6. The ground state bleach was included by subtracting the XAS of the S_0 state at a delay time of −40 fs from the transient spectrum. As the underlying PESs have been proven to be adequate,[9,10] we assume that the predicted time-resolved XAS will also be reliable, as they depend only on the NEMol results and the nuclear geometries used to calculate the surfaces. During the relatively short simulation time (210 fs in total) it was shown that additional nuclear coordinates play only an insignificant role in the S_2-S_1 relaxation dynamics.[9] For longer simulation times, the chosen two-dimensional subspace will most likely

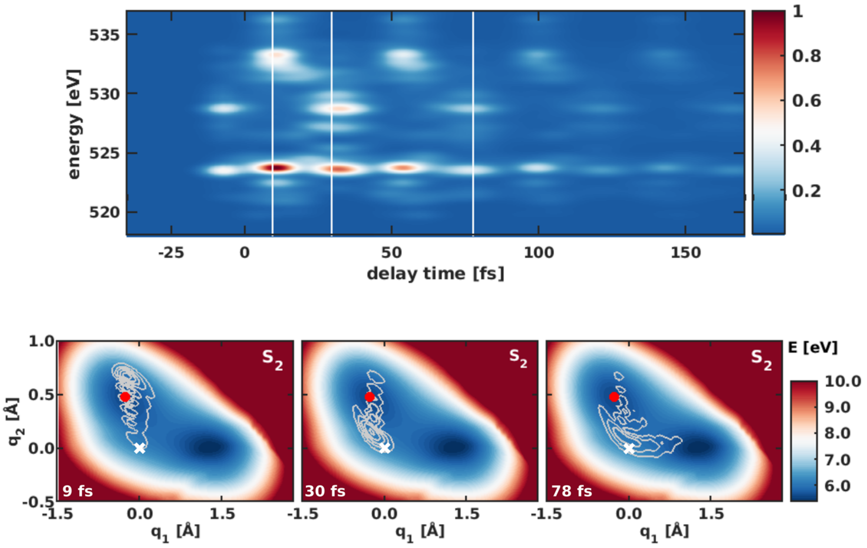

Figure 6. Top: Transient oxygen K-edge XAS of the S_2 state. Ground state bleach is neglected for simplicity. Bottom: Position of the nuclear wavepacket (gray), the Franck–Condon point (white cross), and the optimized S_2 minimum (red dot) on the S_2 potential energy surface for three different points in time.

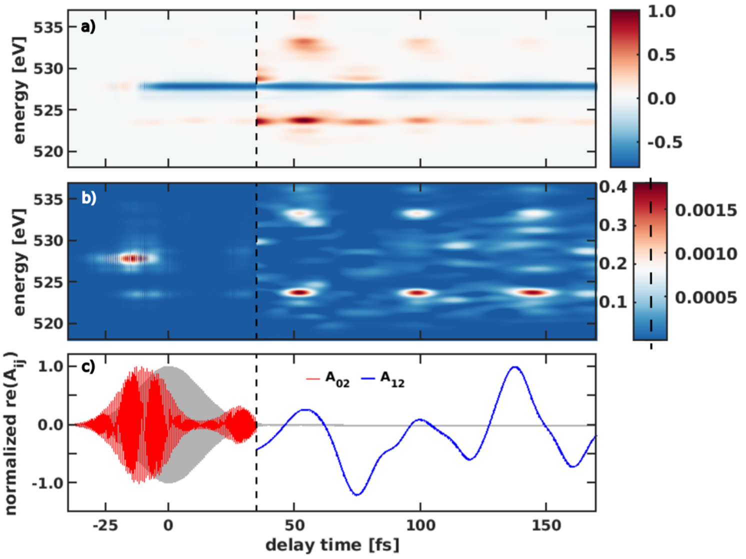

Figure 7. (a) Transient oxygen K-edge XAS based on the nuclear wavepacket dynamics in the three relevant states (S_0, S_1, and S_2) with the inclusion of electronic coherence. The spectrum of the excitation process (−40 to 35 fs, left side) and the dynamics on the S_2 surface (from 35 fs onward, right side) are normalized, respectively. The maximum of the pump pulse lies at 0 fs. (b) Difference spectrum between neglecting and including electronic coherence. The difference spectra (b) are normalized to their respective maximal value for the excitation process (left) and the dynamics on the S_2 PES (right). The mean of the real part of the wavepacket overlap (c) between $S_{0/2}$ (red) and $S_{1/2}$ (blue) averaged over the grid is normalized, respectively. The normalized pump pulse is shown in gray.

not be sufficient, so we focus only on the initial steps of the dynamics. To allow an in-depth analysis of the XAS, the dynamics induced by the pump pulse (−40 to 35 fs) and by the CoIn seam (from 35 fs) are treated separately according to our previous work.[14] The maximum of the pump pulse (fwhm of 30 fs) is positioned at 0 fs, therefore, the pulse is negligible after 35 fs (Figure 3 bottom).

Before analyzing the full time-resolved XAS, we discuss the spectral features of the relaxation dynamics that can be attributed solely to the dynamics in the S_2 state. Figure 6 shows the time-resolved XAS of the S_2 state and snapshots of the nuclear wavepacket evolving on the S_2 PES.

After excitation to the S_2 state, the wavepacket dynamics significantly changes the static picture. More geometries in addition to the critical points contribute to the time-resolved XAS. Therefore, different signals become relevant for the interpretation. The signal at 524 eV is present throughout the dynamics of the excited state. As seen in Figure 5 all critical points in the S_2 state contribute to this signal with only small variations in energy and intensity. The signal is not sensitive to geometric changes, but characteristic of a populated S_2 state. At the end of the simulation time, this signal fades, as more and more parts of the wavepacket relax through the CoIn to the S_1 state. Tracking the intensity of the signal at 524 eV allows one to follow the passage of the wavepacket through the CoIn. For the structurally similar thymine molecule the depopulation of the S_2 state has been shown to be also experimentally observable.[80] In addition to the prominent signal at 524 eV, a recurrence of time-displaced signals around 529 eV and a double peak structure at 533 eV is clearly visible. These signals originate from the nuclear wavepacket oscillating between the FC geometry and the S_2 minimum in the S_2 state. Their oscillatory behavior agrees well with the temporal evolution of the wavepacket on the S_2 PES shown in the bottom panels of Figure 6. The dynamics of the wavepacket also explains the slight shift of the characteristic signatures, for example, the one relevant for the observation of the FC geometry in the S_2 state. The corresponding signal is shifted from 528 to 529 eV, since the main part of the nuclear wavepacket no longer reaches exactly the FC geometry.

For the full time-resolved XAS shown in Figure 7, the normalization was performed separately for the excitation-induced dynamics (left of the black dotted line) and the CoIn-induced process (right of the black dotted line). Figure 7a) shows the time-resolved XAS based on the coupled dynamics in the three relevant states (S_0, S_1, and S_2), taking into account the ground-state bleaching that occurs around 528 eV. The electronic coherence created by overlapping wavepackets of different electronic states was included by using the data from our NEMol calculations. In Figure 7b, the influence of electronic coherence on the XAS is shown. This spectrum is derived as the difference between a transient XAS based solely on the dynamics of the nuclear wavepacket and the one shown in Figure 7a which includes also the electronic coherence. In the case of the difference spectrum, the two colorbars have been chosen to correspond to the value of maximal difference for the excitation process and the CoIn induced dynamics, respectively. The temporal evolution of the normalized real part of the overlap between $S_{0/2}$ (red) and $S_{1/2}$ (blue) averaged over the grid is depicted in Figure 7c). The $S_{0/2}$ coupling is relevant for the excitation process by the femtosecond pulse, and the $S_{1/2}$ coupling is relevant for the area at the CoIn.

During the excitation process, the maximum of the electronic coherence is reached at −10 fs. Here, the population is almost equally distributed between S_0 and S_2 (see Figure 3) resulting in a maximal A_{ij} term (Figure 7c), respectively, electronic coherence. Consequently, electronic coherence emerges most prominently in the difference spectrum around this time, see Figure 7b). At 30 fs a recurrence of electronic coherence at 524 and 529 eV is also visible.[81,82] This is caused by parts of the nuclear wavepacket having traveled back to the FC area and overlapping again with the nuclear wavepacket in the ground state, increasing the value of A_{ij}. The difference spectrum shows fast oscillations of the same frequency as the pump pulse. A 1D cut through the time-resolved XAS at an energy of 528 eV, neglecting the ground state bleach, with a comparison between the fast oscillations and the pump pulse, can be found in Figure S11 in the SI. Both features are not or barely visible in the full transient XAS (Figure 7a), as they are mainly overshadowed by the ground state bleach. In the case of the CoIn-induced dynamics, much slower oscillations are present in accordance with the small energy gap between the states involved. A periodic recurrence of the signals in the difference spectrum can be seen. These are created by different parts of the wavepacket reaching the CoIn and inducing electronic coherence there. These events occur after one or more vibrational oscillations between the FC geometry and the S_2 minimum or after a bifurcation of the nuclear wavepacket at the CoIn with a part remaining in the S_2 state and returning to the CoIn area. For the CoIn-induced dynamics, the maximum value of the difference spectrum of 0.18% lies at 52 fs, where the A_{ij} term also shows a maximum (Figure 7c). As the nuclear wavepacket becomes more and more delocalized in the S_2 state and the S_1 state, the XAS contributions due to electronic coherence become more and more washed out. Overall, the effect of electronic coherence on the time-resolved XAS of the relaxation dynamics of uracil is rather small but still not negligible. As suggested in the literature,[83] the intrinsically weak signal of electronic coherence in uracil can be enhanced using optimal control theory. This proposed idea may also increase the contribution due to electronic coherence on XAS and perhaps allow experimental observation.

■ CONCLUSIONS

We simulated time-resolved XAS for the nucleobase uracil based on coupled nuclear and electron dynamics realized in the NEMol approach and combine with a RASPT2 protocol.[37] We extract important spectral features to follow the photoinduced dynamics that might be suitable for experimental observability using the oxygen K-edge. We find that different, well-distinguishable spectral signatures become important when changing from the static to the dynamic description. During the initial dynamics, the nuclear wavepacket oscillates between the FC region and the S_2 minimum area. This behavior is reflected in the time-resolved XAS through the periodic occurrence of distinct spectral features that characterize these areas. The constant signal at 524 eV reflects the population of the S_2 state and allows one to track the process from excitation to relaxation through the CoIn highly time-resolved. Apart from following the nuclear wavepacket dynamics with XAS, we also determined the influence of the electronic coherence introduced in the excitation process and later at the CoIn. In both cases we saw a small but relevant effect on the XAS. This effect is especially prominent in the cases of very localized nuclear wavepackets, leading to a large overlap term A_{ij} between wavepackets on different PESs. This situation is present during the excitation-pulse dynamics, where fast oscillations of the same frequency as the pump pulse are observed. An interesting revival[81,82] of these fast oscillations can be seen after the excitation process. This is due to the fact that parts of the nuclear wavepacket in the S_2 are revisiting the FC region, so the overlap term A_{ij} increases again. For the CoIn-induced dynamics, the term A_{ij} plays an even more important role. Here, the periodic reappearance of weak electronic coherence can be attributed again to the nuclear wavepacket dynamics. Every time parts of the wavepacket approach the CoIn seam, the critical A_{ij} term becomes nonzero. In this sense, XAS are a very sensitive probe for detecting the dynamics at the CoIn. With the current study, we were able to show that XAS are in principal sensitive even to weak electronic coherence.

■ ASSOCIATED CONTENT

Supporting Information

The Supporting Information is available free of charge at https://pubs.acs.org/doi/10.1021/acs.jpca.3c06509.

Details on the XAS simulation setup, additional figures and tables for the benchmark calculations, and the analysis of the time-resolved XAS (PDF)

AUTHOR INFORMATION

Corresponding Author

Thomas Schnappinger – *Department of Chemistry, LMU Munich, Munich 81377, Germany;* Present Address: Department of Physics, Stockholm University, AlbaNova University Center, Stockholm, 106 91, Sweden; orcid.org/0000-0003-4538-811X; Email: thomas.schnappinger@fysik.su.se

Authors

Lena Bäuml – *Department of Chemistry, LMU Munich, Munich 81377, Germany*

Florian Rott – *Department of Chemistry, LMU Munich, Munich 81377, Germany*

Regina de Vivie-Riedle – *Department of Chemistry, LMU Munich, Munich 81377, Germany;* orcid.org/0000-0002-7877-5979

Complete contact information is available at: https://pubs.acs.org/10.1021/acs.jpca.3c06509

Notes

The authors declare no competing financial interest.

ACKNOWLEDGMENTS

L.B., F.R., and R.d.V. acknowledge funding from the DFG Normalverfahren. The authors gratefully acknowledge the computational and data resources provided by the Leibniz Supercomputing Center (www.lrz.de).

REFERENCES

(1) Avery, O. T.; MacLeod, C. M.; McCarty, M. Studies on the Chemical Nature of the Substance Inducing Transformation of Pneumococcal Types: Induction of Transformation by a Desoxyribonucleic Acid Fraction Isolated from Pneumococcus Type III. *Journal of Experimental Medicine* **1944**, *79*, 137–158.

(2) Hershey, A. D.; Chase, M. Independent Functions of Viral Protein and Nucleic Acid in Growth of Bacteriophage. *J. Gen. Physiol.* **1952**, *36*, 39–56.

(3) Watson, J. D.; Crick, F. H. C. Genetical Implications of the Structure of Deoxyribonucleic Acid. *Nature* **1953**, *171*, 964–967.

(4) Gamow, G. Possible Relation between Deoxyribonucleic Acid and Protein Structures. *Nature* **1954**, *173*, 318–318.

(5) Middleton, C. T.; de La Harpe, K.; Su, C.; Law, Y. K.; Crespo-Hernández, C. E.; Kohler, B. DNA Excited-State Dynamics: From Single Bases to the Double Helix. *Annu. Rev. Phys. Chem.* **2009**, *60*, 217–239.

(6) Barbatti, M. A.; Aquino, A. J.; Lischka, H. The UV Absorption of Nucleobases: Semi-Classical Ab Initio Spectra Simulations. *Phys. Chem. Chem. Phys.* **2010**, *12*, 4959–4967.

(7) Esposito, L.; Banyasz, A.; Douki, T.; Perron, M.; Markovitsi, D.; Improta, R. Effect of C5-Methylation of Cytosine on the Photoreactivity of DNA: A Joint Experimental and Computational Study of TCG Trinucleotides. *J. Am. Chem. Soc.* **2014**, *136*, 10838–10841.

(8) Tommasi, S.; Denissenko, M. F.; Pfeifer, G. P. Sunlight Induces Pyrimidine Dimers Preferentially at 5-Methylcytosine Bases1. *Cancer Res.* **1997**, *57*, 4727–4730.

(9) Keefer, D.; Thallmair, S.; Matsika, S.; de Vivie-Riedle, R. Controlling Photorelaxation in Uracil with Shaped Laser Pulses: A Theoretical Assessment. *J. Am. Chem. Soc.* **2017**, *139*, 5061–5066.

(10) Reiter, S.; Keefer, D.; de Vivie-Riedle, R. RNA Environment Is Responsible for Decreased Photostability of Uracil. *J. Am. Chem. Soc.* **2018**, *140*, 8714–8720.

(11) Yarkony, D. R. Diabolical Conical Intersections. *Rev. Mod. Phys.* **1996**, *68*, 985–1013.

(12) Baer, M. Introduction to the Theory of Electronic Non-Adiabatic Coupling Terms in Molecular Systems. *Phys. Rep.* **2002**, *358*, 75–142.

(13) Domcke, W., Yarkony, D., Köppel, H., Eds. *Conical Intersections: Electronic Structure, Dynamics & Spectroscopy*; World Scientific: Singapore, 2004.

(14) Bäuml, L.; Schnappinger, T.; Kling, M. F.; de Vivie-Riedle, R. Photo-Induced Coupled Nuclear and Electron Dynamics in the Nucleobase Uracil. *Frontiers in Physics* **2021**, *9*, 674573.

(15) Geppert, D.; von den Hoff, P.; de Vivie-Riedle, R. Electron Dynamics in Molecules: A New Combination of Nuclear Quantum Dynamics and Electronic Structure Theory. *J. Phys. B: At. Mol. Opt. Phys.* **2008**, *41*, 074006.

(16) von den Hoff, P.; Znakovskaya, I.; Kling, M. F.; de Vivie-Riedle, R. Attosecond Control of the Dissociative Ionization via Electron Localization: A Comparison between D2 and CO. *Chem. Phys.* **2009**, *366*, 139–147.

(17) Znakovskaya, I.; von den Hoff, P.; Zherebtsov, S.; Wirth, A.; Herrwerth, O.; Vrakking, M. J. J.; de Vivie-Riedle, R.; Kling, M. F. Attosecond Control of Electron Dynamics in Carbon Monoxide. *Phys. Rev. Lett.* **2009**, *103*, 103002.

(18) Kling, M. F.; von den Hoff, P.; Znakovskaya, I.; de Vivie-Riedle, R. Sub-)Femtosecond Control of Molecular Reactions via Tailoring the Electric Field of Light. *Phys. Chem. Chem. Phys.* **2013**, *15*, 9448–9467.

(19) Schnappinger, T.; de Vivie-Riedle, R. Coupled Nuclear and Electron Dynamics in the Vicinity of a Conical Intersection. *J. Chem. Phys.* **2021**, *154*, 134306.

(20) Keefer, D.; Schnappinger, T.; de Vivie-Riedle, R.; Mukamel, S. Visualizing Conical Intersection Passages via Vibronic Coherence Maps Generated by Stimulated Ultrafast X-ray Raman Signals. *Proc. Natl. Acad. Sci. U. S. A.* **2020**, *117*, 24069–24075.

(21) Hentschel, M.; Kienberger, R.; Spielmann, C.; Reider, G. A.; Milosevic, N.; Brabec, T.; Corkum, P.; Heinzmann, U.; Drescher, M.; Krausz, F. Attosecond Metrology. *Nature* **2001**, *414*, 509–513.

(22) Itatani, J.; Quéré, F.; Yudin, G. L.; Ivanov, M. Y.; Krausz, F.; Corkum, P. B. Attosecond Streak Camera. *Phys. Rev. Lett.* **2002**, *88*, 173903.

(23) Baltuška, A.; Udem, T.; Uiberacker, M.; Hentschel, M.; Goulielmakis, E.; Gohle, C.; Holzwarth, R.; Yakovlev, V. S.; Scrinzi, A.; Hänsch, T. W.; et al. Attosecond Control of Electronic Processes by Intense Light Fields. *Nature* **2003**, *421*, 611–615.

(24) Krausz, F.; Ivanov, M. Attosecond Physics. *Rev. Mod. Phys.* **2009**, *81*, 163.

(25) Zewail, A. H. Femtochemistry: Atomic-Scale Dynamics of the Chemical Bond. *J. Phys. Chem. A* **2000**, *104*, 5660–5694.

(26) Fushitani, M. Applications of Pump-Probe Spectroscopy. *Annu. Rep. Prog. Chem., Sect. C: Phys. Chem.* **2008**, *104*, 272–297.

(27) Leone, S. R.; Neumark, D. M. Attosecond Science in Atomic, Molecular, and Condensed Matter Physics. *Faraday Discuss.* **2016**, *194*, 15–39.

(28) Nisoli, M.; Decleva, P.; Calegari, F.; Palacios, A.; Martín, F. Attosecond Electron Dynamics in Molecules. *Chem. Rev.* **2017**, *117*, 10760–10825.

(29) Goulielmakis, E.; Loh, Z.-H.; Wirth, A.; Santra, R.; Rohringer, N.; Yakovlev, V. S.; Zherebtsov, S.; Pfeifer, T.; Azzeer, A. M.; Kling, M. F.; et al. Real-Time Observation of Valence Electron Motion. *Nature* **2010**, *466*, 739–743.

(30) Wollenhaupt, M.; Baumert, T. Ultrafast laser control of electron dynamics in atoms, molecules and solids. *Faraday Discuss.* **2011**, *153*, 9–26.

(31) Kleine, C.; Winghart, M.-O.; Zhang, Z.-Y.; Richter, M.; Ekimova, M.; Eckert, S.; Vrakking, M. J. J.; Nibbering, E. T. J.; Rouzée, A.; Grant, E. R. Electronic State Population Dynamics upon

Ultrafast Strong Field Ionization and Fragmentation of Molecular Nitrogen. *Phys. Rev. Lett.* **2022**, *129*, 123002.

(32) Mukamel, S. Multidimensional Femtosecond Correlation Spectroscopies of Electronic and Vibrational Excitations. *Annu. Rev. Phys. Chem.* **2000**, *51*, 691−729.

(33) List, N. H.; Dempwolff, A. L.; Dreuw, A.; Norman, P.; Martínez, T. J. Probing competing relaxation pathways in malonaldehyde with transient X-ray absorption spectroscopy. *Chem. Sci.* **2020**, *11*, 4180−4193.

(34) Rouxel, J. R.; Keefer, D.; Aleotti, F.; Nenov, A.; Garavelli, M.; Mukamel, S. Coupled Electronic and Nuclear Motions during Azobenzene Photoisomerization Monitored by Ultrafast Electron Diffraction. *J. Chem. Theory Comput.* **2022**, *18*, 605−613.

(35) Schuurman, M. S.; Blanchet, V. Time-resolved photoelectron spectroscopy: the continuing evolution of a mature technique. *Phys. Chem. Chem. Phys.* **2022**, *24*, 20012−20024.

(36) Schnappinger, T.; Jadoun, D.; Gudem, M.; Kowalewski, M. Time-Resolved X-ray and XUV Based Spectroscopic Methods for Nonadiabatic Processes in Photochemistry. *Chem. Commun.* **2022**, *58*, 12763−12781.

(37) Rott, F.; Reduzzi, M.; Schnappinger, T.; Kobayashi, Y.; Chang, K. F.; Timmers, H.; Neumark, D. M.; Vivie-Riedle, R. d.; Leone, S. R. Ultrafast Strong-Field Dissociation of Vinyl Bromide: An Attosecond Transient Absorption Spectroscopy and Non-Adiabatic Molecular Dynamics Study. *Structural Dynamics* **2021**, *8*, 034104.

(38) Lackner, F.; Chatterley, A. S.; Pemmaraju, C. D.; Closser, K. D.; Prendergast, D.; Neumark, D. M.; Leone, S. R.; Gessner, O. Direct Observation of Ring-Opening Dynamics in Strong-Field Ionized Selenophene Using Femtosecond Inner-Shell Absorption Spectroscopy. *J. Chem. Phys.* **2016**, *145*, 234313.

(39) Zinchenko, K. S.; Ardana-Lamas, F.; Seidu, I.; Neville, S. P.; van der Veen, J.; Lanfaloni, V. U.; Schuurman, M. S.; Wörner, H. J. Sub-7-fs Conical-Intersection Dynamics Probed at the Carbon K-edge. *Science* **2021**, *371*, 489−494.

(40) Scutelnic, V.; Tsuru, S.; Papai, M.; Yang, Z.; Epshtein, M.; Xue, T.; Haugen, E.; Kobayashi, Y.; Krylov, A. I.; Møller, K. B.; Coriani, S.; Leone, S. R.; et al. X-ray transient absorption reveals the $^1A_u(n\pi^*)$ state of pyrazine in electronic relaxation. *Nat. Commun.* **2021**, *12*, 2041−1723.

(41) Tsuru, S.; Vidal, M. L.; Pápai, M.; Krylov, A. I.; Møller, K. B.; Coriani, S. Time-resolved near-edge X-ray absorption fine structure of pyrazine from electronic structure and nuclear wave packet dynamics simulations. *J. Chem. Phys.* **2019**, *151*, 124114.

(42) Neville, S. P.; Chergui, M.; Stolow, A.; Schuurman, M. S. Ultrafast X-Ray Spectroscopy of Conical Intersections. *Phys. Rev. Lett.* **2018**, *120*, 243001.

(43) Northey, T.; Norell, J.; Fouda, A. E. A.; Besley, N. A.; Odelius, M.; Penfold, T. J. Ultrafast nonadiabatic dynamics probed by nitrogen K-edge absorption spectroscopy. *Phys. Chem. Chem. Phys.* **2020**, *22*, 2667−2676.

(44) Oliver, T. A. A.; Fleming, G. R. Following Coupled Electronic-Nuclear Motion through Conical Intersections in the Ultrafast Relaxation of β-Apo-8-Carotenal. *J. Phys. Chem. B* **2015**, *119*, 11428−11441.

(45) Bhattacherjee, A.; Leone, S. R. Ultrafast X-ray Transient Absorption Spectroscopy of Gas-Phase Photochemical Reactions: A New Universal Probe of Photoinduced Molecular Dynamics. *Acc. Chem. Res.* **2018**, *51*, 3203−3211.

(46) Kobayashi, Y.; Chang, K. F.; Zeng, T.; Neumark, D. M.; Leone, S. R. Direct mapping of curve-crossing dynamics in IBr by attosecond transient absorption spectroscopy. *Science* **2019**, *365*, 79−83.

(47) Timmers, H.; Zhu, X.; Li, Z.; Kobayashi, Y.; Sabbar, M.; Hollstein, M.; Reduzzi, M.; Martínez, T. J.; Neumark, D. M.; Leone, S. R. Disentangling Conical Intersection and Coherent Molecular Dynamics in Methyl Bromide with Attosecond Transient Absorption Spectroscopy. *Nat. Commun.* **2019**, *10*, 3133.

(48) Toulson, B. W.; Borgwardt, M.; Wang, H.; Lackner, F.; Chatterley, A. S.; Pemmaraju, C. D.; Neumark, D. M.; Leone, S. R.; Prendergast, D.; Gessner, O. Probing Ultrafast C−Br Bond Fission in the UV Photochemistry of Bromoform with Core-to-Valence Transient Absorption Spectroscopy. *Structural Dynamics* **2019**, *6*, 054304.

(49) Chang, K. F.; Reduzzi, M.; Wang, H.; Poullain, S. M.; Kobayashi, Y.; Barreau, L.; Prendergast, D.; Neumark, D. M.; Leone, S. R. Revealing Electronic State-Switching at Conical Intersections in Alkyl Iodides by Ultrafast XUV Transient Absorption Spectroscopy. *Nat. Commun.* **2020**, *11*, 4042.

(50) Chang, K. F.; Wang, H.; Poullain, S. M.; Prendergast, D.; Neumark, D. M.; Leone, S. R. Mapping Wave Packet Bifurcation at a Conical Intersection in CH3I by Attosecond XUV Transient Absorption Spectroscopy. *J. Chem. Phys.* **2021**, *154*, 234301.

(51) Wernet, P.; Kunnus, K.; Schreck, S.; Quevedo, W.; Kurian, R.; Techert, S.; de Groot, F. M. F.; Odelius, M.; Föhlisch, A. Dissecting Local Atomic and Intermolecular Interactions of Transition-Metal Ions in Solution with Selective X-ray Spectroscopy. *J. Phys. Chem. Lett.* **2012**, *3*, 3448−3453.

(52) Josefsson, I.; Kunnus, K.; Schreck, S.; Föhlisch, A.; de Groot, F.; Wernet, P.; Odelius, M. Ab Initio Calculations of X-ray Spectra: Atomic Multiplet and Molecular Orbital Effects in a Multiconfigurational SCF Approach to the L-Edge Spectra of Transition Metal Complexes. *J. Phys. Chem. Lett.* **2012**, *3*, 3565−3570.

(53) Gendron, F.; Moore, B.; Cador, O.; Pointillart, F.; Autschbach, J.; Le Guennic, B. Ab Initio Study of Circular Dichroism and Circularly Polarized Luminescence of Spin-Allowed and Spin-Forbidden Transitions: From Organic Ketones to Lanthanide Complexes. *J. Chem. Theory Comput.* **2019**, *15*, 4140−4155.

(54) Cederbaum, L. S.; Domcke, W.; Schirmer, J. Many-Body Theory of Core Holes. *Phys. Rev. A* **1980**, *22*, 206−222.

(55) Barth, A.; Cederbaum, L. S. Many-Body Theory of Core-Valence Excitations. *Phys. Rev. A* **1981**, *23*, 1038−1061.

(56) Josefsson, I.; Kunnus, K.; Schreck, S.; Föhlisch, A.; de Groot, F.; Wernet, P.; Odelius, M. Ab Initio Calculations of X-ray Spectra: Atomic Multiplet and Molecular Orbital Effects in a Multiconfigurational SCF Approach to the L-Edge Spectra of Transition Metal Complexes. *J. Phys. Chem. Lett.* **2012**, *3*, 3565−3570.

(57) Wang, H.; Odelius, M.; Prendergast, D. A Combined Multi-Reference Pump-Probe Simulation Method with Application to XUV Signatures of Ultrafast Methyl Iodide Photodissociation. *J. Chem. Phys.* **2019**, *151*, 124106.

(58) Finley, J.; Malmqvist, P.-A.; Roos, B. O.; Serrano-Andrés, L. The Multi-State CASPT2Method. *Chem. Phys. Lett.* **1998**, *288*, 299−306.

(59) Granovsky, A. A. Extended Multi-Configuration Quasi-Degenerate Perturbation Theory: The New Approach to Multi-State Multi-Reference Perturbation Theory. *J. Chem. Phys.* **2011**, *134*, 214113.

(60) Shiozaki, T.; Györffy, W.; Celani, P.; Werner, H.-J. Communication: Extended Multi-State Complete Active Space Second-Order Perturbation Theory: Energy and Nuclear Gradients. *J. Chem. Phys.* **2011**, *135*, 081106.

(61) Ghigo, G.; Roos, B. O.; Malmqvist, P.-Å. A Modified Definition of the Zeroth-Order Hamiltonian in Multiconfigurational Perturbation Theory (CASPT2). *Chem. Phys. Lett.* **2004**, *396*, 142−149.

(62) Forsberg, N.; Malmqvist, P.-Å. Multiconfiguration Perturbation Theory with Imaginary Level Shift. *Chem. Phys. Lett.* **1997**, *274*, 196−204.

(63) Malmqvist, P.-Å. Calculation of Transition Density Matrices by Nonunitary Orbital Transformations. *Int. J. Quantum Chem.* **1986**, *30*, 479−494.

(64) Malmqvist, P.-Å.; Roos, B. O. The CASSCF State Interaction Method. *Chem. Phys. Lett.* **1989**, *155*, 189−194.

(65) Malmqvist, P.-Å.; Roos, B. O.; Schimmelpfennig, B. The Restricted Active Space (RAS) State Interaction Approach with Spin−Orbit Coupling. *Chem. Phys. Lett.* **2002**, *357*, 230−240.

(66) Schüppel, F.; Schnappinger, T.; Bäuml, L.; de Vivie-Riedle, R. Waveform control of molecular dynamics close to a conical intersection. *J. Chem. Phys.* **2020**, *153*, 224307.

(67) Franck, J.; Dymond, E. G. Elementary processes of photochemical reactions. *Trans. Faraday Soc.* **1926**, *21*, 536−542.

(68) Condon, E. U. Nuclear Motions Associated with Electron Transitions in Diatomic Molecules. *Phys. Rev.* **1928**, *32*, 858−872.

(69) Roos, B. O.; Veryazov, V.; Widmark, P.-O. Relativistic atomic natural orbital type basis sets for the alkaline and alkaline-earth atoms applied to the ground-state potentials for the corresponding dimers. *Theor. Chem. Acc.* **2004**, *111*, 345−351.

(70) Roos, B. O.; Lindh, R.; Malmqvist, P.-Å.; Veryazov, V.; Widmark, P.-O. Main group atoms and dimers studied with a new relativistic ANO basis set. *J. Phys. Chem. A* **2004**, *108*, 2851−2858.

(71) Roos, B. O.; Lindh, R.; Malmqvist, P.-Å.; Veryazov, V.; Widmark, P.-O. New relativistic ANO basis sets for transition metal atoms. *J. Phys. Chem. A* **2005**, *109*, 6575−6579.

(72) Roos, B. O.; Lindh, R.; Malmqvist, P.-Å.; Veryazov, V.; Widmark, P.-O. New relativistic ANO basis sets for actinide atoms. *Chem. Phys. Lett.* **2005**, *409*, 295−299.

(73) Roos, B. O.; Lindh, R.; Malmqvist, P.-Å.; Veryazov, V.; Widmark, P.-O.; Borin, A. C. New relativistic atomic natural orbital basis sets for lanthanide atoms with applications to the Ce diatom and LuF3. *J. Phys. Chem. A* **2008**, *112*, 11431−11435.

(74) Fdez Galvan, I.; Vacher, M.; Alavi, A.; Angeli, C.; Aquilante, F.; Autschbach, J.; Bao, J. J.; Bokarev, S. I.; Bogdanov, N. A.; Carlson, R. K.; Chibotaru, L. F.; Creutzberg, J.; Dattani, N.; Delcey, M. G.; Dong, S. S.; Dreuw, A.; Freitag, L.; Frutos, L. M.; Gagliardi, L.; Gendron, F.; Giussani, A.; Gonzalez, L.; Grell, G.; Guo, M.; Hoyer, C. E.; Johansson, M.; Keller, S.; Knecht, S.; Kovacevic, G.; Kallman, E.; Li Manni, G.; Lundberg, M.; Ma, Y.; Mai, S.; Malhado, J. P.; Malmqvist, P. A.; Marquetand, P.; Mewes, S. A.; Norell, J.; Olivucci, M.; Oppel, M.; Phung, Q. M.; Pierloot, K.; Plasser, F.; Reiher, M.; Sand, A. M.; Schapiro, I.; Sharma, P.; Stein, C. J.; Sørensen, L. K.; Truhlar, D. G.; Ugandi, M.; Ungur, L.; Valentini, A.; Vancoillie, S.; Veryazov, V.; Weser, O.; Wesołowski, T. A.; Widmark, P.-O.; Wouters, S.; Zech, A.; Zobel, J. P.; Lindh, R.; et al. OpenMolcas: From Source Code to Insight. *J. Chem. Theory Comput.* **2019**, *15*, 5925−5964.

(75) Aquilante, F.; Autschbach, J.; Baiardi, A.; Battaglia, S.; Borin, V. A.; Chibotaru, L. F.; Conti, I.; De Vico, L.; Delcey, M.; Fdez Galvan, I.; Ferre, N.; Freitag, L.; Garavelli, M.; Gong, X.; Knecht, S.; Larsson, E. D.; Lindh, R.; Lundberg, M.; Malmqvist, P. A.; Nenov, A.; Norell, J.; Odelius, M.; Olivucci, M.; Pedersen, T. B.; Pedraza-Gonzalez, L.; Phung, Q. M.; Pierloot, K.; Reiher, M.; Schapiro, I.; Segarra-Marti, J.; Segatta, F.; Seijo, L.; Sen, S.; Sergentu, D.-C.; Stein, C. J.; Ungur, L.; Vacher, M.; Valentini, A.; Veryazov, V.; et al. Modern quantum chemistry with [Open]Molcas. *J. Chem. Phys.* **2020**, *152*, 214117.

(76) Felicetti, S.; Fregoni, J.; Schnappinger, T.; Reiter, S.; de Vivie-Riedle, R.; Feist, J. Photoprotecting Uracil by Coupling with Lossy Nanocavities. *J. Phys. Chem. Lett.* **2020**, *11*, 8810−8818.

(77) Asban, S.; Keefer, D.; Chernyak, V. Y.; Mukamel, S. Sensing ultrashort electronic coherent beating at conical intersections by single-electron pulses. *Proc. Natl. Acad. Sci. U.S.A.* **2022**, *119*, No. e2205510119.

(78) Chakraborty, P.; Liu, Y.; Weinacht, T.; Matsika, S. Effect of dynamic correlation on the ultrafast relaxation of uracil in the gas phase. *Faraday Discuss.* **2021**, *228*, 266−285.

(79) Feyer, V.; Plekan, O.; Richter, R.; Coreno, M.; de Simone, M.; Prince, K. C.; Trofimov, A. B.; Zaytseva, I. L.; Schirmer, J. Tautomerism in Cytosine and Uracil: A Theoretical and Experimental X-ray Absorption and Resonant Auger Study. *J. Phys. Chem. A* **2010**, *114*, 10270−10276.

(80) Wolf, T. J. A.; Myhre, R. H.; Cryan, J. P.; Coriani, S.; Squibb, R. J.; Battistoni, A.; Berrah, N.; Bostedt, C.; Bucksbaum, P.; Coslovich, G.; Feifel, R.; Gaffney, K. J.; Grilj, J.; Martinez, T. J.; Miyabe, S.; Moeller, S. P.; Mucke, M.; Natan, A.; Obaid, R.; Osipov, T.; Plekan, O.; Wang, S.; Koch, H.; Guhr, M. Probing ultrafast $\pi\pi^*/n\pi^*$ internal conversion in organic chromophores via K-edge resonant absorption. *Nat. Commun.* **2017**, *8*, 29 DOI: 10.1038/s41467-017-00069-7.

(81) von den Hoff, P.; Thallmair, S.; Kowalewski, M.; Siemering, R.; de Vivie-Riedle, R. Optimal control theory − closing the gap between theory and experiment. *Phys. Chem. Chem. Phys.* **2012**, *14*, 14460−14485.

(82) Krebs, N.; Pugliesi, I.; Hauer, J.; Riedle, E. Two-dimensional Fourier transform spectroscopy in the ultraviolet with sub-20 fs pump pulses and 250−720 nm supercontinuum probe. *New J. Phys.* **2013**, *15*, 085016.

(83) Keefer, D.; Mukamel, S. Selective Enhancement of Spectroscopic Features by Quantum Optimal Control. *Phys. Rev. Lett.* **2021**, *126*, 163202.

3.3 Chlorophyll: A Case of Global Coupling

Based on the quantum dynamics simulations shown in chapter 2 the natural pigment chlorophyll a does not exhibit an accessible CoIn. However, the first two excited states are energetically close and non-adiabatic coupling is present between them throughout the whole coordinate space. Compared to uracil this situation is very different, where the influence of the electronic coherence is equal, if not even more significant. In the case of chlorophyll a the transient XAS might also offer an experimental possibility to verify that the Q_y and Q_x form a system of highly coupled states, as indicated by theory [82] and transient absorption anisotropy experiments [175]. As they are coupled, ultrafast population transfer from one state to the other and back takes place. With the high temporal resolution of XAS this population transfer might be observable, thus proving the coupling of Q_y and Q_x. Time-resolved XAS for systems like chlorophyll a still pose problems for experimental realisation. However, in recent years advances in experimental set-ups including, among others, the extension to attosecond resolution of solution-phase water-window XAS [143, 176], as well as developments for the application of XAS to larger (bio)molecules [38, 177] may pave the way to a realisation of complementary experiments to the proposed theoretical spectra.

The workflow described in the beginning of this chapter is applicable to molecules of various sizes, as long as the RASPT2 calculation converges in a reasonable amount of time. With increasing computational power this will be fulfilled for larger and larger molecular systems. With the current computational performance limits a few modifications were necessary to make the calculations of XAS feasible for chlorophyll. Whereas for uracil the same basis set was used for all elements it became necessary to treat different elements with basis sets of different sizes when going to larger molecules. When benchmarking the basis sets a compromise between accuracy and convergence of the calculation has to be found. If feasible, one would aim for basis sets with a better description of the core orbitals for the element that is probed. In `OpenMolcas` it is also possible to restrict the definition of the correlation orbital space in XMS-CASPT2 to reduce its size by freezing orbitals that are, e.g., located at peripheral atoms. For chlorophyll orbitals located at the central magnesium atom and the rings surrounding it were considered, while neglecting the hydrogen atoms, methyl groups and chains. This means a significant speed up in calculation time, but has to be carefully benchmarked as not to exclude relevant orbital contributions. Exemplary inputs as used for uracil and chlorophyll can be found in appendix B together with an overview of the changes that were necessary.

The article "Coupled Nuclear and Electron Dynamics in Chlorophyll Unraveled by XMS-CASPT2 X-Ray Absorption Spectra" was published in *The Journal of Physical Chemistry B*. The key findings presented in the article are:

- The workflow for the combination of the coupled nuclear and electron dynamics with XAS at the XMS-CASPT2 level of theory was extended to cover also larger molecules, like chlorophyll a. Here, time-resolved XAS at the nitrogen and magnesium K-edge were simulated.

- Using the static XAS we found characteristic signals for the Q_y and Q_x to follow the ultrafast population transfer between these two states and in this way corroborate the coupling between them. The peaks of the magnesium K-edge exhibit only a small shift in energy between signals from Q_y and Q_x, but show a great difference in intensity. The peaks of the nitrogen K-edge are farther separated in energy, also due to their better experimental resolution. In both cases the ground state features are lying at higher energies and should not interfere with the observation of the population transfer.

- The time-resolved XAS of the magnesium and nitrogen K-edge have been computed for two different excitation situations. In the first case a delta excitation into the Q_x was assumed. Therefore, the wavepacket is excited into the manifold of vibrational levels of this excited state. In the second case the population was excited into both Q-states via an explicitly simulated pump pulse.

- For the transient XAS at the magnesium K-edge the ultrafast population transfer after delta excitation into Q_x could be followed via the characteristic spectral features of Q_x at 1324.0 eV and the Q_y signals at 1322.5 eV, which were alternating in the spectrum. For the nitrogen K-edge a similar situation was found.

- The spectra obtained with an explicitly simulated pump pulse show initially intense signals of the ground state above 1328.5 eV. The excitation process can be followed via the subsequently arising peaks of the excited states at 1325.4 eV (Q_x) and 1324.2 eV (Q_y). The population transfer can be followed by the oscillations between these two spectral ranges or by tracking the appearance and disappearance of the significantly more intense Q_x features.

- A periodic influence of the electronic coherence was found to be present over the whole simulation time. It was observed, that the main contribution toward the electronic coherence arises from the overlap of the wavepackets on the different electronic states.

- Tracking the oscillatory behaviour of Q_y and Q_x signals was shown to be possible for both, the nitrogen and magnesium K-edge. As the magnesium edge exhibits fewer signals it is easier to observe the spectral changes for this edge. The theoretical results indicate, that time-resolved XAS might offer an opportunity to experimentally corroborate the ultrafast population transfer in the Q-band and therefore the coupling between these states.

Hereafter, the article "Coupled Nuclear and Electron Dynamics in Chlorophyll Unraveled by XMS-CASPT2 X-Ray Absorption Spectra" is reproduced from *The Journal of Physical Chemistry B* **129**, 2159 (2025). Copyright 2025 American Chemical Society. The supporting information of this article is available under https://pubs.acs.org/doi/10.1021/acs.jpcb.4c07787.

THE JOURNAL OF PHYSICAL CHEMISTRY B
A JOURNAL OF THE AMERICAN CHEMICAL SOCIETY

pubs.acs.org/JPCB

Article

Coupled Nuclear and Electron Dynamics in Chlorophyll Unraveled by XMS-CASPT2 X-ray Absorption Spectra

Lena Bäuml* and Regina de Vivie-Riedle

Cite This: *J. Phys. Chem. B* 2025, 129, 2159−2167

Read Online

ACCESS | Metrics & More | Article Recommendations | Supporting Information

ABSTRACT: Attosecond spectroscopy, especially time-resolved X-ray absorption spectra (XAS), enables direct observation of ultrafast molecular dynamics. The complementary and even preceding development of theoretical simulations can offer the necessary guidance and stimulate new experiments. In this work, we simulated high-level XAS for the magnesium and nitrogen K-edge of chlorophyll *a*. In our previous work on the ultrafast relaxation process in the Q-band, our quantum dynamics simulations found the Q_x and Q_y states to be energetically close and therefore strongly coupled. Here, we analyze the strong coupling between Q_x and Q_y via XAS, indicating promising possibilities for experimental observation. The excited-state energies, potential energy surfaces, and XAS are computed at the XMS-CASPT2 level of theory to capture the complex multireference character of chlorophyll excitations. In our simulated spectra, we could follow the ultrafast population transfer between Q_x and Q_y and thus draw conclusions about the strong vibrational coupling between them.

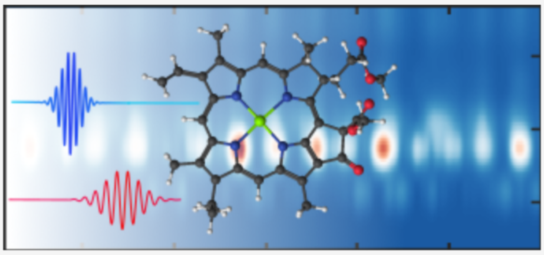

■ INTRODUCTION

Attosecond transient absorption spectroscopy provides, among others, the possibility to experimentally determine the population of different states[1] and its change over time, as its spectral and temporal resolution is able to resolve the coupled nuclear and electron dynamics.[2−4] Attosecond pulses in the X-ray regime can create well-localized electronic wavepackets. As the inner valence and core states of the excited molecule are probed, these pulses are sensitive toward chemical elements, charge, and population of the electronic states.[2,4−12] Attosecond spectroscopy is a rapidly evolving field. Recent advances in experimental setups include, among others, the extension to attosecond resolution of solution-phase water-window X-ray absorption spectra (XAS),[4,13] as well as developments for the application of XAS to larger (bio)-molecules.[14,15] The ongoing research in this direction offers the prospect of a broader application of transient XAS with high temporal resolution in the future. At the same time, the computational capabilities to simulate excited-state dynamics and thereby explain experimental data on a molecular level are steadily advancing.[16] In particular, the parallel and even preceding development of theoretical workflows to simulate XAS for larger molecules is crucial to evaluating and predicting experiments. The advantages of a successful combination of experimental XAS with theoretical simulations for the assignment of spectral features or the verification of observations has been shown in different contexts.[2,14,17] In this paper, we derive a workflow to simulate transient XAS for a large, biologically relevant molecule at a high level of theory, namely, extended multistate complete active space perturbation theory (XMS-CASPT2). This method has been shown to be one of the most accurate ones in the context of pump−probe spectroscopy.[18] As an example, we chose the ubiquitous natural pigment chlorophyll *a* with its unique nonadiabatic dynamics. Our simulations include the coupled nuclear and electron dynamics and have been performed both under the assumption of a delta pulse excitation and including the explicit simulation of the pump pulse. Static XAS for the magnesium and carbon K-edges of chlorophyll *a* in liquid samples or on membranes have shown to be experimentally feasible.[19,20] Especially, the nonradiative relaxation of chlorophylls after photoexcitation is an important process during photosynthetic light harvesting. The most prominent bands of the absorption spectrum in the visible range are the B-band, also called the Soret band, with a strong absorption around 400 nm and the less intense Q-band, which absorbs around 700 nm. For the latter, an extensive pattern of vibrational side bands can be observed. In theoretical simulations, sometimes, a dark state is found between the B- and Q-band, whether this state is present and its exact energetic position depends strongly on the applied quantum chemistry method.[21−24] The B- and Q-bands both consist of two excited states, called B_x/B_y and Q_x/Q_y,

Received: November 18, 2024
Revised: January 17, 2025
Accepted: February 6, 2025
Published: February 17, 2025

https://doi.org/10.1021/acs.jpcb.4c07787
J. Phys. Chem. B 2025, 129, 2159−2167

depending on the polarization of their respective transition dipole moment vector. Despite its importance in photosynthesis, excited-state dynamics of chlorophyll, especially within the Q-band, is still under debate.[25−28] Until a recent reconsideration, Q_y and Q_x were seen as two separate states. Their assignment to electronic states has been long discussed and changed over time.[29−32] In recent years, the two states are more and more seen as one system of highly coupled states. This concept evolved from the re-evaluation of existing experiments,[25] as well as high-level quantum mechanical calculations.[25,33,34] Theoretical work, mostly using semi-classical methods, could show a strong vibrational coupling between the two Q states.[26−28,35] Also, our recently published investigation of the ultrafast relaxation process in the Q-band using grid-based wavepacket quantum dynamics on representative XMS-CASPT2 potential energy surfaces (PESs) could confirm the strong coupling between Q_y and Q_x.[36] In a collaboration with the group of Prof. Jürgen Hauer, polarized transient absorption experiments did not show any signal of the Q_x, which was attributed to a sub 30 fs population transfer to Q_y.[37] As the population exchange takes place on a time scale of a few femtoseconds, it is experimentally demanding to resolve. Here, attosecond spectroscopy offers a possibility to shed light on the ultrafast dynamics.

In this paper, we build on our study of the ultrafast relaxation process in the Q-band.[36] Our previous results showed that the Q_y and Q_x PESs do not cross in an energetically accessible region but are strongly coupled along the 2D coordinates after laser pulse excitation. In this work, we propose XAS as a potential experimental possibility to study the ultrafast relaxation dynamics and corroborate the strong coupling between the two Q states by tracking their population. We adapted our previously described workflow[38] for the simulation of XAS to enable the calculation of time-resolved spectra at the XMS-CASPT2 level of theory for larger molecules, such as chlorophyll. The obtained spectra at the magnesium and nitrogen K-edges enable us to follow the ultrafast population transfer within the Q-band and estimate the influence of the electronic coherence on time-resolved XAS.

■ METHODS

Simulation of Transient X-ray Absorption Spectra. To simulate the time-resolved XAS, we adapted a previously described workflow.[38] To make the simulation of especially the core excitation feasible for large molecules, we modified our calculations as described in the section on Computational Details. The general approach closely follows our previous work on XAS of uracil[38] and other work,[2,39] and the reader is referred there for details on the theory. For convenience, the principal steps and equations are given in the following. Building on our study of the Q-band relaxation in chlorophyll *a*,[36] the nuclear coordinate space is represented on a 2D numerical grid. At each grid point, a static XAS is calculated at the XMS-CASPT2 level of theory. For the valence- and core-excited states, a complete active space self-consistent field with a subsequent restricted active space configuration interaction (RASCI) calculation is performed under application of the core−valence separation.[40−43] Using RASCI, the molecular orbitals are not reoptimized along with the CI coefficients, which has been shown to be reasonable for the core-excited states.[42,44,45] For both valence- and core-excited states, the thus obtained wave functions are used for an XMS-CASPT2[46−48] calculation to include dynamic electron correlation. The interactions between all states are then calculated using the restricted active space state interaction (RASSI) method[49−51] with the valence and core wave functions as basis. Finally, the static XAS is derived by extracting the electronic dipole moments and excitation energies of the desired valence-excited states from the RASSI calculation. The applied active space (see Figure 1) consists of three π and three π^* orbitals in RAS2 and the magnesium 1s orbital in RAS1. For the calculation of nitrogen K-edge XAS, the four nitrogen 1s orbitals were used instead.

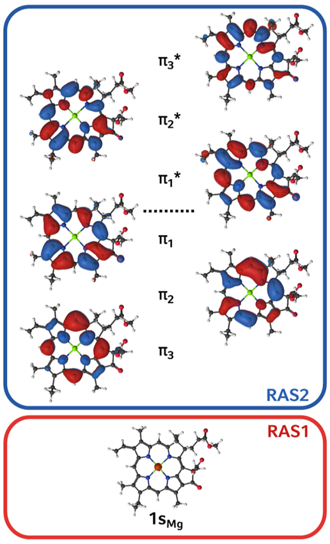

Figure 1. Active space for RAS2 and the magnesium 1s orbital in RAS1. All orbitals in RAS2 are rendered with an isovalue of 0.02, and the orbital in RAS1 with an isovalue of 0.001.

To obtain the transient XAS, the static spectra resulting from the RASSI calculation are combined with the coupled nuclear and electron dynamics derived with the NEMol ansatz.[52−58] We focus on the three valence states S_0, Q_y, and Q_x. For the probe pulse, no specific alignment of the molecules is assumed. However, for the pump pulse, it is assumed that the electric component of the pulse is optimally aligned with the transition dipole moment of the molecule. In our method, a delta pulse is applied as the probe pulse that simultaneously excites the superposition of the three valence states into the multitude of core-hole states. Due to the extremely short pulse duration of the X-ray probe pulse, its approximation with an idealized delta pulse seems reasonable. The probe pulse creates a nuclear wavepacket $\chi_c(R,t)$ for each core-hole state c, that includes the information on all three valence states. As a first approximation, we construct this wavepacket as a superposition of the nuclear wavepackets in the three valence states. We thereby take into account the interference that can occur since the core-hole state c can be populated by all three valence states simultaneously. With this approximation, the total wave function $\Psi_c(r,R,t)$ of the core-hole state can be defined as a linear combination of the nuclear wave functions of the valence states and the electronic wave function of the core-hole state:

$$\Psi_c(r, R, t) = \chi_c(R, t)\varphi_c(r; R) = \sum_j^{N_{\text{val}}} \chi_j(R, t)\varphi_c(r; R) \tag{1}$$

Based on this, the transition dipole moment $\mu_{ic}(t)$ between a specific core-hole state c and valence state i can be written as:

$$\mu_{ic}(t) = \langle \chi_i(R, t)\varphi_i(r; R)|\hat{\mu}|\sum_{j}^{N_{\text{val}}} \chi_j(R, t)\varphi_c(r; R)\rangle \tag{2}$$

As the probe pulse is short under experimental conditions, we assume the operator $\hat{\mu}$ to be only dependent on the electronic wave functions. Thus, the electronic transition dipole moment integral can be separated from the nuclear wave functions, leading to the following approximation for μ_{ic}:

$$\begin{aligned}\mu_{ic}(t) &= \langle \varphi_i(r; R)|\hat{\mu}|\varphi_c(r; R)\rangle \sum_{j}^{N_{\text{val}}} \langle \chi_i(R, t)|\chi_j(R, t)\rangle \\ &= \mu_{ic}^{P}(t) + \mu_{ic}^{C}(t).\end{aligned} \tag{3}$$

The sum over all valence states can be split into two parts. One, μ_{ic}^{P}, being defined by i and j being equal, which can therefore be formulated as the electronic transition dipole moment multiplied by the time-dependent population $A_{ii}(t) = \langle \chi_i(R,t)|\chi_i(R,t)\rangle$:

$$\mu_{ic}^{P}(t) = \langle \varphi_i(r; R)|\hat{\mu}|\varphi_c(r; R)\rangle A_{ii}(t) \tag{4}$$

This term is based on the nuclear wavepacket dynamics in a specific state i. The other part, μ_{ic}^{C}, takes into account the time-dependent overlap of the nuclear wavepacket in different valence states i and j and therefore contains the electronic coherence.

$$\mu_{ic}^{C}(t) = \langle \varphi_i(r; R)|\hat{\mu}|\varphi_c(r; R)\rangle \sum_{(j\neq i)}^{N_{\text{val}}} A_{ij}(t) \tag{5}$$

with the time-dependent overlap $A_{ij}(t) = \langle \chi_i(R,t)|\chi_j(R,t)\rangle$. The oscillator strength f_{ic}, that describes the probability of a transition between valence state i and core-hole state c, takes into account the population-induced component μ_{ic}^{P}, as well as the coherence-induced part μ_{ic}^{C} of the transition dipole moment:

$$f_{ic} = \frac{2}{3}\Delta E_{ic}|\mu_{ic}^{P}(t) + \mu_{ic}^{C}(t)|^2 \tag{6}$$

The coupled quantum dynamics simulation is performed on a 2D PES that has shown to be adequate.[36] The tests that were conducted to ascertain the adequacy of the reduced coordinate space are described in the Computational Details section, as well as in Supporting Information section I. The latter also includes details on the quantum dynamics simulation. The energy difference ΔE_{ic} and the electronic dipole moment are obtained by RASSI calculations. The time-dependent population $A_{ii}(t)$ and wave function overlap terms $A_{ij}(t)$ are derived from the NEMol ansatz in the NEMol-grid extension.[58] There, the nuclear coordinate space is split into segments, for each of which ΔE_{ic} and the electronic dipole moment were calculated and weighted with the partial population and nuclear wavepacket overlap in accordance with eq 6. To derive the transient XAS for each transition i to c, the segments are added, and all relevant core-hole excitations are combined. Coupling to environmental modes or decoherence effects, which would dominate at long time scales, are not included in this model. In the literature, different time scales for the environmental effects on chlorophyll dynamics are reported with most lying around 3 ps.[59−61] We therefore limit our simulations to the initial dynamics (maximal 325 fs), where these effects do not play a significant role.

■ COMPUTATIONAL DETAILS

X-ray absorption spectra are obtained experimentally via pump−probe spectroscopy. In our simulations, we tested two cases. In the first, we are assuming a delta pulse excitation into the Q_x state as the pump pulse and start with 100% of the population in this state. In the second case, we explicitly simulate the pump pulse with a central frequency of ω_0 of 2.43 eV, a full width at half-maximum (fwhm) of 30 fs, and a maximum field strength of 4.9×10^{-3} GV cm^{-1}. Due to the closeness of their respective energy levels, the pulse excites population into both Q states. The NEMol ansatz[58] within the NEMol-grid extension was applied to simulate the dynamic response of the molecule to the pump pulse. The nuclear coordinate space was divided into 5 × 5 equally distributed segments between −0.1 and 0.1 Å in both dimensions, as this is the area covered by the wavepacket during our propagation. To obtain suitable molecular coordinates, we relied on our previous work,[36] where we determined the overlap between the normal modes and the NAC vector at the Q_y geometry. Upon testing several PESs using normal modes from different frequency ranges, we found that the overall topography of the PESs was similar for all choices of coordinates. The resulting dynamics were in good agreement with those of related compounds,[62] corroborating the choice of coordinates. The relaxation dynamics was expectedly faster in coordinate spaces that overlapped more strongly with the NAC vector. However, the wavepacket dynamics was comparable in all tested 2D spaces.[36] Therefore, we decided on normal modes 195 and 194 as coordinates to simulate the XAS, as these exhibit the highest overlap with the NAC vector at the Q_y geometry.

In the first step, a CAS(6/6) calculation with state averaging over six states is performed. In a next step, the valence- and core-excited states are calculated using RASCI with six states and 40 states, respectively. To partially parallelize the process, the CASPT2 calculations of the different states were first run separately and the coupling between them was then derived in a subsequent calculation. This represents a significant speedup without adding any approximations. In a last step, the interactions between all states, core as well as valence states, are accounted for, using the RASSI method.[49−51] The oscillator strengths and excitation energies of the desired valence-excited states are then extracted and plotted against each other. For the magnesium K-edge, an overall Gaussian convolution of σ = 0.565 eV was applied to broaden the simulated line spectrum. For the nitrogen K-edge, σ = 0.170 eV was chosen. These values are based on the assumption of an experimental resolving power ($E/\Delta E$) equal to 1000. For all calculations at the K-edge, we used the ANO-R0[63,64] basis set for the element that was probed (magnesium or nitrogen) and the relativistic atomic natural orbital basis (ANO-RCC),[65−69] contracted to VDZP quality (ANO-RCC-VDZP) for all other elements. The calculations were performed in OpenMolcas[70,71] using the XMS-CASPT2 method[46−48] with an IPEA shift of 0.1 and an imaginary shift of 0.2. The definition of the correlation orbital space in XMS-CASPT2 was restricted to the central magnesium atom and the rings surrounding it, neglecting the hydrogen atoms, methyl groups, and chains. This reduces the size and, therefore, the resources needed for the CASPT2 calculation by freezing orbitals that are located at peripheral atoms.

■ RESULTS AND DISCUSSION

The following simulations of XAS are based on our previous work[36] and the 2D PESs described therein. For completeness, the main findings are summarized in the following. We found the PESs to be quasi-harmonic for all states and the Q_y and Q_x to be lying very close together in energy. A conical intersection (CoIn) could not be found along the selected coordinates, but strong nonadiabatic coupling elements (NACs) were present between these two states throughout the whole area of the PES. By analyzing their vibrational energy levels, the $\nu = 2$ vibrational eigenfunction of the Q_y PES was found to be nearly degenerate with the vibronic ground state of Q_x ($\nu = 0$), resulting in an ultrafast population transfer between these two. The adequacy of the selected coordinates and resulting PESs has been demonstrated in detail in our previous work[36] and the main reasons are shortly summarized in the Supporting Information, section I.

Static X-ray Absorption Spectra. In this section, the static XAS of the magnesium and nitrogen K-edge at the ground state minimum geometry are discussed. The theoretical static spectrum allows assigning the peaks to the individual transitions and the actual geometry or molecular structure and identifying suitable peaks to follow the dynamics. An overview of the excitations of the most intense peaks for the static XAS at the magnesium, as well as the nitrogen K-edge, can be found in Tables S1 and S2. The calculated spectrum reproduces the main spectral features that are found in experimental data[19] (see Figure S2). The theoretical XAS was thereby shifted by 15.6 eV toward lower energies. To be able to experimentally observe the ultrafast population transfer between Q_x and Q_y, it is important to find characteristic signals for these states that are not overlapping with signals of other states or show at least a significant difference in intensity. Especially, peaks toward lower energies are crucial for experimental observability, as peaks at higher energies might be obscured by the more intense ionization bands and Rydberg series. From Figure 2, it is evident that for the magnesium K-edge, the signals of the three states mainly exhibit a difference in intensity, whereas for the nitrogen K-edge, they are separated in energy.

In the case of the magnesium K-edge, the population transfer from the higher lying Q_x (green) to Q_y (blue) can be detected by a significant decrease in intensity of the signal at 1324.0 eV accompanied by a shift of 1.5 eV toward higher energies. The ground-state signals (red) are present only at higher energies, so that the described peaks should not be affected by the ground-state bleach. For the nitrogen K-edge characteristic signals for the Q-band are the signals at 385.8 eV (Q_x, green) and at 387.9 eV (Q_y, blue). All of the mentioned peaks are well separated in energy. This is partially due to the better experimental resolution power at this edge, which has been taken into account in the broadening of the simulated XAS. As was the case for the magnesium K-edge, the signals of the ground state lie at higher energies, so that the ground-state bleach should not interfere with the observation of the population transfer between Q_x and Q_y.

Time-Resolved X-ray Absorption Spectra. To obtain the transient spectra, the static XAS of each grid point is weighted with the corresponding time-dependent population and overlap terms as described in eqs 4 and 5. Unless specified otherwise, all spectra include both nuclear wavepacket dynamics as well as the electronic coherence.

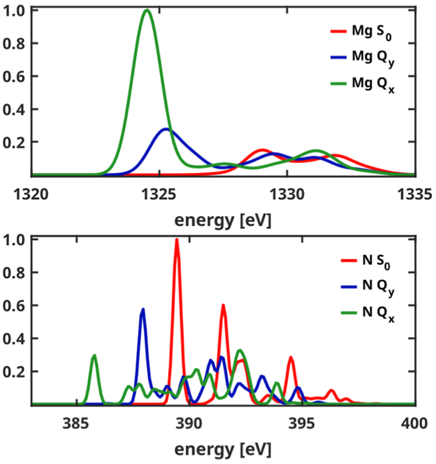

Figure 2. XAS at the ground-state minimum geometry for the magnesium (top) and nitrogen K-edge (bottom). The XAS are each normalized to the overall maximum of all three states. No energy shift was applied. Calculated spectrum broadened using an overall Gaussian convolution with $\sigma = 0.565$ eV for the magnesium edge and $\sigma = 0.170$ eV for the nitrogen edge. This corresponds to an experimental resolving power ($E/\Delta E$) equal to 1000.

First, we simulated time-resolved XAS assuming a delta pulse excitation into the second excited state Q_x, i.e., the wavepacket propagation starts with 100% of the population in this state. The temporal evolution of the population, depicted in Figure 3b, shows a constant, ultrafast population transfer between Q_x and Q_y. Our aim was to identify signals in the transient XAS (Figure 3a) by which this oscillatory behavior can be tracked. Therefore, we separated the signals coming from Q_y and Q_x shown in Figure 3c,d, while the XAS in Figure 3a includes signals from both Q_x and Q_y. In this simulation, we did not include signals of the ground state, which would be at 1329.1 and 1332.3 eV. The ground state signals do not interfere with the characteristic signals of Q_x and Q_y, as they have different energies. The effect of the ground state will be discussed later in context of an explicitly simulated pump pulse. All of the XAS are normalized with respect to the overall maximum of the combined XAS (Figure 3a).

In general, the signals in the Q_x spectrum are more intense than those of Q_y. The population transfer between the two states was followed by tracking the 1324.0 eV signal, characteristic for Q_x and the 1322.5 eV signal for Q_y, which are alternating in the combined XAS. The signals of Q_y at 1325.3 eV are less suited as they are partially obscured by the Q_x features. The situation for the nitrogen K-edge is very similar (Figure S3). A detailed analysis is given in the Supporting Information, section III.

In a next step, we analyze the influence of the electronic coherence on the time-resolved XAS. In Figure 4a, the difference between the XAS based on the nuclear wavepacket dynamics and the one additionally including the electronic coherence is depicted. The temporal evolution of the normalized mean real part of the wavepacket overlap between the two Q states is given in Figure 4b accompanied by a cut through the difference spectrum at 1324.3 eV.

The difference spectrum shows oscillations in the electronic coherence with a periodicity of about 12 fs. These are in

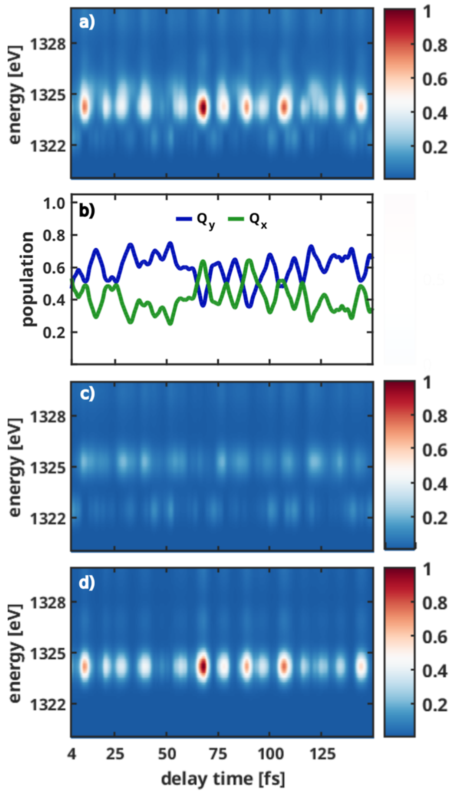

Figure 3. Transient magnesium K-edge XAS including the nuclear wavepacket dynamics and electronic coherence. For (a) all populated states, (c) only the Q_y state, and (d) only the Q_x state. All XAS are normalized to the overall maximum of (a). The temporal evolution of the population is shown in (b).

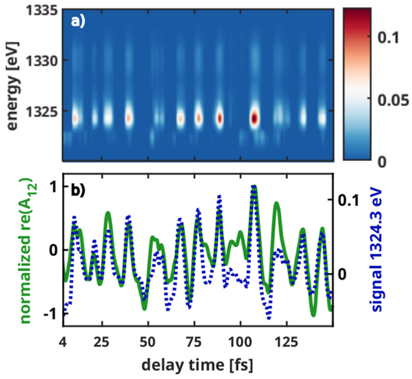

Figure 4. Illustration of the effects of electronic coherence by (a) difference spectrum between the transient magnesium K-edge XAS based on the nuclear wavepacket dynamics and one additionally including the electronic coherence. (b) Normalized mean real part of the wavepacket overlap between Q_y and Q_x (green) averaged over the grid together with a cut (blue) through the difference spectrum at 1324.3 eV.

accordance with the small energy gap between the coupled states and with the dynamics in the wavepacket overlap, A_{12}. The oscillations prevail for the entire simulation time due to the lack of vibrational cooling in the calculation. The maximal value of the electronic coherence amounts to 12% and lies at 107 fs. In Figure 4b, the wavepacket overlap A_{12} (green curve) matches the cut through the difference spectrum (blue curve) well, indicating that A_{12} is the main contributor to the electronic coherence. The remaining discrepancies can be explained by the fact that the wavepacket overlap is averaged over the grid, but for the spectrum, the oscillator strengths and overlap terms of each grid point are combined. As the wavepacket overlap is the main contributor to the electronic coherence, the spectral features are enhanced at points in time where A_{12} is high. For the nitrogen K-edge, the same tendencies can be remarked (see Figure S5) and are discussed in Supporting Information section IV.

For better comparison with the experiment, we included an explicitly simulated excitation pulse in our calculations that pumps population into both Q states, instead of assuming a delta excitation into Q_x. The delta pulse populates all vibrational levels of the target state, whereas an explicit pump pulse only populates an energetically accessible subset. The simulated Gaussian pulse has a fwhm of 30 fs with a maximum field strength of 4.9 × 10^{-3} GV cm^{-1} and a central frequency of 2.43 eV. Due to their closeness in energy, the laser pumps population into both Q states. For the analysis, we separated the excitation pulse-induced dynamics (until 35 fs) and the dynamics after the pulse (from 35 fs onward), by renormalizing the XAS signals in Figure 5. The pump pulse

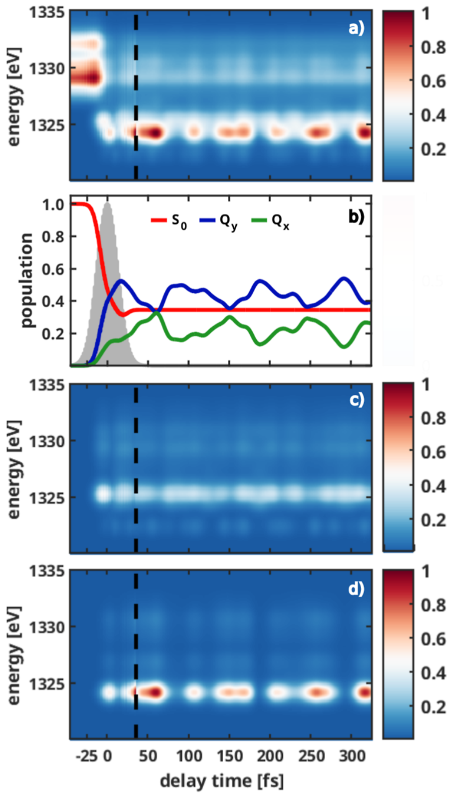

Figure 5. Transient magnesium K-edge XAS for (a) all populated states, (c) only the Q_y state, and (d) only the Q_x state. All XAS are normalized to the overall maximum of (a) for the excitation pulse-induced dynamics (until 35 fs) and the dynamics after the pulse (from 35 fs onward) separately. The temporal evolution of the population is shown in (b) with the normalized pump pulse in gray.

excites about 65% of the population, while the rest remains in the ground state (Figure 5b). As before, the excited-state populations oscillate strongly such that Q_x and Q_y are populated equally every 100 fs. In general, the dynamics are the same when applying a delta excitation or explicitly simulating the pump pulse. However, the time scale is slower with the explicit pulse, as fewer vibrational levels are occupied. In the case of chlorophyll, several vibrational levels of Q_x and Q_y are nearly degenerate, as we could show in our previous paper.[36] If more of these vibrational levels are occupied, as in a hypothetical delta pulse excitation, then the population transfer within the Q-band becomes faster.

The transient XAS in Figure 5a is based on both nuclear and electronic wavepacket dynamics and includes signals from all three states, S_0, Q_y, and Q_x. At the beginning of the simulation, the spectrum is dominated by the signals of the ground state above 1328.5 eV. These signals become less intense, as population is pumped to the excited states, but remain present throughout the whole simulation time. As soon as the population is excited to the Q-band, new peaks arise at 1325.4 eV (Q_y) and 1324.2 eV (Q_x). The suggested spectral features to follow the Q_y population occur at a different energy, as in the case of a delta excitation to Q_x, because the different nuclear dynamics also change the relative intensity of the spectral features, as the oscillator strengths are weighted with the populations at each grid point. The spectrum of Q_y in Figure 5c shows signals at around 1322.5 eV, as before. However, they are less suited for the observation of population transfer because they are less pronounced and obscured by Q_x peaks. As initially more population is excited into Q_y, the corresponding signals are visible slightly earlier than those of Q_x. The signals attributed to Q_x are again much more intense than those of the Q_y. The population transfer can be followed most easily by tracking the periodic appearance of the Q_x signals at 1324.2 eV. Alternatively, also the shift in energy between the signals at 1325.4 eV (Q_y) and 1324.2 eV (Q_x) can be used. A comparison between the temporal evolution of the population and the XAS data including all three states (Figure 5a) shows that the signal at 1324.2 eV appears when the Q_x population is at a local maximum. This gives additional proof that this signal is characteristic for Q_x. The fast oscillations visible in the XAS up to 35 fs are due to the electronic coherence created by the pump pulse, discernible by their frequency coinciding with the pulse frequency. A zoomed-in view of these features is shown in Figure S7. This also illustrates, how the simulation of XAS via coupled wavepacket dynamics is one of the few methods available to visualize the influence of an excitation pulse on the electron dynamics, justifying the computational cost for the high-level PESs. In the XAS that does not include the electronic coherence (see Figure S6a), the fast oscillations are not present. The same figure also depicts the difference spectrum between the XAS based on the coupled nuclear and electronic wavepacket dynamics, as well as the normalized mean real part of the wavepacket overlap. As before, the influence of the electronic coherence exhibits oscillations that coincide well with the wavepacket overlap A_{12}.

The XAS for the nitrogen K-edge (Figures S4 and S8) are discussed in Supporting Information sections III and IV. Also, here, a high coincidence of the electronic coherence with the wavepacket overlap can be observed.

■ CONCLUSIONS

We applied a protocol that combines the coupled nuclear and electron dynamics derived with the NEMol approach[58] and XAS on the XMS-CASPT2 level of theory to simulate time-resolved XAS. The spectra are simulated for two situations, one assuming a hypothetical delta excitation into Q_x, and the other one simulating a pump pulse that excites population into both Q states. With the obtained transient XAS at the magnesium and nitrogen K-edge, we could show that it is in principle possible to follow the ultrafast population transfer between Q_x and Q_y and therefore confirm the strong vibrational coupling between these states. This is more easily achieved at the magnesium K-edge, which exhibits fewer and more distinct signals. Here, the population transfer can be followed by tracking the oscillatory appearance of a very intense spectral feature characteristic of Q_x at 1324.0 eV. The Q_y population can, depending on the type of the excitation pulse, be followed via the much less intense signals at 1322.5 eV (delta excitation) or 1325.4 eV (explicit excitation pulse). For the nitrogen K-edge, the situation is more complex, as a higher number of signals with similar intensity is present. However, also for this edge, it is possible to follow the population transfer by tracking either a signal characteristic for Q_x or for Q_y. In the case of an explicitly simulated pump pulse, this could, for example, be achieved using the Q_x signal at 385.8 eV. For both edges, the ground state bleach lies at higher energies and should not interfere with the observation. An analysis of the influence of the electronic coherence on the time-resolved XAS showed that for both edges, it is mainly determined by the wavepacket overlap A_{ij}. A periodic occurrence of the electronic coherence with a similar, relevant influence on the XAS could be observed for both K-edges. With this work, we could show the feasibility of high-level time-resolved XAS including both nuclear dynamics, as well as electronic coherence, for molecules as large as chlorophyll *a*. Our simulations indicate that XAS offers the possibility to verify the strong coupling between Q_x and Q_y via the resulting ultrafast population transfer. For a more precise prediction of concrete experimental XAS, the inclusion of more dimensions, as well as the coupling to environmental modes, would be desirable. The results of this study are promising with respect to the observability of the ultrafast population transfer between Q_x and Q_y, indicating future research in this direction to be worthwhile.

■ ASSOCIATED CONTENT

Data Availability Statement

All data underlying this study are available from the corresponding author upon reasonable request.

Supporting Information

The Supporting Information is available free of charge at https://pubs.acs.org/doi/10.1021/acs.jpcb.4c07787.

> Details on the XAS simulation setup, additional figures and tables, and the analysis of the time-resolved XAS of the nitrogen K-edge (PDF)

■ AUTHOR INFORMATION

Corresponding Author

Lena Bäuml – *Department of Chemistry, LMU Munich, Munich 81377, Germany*; orcid.org/0009-0005-0118-9081; Email: L.Baeuml@campus.lmu.de

Author

Regina de Vivie-Riedle − *Department of Chemistry, LMU Munich, Munich 81377, Germany*; orcid.org/0000-0002-7877-5979

Complete contact information is available at:
https://pubs.acs.org/10.1021/acs.jpcb.4c07787

Notes

The authors declare no competing financial interest.

■ ACKNOWLEDGMENTS

I thank Prof. Dr. Regina de Vivie-Riedle, who sadly passed away on 20 June 2024, for her great contribution in conceptualization and writing of this project and for providing the crucial resources and support. We thank Sebastian Reiter for fruitful discussions. We gratefully acknowledge funding by the Deutsche Forschungsgemeinschaft (DFG, German Research Foundation) through the cluster of excellence e-conversion under Germany's Excellence Strategy (EXC 2089/1-390776260) and through the grant with the number TRR 325−444632635.

■ REFERENCES

(1) Scutelnic, V.; Tsuru, S.; Pápai, M.; Yang, Z.; Epshtein, M.; Xue, T.; Haugen, E.; Kobayashi, Y.; Krylov, A. I.; Møller, K. B.; et al. X-ray transient absorption reveals the $^1A_u(n\pi^*)$ state of pyrazine in electronic relaxation. *Nat. Commun.* **2021**, *12*, 5003.

(2) Rott, F.; Reduzzi, M.; Schnappinger, T.; Kobayashi, Y.; Chang, K. F.; Timmers, H.; Neumark, D. M.; Vivie-Riedle, R. d.; Leone, S. R. Ultrafast Strong-Field Dissociation of Vinyl Bromide: An Attosecond Transient Absorption Spectroscopy and Non-Adiabatic Molecular Dynamics Study. *Struct. Dyn.* **2021**, *8*, 034104.

(3) Lackner, F.; Chatterley, A. S.; Pemmaraju, C. D.; Closser, K. D.; Prendergast, D.; Neumark, D. M.; Leone, S. R.; Gessner, O. Direct Observation of Ring-Opening Dynamics in Strong-Field Ionized Selenophene Using Femtosecond Inner-Shell Absorption Spectroscopy. *J. Chem. Phys.* **2016**, *145*, 234313.

(4) Zinchenko, K. S.; Ardana-Lamas, F.; Seidu, I.; Neville, S. P.; van der Veen, J.; Lanfaloni, V. U.; Schuurman, M. S.; Wörner, H. J. Sub-7-fs Conical-Intersection Dynamics Probed at the Carbon K-edge. *Science* **2021**, *371*, 489−494.

(5) Goulielmakis, E.; Loh, Z.-H.; Wirth, A.; Santra, R.; Rohringer, N.; Yakovlev, V. S.; Zherebtsov, S.; Pfeifer, T.; Azzeer, A. M.; Kling, M. F.; et al. Real-Time Observation of Valence Electron Motion. *Nature* **2010**, *466*, 739−743.

(6) Oliver, T. A. A.; Fleming, G. R. Following Coupled Electronic-Nuclear Motion through Conical Intersections in the Ultrafast Relaxation of β-Apo-8′-Carotenal. *J. Phys. Chem. B* **2015**, *119*, 11428−11441.

(7) Bhattacherjee, A.; Leone, S. R. Ultrafast X-ray Transient Absorption Spectroscopy of Gas-Phase Photochemical Reactions: A New Universal Probe of Photoinduced Molecular Dynamics. *Acc. Chem. Res.* **2018**, *51*, 3203−3211.

(8) Kobayashi, Y.; Chang, K. F.; Zeng, T.; Neumark, D. M.; Leone, S. R. Direct mapping of curve-crossing dynamics in IBr by attosecond transient absorption spectroscopy. *Science* **2019**, *365*, 79−83.

(9) Timmers, H.; Zhu, X.; Li, Z.; Kobayashi, Y.; Sabbar, M.; Hollstein, M.; Reduzzi, M.; Martínez, T. J.; Neumark, D. M.; Leone, S. R. Disentangling Conical Intersection and Coherent Molecular Dynamics in Methyl Bromide with Attosecond Transient Absorption Spectroscopy. *Nat. Commun.* **2019**, *10*, 3133.

(10) Toulson, B. W.; Borgwardt, M.; Wang, H.; Lackner, F.; Chatterley, A. S.; Pemmaraju, C. D.; Neumark, D. M.; Leone, S. R.; Prendergast, D.; Gessner, O. Probing Ultrafast C−Br Bond Fission in the UV Photochemistry of Bromoform with Core-to-Valence Transient Absorption Spectroscopy. *Struct. Dyn.* **2019**, *6*, 054304.

(11) Chang, K. F.; Reduzzi, M.; Wang, H.; Poullain, S. M.; Kobayashi, Y.; Barreau, L.; Prendergast, D.; Neumark, D. M.; Leone, S. R. Revealing Electronic State-Switching at Conical Intersections in Alkyl Iodides by Ultrafast XUV Transient Absorption Spectroscopy. *Nat. Commun.* **2020**, *11*, 4042.

(12) Chang, K. F.; Wang, H.; Poullain, S. M.; Prendergast, D.; Neumark, D. M.; Leone, S. R. Mapping Wave Packet Bifurcation at a Conical Intersection in CH3I by Attosecond XUV Transient Absorption Spectroscopy. *J. Chem. Phys.* **2021**, *154*, 234301.

(13) Yin, Z.; Chang, Y.-P.; Balčiūnas, T.; Shakya, Y.; Djorović, A.; Gaulier, G.; Fazio, G.; Santra, R.; Inhester, L.; Wolf, J.-P.; et al. Femtosecond Proton Transfer in Urea Solutions Probed by X-ray Spectroscopy. *Nature* **2023**, *619*, 749−754.

(14) Wolf, T.; Myhre, R.; Cryan, J.; Coriani, S.; Squibb, R. J.; Battistoni, A.; Berrah, N.; Bostedt, C.; Bucksbaum, P.; Coslovich, G.; et al. Probing ultrafast $\pi\pi^*/n\pi^*$ internal conversion in organic chromophores via K-edge resonant absorption. *Nat. Commun.* **2017**, *8*, 29.

(15) Ryland, E. S.; Lin, M.-F.; Verkamp, M. A.; Zhang, K.; Benke, K.; Carlson, M.; Vura-Weis, J. Tabletop Femtosecond M-edge X-ray Absorption Near-Edge Structure of FeTPPCl: Metalloporphyrin Photophysics from the Perspective of the Metal. *J. Am. Chem. Soc.* **2018**, *140*, 4691−4696.

(16) Hammes-Schiffer, S. Theoretical Perspectives on Non-Born−Oppenheimer Effects in Chemistry. *Philos. Trans. R. Soc., A* **2022**, *380*, 20200377.

(17) Mayer, D.; Lever, F.; Picconi, D.; Metje, J.; Alisauskas, S.; Calegari, F.; Düsterer, S.; Ehlert, C.; Feifel, R.; Niebuhr, M.; et al. Following Excited-State Chemical Shifts in Molecular Ultrafast x-Ray Photoelectron Spectroscopy. *Nat. Commun.* **2022**, *13*, 198.

(18) Chakraborty, P.; Liu, Y.; McClung, S.; Weinacht, T.; Matsika, S. Time Resolved Photoelectron Spectroscopy as a Test of Electronic Structure and Nonadiabatic Dynamics. *J. Phys. Chem. Lett.* **2021**, *12*, 5099−5104.

(19) Witte, K.; Streeck, C.; Mantouvalou, I.; Suchkova, S. A.; Lokstein, H.; Grötzsch, D.; Martyanov, W.; Weser, J.; Kanngießer, B.; Beckhoff, B.; et al. Magnesium K-Edge NEXAFS Spectroscopy of Chlorophyll a in Solution. *J. Phys. Chem. B* **2016**, *120*, 11619−11627.

(20) Legall, H.; Stiel, H.; Beck, M.; Leupold, D.; Gruszecki, W. I.; Lokstein, H. Near Edge X-ray Absorption Fine Structure Spectroscopy (NEXAFS) of Pigment−Protein Complexes: Peridinin−Chlorophyll a Protein (PCP) of Amphidinium Carterae. *J. Biochem. Biophys. Methods* **2007**, *70*, 369−376.

(21) Graczyk, A.; Żurek, J. M.; Paterson, M. J. On the Linear and Non-Linear Electronic Spectroscopy of Chlorophylls: A Computational Study. *Photochem. Photobiol. Sci.* **2013**, *13*, 103−111.

(22) Parusel, A. B. J.; Grimme, S. A Theoretical Study of the Excited States of Chlorophyll a and Pheophytin a. *J. Phys. Chem. B* **2000**, *104*, 5395−5398.

(23) Sirohiwal, A.; Berraud-Pache, R.; Neese, F.; Izsák, R.; Pantazis, D. A. Accurate Computation of the Absorption Spectrum of Chlorophyll a with Pair Natural Orbital Coupled Cluster Methods. *J. Phys. Chem. B* **2020**, *124*, 8761−8771.

(24) Götze, J. P.; Anders, F.; Petry, S.; Witte, J. F.; Lokstein, H. Spectral Characterization of the Main Pigments in the Plant Photosynthetic Apparatus by Theory and Experiment. *Chem. Phys.* **2022**, *559*, 111517.

(25) Reimers, J. R.; Cai, Z.-L.; Kobayashi, R.; Rätsep, M.; Freiberg, A.; Krausz, E. Assignment of the Q -Bands of the Chlorophylls: Coherence Loss via Q x - Q y Mixing. *Sci. Rep.* **2013**, *3*, 2761−2768.

(26) Bricker, W. P.; Shenai, P. M.; Ghosh, A.; Liu, Z.; Enriquez, M. G. M.; Lambrev, P. H.; Tan, H.-S.; Lo, C. S.; Tretiak, S.; Fernandez-Alberti, S.; et al. Non-Radiative Relaxation of Photoexcited Chlorophylls: Theoretical and Experimental Study. *Sci. Rep.* **2015**, *5*, 13625.

(27) Shenai, P. M.; Fernandez-Alberti, S.; Bricker, W. P.; Tretiak, S.; Zhao, Y. Internal Conversion and Vibrational Energy Redistribution in Chlorophyll A. *J. Phys. Chem. B* **2016**, *120*, 49−58.

(28) Fortino, M.; Collini, E.; Bloino, J.; Pedone, A. Unraveling the Internal Conversion Process within the Q-bands of a Chlorophyll-like-System through Surface-Hopping Molecular Dynamics Simulations. *J. Chem. Phys.* **2021**, *154*, 094110.

(29) Houssier, C.; Sauer, K. Circular Dichroism and Magnetic Circular Dichroism of the Chlorophyll and Protochlorophyll Pigments. *J. Am. Chem. Soc.* **1970**, *92*, 779−791.

(30) Weiss, C. The Pi Electron Structure and Absorption Spectra of Chlorophylls in Solution. *J. Mol. Spectrosc.* **1972**, *44*, 37−80.

(31) Avarmaa, R. A.; Rebane, K. K. High-Resolution Optical Spectra of Chlorophyll Molecules. *Spectrochim. Acta, Part A* **1985**, *41*, 1365−1380.

(32) Umetsu, M.; Wang, Z.-Y.; Kobayashi, M.; Nozawa, T. Interaction of Photosynthetic Pigments with Various Organic Solvents: Magnetic Circular Dichroism Approach and Application to Chlorosomes. *Biochim. Biophys. Acta, Bioenerg.* **1999**, *1410*, 19−31.

(33) Anda, A.; Hansen, T.; De Vico, L. Multireference Excitation Energies for Bacteriochlorophylls A within Light Harvesting System 2. *J. Chem. Theory Comput.* **2016**, *12*, 1305−1313.

(34) Anda, A.; Hansen, T.; De Vico, L. Qy and Qx Absorption Bands for Bacteriochlorophyll a Molecules from LH2 and LH3. *J. Phys. Chem. A* **2019**, *123*, 5283−5292.

(35) Zheng, F.; Fernandez-Alberti, S.; Tretiak, S.; Zhao, Y. Photoinduced Intra- and Intermolecular Energy Transfer in Chlorophyll a Dimer. *J. Phys. Chem. B* **2017**, *121*, 5331−5339.

(36) Reiter, S.; Bäuml, L.; Hauer, J.; de Vivie-Riedle, R. Q-Band Relaxation in Chlorophyll: New Insights from Multireference Quantum Dynamics. *Phys. Chem. Chem. Phys.* **2022**, *24*, 27212−27223.

(37) Keil, E.; Kumar, A.; Bäuml, L.; Reiter, S.; Thyrhaug, E.; Moser, S.; Duffy, C. D. P.; de Vivie-Riedle, R.; Hauer, J. Reassessing the role and lifetime of Qx in the energy transfer dynamics of chlorophyll a. *Chem. Sci.* **2025**, *16*, 1684.

(38) Bäuml, L.; Rott, F.; Schnappinger, T.; de Vivie-Riedle, R. Following the Nonadiabatic Ultrafast Dynamics of Uracil via Simulated X-ray Absorption Spectra. *J. Phys. Chem. A* **2023**, *127*, 9787−9796.

(39) Rott, F. Photo initiated molecular processes elucidated by quantum chemistry and theoretical spectroscopy. Ph.D. Thesis, Maximilian Univeristy Munich, Ludwig, 2022.

(40) Cederbaum, L. S.; Domcke, W.; Schirmer, J. Many-Body Theory of Core Holes. *Phys. Rev. A* **1980**, *22*, 206−222.

(41) Barth, A.; Cederbaum, L. S. Many-Body Theory of Core-Valence Excitations. *Phys. Rev. A* **1981**, *23*, 1038−1061.

(42) Josefsson, I.; Kunnus, K.; Schreck, S.; Föhlisch, A.; de Groot, F.; Wernet, P.; Odelius, M. Ab Initio Calculations of X-ray Spectra: Atomic Multiplet and Molecular Orbital Effects in a Multiconfigurational SCF Approach to the L-Edge Spectra of Transition Metal Complexes. *J. Phys. Chem. Lett.* **2012**, *3*, 3565−3570.

(43) Wang, H.; Odelius, M.; Prendergast, D. A Combined Multi-Reference Pump-Probe Simulation Method with Application to XUV Signatures of Ultrafast Methyl Iodide Photodissociation. *J. Chem. Phys.* **2019**, *151*, 124106.

(44) Wernet, P.; Kunnus, K.; Schreck, S.; Quevedo, W.; Kurian, R.; Techert, S.; de Groot, F. M. F.; Odelius, M.; Föhlisch, A. Dissecting Local Atomic and Intermolecular Interactions of Transition-Metal Ions in Solution with Selective X-ray Spectroscopy. *J. Phys. Chem. Lett.* **2012**, *3*, 3448−3453.

(45) Gendron, F.; Moore, B.; Cador, O.; Pointillart, F.; Autschbach, J.; Le Guennic, B. Ab Initio Study of Circular Dichroism and Circularly Polarized Luminescence of Spin-Allowed and Spin-Forbidden Transitions: From Organic Ketones to Lanthanide Complexes. *J. Chem. Theory Comput.* **2019**, *15*, 4140−4155.

(46) Finley, J.; Malmqvist, P.-Å.; Roos, B. O.; Serrano-Andrés, L. The Multi-State CASPT2Method. *Chem. Phys. Lett.* **1998**, *288*, 299−306.

(47) Granovsky, A. A. Extended Multi-Configuration Quasi-Degenerate Perturbation Theory: The New Approach to Multi-State Multi-Reference Perturbation Theory. *J. Chem. Phys.* **2011**, *134*, 214113.

(48) Shiozaki, T.; Győrffy, W.; Celani, P.; Werner, H.-J. Communication: Extended Multi-State Complete Active Space Second-Order Perturbation Theory: Energy and Nuclear Gradients. *J. Chem. Phys.* **2011**, *135*, 081106.

(49) Malmqvist, P.-Å. Calculation of Transition Density Matrices by Nonunitary Orbital Transformations. *Int. J. Quantum Chem.* **1986**, *30*, 479−494.

(50) Malmqvist, P.-Å.; Roos, B. O. The CASSCF State Interaction Method. *Chem. Phys. Lett.* **1989**, *155*, 189−194.

(51) Malmqvist, P.-Å.; Roos, B. O.; Schimmelpfennig, B. The Restricted Active Space (RAS) State Interaction Approach with Spin−Orbit Coupling. *Chem. Phys. Lett.* **2002**, *357*, 230−240.

(52) Geppert, D.; von den Hoff, P.; de Vivie-Riedle, R. Electron Dynamics in Molecules: A New Combination of Nuclear Quantum Dynamics and Electronic Structure Theory. *J. Phys. B: At., Mol. Opt. Phys.* **2008**, *41*, 074006.

(53) von den Hoff, P.; Znakovskaya, I.; Kling, M. F.; de Vivie-Riedle, R. Attosecond Control of the Dissociative Ionization via Electron Localization: A Comparison between D2 and CO. *Chem. Phys.* **2009**, *366*, 139−147.

(54) Znakovskaya, I.; von den Hoff, P.; Zherebtsov, S.; Wirth, A.; Herrwerth, O.; Vrakking, M. J. J.; de Vivie-Riedle, R.; Kling, M. F. Attosecond Control of Electron Dynamics in Carbon Monoxide. *Phys. Rev. Lett.* **2009**, *103*, 103002.

(55) Kling, M. F.; von den Hoff, P.; Znakovskaya, I.; de Vivie-Riedle, R. Sub-Femtosecond Control of Molecular Reactions via Tailoring the Electric Field of Light. *Phys. Chem. Chem. Phys.* **2013**, *15*, 9448−9467.

(56) Schnappinger, T.; de Vivie-Riedle, R. Coupled Nuclear and Electron Dynamics in the Vicinity of a Conical Intersection. *J. Chem. Phys.* **2021**, *154*, 134306.

(57) Bäuml, L.; Schnappinger, T.; Kling, M. F.; de Vivie-Riedle, R. Photo-Induced Coupled Nuclear and Electron Dynamics in the Nucleobase Uracil. *Front. Phys.* **2021**, *9*, 674573.

(58) Bäuml, L.; Schnappinger, T.; de Vivie-Riedle, R. *NEMol.: Nuclear and Electron dynamics in Molecular systems*; Zenodo, 2024.

(59) Shi, Y.; Shiu, Y. J.; Su, C.; Lin, S. H.; Han, K.-L. Transient Absorption of the Chlorophyll a in Ethanol. *Chin. J. Chem. Phys.* **2006**, *19*, 6−10.

(60) Martinsson, P.; Oksanen, J. A. I.; Hilgendorff, M.; Hynninen, P. H.; Sundström, V.; Åkesson, E. Dynamics of Ground and Excited State Chlorophyll *a* Molecules in Pyridine Solution Probed by Femtosecond Transient Absorption Spectroscopy. *Chem. Phys. Lett.* **1999**, *309*, 386−394.

(61) Oksanen, J. A. I.; Martinsson, P.; Åkesson, E.; Hynninen, P. H.; Sundström, V. Transient Hole Burning and Solvation Dynamics of Chlorophyll b Monomers in Various Solvent Environments. *J. Phys. Chem. A* **1998**, *102*, 4328−4336.

(62) Petropoulos, V.; Rukin, P. S.; Quintela, F.; Russo, M.; Moretti, L.; Moore, A.; Moore, T.; Gust, D.; Prezzi, D.; Scholes, G. D.; et al. Vibronic Coupling Drives the Ultrafast Internal Conversion in a Functionalized Free-Base Porphyrin. *J. Phys. Chem. Lett.* **2024**, *15*, 4461−4467.

(63) Zobel, J. P.; Widmark, P.-O.; Veryazov, V. The ANO-R Basis Set. *J. Chem. Theory Comput.* **2020**, *16*, 278−294.

(64) Zobel, J. P.; Widmark, P.-O.; Veryazov, V. Correction to "The ANO-R Basis Set. *J. Chem. Theory Comput.* **2021**, *17*, 3233−3234.

(65) Roos, B. O.; Veryazov, V.; Widmark, P.-O. Relativistic atomic natural orbital type basis sets for the alkaline and alkaline-earth atoms applied to the ground-state potentials for the corresponding dimers. *Theor. Chem. Acc.* **2004**, *111*, 345−351.

(66) Roos, B. O.; Lindh, R.; Malmqvist, P.-Å.; Veryazov, V.; Widmark, P.-O. Main group atoms and dimers studied with a new relativistic ANO basis set. *J. Phys. Chem. A* **2004**, *108*, 2851−2858.

(67) Roos, B. O.; Lindh, R.; Malmqvist, P.-Å.; Veryazov, V.; Widmark, P.-O. New relativistic ANO basis sets for transition metal atoms. *J. Phys. Chem. A* **2005**, *109*, 6575−6579.

(68) Roos, B. O.; Lindh, R.; Malmqvist, P.-Å.; Veryazov, V.; Widmark, P.-O. New relativistic ANO basis sets for actinide atoms. *Chem. Phys. Lett.* **2005**, *409*, 295−299.

(69) Roos, B. O.; Lindh, R.; Malmqvist, P.-Å.; Veryazov, V.; Widmark, P.-O.; Borin, A. C. New relativistic atomic natural orbital basis sets for lanthanide atoms with applications to the Ce diatom and LuF3. *J. Phys. Chem. A* **2008**, *112*, 11431−11435.

(70) Fdez Galván, I.; Vacher, M.; Alavi, A.; Angeli, C.; Aquilante, F.; Autschbach, J.; Bao, J. J.; Bokarev, S. I.; Bogdanov, N. A.; Carlson, R. K.; et al. OpenMolcas: From Source Code to Insight. *J. Chem. Theory Comput.* **2019**, *15*, 5925−5964.

(71) Aquilante, F.; Autschbach, J.; Baiardi, A.; Battaglia, S.; Borin, V. A.; Chibotaru, L. F.; Conti, I.; De Vico, L.; Delcey, M.; Fdez Galván, I.; et al. Modern quantum chemistry with [Open]Molcas. *J. Chem. Phys.* **2020**, *152*, 214117.

4

Summary and Outlook

This thesis describes the way from simulating the coupled nuclear and electron dynamics with the NEMol approach to the observation of this coupled dynamics and the corresponding electronic coherence via time-resolved XAS. The relevant methods and workflows have first been developed for the nucleobase uracil, which is a relatively small molecule with 12 atoms. They have subsequently been extended to a quite realistic model of the natural pigment chlorophyll *a*, of 82 atoms.

In the first chapter an extended version of the NEMol approach for the simulation of the coupled nuclear and electron dynamics is derived and applied to the nucleobase uracil in the gas phase. This improved ansatz is called the NEMol-grid version. In the NEMol-grid ansatz the nuclear coordinate space is split up into segments for each of which the coupled one-electron-density is determined. Summation of the partial densities of these segments results in the total electron density coupled to multiple grid points. In the original NEMol approach only one geometry per time step is used to determine the coupled density. Therefore, this approach only works well with very localized nuclear wavepackets. With the NEMol-grid version it is now possible to treat delocalized wavepackets, which are a common feature. Additionally, a simplification, the 1e-2o picture, was derived, which describes the state specific and transition electron density via spin orbitals. The 1e-2o approximation is applicable when the process of interest can be described by the transition of one electron between two orbitals. Through simulations of the coupled dynamics of uracil with the NEMol-grid ansatz it was found, that upon excitation the wavepacket first oscillates between the FC region and the S_2 minimum, before more and more parts reach the CoIn seam and relax to the S_1. The delocalized nature of the wavepacket was found to cause a seemingly long-lived electronic coherence. This very delocalized wavepacket would not have been described adequately with the original NEMol approach. However, it was found that the NEMol-grid method, both in the density, as well as in the 1e-2o picture, works well.

In the second chapter the NEMol-grid approach was used to investigate the ultrafast relaxation dynamics of chlorophyll a in the gas phase. When studying the Q-band relaxation, the Q_y and Q_x were found to be coupled throughout the entire PES without an accessible CoIn. The two states were close in energy with vibrational energy levels being nearly degenerate between Q_y and Q_x. Upon excitation into one of the states there is an ultrafast population transfer to the other Q-state and a subsequent oscillation of the population. The excitation into Q_y is favoured, due to the small oscillator strength of Q_x. The PES of all excited states as well as of the ground state are nearly harmonic and only shifted in energy without spatial displacement. Additionally, the relaxation after excitation into the B-band both from a theoretical and an experimental point of view was studied. The simulations focused on the population transfer between B_x and B_y, as well as the ensuing relaxation to the Q-band. Again the PES of the different states were only shifted in energy without spatial displacement and did not exhibit a CoIn in an accessible area. After excitation into the B-band (mainly into the energetically higher B_y) at first an ultrafast population transfer to B_x and a subsequent relaxation to the Q-band was observed. The theoretical results suggested, that the $B \rightarrow Q$ relaxation mostly happens via Q_x. The relaxation dynamics of chlorophyll is reported in literature to exhibit a strong solvent dependence. Different possibilities to include environmental effects into the conducted simulations are presented at the end of the second chapter. Two of the methods are also discussed in the appendix A in more detail. There, results for the inclusion of explicit solvent molecules, exemplarily using ethanol, are presented. Additionally, a mixed QD/MD approach is described together with the necessary details for its application to chlorophyll. For a systematic analysis of the solvent effect the QD/MD approach could be applied to various solvents to compare their respective influence on the gas phase dynamics. Furthermore, all studies of this thesis were conducted using 2D PESs, which leads to artificially long oscillations between the states due to missing dephasing effects. The NEMol approach itself is not limited to two dimensions, but could also be combined with methods such as AIMS [178, 179] or MCTDH [180–182] to treat small molecules in full dimensionality.

The last chapter discusses the possibility of observing the coupled nuclear and electron dynamics with time-resolved XAS. To this end, a workflow was derived that combines coupled dynamics obtained with NEMol and XAS calculated at the XMS-CASPT2 level of theory. With the resulting transient XAS it is possible to follow the nuclear wavepacket dynamics and to qualitatively determine the influence of the electronic coherence on the spectra. The workflow was first derived to study the nuclear wavepacket dynamics of uracil. With the XAS it was possible to follow the oscillatory behaviour of the wavepacket on the PES. The second study focused on the coupled dynamics of the chlorophyll a Q-band. Therefore, the workflow was modified to work also for significantly larger molecules. In the transient XAS oscillating signals of the Q_y and Q_x were observed, corroborating the coupling between these states. The crucial factor for a large electronic coherence was found to be the overlap of the nuclear wavepackets on the different electronic states, which can be preserved over time under certain conditions, like present for chlorophyll. The influence of the electronic coherence was largest for the excitation pulse induced dynamics of uracil, as the wavepacket is very localized and the coupling created by the pulse is strong. In the chlorophyll case the electronic coherence was considerably smaller, but still much larger than for the CoIn induced dynamics of uracil. In the chlorophyll case the nuclear wavepacket is quite localised, offering good chance for wavepacket overlap, but the couplings are not as high as for, e.g., a CoIn. The passage through the CoIn in the uracil case exhibits the smallest influence of the electronic coherence, as the wavepacket is quite delocalized, limiting the possible overlap. However, in all cases a non-negligible influence of the coherence on the XAS could be detected, which is especially interesting, as most other methods for the simulation of XAS do not include the electronic coherence whereas it is always present in experiments. To get even closer to a fully realistic XAS the NEMol approach could be extended to cover more degrees of freedom or include effects of a complex environment. As the measurement of XAS in liquid beams is becoming more common, the influence of the solvent motion on the spectra is of interest. Additionally, it would be valuable to simulate the interaction of a pump pulse of given intensity with the molecule in such a way as to obtain the resulting populated states and possible fragmentation or ionization products. A great difficulty in the interpretation of experimental spectra with the help of theory is often the lack of information on all involved species, that contribute to the XAS. Nevertheless, the proposed combination of XAS with NEMol can aid in obtaining a more realistic transient XAS and help in understanding potential causes of discrepancies of simulated and experimental XAS.

This work combines the generalisation of the NEMol approach, that now also accurately describes the coupled nuclear and electron dynamics for systems with delocalised nuclear wavepackets with the simulation of time-resolved XAS at the XMS-CASPT2 level of theory to follow the coupled dynamics and qualitatively determine the influence of the electronic coherence on the spectra. These theoretical advances offer new opportunities for the interpretation of experimental studies, but may also help to initiate new experimental works. The developed methods and workflows of this thesis represent a step towards a more accurate description of related experimental data.

A

Appendix for the Quantum Dynamics of Chlorophyll *a* in Ethanol

In chapter 2 the quantum dynamics of chlorophyll *a* was studied in the gas phase to obtain a deeper insight into the ultrafast relaxation dynamics of the Q- and B-band. There are various ways to include solvent effects. One is the inclusion of explicit solvent molecules. The results of such a simulation, exemplarily performed with chlorophyll and two coordinating ethanol molecules at the XMS-CASPT2 level of theory is discussed in section A.1. Another, more evolved possibility is a mixed quantum and molecular dynamics (QD/MD) approach. In section A.2 an adapted version of the QD/MD ansatz, that was already successfully employed for a study on the nucleobase uracil [100] is explained. Information on the coordinate selection, the quantum and molecular dynamics simulations can be found in sections A.3, A.4, and A.5, respectively.

A.1 Dynamics Including Explicit Solvent Molecules

For the simulations with explicit solvent molecules, the ones in direct vicinity to chlorophyll have been chosen. From an analysis of the MD simulations presented in section A.5 it resulted that with ethanol as solvent there are only two solvent molecules found in a radius of 3 Å around the central magnesium atom of chlorophyll. The calculation of PESs at the XMS-CASPT2 level of theory is still feasible when chlorophyll together with these two ethanol molecules is considered. The quantum dynamics simulations were performed on 2D PESs. Details on the coordinate selection are given in section A.3. The coordinates take into account not only the chlorophyll displacement, but also that of the solvent. This means, that the solvent is not static throughout the PES, but varies for each grid point.

Cuts through the two coordinates, that span the PESs, reveal, that the potentials are rather harmonic (see Figure A.1). In both coordinates the potentials of the first two excited states lie close together in energy. In the case of the principal component 0, the Q_y and

Q_x even cross each other. This crossing point, however, is not energetically accessible. Additionally, it can be observed, that the minima of the different states are slightly shifted with respect to each other. In full dimensional simulations of chlorophyll in methanol [111] it was observed, that the potentials in solvent were lying closer together in energy than in the gas phase.

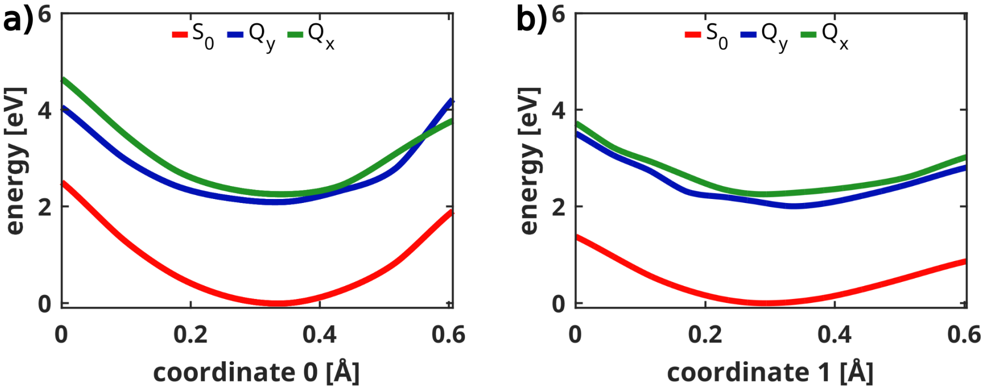

Figure A.1: 1D cuts through the coordinates that span the 2D PES of the simulation with explicit solvent.

The NACs reveal, that for one dimension (Figure A.2a) the NACs are spread over large parts of the coordinate space, whereas for the other dimension (Figure A.2b) the highest NACs are located outside the centre of the PES. The nuclear wavepacket is mainly located at the centre throughout the whole simulation time.

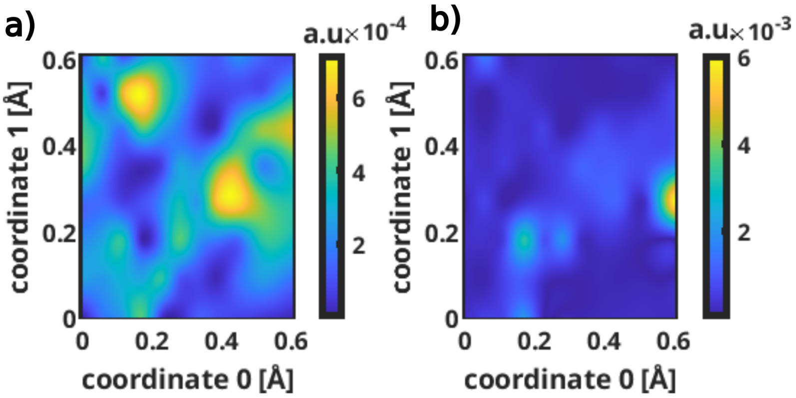

Figure A.2: NACs for the simulation with explicit solvent.

To evaluate the solvent effect of the two closest ethanol molecules, a quantum dynamics simulation was performed on the obtained PESs. Therefore, a delta pulse was applied to excite the wavepacket into the second excited state, Q_x. The resulting temporal evolution of the population is depicted in Figure A.3.

There, it can be seen, that during the first few femtoseconds an ultrafast population transfer between Q_x and Q_y takes place. The point of equal population is reached at 6 fs. Afterwards, an oscillatory behaviour of the population is observed, as it is constantly transferred between the two Q-states. As the calculations are performed on 2D PESs

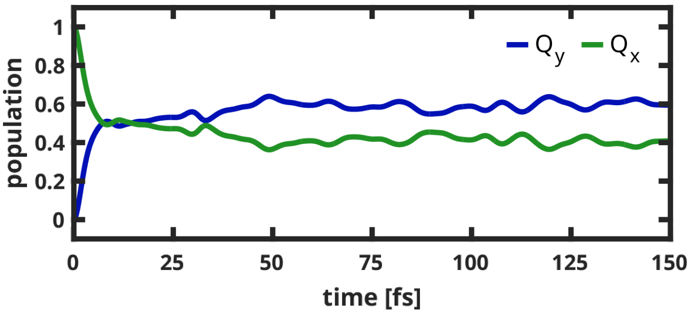

Figure A.3: Temporal evolution of the population after delta pulse excitation into Q_x for the simulation with explicit solvent.

and no loss of energy due to environmental effects or dephasing is taken into account, the oscillations will continue even at long time scales. In literature different time scales for the cooling effects are reported, with the majority lying around 3 ps [118, 183, 184]. Therefore, the analysis is limited to the initial dynamics. In the present case a simulation time of 150 fs was chosen. From the quantum dynamics simulations with its ultrafast population transfer and oscillatory behaviour of the population, as well as from the cuts through the PESs it can be deduced, that there is coupling between Q_y and Q_x when two explicit ethanol molecules are considered as solvent.

A direct comparison with the results of the gas phase calculations of the Q-band presented in chapter 2 is not possible. Both, the coordinate selection and the construction of the G-matrix differ between the two simulations. For the gas phase the normal modes with the highest overlap with the NAC vector at the optimised Q_y geometry, which represents the centre of the PES, were chosen. The method of choice for the coordinate selection of the calculations in ethanol, which is described in section A.3, differs significantly from that approach. For the gas phase calculation the G-matrix elements were constant over the whole PES, while they differ for each grid point in the solvent simulation. The construction of the G-matrix with solvent is described in section A.4.

A.2 QD/MD Approach for Environmental Influence

For a more complete inclusion of the environmental effects a QD/MD approach can be applied. Here, the system is divided into two parts, one including the molecule and explicit solvent molecules and the other one being composed of the solvent box. The general outline of the QD/MD approach is visualized in Figure 2.3 in chapter 2. There the meaning of the terms *molecular region* and *solvent region*, which in the chlorophyll case stand for the isolated molecule plus two explicit solvent molecules and the remaining solvent box, respectively, and *full system* which is the combination of both parts become more apparent. Additionally, the expressions V_{mol} (potential of the molecular region), V_{sol} (potential of the solvent region), and V_{tot} (potential of the full system) are visualized. The QD/MD approach is valid for situations where the molecular dynamics occurs on a much faster time scale than the solvent dynamics, which can therefore be considered as a static environment. As the process of interest is the ultrafast relaxation dynamics of the Q-band, which occurs in the first one to two hundred femtoseconds after laser excitation, this assumption is reasonable.

The *molecular region* consists of the chlorophyll a model without phytyl chain, which was already used in the gas phase calculations presented in section 2.1 of chapter 2. Additionally, the two ethanol molecules coordinated to the central magnesium atom of chlorophyll a were included. All other solvent molecules are located noticeably farther away from the chlorophyll monomer and were placed in the *solvent region*, which was treated at a lower level of theory. For the construction of the coordinate space the two principal vectors, that span the plane given by the optimised geometries for the FC point, the Q_y and Q_x minimum in solvent environment were used. These were determined using the `MonicaMD` package developed in house. In this way the coordinates include solvent motion of the two explicit solvent molecules coordinated to the central magnesium. The consideration of explicit solvent molecules in the *molecular region* and the construction of coordinates, that take their motion into account, present improvements on the QD/MD approach formerly applied to uracil [100]. The NACs and transition dipole moments (TDMs) between the considered states are both determined at the high XMS-CASPT2 level of theory. As a first step a high-level PES (V_{mol}), in our case at the XMS-CASPT2 level of theory, is calculated for the *molecular region.* Here, the PESs of the previous section can be used. In a second step many solvent potentials V_{sol} are calculated at a lower level of theory, here TD-DFT. Therefore, either in parallel or beforehand a MD simulation for the *full system* (chlorophyll in a box of solvent molecules) is performed. The specifics of this MD simulation are given in section A.5. From this MD simulation snapshots are extracted. For each of these, a low-level PES is calculated for the *full system.* As V_{sol} should only include the potential of the solvent, the contributions from the *molecular region* have to be subtracted, so that they are not included in V_{sol}. Therefore, a PES for the *molecular region* at the lower level of theory (here TD-DFT) is determined and subtracted from each of the potentials of the *full system.* In a last step the final PESs (V_{tot}) on which quantum dynamics simulations are performed are obtained by adding V_{sol} to the high-level PES of the *molecular region* (V_{mol}). All of these steps are visualised in Figure 2.3 in chapter 2. Information on the setup of these quantum dynamics simulations may be found in section A.4. With the QD/MD ansatz the interaction between the *molecular* and the *solvent region* is taken into account via electrostatic embedding, as the *solvent region* is also treated with a quantum mechanical method, although at a lower level of theory. Therefore, the polarisation of the classical part of the wavefunction is included. As the MD simulation is conducted in the electronic ground state also the obtained potentials of the environment are rooted on the S_0. These are then added to the PESs of the *molecular region* (V_{mol}) of the excited states. The potentials of the ground and excited states of chlorophyll are nearly nested above each other. As becomes evident from the cuts through the 1D PES shown in Figure A.1 the potentials shift slightly when explicit ethanol molecules are considered. Nevertheless, the relative shifts of the respective minima are small enough to deem it reasonable using the ground state environmental potential V_{sol} in combination with the excited state potential V_{mol}. For each of the selected MD snapshots a PES V_{tot} of the *full system* is constructed in the described manner. Evaluating the relaxation dynamics on all of these V_{tot} in comparison with the gas phase dynamics then gives statistical information of the influence of ethanol on the Q-band dynamics in chlorophyll a.

A.3 Coordinate Selection

The program package `MonicaMD`, developed in house, was used for the selection of coordinates. Here, the optimised geometries of the FC point, the Q_y and Q_x minimum were used. The optimisation was performed at the CAM-B3YP/6-311G*/MM [185–188] level of theory, including a 15 Å solvent shell around the chlorophyll molecule. As coordinates, the vectors that span the plane created by these three geometries, were chosen. The resulting internal coordinates were normalized, meaning that all angles were divided by 180°, all dihedral angles by 360° and all bond lengths by the maximal bond length. As the optimized geometries include solvent atoms, the resulting coordinates not only describe the vibrational motion of chlorophyll, but also that of the solvents around it. This represents an important improvement with respect to the previous QD/MD approach that was applied to uracil [100]. There the Cartesian difference vectors between the FC point and the S_2 minimum and between the FC point and the CoIn were chosen as coordinates. However, the geometries of these three points had not been optimised in solvent environment and the resulting coordinates therefore did not include the solvent motion. The inclusion of solvent distortion into the coordinates enables the simulation of quantum dynamics on PES that were constructed with the molecule of interest and explicit solvent molecules around it.

A.4 Quantum Dynamics Simulation

The propagation of the wavepacket on the PES is achieved by integration of the time-dependent Schrödinger equation according to

$$\chi(t)(t+dt) = e^{(-i\hat{H}dt)}\chi(t) = \hat{U}\chi(t). \tag{A.1}$$

The evolution operator $\hat{U}$ is thereby expanded in a Chebyshev series [189] with a time step of 0.25 a u over a simulation time of 150 fs. The propagation starts in the second excited state Q_x, assuming a delta excitation from the ground state. All quantum dynamics simulations have been conducted with the `QDng` program [81]. The NACs between Q_y and Q_x were obtained at the XMS-CASPT2 level of theory, using `OpenMolcas` [190]. The kinetic energy operator is determined via the G-matrix formalism [191–193]:

$$\hat{T}_q \approx -\frac{\hbar^2}{2m}\sum_{r=1}^{M}\sum_{s=1}^{M}\frac{\partial}{\partial q_r}\left[G_{rs}\frac{\partial}{\partial q_s}\right] \tag{A.2}$$

with the G-Matrix being computed via its inverse elements

$$\left(G^{-1}\right)_{rs} = \sum_{i=1}^{3N} m_i \frac{\partial x_i}{\partial q_r} \frac{\partial x_i}{\partial q_s}, \tag{A.3}$$

meaning that the molecular geometry is narrowly displaced along the coordinates. This is done for all grid points. The final G-matrixes represent the reciprocal masses of the kinetic energy operator.

A.5 Molecular Dynamics Simulation

For the calculation of the potential of the solvent box, snapshots of a MD simulation are extracted. The MD simulations were performed with `Gromacs 2023.2` [194]. A chlorophyll *a* molecule was placed in a cubic box of 10 nm edge length with ethanol as solvent. The force field parameters of the solvent were created with `antechamber 22.0` [195] using GAFF2 [196], whereas those of chlorophyll were taken from the literature [197, 198]. Partial charges were calculated at the HF/6-31G* level of theory with `Gaussian 16` [199] and fitted via restrained electrostatic potential fitting (RESP) [200]. As a first step, the steepest-descent algorithm was used to minimise the energy of the solvated chlorophyll until the maximum force fell below 500 $\mathrm{kJmol^{-1}nm^{-1}}$. For all further calculations the leap-frog integrator with a time step of 2 fs was applied. During the calculations the bonds to hydrogen atoms were constrained with the LINCS algorithm [201] and the short-range electrostatics were determined via Verlet lists [202], applying a cut-off distance of 1.2 nm. For the long-range electrostatics the smooth particle-mesh Ewald (SPME) method [203, 204] was applied with a fourth-order interpolation and a Fourier grid spacing of 0.16 nm. As a second step the system was equilibrated, first using an NVT ensemble (annealing over 50 ps from 10 K to 100 K with subsequent propagation over 50 ps at 100 K using a V-rescale thermostat [205] with a time constant of $\tau_T = 0.1\,\mathrm{ps}$), then with an NPT ensemble in combination with the Berendsen barostat [206] (heated to 300 K in 100 ps with subsequent propagation for 300 ps at constant temperature and pressure with an isotropic reference pressure of 1 bar, a time constant of $\tau_T = 2.5\,\mathrm{ps}$ and an isothermal compressibility of $11.19 \times 10^{-5}\ \mathrm{bar^{-1}}$ [207]) and finally via an NPT ensemble using the Nosé-Hoover thermostat [208, 209] and the Parrinello-Rahman barostat [210, 211] (equilibration over 4 ns with $T = 2.5\,\mathrm{ps}$ and $\tau_P = 10\,\mathrm{ps}$). In a third step the production simulations were conducted for 20 ns with the equilibrated NPT ensembles extracting a total of 2000 snapshots in intervals of 10 ps.

B

Appendix for Following the Coupled Dynamics using X-ray Absorption Spectra

In the following two sections input examples for the calculation of static XAS are given. The inputs for the nucleobase uracil and the general procedure are described in section B.1. The specific changes that were necessary for the significantly larger molecule chlorophyll *a* are discussed together with the respective inputs in section B.2. All calculations were conducted with the program package `OpenMolcas 23.06` [190]. Details on all keywords can be found in the `OpenMolcas` manual.

B.1 Input Examples for Small Molecules

As a first step, a stable active space has to be found. This is often done via a CASSCF calculation, which is not described here. Once an active space is obtained one RASSCF calculation for the valence excitations and one RASSCF calculation for the core excitations is performed. If more than one multiplicity is to be considered additional RASSCF calculations have to be performed. The active space for both core and valence excitations should be identical. Therefore, for both cases the core orbitals that are probed are rotated into the RAS1, which is positioned directly below RAS2. After rotation the orbitals should not be optimised any more, as otherwise the rotation will be reversed. This is achieved with the keyword `CIONly`. To correlate all orbitals during the calculation the keyword `FROZen=0` is used. Otherwise, per default, the deep core orbitals would be frozen and not correlated. In case of the core excitations the `HEXS` keyword is used to force a hole into the RAS1.

Listing B.1: Input for a RASSCF calculation for the valence excitations to obtain an oxygen K-edge XAS of uracil. The core orbitals that will be probed are rotated into the RAS1 to keep the active space continuous.

```
&GATEWAY
    Title= raspt2_s_vale
    Coord= geom.xyz
    Basis= ANO-RCC-VTZP
    Group= NOSYM
    ANGMOM
     0.0 0.0 0.0
    SDIPole
     RICD

&SEWARD

&RASSCF
    FILEorb= cas.RasOrb
    EXPErt
    ALTER= 2
    1 2 22
    1 1 21
    SPIN= 1
    NACTEL= 18 1 0
    INACTIVE= 20
    RAS2= 10
    RAS1= 2
    CIROOT= 6 6 1
    CIONly
    MAXOrb
    0

&CASPT2
    IMAGinary= 0.6
    IPEA= 0.25
    FROZen= 0
    XMULTistate
    ALL
    MAXIter
    500
```

Listing B.2: Input for a RASSCF calculation for the core excitations to obtain an oxygen K-edge XAS of uracil. The core orbitals that are probed are rotated into the RAS1, where a hole is forced with the HEXS keyword.

```
&GATEWAY
    Title= raspt2_s_core
    Coord= geom.xyz
    Basis= ANO-RCC-VTZP
    Group= NOSYM
    ANGMOM
     0.0 0.0 0.0
    SDIPole
     RICD

&SEWARD

&RASSCF
    FILEorb= cas.RasOrb
    EXPErt
    ALTER= 2
    1 2 22
    1 1 21
    SPIN= 1
    NACTEL= 18 1 0
    INACTIVE= 20
    RAS2= 10
    RAS1= 2
    HEXS
    1
    1
    CIROOT= 40 40 1
    CIONly
    MAXOrb
    0

&CASPT2
    IMAGinary= 0.6
    IPEA= 0.25
    FROZen= 0
    XMULTistate
    ALL
    MAXIter
    500
```

With the JobMix files and the XMS-CASPT2 energies of the RASSCF calculations a RASSI calculation is performed. The input is outlined in the following. In the RASSI module the number of roots that were considered for valence and core excitations for each multiplicity have to be stated with the keyword `Nrofjobiphs`. After the `HDIAG` keyword all XMS-CASPT2 energies are listed in the same order in which the JobMix files and `Nrofjobiphs` are given. In this way the overall Hamiltonian is corrected by shifting the Hamilton matrix elements.

Listing B.3: Input for a RASSI calculation to combine core and valence excitations and obtain the oscillator strengths and excitation energies for an oxygen K-edge XAS of uracil.

```
&GATEWAY
    Title= xas
    Coord= geom.xyz
    Basis= ANO-RCC-VTZP
    Group= NOSYM
    ANGMOM
     0.0 0.0 0.0
    SDIPole
     RICD

&SEWARD

>>> COPY raspt2_s_vale.JobMix JOB001
>>> COPY raspt2_s_core.JobMix JOB002
>>> COPY raspt2_t_vale.JobMix JOB003
>>> COPY raspt2_t_core.JobMix JOB004

&RASSI
    Nrofjobiphs= 4 6 40 6 40
    1 2 3 4 5 6
    1 2 ... 40
    1 2 3 4 5 6
    1 2 ... 40
    SPIN
    TRDI
    HDIAG
-414.23791206
-414.08130603
... <all XMS-CASPT2 energies>
```

B.2 Input Examples for Larger Molecules

For the simulation of XAS for the much larger molecule chlorophyll *a* some adaptions of the input were necessary. These are outlined in the following and might also help to make the calculation of XAS of even larger molecules feasible. To limit computational costs different basis sets were chosen for different atoms. If possible one would try to use a basis set with more core functions for the atoms that are probed. In a first step, a stable active space has to be determined using, e.g., a CASSCF calculation. The ensuing RASSCF calculations for the valence and core excitations were then run in parallel for the different roots using the keyword `ONLY` (for syntax specifics see the `OpenMolcas` manual). From these calculations the Hamiltonian effective couplings for each root are obtained. In the case of 6 valence roots one would receive $6 \times 6 = 36$ Hamiltonian effective couplings. To calculate the interaction between all roots these couplings are included in a CASPT2 calculation with the `EFFE` keyword, as illustrated below for the valence and core excitations. To further speed up the calculations the definition of the correlation orbital space in XMS-CASPT2 is restricted with the `AFREeze` keyword, which reduces its size by freezing orbitals that are, e.g., located at peripheral atoms. For chlorophyll orbitals located at the central magnesium atom and the rings surrounding it were considered, while neglecting the hydrogen atoms, methyl groups and chains. The specific parameters were carefully benchmarked so as not to neglect relevant contributions. The JobMix files and XMS-CASPT2 energies of the RASSCF calculations are then again read into a RASSI calculation to obtain the excitation energies and oscillator strengths for the XAS.

Listing B.4: Input for a RASSCF calculation for the valence excitations to obtain a magnesium K-edge XAS of chlorophyll *a*. The core orbitals that will be probed are rotated into the RAS1 to keep the active space continuous.

```
&GATEWAY
  TITLE= raspt2_s_vale_effe
  EXPERT
  RICD
  Basis set
    C.ANO-RCC-VDZP
    ... <all coordinates of carbon atoms>
  End of basis

  Basis set
    H.ANO-RCC-VDZP
    ... <all coordinates of hydrogen atoms>
  End of basis

  Basis set
    Mg.ANO-RO
    ... <all coordinates of magnesium atoms>
  End of basis

  Basis set
```

```
    N.ANO-RCC-VDZP
   ... <all coordinates of nitrogen atoms>
  End of basis

  Basis set
    O.ANO-RCC-VDZP
    ... <all coordinates of oxygen atoms>
  End of basis

&SEWARD
    RELAtivistic
        R02O02

&RASSCF
  FILEorb= cas.RasOrb
  EXPERT
  ALTER=1
  1 163 1
  SPIN= 1
  RASSCF= 1 0
  NACTEL= 8
  INACTIVE= 162
  RAS1= 1
  RAS2= 6
  CIROOT= 6 6 1
  CIONly
  MAXORB
  0

&CASPT2
  IPEAshift= 0.1
  IMAGinary= 0.2
  MAXIter= 500
  XMULTistate
    ALL
  AFREeze
   27 0.05 0.00
    Mg1 C2 C3 C4 C5 N6 C7 C8 C9 C10 N17 C18 C19 C20 C21 N25 C26 C27 C28 C29 N33 C34 C35 C36 C37 C39 C41
  EFFE
    6
    -2.18161321610118E+03
    -9.50812957570344E-03
    ... <all Hamiltonian Effective Couplings
               for 6 states these are 6x6=36>
```

Listing B.5: Input for a RASSCF calculation for the core excitations to obtain a magnesium K-edge XAS of chlorophyll *a*. The core orbitals that are probed are rotated into the RAS1, where a hole is forced with the HEXS keyword.

```
&GATEWAY
  TITLE= raspt2_s_core_effe
  EXPERT
  RICD
  Basis set
    C.ANO-RCC-VDZP
    ... <all coordinates of carbon atoms>
  End of basis

  Basis set
    H.ANO-RCC-VDZP
    ... <all coordinates of hydrogen atoms>
  End of basis

  Basis set
    Mg.ANO-RO
    ... <all coordinates of magnesium atoms>
  End of basis

  Basis set
    N.ANO-RCC-VDZP
    ... <all coordinates of nitrogen atoms>
  End of basis

  Basis set
    O.ANO-RCC-VDZP
    ... <all coordinates of oxygen atoms>
  End of basis

&SEWARD
    RELAtivistic
        R02O02
 
&RASSCF
  FILEorb= cas.RasOrb
  EXPERT
  ALTER=1
  1 163 1
  SPIN= 1
  RASSCF= 1 0
  NACTEL= 8
  INACTIVE= 162
  RAS1= 1
  RAS2= 6
  HEXS
  1
  1
  CIROOT= 40 40 1
```

```
  CIONly
  MAXORB
  0

&CASPT2
  IPEAshift= 0.1
  IMAGinary= 0.2
  MAXIter= 500
  XMULTistate
    ALL
  AFREeze
   27 0.05 0.00
    Mg1 C2 C3 C4 C5 N6 C7 C8 C9 C10 N17 C18 C19 C20 C21 N25 C26 C27 C28 C29 N33 C34 C35 C36 C37 C39 C41
  EFFE
    40
    -2.13283266308447E+03
    -3.52628350969986E-03
    ... <all Hamiltonian Effective Couplings
          for 40 states these are 40x40=1600>
```

List of Abbreviations

1e-2o	One-Electron-Two-Orbital
AIMS	*Ab Initio* Multiple Spawning
CASPT2	Complete Active Space Perturbation Theory
CASSCF	Complete Active Space Self-Consistent Field
CC	Coupled Cluster
CI	Configuration Interaction
CoIn	Conical Intersection
CVS	Core-Valence Separation
DCD-CAS	Dynamic Correlation Dressed Complete Active Space
DFT/MRCI	Density Functional Theory/Multireference Configuration Interaction
DMRG	Density Matrix Renormalization Group
DNA	Deoxyribonucleic Acid
FC	Franck-Condon
GAS	Generalized Active Space Self-Consistent Field
MC-PDFT	Multi-Configurational Pair-Density Functional Theory
MCTDH	Multi-Configuration Time-Dependent Hartree
MD	Molecular Dynamics
NACs	Non-Adiabatic Coupling Elements
NEMol	Coupled Nuclear and Electron Dynamics in Molecules
NEO	Nuclear-Electron Orbital
PES	Potential Energy Surface
PSI	Photosystem I
PSII	Photosystem II
QD/MD	Quantum Dynamics/Molecular Dynamics
RASPT2	Restricted Active Space Perturbation Theory
RASSCF	Restricted Active Space Self-Consistent Field
RASSI	Restricted Active Space State Interaction

RESP	Restrained Electrostatic Potential Fitting
RIXS	Resonant Inelastic X-ray Scattering
RNA	Ribonucleic Acid
SPME	Smooth Particle-Mesh Ewald
TD-DFT	Time-Dependent Density Functional Theory
TDMs	Transition Dipole Moments
TDSE	Time-Dependent Schrödinger Equation
TRPES	Time-Resolved Photoelectron Spectra
UV	Ultraviolet
XAS	X-ray Absorption Spectra
XMS-CASPT2	Extended Multi-State Complete Active Space Perturbation Theory

List of Figures

Bibliography

[1] R. E. Blankenship, *Molecular Mechanisms of Photosynthesis*, John Wiley & Sons, Ltd, Chichester, UK, **2002**.

[2] O. G. Poluektov, S. V. Paschenko, L. M. Utschig, K. V. Lakshmi, M. C. Thurnauer, Bidirectional Electron Transfer in Photosystem I: Direct Evidence from High-Frequency Time-Resolved EPR Spectroscopy, *Journal of the American Chemical Society* **2005**, *127*, 11910–11911.

[3] M. G. Müller, C. Slavov, R. Luthra, K. E. Redding, A. R. Holzwarth, Independent Initiation of Primary Electron Transfer in the Two Branches of the Photosystem I Reaction Center, *Proceedings of the National Academy of Sciences* **2010**, *107*, 4123–4128.

[4] C. E. Crespo-Hernández, B. Cohen, P. M. Hare, B. Kohler, Ultrafast Excited-State Dynamics in Nucleic Acids, *Chemical Reviews* **2004**, *104*, 1977–2020.

[5] C. Canuel, M. Mons, F. Piuzzi, B. Tardivel, I. Dimicoli, M. Elhanine, Excited States Dynamics of DNA and RNA Bases: Characterization of a Stepwise Deactivation Pathway in the Gas Phase, *The Journal of Chemical Physics* **2005**, *122*, 074316.

[6] L. Esposito, A. Banyasz, T. Douki, M. Perron, D. Markovitsi, R. Improta, Effect of C5-Methylation of Cytosine on the Photoreactivity of DNA: A Joint Experimental and Computational Study of TCG Trinucleotides, *Journal of the American Chemical Society* **2014**, *136*, 10838–10841.

[7] T. Yoshizawa, G. Wald, Pre-Lumirhodopsin and the Bleaching of Visual Pigments, *Nature* **1963**, *197*, 1279–1286.

[8] R. Send, D. Sundholm, Stairway to the Conical Intersection: A Computational Study of the Retinal Isomerization, *The Journal of Physical Chemistry A* **2007**, *111*, 8766–8773.

[9] D. Polli, P. Altoè, O. Weingart, K. M. Spillane, C. Manzoni, D. Brida, G. Tomasello, G. Orlandi, P. Kukura, R. A. Mathies, M. Garavelli, G. Cerullo, Conical Intersection Dynamics of the Primary Photoisomerization Event in Vision, *Nature* **2010**, *467*, 440–443.

[10] S. Tommasi, M. F. Denissenko, G. P. Pfeifer, Sunlight Induces Pyrimidine Dimers Preferentially at 5-Methylcytosine Bases, *Cancer Research* **1997**, *57*, 4727–4730.

[11] H. Kang, K. T. Lee, B. Jung, Y. J. Ko, S. K. Kim, Intrinsic Lifetimes of the Excited State of DNA and RNA Bases, *Journal of the American Chemical Society* **2002**, *124*, 12958–12959.

[12] E. M. Arpa, M. M. Brister, S. J. Hoehn, C. E. Crespo-Hernández, I. Corral, On the Origin of the Photostability of DNA and RNA Monomers: Excited State Relaxation Mechanism of the Pyrimidine Chromophore, *The Journal of Physical Chemistry Letters* **2020**, *11*, 5156–5161.

[13] M. A. K. Jansen, A. K. Mattoo, M. Edelman, D1-D2 Protein Degradation in the Chloroplast, *European Journal of Biochemistry* **1999**, *260*, 527–532.

[14] N. Ohnishi, S. I. Allakhverdiev, S. Takahashi, S. Higashi, M. Watanabe, Y. Nishiyama, N. Murata, Two-Step Mechanism of Photodamage to Photosystem II: Step 1 Occurs at the Oxygen-Evolving Complex and Step 2 Occurs at the Photochemical Reaction Center, *Biochemistry* **2005**, *44*, 8494–8499.

[15] Y. Shi, J.-Y. Liu, K.-L. Han, Investigation of the Internal Conversion Time of the Chlorophyll *a* from S3, S2 to S1, *Chemical Physics Letters* **2005**, *410*, 260–263.

[16] W. P. Bricker, P. M. Shenai, A. Ghosh, Z. Liu, M. G. M. Enriquez, P. H. Lambrev, H.-S. Tan, C. S. Lo, S. Tretiak, S. Fernandez-Alberti, Y. Zhao, Non-Radiative Relaxation of Photoexcited Chlorophylls: Theoretical and Experimental Study, *Scientific Reports* **2015**, *5*, 13625.

[17] E. Meneghin, C. Leonardo, A. Volpato, L. Bolzonello, E. Collini, Mechanistic Insight into Internal Conversion Process within Q-bands of Chlorophyll a, *Scientific Reports* **2017**, *7*, 11389.

[18] S. Reiter, F. L. Kiss, J. Hauer, R. de Vivie-Riedle, Thermal Site Energy Fluctuations in Photosystem I: New Insights from MD/QM/MM Calculations, *Chemical Science* **2023**, *14*, 3117–3131.

[19] M. Hentschel, R. Kienberger, C. Spielmann, G. A. Reider, N. Milosevic, T. Brabec, P. Corkum, U. Heinzmann, M. Drescher, F. Krausz, Attosecond Metrology, *Nature* **2001**, *414*, 509–513.

[20] H. Timmers, X. Zhu, Z. Li, Y. Kobayashi, M. Sabbar, M. Hollstein, M. Reduzzi, T. J. Martínez, D. M. Neumark, S. R. Leone, Disentangling Conical Intersection and Coherent Molecular Dynamics in Methyl Bromide with Attosecond Transient Absorption Spectroscopy, *Nature Communications* **2019**, *10*, 3133.

[21] K. F. Chang, M. Reduzzi, H. Wang, S. M. Poullain, Y. Kobayashi, L. Barreau, D. Prendergast, D. M. Neumark, S. R. Leone, Revealing Electronic State-Switching at Conical Intersections in Alkyl Iodides by Ultrafast XUV Transient Absorption Spectroscopy, *Nature Communications* **2020**, *11*, 4042.

[22] K. F. Chang, H. Wang, S. M. Poullain, D. Prendergast, D. M. Neumark, S. R. Leone, Mapping Wave Packet Bifurcation at a Conical Intersection in CH_3I by Attosecond XUV Transient Absorption Spectroscopy, *The Journal of Chemical Physics* **2021**, *154*, 234301.

[23] V. Feyer, O. Plekan, R. Richter, M. Coreno, M. de Simone, K. C. Prince, A. B. Trofimov, I. L. Zaytseva, J. Schirmer, Tautomerism in Cytosine and Uracil: A Theoretical and Experimental X-ray Absorption and Resonant Auger Study, *The Journal of Physical Chemistry A* **2010**, *114*, 10270–10276.

[24] I. Josefsson, K. Kunnus, S. Schreck, A. Föhlisch, F. de Groot, P. Wernet, M. Odelius, Ab Initio Calculations of X-ray Spectra: Atomic Multiplet and Molecular Orbital Effects in a Multiconfigurational SCF Approach to the L-Edge Spectra of Transition Metal Complexes, *The Journal of Physical Chemistry Letters* **2012**, *3*, 3565–3570.

[25] P. Wernet, K. Kunnus, S. Schreck, W. Quevedo, R. Kurian, S. Techert, F. M. F. de Groot, M. Odelius, A. Föhlisch, Dissecting Local Atomic and Intermolecular Interactions of Transition-Metal Ions in Solution with Selective X-ray Spectroscopy, *The Journal of Physical Chemistry Letters* **2012**, *3*, 3448–3453.

[26] K. Atak, S. I. Bokarev, M. Gotz, R. Golnak, K. M. Lange, N. Engel, M. Dantz, E. Suljoti, O. Kühn, E. F. Aziz, Nature of the Chemical Bond of Aqueous Fe^{2+} Probed by Soft X-ray Spectroscopies and Ab Initio Calculations, *The Journal of Physical Chemistry B* **2013**, *117*, 12613–12618.

[27] K. Kunnus, I. Josefsson, S. Schreck, W. Quevedo, P. S. Miedema, S. Techert, F. M. F. de Groot, M. Odelius, P. Wernet, A. Föhlisch, From Ligand Fields to Molecular Orbitals: Probing the Local Valence Electronic Structure of Ni^{2+} in Aqueous Solution with Resonant Inelastic X-ray Scattering, *The Journal of Physical Chemistry B* **2013**, *117*, 16512–16521.

[28] E. Suljoti, R. Garcia-Diez, S. I. Bokarev, K. M. Lange, R. Schoch, B. Dierker, M. Dantz, K. Yamamoto, N. Engel, K. Atak, O. Kühn, M. Bauer, J.-E. Rubensson, E. F. Aziz, Direct Observation of Molecular Orbital Mixing in a Solvated Organometallic Complex, *Angewandte Chemie International Edition* **2013**, *52*, 9841–9844.

[29] N. Engel, S. I. Bokarev, E. Suljoti, R. Garcia-Diez, K. M. Lange, K. Atak, R. Golnak, A. Kothe, M. Dantz, O. Kühn, E. F. Aziz, Chemical Bonding in Aqueous Ferrocyanide: Experimental and Theoretical X-ray Spectroscopic Study, *The Journal of Physical Chemistry B* **2014**, *118*, 1555–1563.

[30] D. Maganas, P. Kristiansen, L.-C. Duda, A. Knop-Gericke, S. DeBeer, R. Schlögl, F. Neese, Combined Experimental and Ab Initio Multireference Configuration Interaction Study of the Resonant Inelastic X-ray Scattering Spectrum of CO_2, *The Journal of Physical Chemistry C* **2014**, *118*, 20163–20175.

[31] S. I. Bokarev, M. Khan, M. K. Abdel-Latif, J. Xiao, R. Hilal, S. G. Aziz, E. F. Aziz, O. Kühn, Unraveling the Electronic Structure of Photocatalytic Manganese Complexes by L-Edge X-ray Spectroscopy, *The Journal of Physical Chemistry C* **2015**, *119*, 19192–19200.

[32] L. Weinhardt, E. Ertan, M. Iannuzzi, M. Weigand, O. Fuchs, M. Bär, M. Blum, J. D. Denlinger, W. Yang, E. Umbach, M. Odelius, C. Heske, Probing Hydrogen Bonding Orbitals: Resonant Inelastic Soft X-ray Scattering of Aqueous NH_3, *Physical Chemistry Chemical Physics* **2015**, *17*, 27145–27153.

[33] P. Wernet, K. Kunnus, I. Josefsson, I. Rajkovic, W. Quevedo, M. Beye, S. Schreck, S. Grübel, M. Scholz, D. Nordlund, W. Zhang, R. W. Hartsock, W. F. Schlotter, J. J. Turner, B. Kennedy, F. Hennies, F. M. F. de Groot, K. J. Gaffney, S. Techert, M. Odelius, A. Föhlisch, Orbital-Specific Mapping of the Ligand Exchange Dynamics of $Fe(CO)_5$ in Solution, *Nature* **2015**, *520*, 78–81.

[34] F. Lackner, A. S. Chatterley, C. D. Pemmaraju, K. D. Closser, D. Prendergast, D. M. Neumark, S. R. Leone, O. Gessner, Direct Observation of Ring-Opening Dynamics in Strong-Field Ionized Selenophene Using Femtosecond Inner-Shell Absorption Spectroscopy, *The Journal of Chemical Physics* **2016**, *145*, 234313.

[35] A. Bhattacherjee, C. D. Pemmaraju, K. Schnorr, A. R. Attar, S. R. Leone, Ultrafast Intersystem Crossing in Acetylacetone via Femtosecond X-ray Transient Absorption at the Carbon K-Edge, *Journal of the American Chemical Society* **2017**, *139*, 16576–16583.

[36] M. Nisoli, P. Decleva, F. Calegari, A. Palacios, F. Martín, Attosecond Electron Dynamics in Molecules, *Chemical Reviews* **2017**, *117*, 10760–10825.

[37] Y. Pertot, C. Schmidt, M. Matthews, A. Chauvet, M. Huppert, V. Svoboda, A. von Conta, A. Tehlar, D. Baykusheva, J.-P. Wolf, H. J. Wörner, Time-Resolved X-ray Absorption Spectroscopy with a Water Window High-Harmonic Source, *Science* **2017**, *355*, 264–267.

[38] T. J. A. Wolf, R. H. Myhre, J. P. Cryan, S. Coriani, R. J. Squibb, A. Battistoni, N. Berrah, C. Bostedt, P. Bucksbaum, G. Coslovich, R. Feifel, K. J. Gaffney, J. Grilj, T. J. Martinez, S. Miyabe, S. P. Moeller, M. Mucke, A. Natan, R. Obaid, T. Osipov, O. Plekan, S. Wang, H. Koch, M. Gühr, Probing Ultrafast $\pi\pi^*/n\pi^*$ Internal Conversion in Organic Chromophores via K-edge Resonant Absorption, *Nature Communications* **2017**, *8*, 29.

[39] B. W. Toulson, M. Borgwardt, H. Wang, F. Lackner, A. S. Chatterley, C. D. Pemmaraju, D. M. Neumark, S. R. Leone, D. Prendergast, O. Gessner, Probing Ultrafast C–Br Bond Fission in the UV Photochemistry of Bromoform with Core-to-Valence Transient Absorption Spectroscopy, *Structural Dynamics* **2019**, *6*, 054304.

[40] F. Rott, M. Reduzzi, T. Schnappinger, Y. Kobayashi, K. F. Chang, H. Timmers, D. M. Neumark, R. de Vivie-Riedle, S. R. Leone, Ultrafast Strong-Field Dissociation of Vinyl Bromide: An Attosecond Transient Absorption Spectroscopy and Non-Adiabatic Molecular Dynamics Study, *Structural Dynamics* **2021**, *8*, 034104.

[41] M. S. Schuurman, V. Blanchet, Time-Resolved Photoelectron Spectroscopy: The Continuing Evolution of a Mature Technique, *Physical Chemistry Chemical Physics* **2022**, *24*, 20012–20024.

[42] J. R. Reimers, Z.-L. Cai, R. Kobayashi, M. Rätsep, A. Freiberg, E. Krausz, Assignment of the Q-Bands of the Chlorophylls: Coherence Loss via Q_x - Q_y Mixing, *Scientific Reports* **2013**, *3*, 2761.

[43] K. C. Kulander, Time-Dependent Hartree-Fock Theory of Multiphoton Ionization: Helium, *Physical Review A* **1987**, *36*, 2726–2738.

[44] E. Runge, E. K. U. Gross, Density-Functional Theory for Time-Dependent Systems, *Physical Review Letters* **1984**, *52*, 997–1000.

[45] T. Klamroth, Laser-Driven Electron Transfer through Metal-Insulator-Metal Contacts: Time-dependent Configuration Interaction Singles Calculations for a Jellium Model, *Physical Review B* **2003**, *68*, 245421.

[46] N. Rohringer, A. Gordon, R. Santra, Configuration-Interaction-Based Time-Dependent Orbital Approach for Ab Initio Treatment of Electronic Dynamics in a Strong Optical Laser Field, *Physical Review A* **2006**, *74*, 043420.

[47] A. S. Skeidsvoll, A. Balbi, H. Koch, Time-Dependent Coupled-Cluster Theory for Ultrafast Transient-Absorption Spectroscopy, *Physical Review A* **2020**, *102*, 023115.

[48] F. D. Vila, J. J. Rehr, J. J. Kas, K. Kowalski, B. Peng, Real-Time Coupled-Cluster Approach for the Cumulant Green's Function, *Journal of Chemical Theory and Computation* **2020**, *16*, 6983–6992.

[49] P. Ehrenfest, Bemerkung über die angenäherte Gültigkeit der klassischen Mechanik innerhalb der Quantenmechanik, *Zeitschrift für Physik* **1927**, *45*, 455–457.

[50] A. McLachlan, A Variational Solution of the Time-Dependent Schrodinger Equation, *Molecular Physics* **1964**, *8*, 39–44.

[51] G. D. Billing, The Semiclassical Coupled States Method, *The Journal of Chemical Physics* **1976**, *65*, 1–6.

[52] H.-D. Meyer, W. H. Miller, A Classical Analog for Electronic Degrees of Freedom in Nonadiabatic Collision Processes, *The Journal of Chemical Physics* **1979**, *70*, 3214–3223.

[53] S.-I. Sawada, A. Nitzan, H. Metiu, Mean-Trajectory Approximation for Charge- and Energy-Transfer Processes at Surfaces, *Physical Review B* **1985**, *32*, 851–867.

[54] A. Ojanperä, V. Havu, L. Lehtovaara, M. Puska, Nonadiabatic Ehrenfest Molecular Dynamics within the Projector Augmented-Wave Method, *The Journal of Chemical Physics* **2012**, *136*, 144103.

[55] J. L. Alonso, A. Castro, P. Echenique, A. Rubio in *Fundamentals of Time-Dependent Density Functional Theory*, (Eds.: M. A. Marques, N. T. Maitra, F. M. Nogueira, E. Gross, A. Rubio), Springer, Berlin, Heidelberg, **2012**, pp. 301–315.

[56] K. Takatsuka, Theory of Molecular Nonadiabatic Electron Dynamics in Condensed Phases, *The Journal of Chemical Physics* **2017**, *147*, 174102.

[57] K. Takatsuka, Nuclear Wavepackets along Quantum Paths in Nonadiabatic Electron Wavepacket Dynamics, *Chemical Physics* **2018**, *515*, 52–59.

[58] D. R. Yarkony, Diabolical Conical Intersections, *Reviews of Modern Physics* **1996**, *68*, 985–1013.

[59] A. D. Bandrauk, S. Chelkowski, H. S. Nguyen, Attosecond localization of electrons in molecules, *International Journal of Quantum Chemistry* **2004**, *100*, 834–844.

[60] Z. M. Jia, Q. Y. Yue, Y. D. Peng, Laser Intensity Effect on the Dissociation of Vibrationally Excited D_{2+} in Intense Fields at 792 and 198 nm, *Journal of Physics B: Atomic Molecular and Optical Physics* **2020**, *53*, 085603.

[61] S. Hammes-Schiffer, Nuclear–Electronic Orbital Methods: Foundations and Prospects, *The Journal of Chemical Physics* **2021**, *155*, 030901.

[62] F. Pavošević, T. Culpitt, S. Hammes-Schiffer, Multicomponent Quantum Chemistry: Integrating Electronic and Nuclear Quantum Effects via the Nuclear–Electronic Orbital Method, *Chemical Reviews* **2020**, *120*, 4222–4253.

[63] A. Kovyrshin, M. Skogh, L. Tornberg, A. Broo, S. Mensa, E. Sahin, B. C. B. Symons, J. Crain, I. Tavernelli, Nonadiabatic Nuclear–Electron Dynamics: A Quantum Computing Approach, *The Journal of Physical Chemistry Letters* **2023**, *14*, 7065–7072.

[64] A. Kovyrshin, M. Skogh, A. Broo, S. Mensa, E. Sahin, J. Crain, I. Tavernelli, A Quantum Computing Implementation of Nuclearelectronic Orbital (NEO) Theory: Toward an Exact Pre-Born–Oppenheimer Formulation of Molecular Quantum Systems, *The Journal of Chemical Physics* **2023**, *158*, 214119.

[65] M. Nest, The Multi-Configuration Electron–Nuclear Dynamics Method, *Chemical Physics Letters* **2009**, *472*, 171–174.

[66] I. S. Ulusoy, M. Nest, The Multi-Configuration Electron-Nuclear Dynamics Method Applied to LiH, *The Journal of Chemical Physics* **2012**, *136*, 054112.

[67] D. V. Shalashilin, Quantum Mechanics with the Basis Set Guided by Ehrenfest Trajectories: Theory and Application to Spin-Boson Model, *The Journal of Chemical Physics* **2009**, *130*, 244101.

[68] V. Pohl, J. C. Tremblay, Adiabatic Electronic Flux Density: A Born-Oppenheimer Broken-Symmetry Ansatz, *Physical Review A* **2016**, *93*, 012504.

[69] R. Matsuzaki, K. Takatsuka, Electronic and Nuclear Flux Analysis on Nonadiabatic Electron Transfer Reaction: A View from Single-Configuration Adiabatic Born–Huang Representation, *Journal of Computational Chemistry* **2019**, *40*, 148–163.

[70] L. S. Cederbaum, Born–Oppenheimer Approximation and beyond for Time-Dependent Electronic Processes, *The Journal of Chemical Physics* **2008**, *128*, 124101.

[71] A. Abedi, N. T. Maitra, E. K. U. Gross, Exact Factorization of the Time-Dependent Electron-Nuclear Wave Function, *Physical Review Letters* **2010**, *105*, 123002.

[72] A. Abedi, N. T. Maitra, E. K. U. Gross, Correlated Electron-Nuclear Dynamics: Exact Factorization of the Molecular Wavefunction, *The Journal of Chemical Physics* **2012**, *137*, 22A530.

[73] Y.-C. Chiang, S. Klaiman, F. Otto, L. S. Cederbaum, The Exact Wavefunction Factorization of a Vibronic Coupling System, *The Journal of Chemical Physics* **2014**, *140*, 054104.

[74] F. Agostini, E. K. U. Gross in *Quantum Chemistry and Dynamics of Excited States*, (Eds.: L. González, R. Lindh), John Wiley & Sons, Ltd, Chichester, UK, **2020**, pp. 531–562.

[75] L. Bäuml, T. Schnappinger, R. de Vivie-Riedle, NEMol: Nuclear and Electron dynamics in Molecular systems, *Zenodo* **2024**, DOI 10.5281/zenodo.10944497.

[76] D. Geppert, P. von den Hoff, R. de Vivie-Riedle, Electron Dynamics in Molecules: A New Combination of Nuclear Quantum Dynamics and Electronic Structure Theory, *Journal of Physics B: Atomic Molecular and Optical Physics* **2008**, *41*, 074006.

[77] P. von den Hoff, I. Znakovskaya, M. F. Kling, R. de Vivie-Riedle, Attosecond Control of the Dissociative Ionization via Electron Localization: A Comparison between D_2 and CO, *Chemical Physics* **2009**, *366*, 139–147.

[78] I. Znakovskaya, P. von den Hoff, S. Zherebtsov, A. Wirth, O. Herrwerth, M. J. J. Vrakking, R. de Vivie-Riedle, M. F. Kling, Attosecond Control of Electron Dynamics in Carbon Monoxide, *Physical Review Letters* **2009**, *103*, 103002.

[79] T. Schnappinger, R. de Vivie-Riedle, Coupled Nuclear and Electron Dynamics in the Vicinity of a Conical Intersection, *The Journal of Chemical Physics* **2021**, *154*, 134306.

[80] L. Bäuml, T. Schnappinger, M. F. Kling, R. de Vivie-Riedle, Photo-Induced Coupled Nuclear and Electron Dynamics in the Nucleobase Uracil, *Frontiers in Physics* **2021**, *9*, 674573.

[81] M. Kowalewski, R. de Vivie-Riedle, QDng: A Grid Based Molecular Quantum Dynamics Package, *Zenodo* **2024**, DOI 10.5281/zenodo.10944497.

[82] S. Reiter, L. Bäuml, J. Hauer, R. de Vivie-Riedle, Q-Band Relaxation in Chlorophyll: New Insights from Multireference Quantum Dynamics, *Physical Chemistry Chemical Physics* **2022**, *24*, 27212–27223.

[83] L. Bäuml, F. Rott, T. Schnappinger, R. de Vivie-Riedle, Following the Nonadiabatic Ultrafast Dynamics of Uracil via Simulated X-ray Absorption Spectra, *The Journal of Physical Chemistry A* **2023**, *127*, 9787–9796.

[84] L. Bäuml, R. de Vivie-Riedle, Coupled Nuclear and Electron Dynamics in Chlorophyll Unraveled by XMS-CASPT2 X-ray Absorption Spectra, *The Journal of Physical Chemistry B* **2025**, *129*, 2159–2167.

[85] O. T. Avery, C. M. MacLeod, M. McCarty, Studies on the Chemical Nature of the Substance Inducing Transformation of Pneumococcal Types : Induction of Transformation by a Desoxyribonucleic Acid Fraction Isolated from Pneumococcus Type III, *Journal of Experimental Medicine* **1944**, *79*, 137–158.

[86] A. D. Hershey, M. Chase, Independent Functions of Viral Protein and Nucleic Acid in Growth of Bacteriophage, *Journal of General Physiology* **1952**, *36*, 39–56.

[87] J. D. Watson, F. H. C. Crick, Genetical Implications of the Structure of Deoxyribonucleic Acid, *Nature* **1953**, *171*, 964–967.

[88] G. Gamow, Possible Relation between Deoxyribonucleic Acid and Protein Structures, *Nature* **1954**, *173*, 318–318.

[89] A. A. Beckstead, Y. Zhang, M. S. de Vries, B. Kohler, Life in the Light: Nucleic Acid Photoproperties as a Legacy of Chemical Evolution, *Physical Chemistry Chemical Physics* **2016**, *18*, 24228–24238.

[90] C. Sagan, Ultraviolet Selection Pressure on the Earliest Organisms, *Journal of Theoretical Biology* **1973**, *39*, 195–200.

[91] C. T. Middleton, K. de La Harpe, C. Su, Y. K. Law, C. E. Crespo-Hernández, B. Kohler, DNA Excited-State Dynamics: From Single Bases to the Double Helix, *Annual Review of Physical Chemistry* **2009**, *60*, 217–239.

[92] G. P. Pfeifer, Y.-H. You, A. Besaratinia, Mutations Induced by Ultraviolet Light, *Mutation Research/Fundamental and Molecular Mechanisms of Mutagenesis* **2005**, *571*, 19–31.

[93] F. R. de Gruijl, Skin Cancer and Solar UV Radiation, *European Journal of Cancer* **1999**, *35*, 2003–2009.

[94] J. Cadet, E. Sage, T. Douki, Ultraviolet Radiation-Mediated Damage to Cellular DNA, *Mutation Research* **2005**, *571*, 3–17.

[95] K. Zhang, F. Wang, Y. Jiang, X. Wang, H. Pan, Z. Sun, H. Sun, J. Xu, J. Chen, New Insights about the Photostability of DNA/RNA Bases: Triplet nπ* State Leads to Effective Intersystem Crossing in Pyrimidinones, *The Journal of Physical Chemistry B* **2021**, *125*, 2042–2049.

[96] S. Ullrich, T. Schultz, M. Z. Zgierski, A. Stolow, Electronic Relaxation Dynamics in DNA and RNA Bases Studied by Time-Resolved Photoelectron Spectroscopy, *Physical Chemistry Chemical Physics* **2004**, *6*, 2796.

[97] Y. He, C. Wu, W. Kong, Decay Pathways of Thymine and Methyl-Substituted Uracil and Thymine in the Gas Phase, *The Journal of Physical Chemistry A* **2003**, *107*, 5145–5148.

[98] H. R. Hudock, B. G. Levine, A. L. Thompson, H. Satzger, D. Townsend, N. Gador, S. Ullrich, A. Stolow, T. J. Martínez, Ab Initio Molecular Dynamics and Time-Resolved Photoelectron Spectroscopy of Electronically Excited Uracil and Thymine, *The Journal of Physical Chemistry A* **2007**, *111*, 8500–8508.

[99] P. M. Hare, C. E. Crespo-Hernández, B. Kohler, Solvent-Dependent Photophysics of 1-Cyclohexyluracil: Ultrafast Branching in the Initial Bright State Leads Nonradiatively to the Electronic Ground State and a Long-Lived $^1\mathrm{n}\pi^*$ State, *The Journal of Physical Chemistry B* **2006**, *110*, 18641–18650.

[100] S. Reiter, D. Keefer, R. de Vivie-Riedle, RNA Environment Is Responsible for Decreased Photostability of Uracil, *Journal of the American Chemical Society* **2018**, *140*, 8714–8720.

[101] T. Gustavsson, Á. Bányász, E. Lazzarotto, D. Markovitsi, G. Scalmani, M. J. Frisch, V. Barone, R. Improta, Singlet Excited-State Behavior of Uracil and Thymine in Aqueous Solution: A Combined Experimental and Computational Study of 11 Uracil Derivatives, *Journal of the American Chemical Society* **2006**, *128*, 607–619.

[102] T. Gustavsson, N. Sarkar, E. Lazzarotto, D. Markovitsi, V. Barone, R. Improta, Solvent Effect on the Singlet Excited-state Dynamics of 5-Fluorouracil in Acetonitrile as Compared with Water, *The Journal of Physical Chemistry B* **2006**, *110*, 12843–12847.

[103] P. Chakraborty, Y. Liu, S. McClung, T. Weinacht, S. Matsika, Time Resolved Photoelectron Spectroscopy as a Test of Electronic Structure and Nonadiabatic Dynamics, *The Journal of Physical Chemistry Letters* **2021**, *12*, 5099–5104.

[104] D. Keefer, T. Schnappinger, R. de Vivie-Riedle, S. Mukamel, Visualizing Conical Intersection Passages via Vibronic Coherence Maps Generated by Stimulated Ultrafast X-ray Raman Signals, *Proceedings of the National Academy of Sciences* **2020**, *117*, 24069–24075.

[105] M. Taniguchi, J. S. Lindsey, Absorption and Fluorescence Spectral Database of Chlorophylls and Analogues, *Photochemistry and Photobiology* **2021**, *97*, 136–165.

[106] L. O. Björn, G. C. Papageorgiou, R. E. Blankenship, Govindjee, A Viewpoint: Why Chlorophyll a?, *Photosynthesis Research* **2009**, *99*, 85–98.

[107] S. M. Keable, A. Kölsch, P. S. Simon, M. Dasgupta, R. Chatterjee, S. K. Subramanian, R. Hussein, M. Ibrahim, I.-S. Kim, I. Bogacz, H. Makita, C. C. Pham, F. D. Fuller, S. Gul, D. Paley, L. Lassalle, K. D. Sutherlin, A. Bhowmick, N. W. Moriarty, I. D. Young, J. P. Blaschke, C. de Lichtenberg, P. Chernev, M. H. Cheah, S. Park, G. Park, J. Kim, S. J. Lee, J. Park, K. Tono, S. Owada, M. S. Hunter, A. Batyuk, R. Oggenfuss, M. Sander, S. Zerdane, D. Ozerov, K. Nass, H. Lemke, R. Mankowsky, A. S. Brewster, J. Messinger, N. K. Sauter, V. K. Yachandra, J. Yano, A. Zouni, J. Kern, Room Temperature XFEL Crystallography Reveals Asymmetry in the Vicinity of the Two Phylloquinones in Photosystem I, *Scientific Reports* **2021**, *11*, 21787.

[108] K. A. Brown, P. W. King, Coupling Biology to Synthetic Nanomaterials for Semi-Artificial Photosynthesis, *Photosynthesis Research* **2020**, *143*, 193–203.

[109] M. Gouterman, Spectra of Porphyrins, *Journal of Molecular Spectroscopy* **1961**, *6*, 138–163.

[110] M. Gouterman, G. H. Wagnière, L. C. Snyder, Spectra of Porphyrins: Part II. Four Orbital Model, *Journal of Molecular Spectroscopy* **1963**, *11*, 108–127.

[111] M. Fortino, E. Collini, J. Bloino, A. Pedone, Unraveling the Internal Conversion Process within the Q-bands of a Chlorophyll-like-System through Surface-Hopping Molecular Dynamics Simulations, *The Journal of Chemical Physics* **2021**, *154*, 094110.

[112] V. Petropoulos, P. S. Rukin, F. Quintela, M. Russo, L. Moretti, A. Moore, T. Moore, D. Gust, D. Prezzi, G. D. Scholes, E. Molinari, G. Cerullo, F. Troiani, C. A. Rozzi, M. Maiuri, Vibronic Coupling Drives the Ultrafast Internal Conversion in a Functionalized Free-Base Porphyrin, *The Journal of Physical Chemistry Letters* **2024**, *15*, 4461–4467.

[113] M. Umetsu, Z.-Y. Wang, M. Kobayashi, T. Nozawa, Interaction of Photosynthetic Pigments with Various Organic Solvents: Magnetic Circular Dichroism Approach and Application to Chlorosomes, *Biochimica et Biophysica Acta (BBA) - Bioenergetics* **1999**, *1410*, 19–31.

[114] M. Gouterman, L. Stryer, Fluorescence Polarization of Some Porphyrins, *The Journal of Chemical Physics* **1962**, *37*, 2260–2266.

[115] C. Weiss, The Pi Electron Structure and Absorption Spectra of Chlorophylls in Solution, *Journal of Molecular Spectroscopy* **1972**, *44*, 37–80.

[116] C. Houssier, K. Sauer, Circular Dichroism and Magnetic Circular Dichroism of the Chlorophyll and Protochlorophyll Pigments, *Journal of the American Chemical Society* **1970**, *92*, 779–791.

[117] R. A. Avarmaa, K. K. Rebane, High-Resolution Optical Spectra of Chlorophyll Molecules, *Spectrochimica Acta Part A: Molecular Spectroscopy* **1985**, *41*, 1365–1380.

[118] Y. Shi, Y. J. Shiu, C. Su, S. H. Lin, K.-l. Han, Transient Absorption of the Chlorophyll a in Ethanol, *Chinese Journal of Chemical Physics* **2006**, *19*, 6–10.

[119] F. Zheng, S. Fernandez-Alberti, S. Tretiak, Y. Zhao, Photoinduced Intra- and Intermolecular Energy Transfer in Chlorophyll a Dimer, *The Journal of Physical Chemistry B* **2017**, *121*, 5331–5339.

[120] J. P. Götze, H. Lokstein, Excitation Energy Transfer between Higher Excited States of Photosynthetic Pigments: 2. Chlorophyll b Is a B Band Excitation Trap, *ACS Omega* **2023**, *8*, 40015–40023.

[121] J. P. Götze, H. Lokstein, Excitation Energy Transfer between Higher Excited States of Photosynthetic Pigments: 1. Carotenoids Intercept and Remove B Band Excitations, *ACS Omega* **2023**, *8*, 40005–40014.

[122] L.-Q. Dong, K. Niu, S.-L. Cong, Theoretical Analysis of Internal Conversion Pathways and Vibrational Relaxation Process of Chlorophyll-a in Ethyl Ether Solvent, *Chemical Physics Letters* **2007**, *440*, 150–154.

[123] P. M. Shenai, S. Fernandez-Alberti, W. P. Bricker, S. Tretiak, Y. Zhao, Internal Conversion and Vibrational Energy Redistribution in Chlorophyll A, *The Journal of Physical Chemistry B* **2016**, *120*, 49–58.

[124] L.-Q. Dong, K. Niu, S.-L. Cong, Theoretical Study of Vibrational Relaxation and Internal Conversion Dynamics of Chlorophyll-a in Ethyl Acetate Solvent in Femtosecond Laser Fields, *Chemical Physics Letters* **2006**, *432*, 286–290.

[125] M. Rätsep, J. Linnanto, A. Freiberg, Mirror Symmetry and Vibrational Structure in Optical Spectra of Chlorophyll a, *The Journal of Chemical Physics* **2009**, *130*, 194501.

[126] T. A. Evans, J. J. Katz, Evidence for 5- and 6-Coordinated Magnesium in Bacteriochlorophyll a from Visible Absorption Spectroscopy, *Biochimica et Biophysica Acta (BBA) - Bioenergetics* **1975**, *396*, 414–426.

[127] R. Moca, S. R. Meech, I. A. Heisler, Two-Dimensional Electronic Spectroscopy of Chlorophyll a: Solvent Dependent Spectral Evolution, *The Journal of Physical Chemistry B* **2015**, *119*, 8623–8630.

[128] I. Renge, K. Mauring, Spectral Shift Mechanisms of Chlorophylls in Liquids and Proteins, *Spectrochimica Acta Part A: Molecular and Biomolecular Spectroscopy* **2013**, *102*, 301–313.

[129] M. Fujiwara, M. Tasumi, Resonance Raman and Infrared Studies on Axial Coordination to Chlorophylls a and b in Vitro, *The Journal of Physical Chemistry* **1986**, *90*, 250–255.

[130] L. Szalay, E. Tombácz, G. S. Singhal, Effect of Solvent on the Absorption Spectra and Stokes' Shift of Absorption and Fluorescence of Chlorophylls, *Acta Physica Academiae Scientiarum Hungaricae* **1974**, *35*, 29–36.

[131] S. Krawczyk, The Effects of Hydrogen Bonding and Coordination Interaction in Visible Absorption and Vibrational Spectra of Chlorophyll a, *Biochimica et Biophysica Acta (BBA) - Bioenergetics* **1989**, *976*, 140–149.

[132] J. P. P. Zauleck, M. T. Peschel, F. Rott, S. Thallmair, R. de Vivie-Riedle, Ultrafast Reactive Quantum Dynamics Coupled to Classical Solvent Dynamics Using an Ehrenfest Approach, *The Journal of Physical Chemistry A* **2018**, *122*, 2849–2857.

[133] F. Santoro, J. A. Green, L. Martinez-Fernandez, J. Cerezo, R. Improta, Quantum and Semiclassical Dynamical Studies of Nonadiabatic Processes in Solution: Achievements and Perspectives, *Physical Chemistry Chemical Physics* **2021**, *23*, 8181–8199.

[134] J. Tomasi, B. Mennucci, R. Cammi, Quantum Mechanical Continuum Solvation Models, *Chemical Reviews* **2005**, *105*, 2999–3094.

[135] J. M. Toldo, M. T. do Casal, E. Ventura, S. A. do Monte, M. Barbatti, Surface Hopping Modeling of Charge and Energy Transfer in Active Environments, *Physical Chemistry Chemical Physics* **2023**, *25*, 8293–8316.

[136] E. Brunk, U. Rothlisberger, Mixed Quantum Mechanical/Molecular Mechanical Molecular Dynamics Simulations of Biological Systems in Ground and Electronically Excited States, *Chemical Reviews* **2015**, *115*, 6217–6263.

[137] M. Bondanza, M. Nottoli, L. Cupellini, F. Lipparini, B. Mennucci, Polarizable Embedding QM/MM: The Future Gold Standard for Complex (Bio)Systems?, *Physical Chemistry Chemical Physics* **2020**, *22*, 14433–14448.

[138] R. L. Fork, C. H. B. Cruz, P. C. Becker, C. V. Shank, Compression of Optical Pulses to Six Femtoseconds by Using Cubic Phase Compensation, *Optics Letters* **1987**, *12*, 483–485.

[139] W. H. Knox, R. L. Fork, M. C. Downer, R. H. Stolen, C. V. Shank, J. A. Valdmanis, Optical Pulse Compression to 8 fs at a 5-kHz Repetition Rate, *Applied Physics Letters* **1985**, *46*, 1120–1121.

[140] D. E. Spence, P. N. Kean, W. Sibbett, 60-fsec Pulse Generation from a Self-Mode-Locked Ti:Sapphire Laser, *Optics Letters* **1991**, *16*, 42–44.

[141] A. Baltuška, T. Udem, M. Uiberacker, M. Hentschel, E. Goulielmakis, C. Gohle, R. Holzwarth, V. S. Yakovlev, A. Scrinzi, T. W. Hänsch, F. Krausz, Attosecond Control of Electronic Processes by Intense Light Fields, *Nature* **2003**, *421*, 611–615.

[142] E. Goulielmakis, Z.-H. Loh, A. Wirth, R. Santra, N. Rohringer, V. S. Yakovlev, S. Zherebtsov, T. Pfeifer, A. M. Azzeer, M. F. Kling, S. R. Leone, F. Krausz, Real-Time Observation of Valence Electron Motion, *Nature* **2010**, *466*, 739–743.

[143] K. S. Zinchenko, F. Ardana-Lamas, I. Seidu, S. P. Neville, J. van der Veen, V. U. Lanfaloni, M. S. Schuurman, H. J. Wörner, Sub-7-Femtosecond Conical-Intersection Dynamics Probed at the Carbon K-edge, *Science* **2021**, *371*, 489–494.

[144] D. Mayer, F. Lever, D. Picconi, J. Metje, S. Alisauskas, F. Calegari, S. Düsterer, C. Ehlert, R. Feifel, M. Niebuhr, B. Manschwetus, M. Kuhlmann, T. Mazza, M. S. Robinson, R. J. Squibb, A. Trabattoni, M. Wallner, P. Saalfrank, T. J. A. Wolf, M. Gühr, Following Excited-State Chemical Shifts in Molecular Ultrafast X-ray Photoelectron Spectroscopy, *Nature Communications* **2022**, *13*, 198.

[145] C. Kleine, M.-O. Winghart, Z.-Y. Zhang, M. Richter, M. Ekimova, S. Eckert, M. J. J. Vrakking, E. T. J. Nibbering, A. Rouzée, E. R. Grant, Electronic State Population Dynamics upon Ultrafast Strong Field Ionization and Fragmentation of Molecular Nitrogen, *Physical Review Letters* **2022**, *129*, 123002.

[146] S. R. Leone, D. M. Neumark, Attosecond Science in Atomic, Molecular, and Condensed Matter Physics, *Faraday Discussions* **2016**, *194*, 15–39.

[147] A. Bhattacherjee, S. R. Leone, Ultrafast X-ray Transient Absorption Spectroscopy of Gas-Phase Photochemical Reactions: A New Universal Probe of Photoinduced Molecular Dynamics, *Accounts of Chemical Research* **2018**, *51*, 3203–3211.

[148] M. Stener, G. Fronzoni, M. de Simone, Time Dependent Density Functional Theory of Core Electrons Excitations, *Chemical Physics Letters* **2003**, *373*, 115–123.

[149] S. Coriani, H. Koch, Communication: X-ray Absorption Spectra and Core-Ionization Potentials within a Core-Valence Separated Coupled Cluster Framework, *The Journal of Chemical Physics* **2015**, *143*, 181103.

[150] L. Gagliardi, D. G. Truhlar, G. Li Manni, R. K. Carlson, C. E. Hoyer, J. L. Bao, Multiconfiguration Pair-Density Functional Theory: A New Way To Treat Strongly Correlated Systems, *Accounts of Chemical Research* **2017**, *50*, 66–73.

[151] M. Guo, E. Källman, L. K. Sørensen, M. G. Delcey, R. V. Pinjari, M. Lundberg, Molecular Orbital Simulations of Metal 1s2p Resonant Inelastic X-ray Scattering, *The Journal of Physical Chemistry A* **2016**, *120*, 5848–5855.

[152] K. Kunnus, W. Zhang, M. G. Delcey, R. V. Pinjari, P. S. Miedema, S. Schreck, W. Quevedo, H. Schröder, A. Föhlisch, K. J. Gaffney, M. Lundberg, M. Odelius, P. Wernet, Viewing the Valence Electronic Structure of Ferric and Ferrous Hexacyanide in Solution from the Fe and Cyanide Perspectives, *The Journal of Physical Chemistry B* **2016**, *120*, 7182–7194.

[153] M. Seel, W. Domcke, Femtosecond Time-resolved Ionization Spectroscopy of Ultrafast Internal-conversion Dynamics in Polyatomic Molecules: Theory and Computational Studies, *The Journal of Chemical Physics* **1991**, *95*, 7806–7822.

[154] Y. Arasaki, K. Takatsuka, K. Wang, V. McKoy, Femtosecond Energy- and Angle-Resolved Photoelectron Spectroscopy, *The Journal of Chemical Physics* **2000**, *112*, 8871–8884.

[155] K. Lopata, B. E. Van Kuiken, M. Khalil, N. Govind, Linear-Response and Real-Time Time-Dependent Density Functional Theory Studies of Core-Level Near-Edge X-Ray Absorption, *Journal of Chemical Theory and Computation* **2012**, *8*, 3284–3292.

[156] L. S. Cederbaum, W. Domcke, J. Schirmer, Many-Body Theory of Core Holes, *Physical Review A* **1980**, *22*, 206–222.

[157] A. Barth, L. S. Cederbaum, Many-Body Theory of Core-Valence Excitations, *Physical Review A* **1981**, *23*, 1038–1061.

[158] R. Faber, S. Coriani, Core–Valence-Separated Coupled-Cluster-Singles-and-Doubles Complex-Polarization-Propagator Approach to X-ray Spectroscopies, *Physical Chemistry Chemical Physics* **2020**, *22*, 2642–2647.

[159] S. R. White, Density-Matrix Algorithms for Quantum Renormalization Groups, *Physical Review B* **1993**, *48*, 10345–10356.

[160] A. Baiardi, M. Reiher, The Density Matrix Renormalization Group in Chemistry and Molecular Physics: Recent Developments and New Challenges, *The Journal of Chemical Physics* **2020**, *152*, 040903.

[161] S. Pathak, L. Lang, F. Neese, A Dynamic Correlation Dressed Complete Active Space Method: Theory, Implementation, and Preliminary Applications, *The Journal of Chemical Physics* **2017**, *147*, 234109.

[162] O. Weser, K. Guther, K. Ghanem, G. Li Manni, Stochastic Generalized Active Space Self-Consistent Field: Theory and Application, *Journal of Chemical Theory and Computation* **2022**, *18*, 251–272.

[163] F. M. Rott, Photo Initiated Molecular Processes Elucidated by Quantum Chemistry and Theoretical Spectroscopy, *Doctoral dissertation*, Ludwig-Maximilians-Universität München, **2022**.

[164] J. Finley, P.-Å. Malmqvist, B. O. Roos, L. Serrano-Andrés, The Multi-State CASPT2 Method, *Chemical Physics Letters* **1998**, *288*, 299–306.

[165] A. A. Granovsky, Extended Multi-Configuration Quasi-Degenerate Perturbation Theory: The New Approach to Multi-State Multi-Reference Perturbation Theory, *The Journal of Chemical Physics* **2011**, *134*, 214113.

[166] T. Shiozaki, W. Győrffy, P. Celani, H.-J. Werner, Communication: Extended Multi-State Complete Active Space Second-Order Perturbation Theory: Energy and Nuclear Gradients, *The Journal of Chemical Physics* **2011**, *135*, 081106.

[167] P. Å. Malmqvist, Calculation of Transition Density Matrices by Nonunitary Orbital Transformations, *International Journal of Quantum Chemistry* **1986**, *30*, 479–494.

[168] P. Å. Malmqvist, B. O. Roos, The CASSCF State Interaction Method, *Chemical Physics Letters* **1989**, *155*, 189–194.

[169] P. Å. Malmqvist, B. O. Roos, B. Schimmelpfennig, The Restricted Active Space (RAS) State Interaction Approach with Spin–Orbit Coupling, *Chemical Physics Letters* **2002**, *357*, 230–240.

[170] M. Guo, E. Källman, R. V. Pinjari, R. C. Couto, L. Kragh Sørensen, R. Lindh, K. Pierloot, M. Lundberg, Fingerprinting Electronic Structure of Heme Iron by Ab Initio Modeling of Metal L-Edge X-ray Absorption Spectra, *Journal of Chemical Theory and Computation* **2019**, *15*, 477–489.

[171] B. N. C. Tenorio, T. Moitra, M. A. C. Nascimento, A. B. Rocha, S. Coriani, Molecular Inner-Shell Photoabsorption/Photoionization Cross Sections at Core-Valence-Separated Coupled Cluster Level: Theory and Examples, *The Journal of Chemical Physics* **2019**, *150*, 224104.

[172] M. L. Vidal, X. Feng, E. Epifanovsky, A. I. Krylov, S. Coriani, New and Efficient Equation-of-Motion Coupled-Cluster Framework for Core-Excited and Core-Ionized States, *Journal of Chemical Theory and Computation* **2019**, *15*, 3117–3133.

[173] H. Wang, M. Odelius, D. Prendergast, A Combined Multi-Reference Pump-Probe Simulation Method with Application to XUV Signatures of Ultrafast Methyl Iodide Photodissociation, *The Journal of Chemical Physics* **2019**, *151*, 124106.

[174] N. H. List, A. L. Dempwolff, A. Dreuw, P. Norman, T. J. Martínez, Probing Competing Relaxation Pathways in Malonaldehyde with Transient X-ray Absorption Spectroscopy, *Chemical Science* **2020**, *11*, 4180–4193.

[175] E. Keil, A. Kumar, L. Bäuml, S. Reiter, E. Thyrhaug, S. Moser, C. D. P. Duffy, R. de Vivie-Riedle, J. Hauer, Reassessing the Role and Lifetime of Q_x in the Energy Transfer Dynamics of Chlorophyll a, *Chemical Science* **2025**, *16*, 1684–1695.

[176] Z. Yin, Y.-P. Chang, T. Balčiūnas, Y. Shakya, A. Djorović, G. Gaulier, G. Fazio, R. Santra, L. Inhester, J.-P. Wolf, H. J. Wörner, Femtosecond Proton Transfer in Urea Solutions Probed by X-ray Spectroscopy, *Nature* **2023**, *619*, 749–754.

[177] E. S. Ryland, M.-F. Lin, M. A. Verkamp, K. Zhang, K. Benke, M. Carlson, J. Vura-Weis, Tabletop Femtosecond M-edge X-ray Absorption Near-Edge Structure of FeTPPCl: Metalloporphyrin Photophysics from the Perspective of the Metal, *Journal of the American Chemical Society* **2018**, *140*, 4691–4696.

[178] M. Ben-Nun, J. Quenneville, T. J. Martínez, Ab Initio Multiple Spawning: Photochemistry from First Principles Quantum Molecular Dynamics, *The Journal of Physical Chemistry A* **2000**, *104*, 5161–5175.

[179] B. F. E. Curchod in *Quantum Chemistry and Dynamics of Excited States*, (Eds.: L. González, R. Lindh), John Wiley & Sons, Ltd, Chichester, UK, **2020**, pp. 435–467.

[180] H.-D. Meyer, U. Manthe, L. S. Cederbaum, The Multi-Configurational Time-Dependent Hartree Approach, *Chemical Physics Letters* **1990**, *165*, 73–78.

[181] H.-D. Meyer, Studying Molecular Quantum Dynamics with the Multiconfiguration Time-Dependent Hartree Method, *WIREs Computational Molecular Science* **2012**, *2*, 351–374.

[182] M. Bonfanti, G. A. Worth, I. Burghardt in *Quantum Chemistry and Dynamics of Excited States*, (Eds.: L. González, R. Lindh), John Wiley & Sons, Ltd, Chichester, UK, **2020**, pp. 383–411.

[183] P. Martinsson, J. A. I. Oksanen, M. Hilgendorff, P. H. Hynninen, V. Sundström, E. Åkesson, Dynamics of Ground and Excited State Chlorophyll a Molecules in Pyridine Solution Probed by Femtosecond Transient Absorption Spectroscopy, *Chemical Physics Letters* **1999**, *309*, 386–394.

[184] J. A. I. Oksanen, P. Martinsson, E. Åkesson, P. H. Hynninen, V. Sundström, Transient Hole Burning and Solvation Dynamics of Chlorophyll b Monomers in Various Solvent Environments, *The Journal of Physical Chemistry A* **1998**, *102*, 4328–4336.

[185] T. Yanai, D. P. Tew, N. C. Handy, A New Hybrid Exchange–Correlation Functional Using the Coulomb-attenuating Method (CAM-B3LYP), *Chemical Physics Letters* **2004**, *393*, 51–57.

[186] A. D. McLean, G. S. Chandler, Contracted Gaussian Basis Sets for Molecular Calculations. I. Second Row Atoms, Z =11–18, *The Journal of Chemical Physics* **1980**, *72*, 5639–5648.

[187] R. Krishnan, J. S. Binkley, R. Seeger, J. A. Pople, Self-Consistent Molecular Orbital Methods. XX. A Basis Set for Correlated Wave Functions, *The Journal of Chemical Physics* **1980**, *72*, 650–654.

[188] M. M. Francl, W. J. Pietro, W. J. Hehre, J. S. Binkley, M. S. Gordon, D. J. DeFrees, J. A. Pople, Self-Consistent Molecular Orbital Methods. XXIII. A Polarization-Type Basis Set for Second-Row Elements, *The Journal of Chemical Physics* **1982**, *77*, 3654–3665.

[189] H. Tal-Ezer, R. Kosloff, An Accurate and Efficient Scheme for Propagating the Time Dependent Schrödinger Equation, *The Journal of Chemical Physics* **1984**, *81*, 3967–3971.

[190] G. Li Manni, I. Fdez. Galván, A. Alavi, F. Aleotti, F. Aquilante, J. Autschbach, D. Avagliano, A. Baiardi, J. J. Bao, S. Battaglia, L. Birnoschi, A. Blanco-González, S. I. Bokarev, R. Broer, R. Cacciari, P. B. Calio, R. K. Carlson, R. Carvalho Couto, L. Cerdán, L. F. Chibotaru, N. F. Chilton, J. R. Church, I. Conti, S. Coriani, J. Cuéllar-Zuquin, R. E. Daoud, N. Dattani, P. Decleva, C. de Graaf, M. G. Delcey, L. De Vico, W. Dobrautz, S. S. Dong, R. Feng, N. Ferré, M. Filatov(Gulak), L. Gagliardi, M. Garavelli, L. González, Y. Guan, M. Guo, M. R. Hennefarth, M. R. Hermes, C. E. Hoyer, M. Huix-Rotllant, V. K. Jaiswal, A. Kaiser, D. S. Kaliakin, M. Khamesian, D. S. King, V. Kochetov, M. Krośnicki, A. A. Kumaar, E. D. Larsson, S. Lehtola, M.-B. Lepetit, H. Lischka, P. López Ríos, M. Lundberg, D. Ma, S. Mai, P. Marquetand, I. C. D. Merritt, F. Montorsi, M. Mörchen, A. Nenov, V. H. A. Nguyen, Y. Nishimoto, M. S. Oakley, M. Olivucci, M. Oppel, D. Padula, R. Pandharkar, Q. M. Phung, F. Plasser, G. Raggi, E. Rebolini, M. Reiher, I. Rivalta, D. Roca-Sanjuán,

T. Romig, A. A. Safari, A. Sánchez-Mansilla, A. M. Sand, I. Schapiro, T. R. Scott, J. Segarra-Martí, F. Segatta, D.-C. Sergentu, P. Sharma, R. Shepard, Y. Shu, J. K. Staab, T. P. Straatsma, L. K. Sørensen, B. N. C. Tenorio, D. G. Truhlar, L. Ungur, M. Vacher, V. Veryazov, T. A. Voß, O. Weser, D. Wu, X. Yang, D. Yarkony, C. Zhou, J. P. Zobel, R. Lindh, The OpenMolcas Web: A Community-Driven Approach to Advancing Computational Chemistry, *Journal of Chemical Theory and Computation* **2023**, *19*, 6933–6991.

[191] B. Podolsky, Quantum-Mechanically Correct Form of Hamiltonian Function for Conservative Systems, *Physical Review* **1928**, *32*, 812–816.

[192] E. B. Wilson, J. C. Decius, P. C. Cross, *Molecular Vibrations: The Theory of Infrared and Raman Vibrational Spectra*, Dover Publications, New York, USA, **1980**.

[193] L. J. Schaad, J. Hu, The Schrödinger Equation in Generalized Coordinates, *Journal of Molecular Structure: THEOCHEM* **1989**, *185*, 203–215.

[194] M. J. Abraham, T. Murtola, R. Schulz, S. Páll, J. C. Smith, B. Hess, E. Lindahl, GROMACS: High Performance Molecular Simulations through Multi-Level Parallelism from Laptops to Supercomputers, *SoftwareX* **2015**, *1–2*, 19–25.

[195] J. Wang, W. Wang, P. A. Kollman, D. A. Case, Automatic Atom Type and Bond Type Perception in Molecular Mechanical Calculations, *Journal of Molecular Graphics and Modelling* **2006**, *25*, 247–260.

[196] J. Wang, R. M. Wolf, J. W. Caldwell, P. A. Kollman, D. A. Case, Development and Testing of a General Amber Force Field, *Journal of Computational Chemistry* **2004**, *25*, 1157–1174.

[197] M. Ceccarelli, P. Procacci, M. Marchi, An Ab Initio Force Field for the Cofactors of Bacterial Photosynthesis, *Journal of Computational Chemistry* **2003**, *24*, 129–142.

[198] L. Zhang, D.-A. Silva, Y. Yan, X. Huang, Force Field Development for Cofactors in the Photosystem II, *Journal of Computational Chemistry* **2012**, *33*, 1969–1980.

[199] M. J. Frisch, G. W. Trucks, H. B. Schlegel, G. E. Scuseria, M. A. Robb, J. R. Cheeseman, G. Scalmani, V. Barone, G. A. Petersson, H. Nakatsuji, X. Li, M. Caricato, A. V. Marenich, J. Bloino, B. G. Janesko, R. Gomperts, B. Mennucci, H. P. Hratchian, J. V. Ortiz, A. F. Izmaylov, J. L. Sonnenberg, D. Williams-Young, F. Ding, F. Lipparini, F. Egidi, J. Goings, B. Peng, A. Petrone, T. Henderson, D. Ranasinghe, V. G. Zakrzewski, J. Gao, N. Rega, G. Zheng, W. Liang, M. Hada, M. Ehara, K. Toyota, R. Fukuda, J. Hasegawa, M. Ishida, T. Nakajima, Y. Honda, O. Kitao, H. Nakai, T. Vreven, K. Throssell, J. A. Montgomery, Jr., J. E. Peralta, F. Ogliaro, M. J. Bearpark, J. J. Heyd, E. N. Brothers, K. N. Kudin, V. N. Staroverov, T. A. Keith, R. Kobayashi, J. Normand, K. Raghavachari, A. P. Rendell, J. C. Burant, S. S. Iyengar, J. Tomasi, M. Cossi, J. M. Millam, M. Klene, C. Adamo, R. Cammi, J. W. Ochterski, R. L. Martin, K. Morokuma, O. Farkas, J. B. Foresman, D. J. Fox, Gaussian 16 Revision A.03, Gaussian Inc. Wallingford CT, **2016**.

[200] C. I. Bayly, P. Cieplak, W. Cornell, P. A. Kollman, A Well-Behaved Electrostatic Potential Based Method Using Charge Restraints for Deriving Atomic Charges: The RESP Model, *The Journal of Physical Chemistry* **1993**, *97*, 10269–10280.

[201] B. Hess, H. Bekker, H. J. C. Berendsen, J. G. E. M. Fraaije, LINCS: A Linear Constraint Solver for Molecular Simulations, *Journal of Computational Chemistry* **1997**, *18*, 1463–1472.

[202] S. Páll, B. Hess, A Flexible Algorithm for Calculating Pair Interactions on SIMD Architectures, *Computer Physics Communications* **2013**, *184*, 2641–2650.

[203] T. Darden, D. York, L. Pedersen, Particle Mesh Ewald: An $N \cdot \log(N)$ Method for Ewald Sums in Large Systems, *The Journal of Chemical Physics* **1993**, *98*, 10089–10092.

[204] U. Essmann, L. Perera, M. L. Berkowitz, T. Darden, H. Lee, L. G. Pedersen, A Smooth Particle Mesh Ewald Method, *The Journal of Chemical Physics* **1995**, *103*, 8577–8593.

[205] G. Bussi, D. Donadio, M. Parrinello, Canonical sampling through velocity rescaling, *The Journal of Chemical Physics* **2007**, *126*, 014101.

[206] H. J. C. Berendsen, J. P. M. Postma, W. F. Van Gunsteren, A. DiNola, J. R. Haak, Molecular Dynamics with Coupling to an External Bath, *The Journal of Chemical Physics* **1984**, *81*, 3684–3690.

[207] D. R. Lide in *CRC Handbook of Chemistry and Physics*, (Eds.: W. Haynes, D. R. Lide, T. J. Bruno), CRC Press/Taylor & Francis Group, Boca Raton, FL, **2014**, pp. 6–156.

[208] W. G. Hoover, Canonical Dynamics: Equilibrium Phase-Space Distributions, *Physical Review A* **1985**, *31*, 1695–1697.

[209] S. Nosé, A Molecular Dynamics Method for Simulations in the Canonical Ensemble, *Molecular Physics* **1984**, *52*, 255–268.

[210] M. Parrinello, A. Rahman, Polymorphic Transitions in Single Crystals: A New Molecular Dynamics Method, *Journal of Applied Physics* **1981**, *52*, 7182–7190.

[211] S. Nosé, M. Klein, Constant Pressure Molecular Dynamics for Molecular Systems, *Molecular Physics* **1983**, *50*, 1055–1076.

Danksagung

> One never notices what has been done;
> one can only see what remains to be done.
> *Marie Curie, 1894*

An erster Stelle möchte ich mich posthum bei meiner langjährigen Doktormutter und Chefin Frau Prof. Dr. Regina de Vivie-Riedle bedanken, die mir einerseits die Freiheit gelassen hat, mich an meinen eigenen wissenschaftlichen Interessen zu orientieren, andererseits aber immer mit Rat und Tat bei Problemen zur Seite stand. Insbesondere ihre Ermutigung zur Teilnahme an zahlreichen Konferenzen und ihre Unterstützung bei der Planung und Umsetzung meines Forschungsaufenthalts im Ausland haben sehr zu meiner wissenschaftlichen und persönlichen Entwicklung beigetragen. Ihr allzu früher Verlust schmerzt. Gerade daher gilt mein Dank für die nicht selbstverständliche, unproblematische weiterführende Betreuung Prof. Dr. Christian Ochsenfeld. Ihm und Prof. Dr. Benjamin Fingerhut möchte ich für die Begutachtung dieser Arbeit danken. Ich möchte mich zudem bei meinem Kooperationspartner Prof. Dr. Jürgen Hauer für die interessante und produktive Zusammenarbeit bedanken.

Ein ganz großes Dankeschön geht auch an alle aktiven und ehemaligen Mitglieder des Arbeitskreises. Hier müssen zu allererst Sebastian Reiter und Ferdinand Pointner erwähnt werden, die bis zuletzt an meiner Seite waren, um den Arbeitskreis zu einem würdigen Abschluss zu bringen. Aber auch allen Ehemaligen möchte ich für die gute Aufnahme in den Arbeitskreis und die vielen konstruktiven Diskussionen danken. Namentlich in umgekehrt chronologischer Reihenfolge: Martin Peschel, Franziska Schüppel, Florian Rott, Thomas Schnappinger, Daniel Keefer und Matthias Roos. Mein Dank gilt auch den Studierenden, die ich in Abschlussarbeiten und Forschungspraktika betreuen durfte, insbesondere meiner späteren studentischen Hilfskraft Johannes Hofmann. Vielen Dank an Sebastian und Thomas für das Korrekturlesen dieser Arbeit.

Schließlich möchte ich mich bei meiner Familie und Freunden bedanken, die mich während des gesamten Studiums unterstützt und mir in den letzten Monaten im Ringen mit der finalen Herausforderung Doktorarbeit immer wieder den Rücken gestärkt haben.